N° **11205896**

UNIVERSITÉ DE LILLE 1 SCIENCES ET TECHNOLOGIES

École Doctorale Sciences Pour l'Ingénieur

THÈSE

pour obtenir le grade de
Docteur de l'Université Lille 1: sciences et technologies

Spécialité: Micro et Nanotechnologies, Acoustique et Télécommunications
préparée à l'Institut d'Electronique de Microélectronique et de Nanotechnologie

présentée et soutenue publiquement le 9 Décembre 2016 par:

Shiqi CHENG

Characterization and Modeling of the Polarimetric MIMO Radio Channel for Highly Diffuse Scenarios

Membres du jury

Rapporteurs:	
Pr. **Aziz BENLARBI-DELAI**	Université Pierre et Marie Curie
Dr. **Guillaume VILLEMAUD, HDR**	INSA Lyon
Examinateurs:	
Pr. **Emmeric TANGHE**	Université de Gand, Belgique
Dr. **Jean-Marc CONRAT**	ORANGE Labs Belfort, France
Directeur de thèse:	
Pr. **Martine LIENARD**	Université de Lille
Encadrant:	
Dr. **Davy GAILLOT**	Université de Lille

Acknowledgments

First of all, I would like to thank Mrs. Martine LIENARD, Professor at University of Lille also my director of thesis, for her kind support and help throughout my thesis. I'd like to express my special appreciation to my advisor Mr. Davy GAILLOT, associate Professor at University of Lille. I am grateful for his patience, motivation, and immense knowledge. His guidance helped me in every step of my PhD work. He has been very present during my research time. I will remember our discussions for a long time.

Besides my advisor, I would like to thank my thesis committee, Mr. Aziz BENLARBI-DELAI, professor at Université Pierre et Marie Curie, Mr. Guillaume VILLEMAUD, HDR at INSA Lyon, Mr. Emmeric TANGHE, professor at Université de Gand, and Mr. Jean-Marc CONRAT at ORANGE Labs Belfort for having accepted to examine my work.

I am also very grateful to all the people who have cooperated with me and provide many insightful discussions and suggestions for me: Maria-Teresa Martinez-Ingles, Jose-Maria Molina-Garcia-Pardo, Pierre Degauque and etc.

I thank all the members of the Telice group for providing one pleasant working environment. I would also like to express my gratitude to my colleagues: Farah, Huaqiang, Raouf, Navish, Rose, Fredy, Ali and etc, for their sympathy and friendship. It is a very nice experience to work with them.

No words can express my appreciation to my family. I am very grateful to my parents for all the supports that they have provided to me. I'd like to thank all my family members for their supports during my study.

Last but not the least, I would also like to thank all my friends who encouraged me and spent many good times with me: Sijia GU, Tianchen ZHANG, Tianjun LIN, Tianqi ZHU, Jianping HAO, Xiaokun DING, Wei WEI, Di ZHOU, Li Shuo, Sizhe LI, Xin YAN, Haoling QI, Zhifang JIANG, Liu LIU and etc. Unfortunately I cannot mention them all individually here, but I'd like to express my highest gratitude for all the good times spent together.

I want to rethank to all the people I mentioned above and also to the people whom I couldn't mention but directly or indirectly helped me during my study. Without your help, I couldn't be here.

Abstract

A deeper understanding of the radio channel propagation phenomena is the key to improve the overall performance of wireless communication systems. This is particularly true for challenging propagation environments wherein strong diffuse scattering mechanisms are observed. However, the most recent radio channel models do not include this component and must be re-evaluated.

In this thesis, it is proposed to decompose the polarimetric MIMO radio channel into specular and dense multipath components (SMC and DMC) where DMC includes diffuse scattering and weak SMC. The purpose of this decomposition is to investigate the contribution of DMC to the radio channel and develop a comprehensive modeling framework; framework which has been applied to two propagation scenarios presenting strong diffuse scattering mechanisms: indoor industrial and outdoor vegetation. Here, novel polarimetric models have been developed and validated from measured radio channels.

Moreover, a multipath component distance (MCD)-based automatic clustering identification algorithm is proposed to group SMC obtained from measured radio channels. Its performance and robustness are compared with the K-means MCD algorithm using cluster data simulated by the WINNER II channel model. The validated clustering algorithm was then directly applied onto data which were estimated from the measured radio channels with or without DMC in the radio channel data model.

The results unambiguously demonstrate that the proposed models not only provide a better understanding of the propagation mechanisms but also that radio channel models without DMC could potentially mislead the interpretation of those mechanisms.

Contents

List of Figures

List of Tables

List of variables, notations and acronyms

List of variables

$\mathbf{X}$	Set of channel observations matrix
γ_{HH}	Complex path weight for HH polarization
γ_{HV}	Complex path weight for HV polarization
γ_{VH}	Complex path weight for VH polarization
γ_{VV}	Complex path weight for VV polarization
$\mathbf{R}$	Covariance matrix
$\mathbf{I}$	Identity matrix
$\mathbf{s}(\theta_{sp})$	Parametric model for specular paths
$\mathbf{B}$	General matrix valued function
$\mathbf{B}_T$	Transmission array response for all specular paths
$\mathbf{B}_R$	Reception array response for all specular paths
$\mathbf{B}_f$	Frequency response for all specular paths
$\mathbf{B}_t$	Time domain response for all specular paths
$\mathbf{A}_T$	Steering vectors of transmission antenna array

$\mathbf{A}_R$	Steering vectors of reception antenna array
$\mathbf{A}$	General complex exponential matrix
ϑ_T	Azimuth of departure
φ_T	Elevation of departure
ϑ_R	Azimuth of arrival
φ_R	Elevation of arrival
$\boldsymbol{\mu}$	Normalized parameter vector
L	Total number of rays
L_k	Number of rays in the k-th cluster
K	Total number of cluster
c_k	Centroid of k-th cluster
c	Global centroid
K_{opt}	Optimal estimated number of cluster
s_l	l-th ray in one cluster
SFg	Fusioned cluster validation indice
n_{pri}^{XY}	Path loss exponent for primary SMC with each polarization link
n_{sec}^{XY}	Path loss exponent for secondary SMC with each polarization link
$\mathbf{G}_0$	Path gain at reference distance
$\mathbf{R}$	Reverberation ratio
d_0	Reference distance
$\mathbf{T}$	Reverberation time

List of notations

$\langle\ \rangle$	Mean value
$\hat{a}$	Estimated value of a
$()^H$	Complex conjugate transposition
$\diamond$	Khatri-Rao product
$\otimes$	Kronecker product
$\det()$	Determinant of matrix
$\mathcal{N}_C(,)$	Complex circular symmetric Gaussian process with defined mean value and variance
$\arg\max()$	Argument that maximizes objective function

List of acronyms

ASA	Azimuth Spread of Arrival
ASD	Azimuth Spread of Departure
AWGN	Additive White Gaussian Noise
BER	Bit Error Rate
CVI	Clustering Validity Indices
DMC	Dense Multipath Component
DOA	Direction of Arrival
DOD	Direction of Departure
DS	Delay Spread
EADF	Effective Aperture Distribution Function
ED	Exponential Decaying
ESA	Elevation Spread of Arrival
ESD	Elevation Spread of Departure
ESPRIT	Estimation of Signal Parameters via Rotational Invariance Techniques
GSCM	Geometry-based stochastic channel model
LOS	Line of Sight
LNA	Low Noise Amplifier
LSP	Large-Scale Parameters
MCD	Multipath Component Distance
MIMO	Multi-Input Multi-Output

MPC	Multipath Component
MUSIC	Multiple Signal Classification
MVDR	Minimum Variance Distorsionless Response
OFDM	Orthogonal Frequency Division Multiplexing
PDP	Power Delay Profile
PL	Path Loss
RMSE	Root-Mean-Square Error
SAGE	Space-Alternating Generalized Expectation Maximization
SNR	Signal to Noise Ratio
SIMO	Single-Input Multi-Output
SMC	Specular Multipath Components
SV	Saleh-Venezuela
TOA	Time of Arrival
UCA	Uniform Circular Array
URA	Uniform Rectangular Array
UTD	Uniform Theory of Diffraction
UWB	Ultra wide band
XPD	Cross-Polarization Discrimination

Introduction

Over the past decade, the continuous and massive arrival of smart and compact equipments such as laptops, smartphones, tablets, or even phablets (contraction of phone and tablet) as well as the growing thirst of third-party applications for data has required the design of novel telecommunication architectures and signal processing techniques. From the basic voice calls to the HD video applications, all of these services generally require a larger throughput with reduced latency. Unfortunately, the limited bandwidths of the existing communication systems can not satisfy the increasing demand and various technical solutions have been proposed and emerged at different layer levels of the system. Multiplexing and diversity-based techniques have been gradually introduced in recent communication systems to support this trend. As an example, MIMO (Multiple-In Multiple-Out) techniques which rely on the use of multiple antennas at the transmitter and/or emitter were proposed to exploit the spatial dimension of the physical radio channel and provide a higher spectrum efficiency solution. For instance, MIMO techniques can either be deployed to increase the total throughput or improve the overall robustness of the communication link under degraded conditions. This technique has been standardized in wireless communication protocols such as the WiFi 802.11n/ac legacy standards, LTE, or WiMAX. This technique takes advantage of the inherent multipath effect in a rich scatterer environment like urban or indoor scenarios. Moreover, polarization diversity in the radio channel can provide another dimension to further increase the robustness or throughput of the radio link.

Communication systems need to operate in the most complex and harsh radio channel propagation environments. As an example, the Internet of Things (IoT), which will be encompassed in the upcoming 5G standard, widen the application range of wireless communication systems and can be deployed in any favorable or not propagation scenarios. As a consequence, the performance of such systems must be evaluated thanks to dedicated radio channel models. It is well-known that the radio channel exhibits different characteristics under different propagation environments. Hence, in order reach a reliable and robust communication link, the radio channel has to be studied for a wide range of propagation scenarios, frequency bands, and antenna types and configurations. For instance, the interest to deploy

wireless systems in the industrial field under the scope of smart factories or factories of the future grows progressively to increase the productivity and flexibility. In addition, another inevitable propagation environment is the vegetation scenario which is widely recognized by the mobile operators as very challenging. Nonetheless, specific applications such as positioning or search and rescue services in forests require robust communication systems.

The Multipath Components (MPCs) which contribute to the radio channel richness are directly linked to the channel fading properties as well as other known physical effects described in this manuscript. For instance, in a geometrically complex propagation environment, multipath fading severely degrades the performance of communication systems and this effect is, as an example, particularly strong for typical indoor scenarios. If the multipath characteristics can be well characterized, then mitigation or dedicated access techniques can be implemented at the system level to reduce the disturbance resulting from multipath fading. Therefore, a deep understanding of the radio channel propagation phenomena and related characteristics is the key to improve the overall system performance. Moreover, this enables the development of more realistic multi-purpose radio channel models which can then be used for wireless network and smart city planning.

Figure 1 presents the typical methodology to characterize the propagation characteristics of any scenarios and to develop realistic radio channels. First, a narrowband or wideband system with single or multiple antennas are used to measure the radio channel transfer functions. Many large-scale features of the radio channel can be estimated from the measurement data such as the delay spread, coherence bandwidth, etc. In addition, path loss models to predict the received signal strength can be derived. These parameters or models have been very popular as simple metrics to deploy and design wireless communication systems. However, they do not provide any understanding of the inherent propagation mechanisms such as the MPC or diffuse scattering. At this point, it was shown that the MPC and diffuse scattering can be subcategorized into specular multipath components (SMC) and dense multipath components (DMC). SMC includes the large Signal-to-Noise Ratio (SNR) SMC whereas DMC includes both diffuse scattering and low SNR SMC. In order to gain this knowledge, parametric estimation of the SMC must be performed to assess the propagation mechanisms on a geometrical level. Basically, one is interested into finding where, when, and from which direction the SMC depart and/or arrive at the transmitter and/or receiver side, respectively. The radio channel propagation characteristics can then be statistically investigated as a function of transmitter/receiver distance, polarization, frequency band, etc. Furthermore, algorithms can be applied to the estimated data to group the MPC into clusters which can be further statistically analyzed. The comprehension of the propagation mechanisms in terms of geometrical parameters and clusters form the basis of the recently developed geometry-based stochastic channel models (GSCM). GSCM aim at providing realistic simulated radio channels at the link and system levels while minimizing the computational time. However, it must be clear that all the devel-

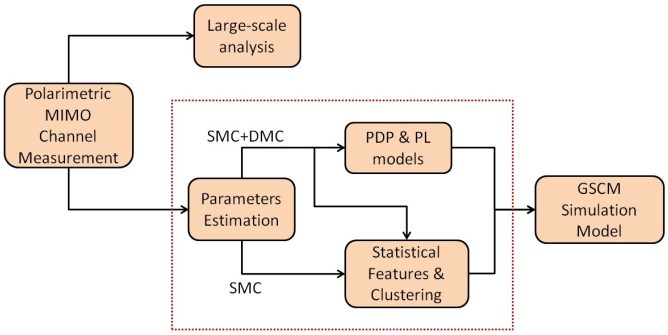

Figure 1: Radio channel modeling methodology.

oped radio channel models and underlying propagation mechanisms do not take into account diffuse scattering (or DMC) and must be re-evaluated. In this context, the motivation behind this thesis lies in the will to investigate and provide a detailed study of the diffuse scattering characteristics in highly diffuse scenarios.

Due to the natural presence of rich scatterers, the industrial and vegetation scenarios, which are not widely studied in the literature, have been identified as challenging propagation scenarios. Thus, the level of understanding of the propagation mechanisms for these scenarios is rather low or not sufficient. In addition, radio channel models such as path loss or clustering-based models for these specific scenarios are not only scarce but also completely undermine the contribution of diffuse scattering. Hence, the originality of this work is to examine the contribution of this component to the polarimetric radio channel with newly built dedicated path gain models. In addition, in order to highlight the impact of diffuse scattering on the goodness and validity of clustering features, the clustering data is studied with the hypothesis that diffuse scattering is included or not in the radio channel. Finally, another originality of this thesis arises from the inherent difficulties to link experimental measurement of polarimetric radio channels including diffuse scattering with theoretical modeling of propagation components and clustering features estimated from these radio channels.

This manuscript is organized around five chapters as follows:

The first chapter is dedicated to the state-of-the-art on radio channel propagation. The multipath components are introduced and associated with the radio channel fading effects. In addition, a comprehensive analysis of the propagation mechanisms and models in industrial and vegetation environments is presented. Finally, a review of the most previous works on this topic is provided.

In the second chapter, the maximum-likelihood (ML) channel parameter estimation technique used to estimate the double-directional multipath component and diffuse scattering is described. This technique is pivotal in this work to assess the radio channel characteristics from measured radio channels. Furthermore, a description of the two MIMO radio channel sounders as well as the antenna array characteristics will be introduced.

The third chapter is the heart of this manuscript in which all models including diffuse scattering are presented. First, the developed polarimetric distance-dependent model of the received path gain and path loss model for indoor scenarios will be presented. Moreover, a novel dedicated automatic clustering identification method will be proposed and its performance and robustness discussed.

The fourth and fifth chapter focus on the propagation characterization and modeling of an industrial and vegetation scenarios, respectively. The measurement campaigns will be introduced in details. The validation of the distance-dependent model is discussed and a discussion on the propagation characteristics is proposed. The clustering of the estimated data and subsequent statistical analysis of the cluster/intra-cluster distributions is finally presented.

Finally, a general conclusion and perspectives are provided to the reader.

List of Publications

Journal paper

- **Polarimetric Distance-Dependent Models For Large Hall Scenarios**

  S. Cheng and D. P. Gaillot and E. Tanghe and P. Laly and T. Demol and W. Joseph and L. Martens and M. Liénard

  IEEE Transactions on Antennas and Propagation, vol. 64, no. 5, pp. 1907-1917, May 2016.

- **Performance of a Novel Automatic Identification Algorithm for the Clustering of Radio Channel Parameters**

  S. Cheng, M. T. Martinez-Ingles, D. P. Gaillot, J. M. Molina-Garcia-Pardo, M. Liénard and P. Degauque

  IEEE Access, vol. 3, pp. 2252-2259, 2015.

Peer-reviewed international conference with proceedings

- **Polarimetric properties and modeling of the power delay profile in large hall scenarios**

  S. Cheng and D. P. Gaillot and P. Laly and M. Liénard and T. Demol and E. Tanghe and W. Joseph and L. Martens

  Networks and Communications (EuCNC), 2015 European Conference on, Paris, 2015, pp. 113-117.

- **Clustering of Radio Channel Parameters: Evaluation of a Novel Automatic Identification Algorithm**

  S. Cheng, D. P. Gaillot, M. Liénard, P. Degauque, M. T. Martinez-Ingles, and J. M. Molina-Garcia-Pardo

2016 IEEE Antennas and Propagation Society International Symposium, Fajardo Puerto Rico, 2016.

International conference without proceedings

- **Evaluation of a Novel Automatic Identification Algorithm for the Clustering of Radio Channels**

  S. Cheng, M. T. Martinez-Ingles, D. P. Gaillot, J. M. Molina-Garcia-Pardo, Martine Liénard, and Pierre Degauque

  2015 Joint NEWCOM/COST Workshop on Wireless Communications (JNCW) 2015, Barcelona, Spain 2015, Temporary Document TD(15)W1015.

Chapter 1

State-of-the-art on radio channel propagation and modeling

1.1 Multipath channel

Basically, wireless radio propagation is the physical process of electromagnetic waves propagating at a given frequency or across a frequency range in both space and time. The simplest radio propagation example is free space propagation where it is considered that the transmitter and receiver are under unobstructed Line-Of-Sight (LOS). If only the direct wave arrives at the receiver, the received signal power is inversely proportional to the square of the distance and is well predicted by the Friis free space equation [7]. However, under most common radio channel propagation scenarios, the propagation environment is far more complex than the free space case and a deeper analysis of the channel propagation mechanisms must be performed.

1.1.1 Channel propagation mechanisms

The electromagnetic waves will interact with all the objects present in the environment. Under the geometrical optics description, the waves are often called rays or paths. Figure 1.1 presents the three fundamental propagation mechanisms: reflection, diffraction, and scattering diffusion.

Reflection mechanisms have been studied for decades on the analytical, numerical, and measurement level. Reflection phenomena occur when an electromagnetic wave impinges on one object which has a large electrical dimension compared to the incident wavelength. During reflection, the angle of incidence and angle of reflection are identical. Typically, specular reflection of the electromagnetic waves would occur off the ground, walls, and ceilings (indoor scenarios) and can be described in terms of Fresnel reflection. Besides, one important propagation model associated to this phenomenon and derived from the free space equation is the ground reflection model [7] which should also be mentioned.

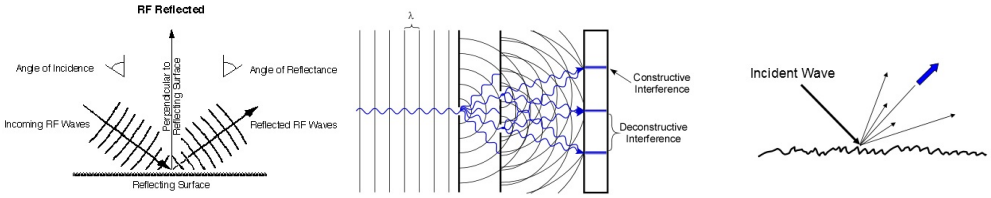

(a) (b) (c)

Figure 1.1: Example of the three basic propagation mechanisms: (a) reflection, (b) diffraction, (c) scattering.

Another classical electromagnetic propagation mechanism is diffraction. This effect happens when a wave impinges on an edge sharp object. According to the Huygens principle, each point on the wave front can be considered as a secondary source. At the boundary of the edge, these secondary sources will illuminate the shadowed region behind the obstacle space. Diffraction is described in details in terms of the Fresnel Zone. The signal attenuation can be well predicted by the single knife-edge diffraction model [7]. This model was further extended in [8] to apply on the multiple knife-edge diffraction problem.

Last but not least, scattering phenomena occur when electromagnetic waves impinge on rough surfaces. The energy is then diffused in all directions. Diffused energy makes an importance part in the received energy of radio channels because they are more likely to arrive at the receiver compared with reflected waves. Diffusion is strongly dependent to the surface roughness characterized by the Rayleigh criterion. Furthermore, one scattering loss factor [8, 9] has been introduced to describe the diffused electrical field.

1.1.2 Radio channel fading

In a complex radio channel propagation environment such as indoor scenarios, the electromagnetic waves arrive at the receiver from different directions (see Figure 1.2) and exhibit different signal strength, phase, and polarization state. In addition, they can individually suffer different propagation mechanisms or a mix of several propagation mechanisms. It follows that the received signal can be understood as a sum of these attenuated and delayed waves. In addition, since the multipath components are filtered by the receiving chain due to the limited bandwidth of analog/digital electronic components, multipath components arriving within the delay resolution of the system coherently add up. This whole process is the cause of multipath propagation and fading.

Fading can be split into large-scale and small-scale fading. Large-scale fading (or path loss) describes the received signal level after traveling over a large area (hundreds of wavelengths) whereas small-scale fading describes the signal level after encountering obstacles (several wavelengths to fractions of wavelengths) in the vicinity of the receiver. These effects are highlighted in Figure 1.3 which presents

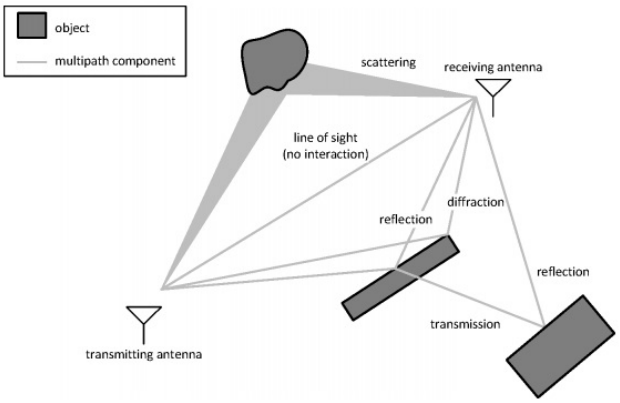

Figure 1.2: Multipath radio channel

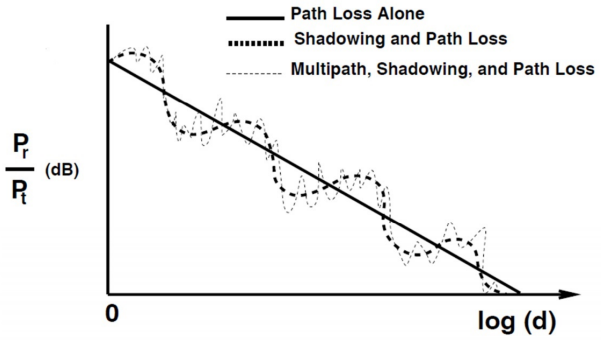

Figure 1.3: Large-scale and small-scale fading effect on the received signal level

the normalized received power over transmitted power as a function of distance.

1.1.2.1 Large-scale fading

Path loss was introduced to characterize the signal strength over large transmitter and receiver distances. Path loss models are important tools to analyze the cellular coverage range and optimize the communication systems.

Typically, the path loss can be modeled as following:

$$PL(d) = PL(d_0) + 10n \cdot log(\frac{d}{d_0}) + \chi_\sigma \tag{1.1}$$

where χ_σ is a log-normally distributed random variable with zero mean (in dB) and standard deviation σ characterizing the shadowing effect, n the path loss exponent, and d_0 is the arbitrary reference distance. The parameters are empirically derived from measurement data using power law fittings. Path loss models are very popular and provide a general behavior of the received signal level for any scenarios [7]. However, it must be noted that they don't provide information about the underlying propagation mechanisms in the radio channel.

1.1.2.2 Small-scale fading

Small-scale fading is a consequence of the multipath propagation nature of the channel. There are generally two factors influencing small-scale fading which are the delay spread and the doppler spread. From the system level, the multipath channel capacity is limited by the delay spread of the channel. If we are under the case of selective fading, see Table. 1.1, the rapid fluctuation of the received signal strength will result in inter-symbol interference which will further cause a degraded communication link with a large Bit Error Rate (BER).

Table 1.1: Delay spread impact to small-scale fading

Flat fading	Selective fading
Signal bandwidth < channel bandwidth	Signal bandwidth > channel bandwidth
Delay spread < symbol period	Delay spread > symbol period

In addition, the doppler spread which is a consequence of the radio link dynamics can also contribute to the small-scale fading as presented in Table. 1.2. When the channel suffers fast fading, the impulse response of the channel will be distorted and the SNR will be decreased resulting in an increased BER.

Table 1.2: Doppler spread impact to small-scale fading

Fast fading	Slow fading
High Doppler spread	Low Doppler spread
Coherence time < symbol period	Coherence time > symbol period
Base-band signal variation < channel variation	Base-band signal variation > channel variation

From the channel modeling point of view, small-scale fading can be well modeled with random variables. For instance, Rayleigh fading model is popular to simulate the radio channel under Non-LOS (NLOS) propagation conditions whereas Rician Fading model is suitable for LOS conditions [7].

1.1.2.3 Polarization

Polarization is yet another electromagnetic characteristic which is a source of radio channel fading and can be used to boost the communication link performance. To date, systems using orthogonal polarization states have been playing an important role in modern wireless communication [10]. If well designed, polarization diversity is a technique that mitigates deep fading due to the random handset orientation and multipath propagation. Also, the transmitted rate can be potentially doubled or tripled compared to single polarized systems [11]. The effect of polarization mechanisms can be seen not only from the radio channel but also from the receiver side. From the electromagnetic propagation point of view, depolarization is caused by the multiple reflections or oblique reflections with objects present

in the environment. The complex reflection coefficients depend on many parameters including the objects properties, roughness, frequency, etc. [7]. Under certain conditions, high-order specular reflections can result in receiving partially canceled orthogonal polarization links. From the antenna point of view, the conventional dual polarization antenna has limited cross-polarization discrimination. This will introduce correlation between the signals received at the ports resulting in a decreased performance.

When polarimetric measurements are considered, the impact of the antennas must be, anyhow, removed from the analysis of the radio channel characteristics since both the emitting/receiving antennas and propagation mechanisms have an effect on the received polarimetric signal levels. This implies that the polarized antenna patterns which describes the received frequency-dependent gain as a function of the polarization vector must be measured [12].

Channel depolarization is characterized using the cross-polarization discrimination (XPD) defined as the ratio of the co-polarization average received power to the cross-polarization average received power. The co-polarization is defined with respect to the emitter polarization state.

$$XPD(dB) = 10log10\left(\frac{\langle P^{co-pol}\rangle}{\langle P^{cross-pol}\rangle}\right) \tag{1.2}$$

where$\langle P^{co-pol}\rangle$ is the average received power for the co-polarization link whereas $\langle P^{cross-pol}\rangle$ is the average received power for the cross-polarization link.

1.1.3 Multipath radio channel

The signal power is one of the key parameters to design robust communications chains. It can evidently be measured from the received signal but also modeled. The modeling complexity will not only depend on the observable frequency, space, and time samples but also on the underlying physical understanding of the radio channel. Let's first consider the Single-Input Single-Ouput (SISO) link with one fixed transmitter and one moving receiver. Assuming a constant speed, the complex time-varying channel impulse response is obtained at each sampling time. For such a case, the channel impulse response is a series of complex values containing various channel information. One of the most classical and simple model for the baseband time-varying channel impulse response is given by:

$$h(t,\tau) = \sum_{i=0}^{N(t)-1} a_i(t)e^{-j\theta_i(t)}\delta(\tau - \tau_i(t)) \tag{1.3}$$

where t is the sampling time, τ the excess delay, a the complex amplitude, θ the phase, and N the number of received paths. It is noteworthy that this delay model is incomplete as it does not take into account the spatial or angular distribution of the paths with respect to the transmitter or receiver. If the measurement time

is smaller than the coherence time of the channel (time duration over which the channel impulse response is considered to be not varying), the channel radio channel is considered to be stationary and the transmitter/receiver distance d can be included such that the impulse response is given by $h(\tau, d)$. Since this manuscript primary focuses on the development of stationary models, the time-varying aspect of the radio channel is not discussed. Also, it has to be mentioned that the impulse response can alternatively be obtained and modeled as the inverse Fourier transform of the complex transfer function with respect to frequency $H(f, d)$.

For the MIMO techniques considered here, the observed impulse response can be simply extended to $h(\tau, d, m, n)$ where m and n are respectively the number of transmit and receive antennas. The power of the multipath components can then be computed as a function of time delay from the channel impulse response. This power delay profile (PDP) is defined as the expectation of the squared amplitude over all antennas.

$$P(\tau, d) = E\left[|h(\tau, d, m, n)|^2\right] \tag{1.4}$$

An arbitrary example of the PDP is illustrated in Figure 1.4.

1.1.4 Specular and Dense Multipath Component

1.1.4.1 Specular Multipath Component

Originally, the radio channel was considered as a mere collection of Specular Multipath Components (SMC) that have well-defined discrete locations in the different radio channel dimension plus Additive White Gaussian Noise (AWGN). Hence, the contribution of the distributed diffuse scattering process was broadly neglected. Basically, SMC include any paths suffering reflection and diffraction mechanism. A given SMC can be described by a set of geometrical parameters including the Time-Of-Arrival (TOA), Direction-Of-Arrival and Departure (DOA/DOD), and doppler. From Figure 1.5, it can be observed that the band-limited radio channel makes it somewhat difficult to extract individual paths in the delay domain. Nonetheless, it is possible to identify a few SMC exhibiting a high SNR as well as their TOA and peak amplitude.

At this point, only typical large scale parameters such as the root-mean-square (rms) delay spread, coherence bandwidth/time, power, signal-to-noise-ratio (SNR), and other characteristics can be computed from the measured channels [7]. Nonetheless, advanced digital signal processing techniques have been developed since the early seventies to extract the geometrical parameters of individual components mostly for radar and localization applications. In particular, high-resolution parametric estimation techniques described later in this manuscript allow to separate the multipaths components from the measured complex impulse response (or transfer function). These techniques rely on the diversity offered by the system to estimate the geometrical parameters. For instance, the TOA can be obtained thanks to the frequency diversity. The DOA/DOD are provided by having multiple anten-

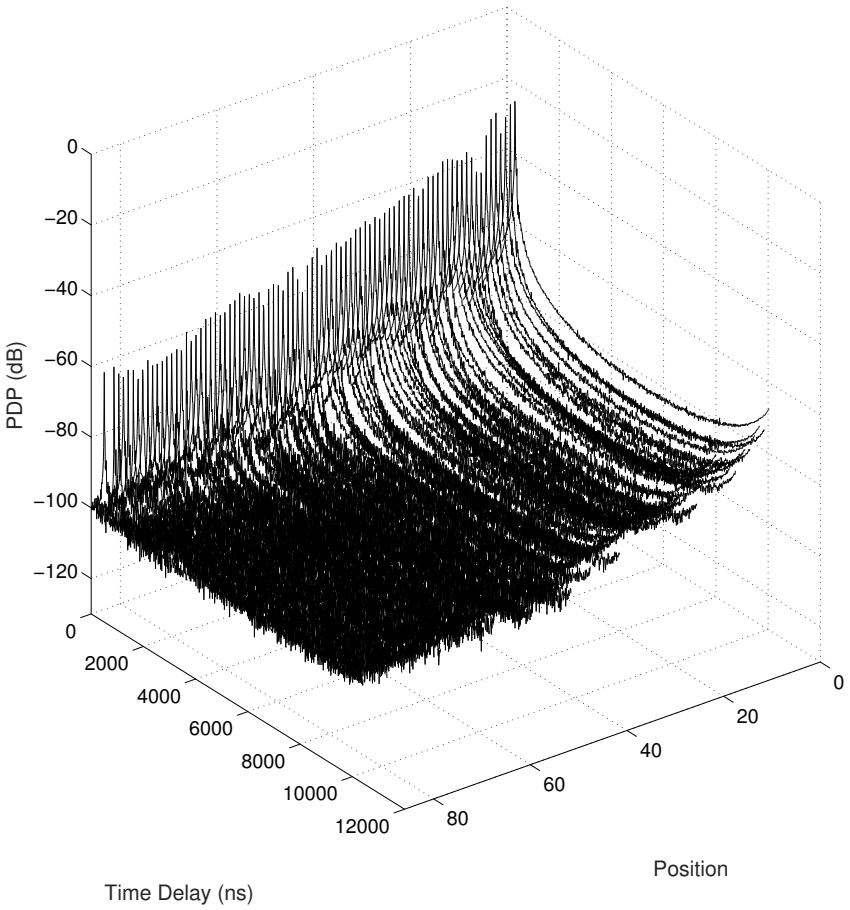

Figure 1.4: Example of a normalized channel at 1.35 GHz with 80 MHz bandwidth under LOS condition for an outdoor scenario.

nas at the receiving and transmitting side, respectively. Finally, the doppler can be estimated from samples of the time-varying radio channels. Depending upon the communication link type and investigated scenario, it is then possible to jointly estimate one or multiple parameters for each SMC.

1.1.4.2 Dense Multipath Component

When these estimated SMC components have been removed from the channel impulse response, it is typically observed that the residual power is still rather large. This power was historically attributed to distributed diffuse scattering which was omitted in the data models of the estimators. It is only recently that it has been revealed that not only the radio channel includes distributed diffuse scattering on electrically small objects but also SMC with low SNR values. Nowadays, it is well-accepted that these effects cannot be distinguished from each other and form the basis for the Dense Multipath Components (DMC) [13] which illustrated in Figure 1.5. In other words, DMC can be alternatively be interpreted as the non-

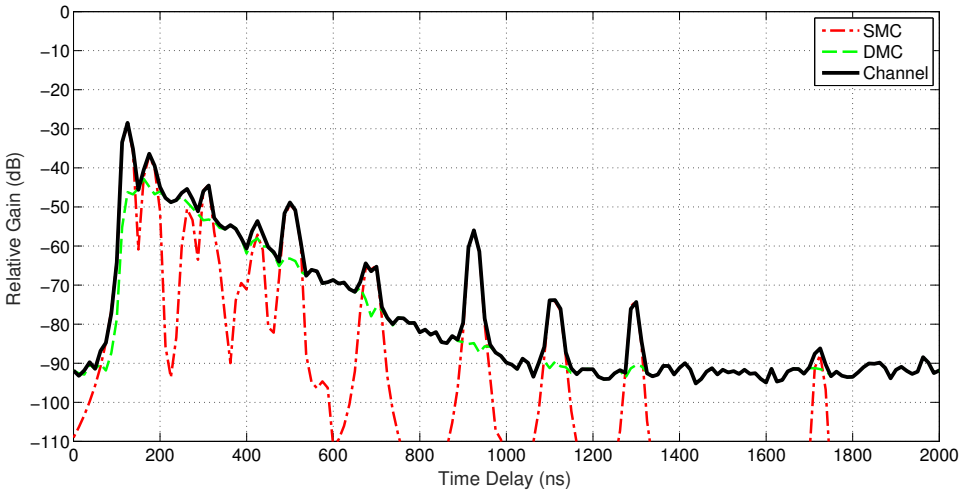

Figure 1.5: Example of a band-limited limited Power Delay Profile for an indoor environment with SMC and DMC.

coherent superposition of paths with weaker SNRs than the SMC, which still follow the specular power decay as a function of distance [14, 15]. Hence, the introduction of DMC in the physical model implies that common radio channel parameters have to be re-evaluated. DMC is introduced to describe the contribution of large number of weak propagation path that cannot be estimated. The contribution of DMC to the total received power can vary between 10% and 90% [16] and is observed to depend strongly on the propagation environment. It also follows that DMC plays an important role in the channel capacity.

Therefore, a faithful DMC model is critical to assess the propagation characteristics of the radio channel model. It is observed that the PDP decays exponentially over time delay and has a base delay corresponding to the first arrived signal components. The most widely used DMC model was introduced in [17]:

$$\mathbf{P}(\tau) = \mathbf{E}[|h(\tau)|^2] = \begin{cases} 0 & ,\tau < \tau_d^{'} \\ \frac{1}{2}\alpha_1 & ,\tau = \tau_d^{'} \\ \alpha_1 e^{-B_d(\tau-\tau_d^{'})} & ,\tau > \tau_d^{'} \end{cases} \tag{1.5}$$

where $\tau_d^{'}$ is the base delay, α_1 the maximum power, and B_d the coherence bandwidth of the diffuse components. Figure 1.6 illustrates the PDP obtained from the DMC parameters where α_0 is the AWGN variance.

Even though the physical interpretation of the radio channel with DMC can differ greatly with a radio channel with only SMC, it still has to be highlighted that the characteristics used for typical coverage analysis (path loss, mean delay, root mean square delay, and others) are still valid. However, the contribution of DMC to these large scale parameters is broadly ignored in the literature.

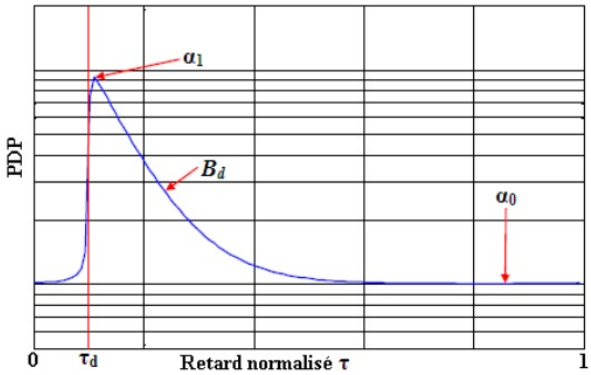

Figure 1.6: Example of Dense Multipath Component.

1.1.4.2.1 room electromagneticss theory One widely accepted assumption is the exponentially decaying tail of the PDP observed in indoor measurement results. This observation coincidentally matches the acoustic reverberation results which describe how the acoustic energy dissipates in a reverberation chamber. Later, this theory has been extended into the radio frequency spectrum in terms of the room electromagnetics theory [18]. The theory and experimental observation from the reverberation chambers confirmed that the exponentially decaying tail happens in the radio frequency domain. Moreover, the decaying rate which is one important factor to describe the PDP decaying tail was introduced. It can be theoretically obtained from the Sabine's [19] and Eyring's [20] reverberation models. From these models, the decaying rate is further described by one reverberation time that is merely a function of propagation environment parameters such as the average absorption coefficient, the room volume, and the surface of the room.

Sabine's reverberation model assumes that a diffuse field is solely contained in a single room. Hence, the incident power source $\mathbf{S}(t)$ splits into the reverberation power and the absorption power. This power balance function of an isotropic diffuse field has been derived in [19]:

$$\mathbf{S}(t) = \underbrace{V\frac{dW}{dt}}_{reverberation\ power} + \underbrace{\frac{c\eta A}{4}W}_{absorption\ power} \tag{1.6}$$

where c is the speed of light, A the energy absorption surface, V the room volume, η the average absorption coefficient of the room, and W the energy density in the room which is also a function of time.

If the energy source is switched off, $\mathbf{S}(t) = 0$, a solution to the homogeneous equation (1.6) is given by:

$$W(t) = W_0 e^{-t/\tau} \tag{1.7}$$

where τ is expressed as the Sabine's reverberation time, it is further represented as:

$$\tau_{Sab} = \frac{4V}{cA\eta} \tag{1.8}$$

In contrast, this equation was slightly modified by Eyring for scenarios with larger room volume. Eyring's reverberation time is defined as:

$$\tau_{Eyr} = -\frac{4V}{cAln(1-\eta)} \tag{1.9}$$

These models provide a simplified approach to predict the PDP characteristics. Nonetheless, based on the room electromagnetics theory, various DMC models were developed for indoor environments [21, 22, 23]. In these models, the DMC is typically observed as the decaying slope of the PDP and characterized by its reverberation time. Recently, the polarization and frequency band dependence to the reverberation time have been investigated in [24]. Besides, measurement campaigns with the aim to study the DMC characteristics have been reported in several works. From the existing literature, the absorption coefficient η was found to be 0.29 in [25] for an industrial environment, and 0.45 in [26] for an indoor office, both using Sabine's model. Very recently, the reverberation effect has been experimentally validated in typical indoor office environments with a dedicated validation process [27]. In this later study, the PDP tail was observed to be independent of the measurement position. It also concluded that Eyring's model is more accurate than Sabine's model when propagation environment with high absorption coefficient are considered. Finally, it has to be noted that these models are not appropriate for outdoor radio channels even though DMC is also typically observed.

1.1.5 MPC Clustering

Depending on the complexity of the environment, Some of the MPC contributing to the radio channel can display a high degree of correlation between each other in the delay, angular and polarization domains resulting in the notion of clustering. This physical correlation is attributed to the spatial distribution of the scatterers in the environment either around the emitter or receiver. The cluster behavior has been firstly observed by Saleh and Valenzuela [28] in the multipath channel propagation of an indoor scenario for wide-band SISO channel measurements. The Saleh-Valenzuela (S-V) model was introduced as an empirical statistical channel model and an example is shown in Figure 1.7.

The cluster model is only defined in the power-delay domain and assumes that the power of each cluster decays exponentially. The overall envelop also decays exponentially with a different decaying rate. This model has been widely accepted but the cluster's definition is only for the TOA due to the SISO configuration. Hence, it does not provide additional information of the MPC distribution in the angular domain. Nonetheless, clustering techniques performed on MIMO radio channels indicate that it is likely that the TOA, DOA, and DOD are correlated in indoor

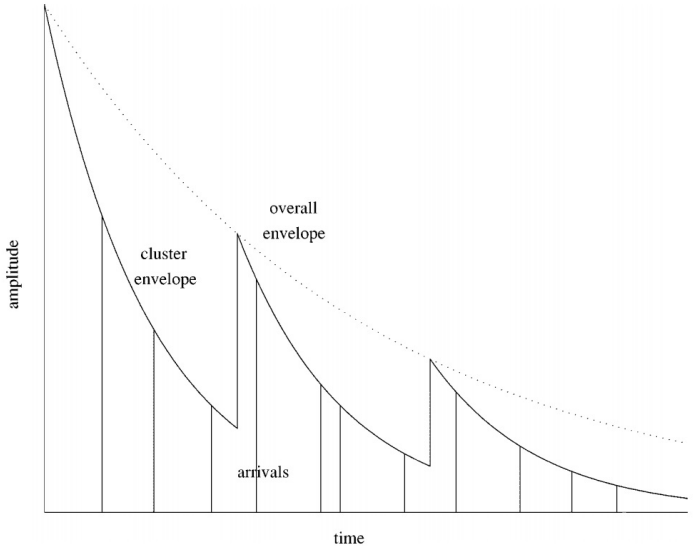

Figure 1.7: Example of Saleh-Valenzuela model for SISO measurement.

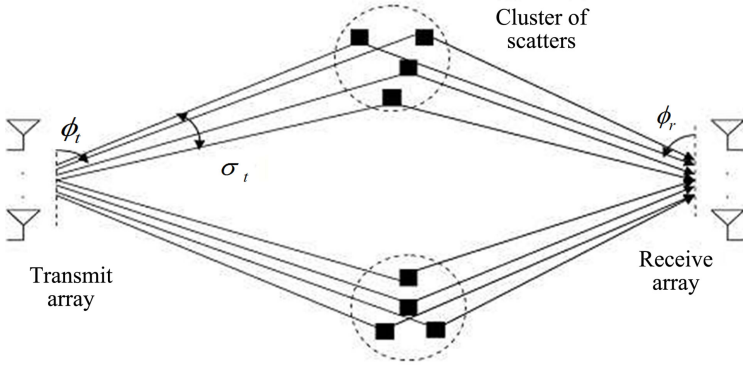

Figure 1.8: Example of cluster in a MIMO radio channel.

scenarios (MPC belonging to a cluster share the same characteristics). Modeling of the radio channel under the clustering assumption is not only appealing because of its simplicity but also because statistical distributions of the clusters and MPC parameters can be derived and then applied to many similar scenarios. In addition, clustering provides more insight into the propagation mechanisms of the radio channel. Figure 1.8 gives an example of a clustered double-directional radio channel in the spatio-temporal domain.

The cluster characteristics of radio channels have been reported in various works [29, 30, 31, 32]. Typically, the average number of clusters, cluster delay spread, cluster angular spreads, cluster lifetime, cluster fading statistic and cluster correlation, etc. are computed after the clustering technique is applied onto the estimated MPC. Besides, the inter-cluster and intra-cluster characteristics of outdoor scenarios have also been reported in [33]. They concluded that the elevation angle should be included in the clustering identification process when the transmitter and receiver are nearby

rich scatterers. More recently, it has been reported that radio channel models which do not include a spatio-temporal clustering hypothesis result in overestimating the channel capacity [34].

The simplest cluster identification technique is to visually inspect the data in the azimuth-delay domain. However, this identification method is very hard to apply on large double-directional channel dataset estimated by high resolution channel parameter estimation algorithms. In addition, the problem is tightly bound to the definition of what a cluster should be. For instance, there are various opposite definitions of the cluster like in [35, 36]. Nonetheless, it is generally accepted that the intra-cluster distribution is rather similar from clusters to clusters and that the inter-cluster distance must be sufficiently large to avoid cluster overlapping. These conditions can be used to improve the definition of a cluster and optimize the sorting process. Needless to say, an automatic cluster identification approach is needed to compute the cluster characteristics for large dataset anyway. A complete approach to study the cluster features was first reported in [37]. They found that the cluster properties are different in LOS and NLOS scenarios.

1.2 Existing radio channel models

To evaluate the link/system performance under certain propagation scenarios, radio channels have to emulated with dedicated radio channel models. These models must reproduce the main propagation characteristics of these scenarios in terms of path loss, delay spread, capacity for example. Evidently, the development of radio channel models must be initially performed by investigating the propagation characteristics of the environment. To study the behavior of the radio channel and evaluate the wireless communication performance at the link or system level, the channel impulse response model is often needed to simulate the distance-dependent $h(\tau, d)$ multipath radio channel. There exists many versatile models which can be classified into three categories: the deterministic model, stochastic model, and geometry-based stochastic model. In the literature, we can find three types radio channel model: the deterministic, the stochastic and the geometry-based stochastic channel model.

1.2.1 Deterministic model

The deterministic model is based on the geometrical optics (GO) hypothesis in an a-priori known electromagnetic environment. Ray-tracing and ray-launching techniques are the main techniques to generate the SMC and rely on the Snell-Descartes law's of reflection for the reflected paths and the Uniform Theory of Diffraction (UTD) [38, 39] for the diffracted paths. These methods need to establish one purely geometric description of the scenario and the frequency-dependent electromagnetic properties of the objects present in the layout (concrete, dry walls, wood, metal, etc.). Ray-tracing computes all the paths between the transmitter and receiver

using the image theory [40]. The order of reflection and/or diffraction which determines the total number of components can be set by the user and will in-fine dictate the complexity of the simulated radio channel. In ray-launching, the environment is discretized and the emitter launches paths onto all potential interaction points. All the rays collected within a certain radius around the receiver are considered to contribute to the radio channel. Since the number of paths can be very large, a threshold is applied to remove the weakest paths and stop the algorithm. These methods are computationally attractive and the resulting radio channels are rather accurate to reproduce the propagation and large-scale characteristics of the channel provided that the numerical map grasps the complexity of the real scenario. However, the approach suffers several drawbacks. First, the simulated radio channels are only valid for the studied scenario. Then, the numerical map is a simplified description of the environment at a given time and, therefore, does not include the details which contribute to radio channel fading such as moving cars, people, urban furniture, etc. However, they provide a general idea of the physical phenomena in the channel and having decent prediction of the radio coverage, thus avoiding costly measurements campaigns.

1.2.2 Stochastic model

Stochastic models describe the stochastic nature of the radio channel and are developed for system evaluation and optimization with the purpose of easy integration in binding simulators during the development phase of the system. From the channel modeling point of view, it considers the channel as a superposition of a finite MPC number whose parameters are drawn from statistical distributions. One well known statistical channel model is the Clark's model [41] from which the Rayleigh and Rice fading model can be derived. Besides, the SV model [28] and its extension model [42] which also fall under the clustering approach should be mentioned here. This model is motivated by the observation of the radio channel measurement that the MPC are found to arrive in clusters. The SV model have been standardized in the IEEE 802.15.3a and IEEE 802.15.4a for UWB systems. Generally these statistical models are developed for each type of environment [43]. However, these models are only valid as long as the defining statistics for the channel being modeled are accurate.

1.2.3 Geometry-based stochastic channel model

Geometry-based stochastic channel models (GSCM) aim at providing realistic simulated radio channel while minimizing the computational time. The MPC parameters are defined in part or completely stochastically while taking into account the geometrical information of the environment.

In deterministic geometrical approaches like ray-tracing discussed in the previous subsection, the scatterer locations are defined in a database and correspond to

real objects in the map. In contrast, GSCM choose the scatterer locations in a stochastic fashion according to a certain probability distribution. MPC will exhibit single-bounce or consecutive multi-bounce scattering with these scatterers such that parameters in both delay and angular domains can be computed at the emitter and receiver side. The number of MPC and scatterers are selected in a pre-defined table and also drawn with distribution laws. Clustering has been included in the most recent GSCM models such as the COST 259 [44], WINNER II [45], Random Cluster Model [46], and COST 2100 model [47]. As mentioned in the previous section, it was observed that MPC tend to appear in groups in the delay and angular domains. By including clustering features into GSCM, it also brings an additional simplicity to the modeling parameters.

GSCM models considering cluster features can be divided into two types: system level and cluster level model. In order to provide more insight into these two different types, the WINNER II is taken as an example for the system level model whereas the COST 2100 is considered for the cluster level model. At each sampled time, the WINNER II will run the modeling process to define the corresponding instant radio channel. This process is briefly introduced as follows:

- Define the large-scale parameters (LSP) according to pre-defined stochastic distributions

- Generate the clusters and MPC according to these LSPs

In contrast, the COST 2100 model will generate the entire environment at once. Also, the concept of cluster visibility region is introduced. Only the clusters within the cluster visibility region around the receiver or mobile station (MS) will contribute to the radio channel.

Then COST 2100 modeling process is:

- Define large number of clusters throughout the simulation environment

- Define the MS location and MPC from visibility region

- Generate LSPs based on the cluster scattering

The different framework between the WINNER II and COST 2100 is significant but both models propose to reproduce the stochastic properties of MIMO radio channels over time, frequency, and space domain. Each model has certain advantages and limitations which are presented in the Table 1.3.

1.3 Radio channel characteristics and related models for industrial scenarios

Recently, there has been a growing interest from the industry to introduce wireless communication systems in the production lines to improve their competitive-

Table 1.3: Comparison between WINNER II and COST 2100

GSCM	WINNER II	COST 2100
Type	system level	cluster level
Advantages	LSP statistic guaranteed	No constraint of LSP Independence environment description Good extension
Limitations	Rigid structure for large MS motion	Large deviation of LSP statistic Complex representation of the clusters

ness [48]. Wireless communication is found to be more flexible and low-cost comparing to conventional wired communication systems already massively deployed as a standard in industry.

Unlike the indoor office environment, the industrial propagation environment includes many metallic objects of any size and geometry such that the number of scatterers around the transmitter and receiver is relatively large. Hence, the received signal is not only subject to heavy multipath propagation but also prone to strong diffuse scattering mechanisms. Therefore, it is expected that the propagation characteristics are rather different compared with indoor offices. Nonetheless, there are to the knowledge of the author limited contributions in the literature dealing with industrial multipath propagation channel. Furthermore, DMC was only discussed in couple of those papers. Table 1.4 presents the most up to date complete list of the measurement campaigns, setups, and study objects in industrial scenarios.

1.3.1 Narrow-band path loss

Large-scale path loss have been studied in several works based on the measurement of radio channels and wireless sensor networks. Table 1.5 provides a summary of the path loss parameters (exponent and shadowing) computed for these environments and scenarios. In these works, path loss was considered to follow a power law and to be affected by shadowing as detailed in (1.1).

It is observed from this table that the narrow-band path loss parameters are strongly dependent to the environment configuration as well as the measurement frequency. When the measurement frequency is large, small metallic objects will act as additional reflectors, thus resulting in an increased multipath propagation. The path loss exponent n is found to be generally less than 2 (free space) for many environments. Again, this fact may result from the heavy multipath propagation in the channel. Meanwhile, it is also found that n is related to the path length and the industrial topology as well as the material type presenting in the environment.

The narrow-band received signal envelop distributions have been reported in [52, 53, 60, 48]. The Rice distribution was originally reported to fit well the signal envelop distribution in the industrial environment and this was also validated by other measurement campaigns. Later, the Nakagami, Lognormal, and Rayleigh distributions were also reported to fit well the received signal envelop distribution

Table 1.4: Measurement summary in industrial environment

Reference	Antenna	Frequency Range	Data processing	Environment Dimension	Study object
[49]	MIMO	1.3 GHz BW:22 MHz	RIMAX	$21.3 \times 77.2 \times 12.2m^3$	Large-scale fading, polarization property
[50][51]	MIMO	800 MHz-2.7 GHz	APDP	$15 \times 17 \times 5m^3$ $18 \times 27 \times 5m^3$ $20 \times 30 \times 6m^3$	small-scale statistic, cluster modeling
[48]	SISO	900,2400,5200 MHz narrow-band	N/A	distance: 15-140 m	large-scale, temporal fading
[52]	SISO	1300 MHz narrow-band	N/A	$74000m^2$ $100000m^2$ $150000m^2$ $280000m^2$ $210000m^2$	large-scale, small-scale fading
[53]	SISO	2450 MHz narrow-band	N/A	distance< 95 m	large-scale small-scale fading
[54]	SISO	3.1-10.6 GHz UWB	CLEAN	distance:1-25 m	large-scale, small-scale fading
[55]	SIMO	3.1-10.6 GHz 3.1-5.5 GHz UWB	APDP	$13.6 \times 9.1 \times 8.2m^3$ $94 \times 70 \times 10m^3$	large-scale fading small-scale statistics, clusters
[25]	MIMO	3 GHz BW: 100 MHz	RIMAX	$20.4 \times 22 \times 4.8m^3$	DMC reverberation time
[56]	MIMO	800 MHz - 4 GHz	APDP	height:7 m	small-scale statistic, cluster
[57]	SIMO	5.2 GHz BW: 120 MHz	ESPRIT	$300 \times 120 \times 10m^3$	temporal, angular characteristics
[58]	SISO	2.4 GHz BW: 80 MHz	PDP	$16 \times 45 \times 10m^3$	large-scale fading, delay spread
[59]	MIMO	2.4 GHz, 5.2 GHz BW: 80 MHz	Channel covariance capacity	N/A	MIMO channel modeling

contradicting the original findings. Therefore, it is concluded that deep studies on this aspect are required.

1.3.2 Wide-band characteristics

The wide-band measurements in [58] reveal the fact that the delay spread varies widely in the radio channel and this is attributed by the random location of the scatterers. The coherence bandwidth is found between 5 MHz and 15 MHz. It is also indicated that the use of directional antenna can diminish the BER of the system. Also in [57], the delay spread is found to vary between 40 ns and 100 ns. Azimuth spread of the DOA varies from 5° to 25° for LOS and from 10° to 35° for NLOS scenarios, respectively. In [50], the cluster is visually identified in the power-delay domain. Therefore, the PDP of the wide-band channel is successfully modeled by the S-V model. Besides, the Weibull distribution was found to fit the MPC small-scale fading.

The Ultra-Wide-Band (UWB) measurement in [55] reported that the delay spread varies from 28 ns and 38 ns for LOS and 34 ns and 51 ns for NLOS, respectively. Small-scale fading is fitted by the Rayleigh distribution whereas path loss is Log-normally distributed. In [54], the average path loss is found to be increasing exponentially. Also, the path loss exponent is larger than for indoor office environments.

Table 1.5: Summary of path loss parameters [3]

Environment type	Frequency(GHz)	scenario	d(m)	n	χ_σ (dB)
Industrial facility [60]	2.4	LOS	100	1.6	-
		NLOS	100	3.73	-
Chemical pulp and cable factories [53]	2.45	LOS	95	1.1	-
Nuclear power plant [53]	2.45	LOS	-	1.86	-
Oil rig installation [61]	2.4	LOS	10	1.39	1.82
	5.8		10	1.76	1.83
	2.4	NLOS	10	2.06	2.17
	5.8		10	2.44	2.45
	2.4	NLOS	10	1.17	1.22
	5.8		10	1.41	1.31
Food and metal processing factories [48]	0.9	LOS	140	3.51	7.70
		LOS	140	2.49	7.35
	2.4	LOS	140	3.44	8.63
		LOS	140	2.16	8.13
	5.2	LOS	140	2.59	6.09
		LOS	140	0.91	4.79
500 Kv Substation [62]	2.4	LOS	20	2.42	3.12
		NLOS	20	3.51	2.95
Underground transformer vault [62]	2.4	LOS	20	1.45	2.45
		NLOS	20	1.45	2.45
Main power room [62]	2.4	LOS	20	1.64	3.29
		NLOS	20	2.38	2.25
Industrial facilities [52]	1.3	mixed	100	2.2	7.9
Corridor [63]	1.9	LOS	-	1.80	-
Laboratory [63]	1.9	LOS	-	2.20	-
Industrial hall [63]	1.9	LOS	-	1.40	-
Assembly room [51]	0.9	LOS	16	1.72	3.80
	1.6	LOS	16	1.37	2.58
	2.45	LOS	16	1.69	3.93
Electronics room [51]	0.9	LOS	16	1.96	2.29
	1.6	LOS	16	1.83	3.48
	2.45	LOS	16	1.83	2.29
Mechanical room [51]	0.9	LOS	16	1.79	5.07
	1.6	LOS	16	1.59	4.01
	2.45	LOS	16	1.69	2.87

For the channel modeling aspect, several radio channel models can be found in the literature. One wide-band statistical channel model was proposed in [64] to simulate the radio channel characteristic in the industrial open hall. Another GSCM was proposed in [65] to simulate the radio channel in an industrial environment within the production line. This model assumes that the scatterer density decays exponentially with distance. Other physical statistical models were reported in [66, 67, 56] for which the S-V model was implemented to model the observed PDP. The cluster definition of the aforementioned models are all under power-time domain. The MIMO channel model in the industrial environment is reported in [59] which concludes that the Weichselberger MIMO channel structure can better estimate the channel capacity than the the Kronecker channel structure in the industrial environment.

Very recently, the experimental analysis of the radio channel MPC in the industrial environment has been reported in [25]. In this analysis, the MPC were split into the SMC and DMC to deepen the analysis. The geometry of the industrial room was found to have a significant influence to the channel characteristics. Also, the DOA and TOA were observed to display different distributions. The DMC power was found to vary from 23% to 70% under all investigated scenarios. One highlighted point in [25] is the explanation of DMC by the room electromagnetics theory and the computation of the average absorption coefficient. The industrial environment was found to be 16% to 22% less absorbing compared to indoor office environments.

Finally, the polarization characteristics have been studied in [49]. Similarly to [25], the polarimetric SMC and DMC have been estimated by de-embedding the polarimetric radiating patterns of the dual-polarized measurement antennas. Under the LOS condition, it was reported that the vertical polarization is more favorable than the horizontal one. Similar results were obtained for the OLOS condition, but the vertical polarization suffered more depolarization effects. Finally, a mean reverberation time of $70ns$ with low standard deviation and no significant difference between polarized subchannels validated the room electromagnetics theory.

1.4 Radio channel characteristics and related models for vegetation scenarios

Similarly to the industrial environment, the vegetation radio channel propagation is a particularly challenging outdoor environment and suffers from important multipath fading. The propagation mechanisms are pervasive to the specific topology of the scatterers in-between the transmitter and receiver. One particular structure brought by the vegetation scenario is the tree canopy. It generally consists of branches, forks and leaves of different dimensions, orientation and densities, which also differ from species to species. On the other hand, throughout the seasons, the density of leaves as well as the water content of trees vary, which could also impact the communication links. The foliage nature is too complicated to provide one

detailed mathematically modeling structure. Therefore, it could be considered to be randomly distributed with asymmetry in the azimuth as well as in the elevation planes. Also, one tree can be considered as a dense cluster of scatterers [68] to simplify the analysis.

The propagation phenomenon through vegetation is complex. The radio signal will be attenuated through the propagation due to a number of effects. Shadowing and attenuation are generally considered to be caused by the leaves and the trunks. Meanwhile, scattering is caused by branches and forks, and reflection and diffraction mainly caused by the trunk. Since the forest is a random medium with many discrete scatterers, radio waves experience a combination of different propagation mechanisms which result in severe fading and introduces an excess vegetation loss to the link budget. Also, fast fading caused by the wind or rain have to be considered to establish reliable near-ground communication links.

1.4.1 Foliage path loss models

Propagation effects on terrestrial communication systems in the microwave and millimeter wave frequency bands have been investigated for decades. The most important effect introduced by the forest is the excess signal attenuation. In the literature, accurate modeling of wave propagation behavior through foliage has attracted significant attentions in recent years for its applications in many civilian and military problems [69] [70]. Since a physical simulation of a complete forest is too complex to conduct, simplification have to be made for the development of a channel model with reasonable complexity.

The quantitative effect of vegetation on the radio wave attenuation is considered as the difference between the measured path loss over a vegetated path and the expected path loss in absence of vegetation for the same systems and path parameters. This additional loss due to the presence of foliage is termed as foliage loss.

The existing foliage path loss models can be classified into three categories: a) empirical, b) semi-empirical , c) and analytical models. They mainly aim at characterizing the effects of vegetation on propagation and the prediction of excess attenuation.

1.4.1.1 Empirical models

The main advantage of these models is the simplicity of the mathematical expressions. However, they depend on specific measured data and they do not provide information of the physical processes involved. The following models are cited according to the band occupied from the lowest to the highest band.

1.4.1.1.1 Tewari models Tewari et al. [71] have realized an empirical model which was later backed with a measurement campaign in an Indian forest [72] with foliage depths from 40 m to 4 km. The vertical and horizontal polarized antenna

Table 1.6: Exponentially Decaying (ED) path loss models

ED models	Recommend frequency	Distance	Parameters: A, B, C
Meng [73]	240 MHz -700 MHz	<5 km	0.48,0.43,0.13
Al-nuaimi [74]	10 GHz-40 GHz	<140 m	0.37,0.18,0.59 out of leaf 0.39,0.39,0.25 in-leaf
ITU-R [75]	200 MHz - 95 GHz	<400 m	0.2,0.3,0.6
Cost 235 [76]	9.6 GHz - 57.6 GHz	<200 m	26.6,-0.2,0.5 out of leaf 15.6,-0.009,0.26 in-leaf
Weissberger [77]	230 MHz -95 GHz	<400 m	1.33,0.284,0.588 (14 m<d≤ 400 m) 0.45,0.284,1(0 m≤ d<14 m)

are both used with frequencies values ranging from 50 to 800 MHz. The predicted transmission loss is given by:

$$\mathbf{L}_{Tewari}(dB) = 26.15 - 20log_{10}\left[\frac{Ae^{-\alpha d}}{d} + \frac{B}{d^2}\right] \tag{1.10}$$

where α is a constant describing the attenuation rate in dBm/m, d the distance in m. The A and B constants are parameters to be fitted from the measurement data. Interestingly, this path loss model predicts a possible dual-slope decaying rate. For instance, it has been reported in [72] that the changeover from exponential to logarithmic decay was at 400 m (which could be variable to different measurement environment).

1.4.1.1.2 Exponentially decaying models Others empirical path loss models fall under the type of exponentially decaying (ED) models. It is found that the excess foliage loss can generally be well represented by the following expression:

$$L_{foliage}(dB) = A * f^B d^C \tag{1.11}$$

The parameters A,B, and C can be empirically chosen or fitted from the measurement data. The excess loss is corrected by the Free space model or by the ground reflection model like the Meng's model [73]. Table 1.6 presents a summary of the existing exponentially decaying models found in the literature. Note a difference is made whether the emitter is in or out of leaf.

These aforementioned models have been recently evaluated in [4, 5] based on measurement campaigns conducted in European forests at 485 MHz with distance under 1 km and at 1.9 GHz with distance up to 110 m. The results presented in Table 1.7 show a good Root-Mean-Square Error (RMSE) for Meng's model among this family of ED models.

1.4.1.2 Semi-empirical models

This model is based on the knowledge of the qualitative behavior of absorption and scattering in homogeneous scattering media. They are usually simply to apply

Table 1.7: RMSE (dB) for the Exponentially Decay Models. (a) from [4] and (b) from [5]

(a) Measurement at 485 MHz

Path Loss Model	RMSE (dB)
COST 235	45.01
Free space	29.30
ITU-R	26.36
Plane Earth	16.64
Weissberger	15.52
Al-Nuaimi et al.	8.78
Meng et al.	6.40

(b) Measurement at 1.9 GHz

Path Loss Model	RMSE (dB)
COST 235	13.2
Weissberger	9.0
ITU-R	7.1

but share the same disadvantages than the semi-empirical models. They do not take account much of the channel dynamic effects and broadband effects of the vegetation medium.

1.4.1.2.1 Seville's model The Seville's model was introduced in [78]. It is a Dual-Gradient (DG) model which was found to give a better prediction than the ITU-R model at 35 GHz, 37.5 GHz and 40 GHz with measured data. It is presented as follows:

$$A_{foliage} = \frac{R_\infty}{f^a W^b} + \frac{k}{W^c}\left(1 - exp\left(-\frac{(R_0 - R_\infty)W^c}{k}d\right)\right) \tag{1.12}$$

where f is the signal frequency in GHz and $a, b, c, k, R_0, R_\infty$ are constants presented in Table 1.8. The DG model takes into consideration of another dimension of the measurement, ex. the illumination width. This gives a measure of the volume of vegetation illuminated by the beam widths between the transmitter and receiver antennas. W is the maximum effective coupling width between the transmit and receive antennas which is derived from the measurement geometry.

Table 1.8: Constant values for Seville's model

Constant Parameter	in leaf	out of leaf
a	0.7	0.64
b	0.81	0.43
c	0.37	0.97
k	68.8	114.7
R_0	16.7	6.59
R_∞	8.77	3.89

1.4.1.3 Theoretical model

While the empirical or semi-empirical models are usually simple to apply, they are based on specific measured data and fail to relate the foliage path-loss to the foliage dependent parameters such as tree species and density. On the other hand, theoretical model provides an insight into the physical processes involved in radio wave propagation through foliage by introducing the incoherent wave component into consideration which is the dominant propagation component for large vegetation depth. However, these models are more complicated, but more generic and applicable to any arbitrary foliage wave propagation scenario and over a large frequency range. Several models were found in the literature.

- Radiative energy transfer theory [79]
- Geometrical and uniform theory of diffraction [80]
- Full wave solutions [81]
- Physical optics [82] [83]
- Statistical wave propagation (SWAP) model [84]

Later, a generic theoretical model covering the 1-60 GHz range [85] [86] was reported. In this model, a combination of Radiative Energy Transfer, ground reflection and edge diffraction models was realized and verified for a wide variety of vegetation media, path geometries and frequencies. This narrow-band model yields an RMSE of 8.38 dB (11.51 dB for ITU-R) from variable measurements.

These models generally assume that the vegetation is a horizontal homogeneous medium. The forest can be modeled into randomly distributed particles or dielectric slab having random orientation. To achieve a reasonable computational time of these models, the simplicity is made in the calculation of first order component of basic function in the theoretical model. Moreover, the mathematical complexity in these models prevent the compatibility to include the higher order propagation mechanism in the model.

These theoretical models generally predict a dual-slope path loss model which correspond to the coherent and incoherent signal components or one exponential decaying function to the path loss. The main disadvantage of all these models is that the final results is presented by the excess attenuation caused by the presence of vegetation.

1.4.2 Lateral waves

In the literature, it is generally accepted that the signal components in the typical vegetation scenario are formed by three parts shown in Figure 1.9: the direct wave, the ground reflected wave and the lateral wave. The lateral wave is a particular signal component presenting which was initially reported by Tamir [87] and Li [88].

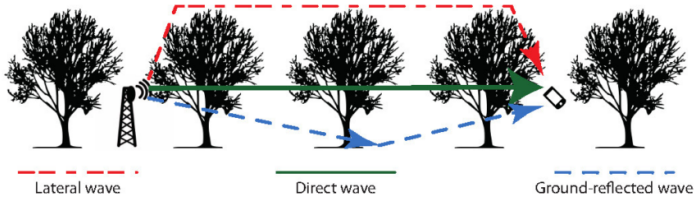

Figure 1.9: Propagation mechanisms through the vegetation.

It is considered to mainly propagate on top of the canopy along the air-canopy interface. The lateral waves are dominant at the treetops over a large forest depth at VHF (30 - 300 MHz) and low UHF (300 MHz - 3 GHz) bands. Therefore, the main contribution to the received signal strength is not only the direct wave and ground reflected wave but also the lateral wave. The lateral waves being essentially a scattered field results in wide fluctuations in the measured data.

1.4.3 Polarization

The radio waves get substantially depolarized due to their scattering by the foliage while propagating through the vegetation medium. It is one of the important aspects of radio wave propagation in terrestrial links and must be considered for the design of communication systems operating through dense or deep foliage. Generally, the depolarization mechanisms were found to strongly depend on wavelength, ground topography, foliage structure such as the size and density of leaves, orientation and number of branches.

The depolarization effect have been studied in several works. In [89], the single tree depolarization effects have been analyzed with measurements in an anechoic chamber conducted at 20 GHz. The measurement focused on the depolarization effect as a function of the incident angle on the tree. They found that the tree structure trends to cause heavy depolarization at certain incident angles. It has been highlighted that the transmitted vertical linearly polarized wave has been depolarized to a near horizontally polarized wave by the vegetation material. Besides, they have observed the random change of polarization state due to the tree structure. The depolarization occurs as a result of the various components of the tree structure. These components are then re-transmitting the waves at different polarization resulting in an overall depolarization of the originally transmitted wave.

In [90], another measurement campaign has been made on the hilly (THF) and flat (TFF) ground, respectively. The 1900 MHz and 390 MHz bands were investigated with a maximal distance of 1.6 km. For short distances, it was found that the 1900 MHz band suffers less depolarization effect compared to the 390 MHz. This gap is further affected by the topography effect. Generally, less depolarization is observed on the flat ground compared to the hilly ground. When the vegetation depth increases to a certain distance, the received signal is completely depolarized.

For both topography condition, the results showed an equal depolarization effect for both transmitted polarization in the 400 MHz band. In the 1900 MHz band, a higher depolarization of the vertical polarized signals with up to 3-4 dB was observed.

1.4.4 Weather impacts

Evidently, the motion of the tree structure caused by the wind and rain has to be considered as it will strongly introduce fast fading. This is particularly true in the millimeter band due to the high level of humidity during the rain periods.

1.4.4.1 Wind

Wide variations in the received signal strength have been reported in [72, 91, 92] during the periods of strong winds in the forest. This fluctuation in the received signal is believed to be caused by the change in orientation of various scatters (like leaves and branches) due to varying wind velocity. Also, a series of vegetation scattering measurement during various wind condition was reported at 0.9, 1.8, 2, 12 and 17 GHz in [93, 94]. A high dependency between wind speed and received signal was found based on measurements in an anechoic chamber and outdoor scenarios. A statistical study of the K-factor confirmed the change of distribution law from Rician to Rayleigh distribution due to the increasing of wind speed (0.51 m/s-7.1 m/s).

1.4.4.2 Rain

The rain effect has been reported in [6]. One measurement campaign was performed inside a tropical forest at 240 MHz carrier wave. The foliage depth covered in this experiment was 710 m. The transmit and receive antennas were both kept stationary and at a constant height of 2.15 m. The rainfall was found to have distinct effects on various parts of the propagating components for the VHF radio wave propagation. The lateral wave at VHF band is the dominant mode of propagation and is not affected by the presence of rain as it is similar to free space propagation over the tree tops. The multipath components induced by the discrete scatterers such as leaves, branches and tree trunks due to the wet foliage channel are significantly affected by the variation in rain intensity.

It is reported in this work that the multipath components are attenuated to different extents under different rain intensity conditions. Moreover, these effect results in a variation of the RMS delay spread (Table. 1.9). Under steady rainfall, the RMS delay spread decreases as the intensity of the rain increases. However, unsteady heavy downpour can induce motion of the damp foliage medium, and thus generates a variation in the multipath components.

Table 1.9: mean RMS delay spread in a tropical forest after [6]

Weather	τ_{RMS} (in μs)
No rain	0.2137
Slight rain	0.1639
Moderate Rain	0.1316
heavy rain	0.2206

1.4.5 Multidimensional measurements in vegetation scenarios

To the knowledge of author, there are very limited multidimensional measurements and studies which were reported in the literature for vegetation scenarios. Furthermore, it appears only SIMO measurements were performed in many different forest types around the world. This is probably due to the difficulty of having a full array system deep in the forest. Table 1.10 presents a summary of these measurement campaigns, frequency parameters, data processing technique, and objectives of the work. Most of these studies focused on the spatial characteristics of the radio channel with the aim of providing a deeper understanding of the propagation mechanisms for this scenario.

Table 1.10: Summary of SIMO measurements in vegetation scenario.

Environment	Antenna	Frequency Range	Data processing	Distance	Study property
Palm plantation [95]	SIMO	240 MHz wideband	N/A	330 m,400 m,710 m	Channel spatial correlation
Chigasaki forest [96]	SIMO	455 MHz, 810 MHz, 2.2 GHz, 3.35 GHz	Wiener-Khintchine	100 m	Spatial angular spread
Kauagawa forest [97]	SIMO	2.22 GHz Bp: 44 MHz	SAGE	109-123 m	Spatial angular spread
Louvain-la-neuve forest [5]	SIMO	1.9 GHz Bp: 80 MHz	N/A	40-110 m	Spatial angular spread delay spread
kanagawa forest [98]	SIMO	2.2 GHz Bp: 50 MHz	Capon spectrum	100 m	Spatial angular spread

1.4.5.1 Delay spread

[99] reported delay spreads at 1.3, 2 and 11 GHz conducted in a park. The results showed an increase in the delay spread values as the vegetation depth was increased with distance up to 50 m. From their observation, the delay spread was generally below 20 ns for the three bands. [5] studied in detail the delay spread characteristics at 1.9 GHz with distance values ranging from 40 to 110 m in a typical forest. The delay spread was found to be ranging from 60 to 120 ns and an increase was also noticed at longer distances (about 100 m). Finally, [70] reported measurements at 1.9 GHz in a forest for a maximum distance of 100 m. For a distance range between 50 and 200 m, delay spreads ranging from 30 ns to 80 ns and 20 ns to 60 ns were obtained using omni-directional and directional antennas, respectively. It was also

observed that wet foliage decreases the delay spread under the same measurement conditions.

1.4.5.2 Angular spread

[97] showed that the azimuth spread for horizontal polarization is larger than that of vertical polarization at 2.22 GHz with 44 MHz bandwidth. In addition, the co-elevation spread for the vertical polarization is always larger than that of horizontal polarization. Mean arrival azimuth and co-elevation spread of 25° and 6° were computed. Also, the frequency characteristics of angular spread is reported in [96]. The study was based on UWB SIMO measurements from 450 MHz - 3.35 GHz and the transmitter height was varied from 5 m to 15 m. The mean angular spread was found to be 25° within the studied frequency range and was not found to be dependent to the transmitter antenna height. [5] reported a mean azimuth spread value of 15° with a maximum 26° value from 1.9 GHz measurements with distance ranging from 40 to 110 m. The azimuth spread was observed to decrease as the distance is increased. Finally, a measurement campaign at 2.22 GHz with 50 MHz bandwidth was reported in [98] using a cylindrical array antenna at the receiver side. The azimuth spreads were calculated at different antenna heights and polarization state. However, due to the rough estimations of the azimuth spreads, it was only observed spreading in the received angles due to the foliage interaction.

1.4.6 Summary of propagation characteristics and models in vegetation scenarios

Typically, propagation studies have been mainly conducted with path loss models as their major advantage is simplicity. In particular, empirical exponential decaying models fitted from measurement data are widely used but are limited to describe propagation mechanisms. On the other hand, both semi-empirical and theoretical studies which take into account more physical propagation mechanisms predict dual-slope path loss behaviors revealing the different interaction of coherent component and incoherent components as a function of distance. However, this comes at the expense of numerical/analytical complexity which is dramatically increased compared with classical path loss models. Also, it can be noted that the polarimetric aspect of the propagation was also included in path loss models. The signal characteristics have been shown to be strongly dependent on the wind and rain which are inevitable dynamic effects. Finally, multidimensional measurements have been performed to evaluate the spatial spreads of the multipath components at the receiver side. However, a description of the double-directional radio channel characteristics is missing.

1.5 Conclusion

In this chapter, the state-of-the-art on wireless radio channel propagation mechanisms has been introduced. Depending on the considered environment, the received signal characteristics can greatly vary and various models have been introduced in the last decades to describe these phenomena. When it comes to the underlying propagation components, it is now acknowledged that MPC can be split into SMC and DMC. The introduction of DMC in the radio channel structure has been proved to be a significant progress to understand the overall propagation mechanism but requires that all existing radio channels must be redefined under this framework. DMC can be explained as a reverberation phenomenon in closed or highly diffuse propagation environments and has been systematically studied under the umbrella of the room electromagnetics theory. Polarization is yet an other important radio channel characteristic as channel capacity can be greatly increased with diversity-based techniques. Finally, clustering was introduced from the observation on how SMC tend to group in the delay and spatial domains. It is an attractive approach to characterize the radio channel features and simplify models. For instance, the deterministic, stochastic, and GSCM modeling approaches were briefly introduced and their advantages/disadvantages were discussed.

Since this thesis focuses on the industrial and vegetation scenarios, the multidimensional characteristics and radio channel models reported in the literature have been presented for these two environments. It is concluded from these studies that neither the industrial nor the vegetation propagation characteristics or channel models include a detailed description of DMC. Furthermore, since DMC is neglected or omitted, one could question the validity of all presented results to correctly grasp and model the propagation properties. Furthermore, it can be argued whether having or not DMC in the data model impacts the propagation characteristics and the development of dedicated radio channel models for highly diffuse scenarios. Hence, the purpose of this thesis is to develop a general framework to characterize and model the radio channel properties when DMC is observed.

Chapter 2

High-resolution parameter estimation technique and radio channel measurement systems

2.1 Introduction

Multiple antenna techniques were originally developed to improve the reliability of the radio link or increase data throughput and will be a key technique to support the deployment of upcoming standards like 5G. In parallel, the added spatial diversity is pivotal to gain a deeper insight of the propagation mechanisms as the SMC angular properties can be estimated and characterized. This estimation process is performed by applying powerful and efficient mathematical algorithms to the measured radio channels. Historically and since the venue of digital processing techniques, several approaches have been developed to solve the multi-dimensional parameter estimation problem. Nowadays, it is well acknowledged that parameter estimation techniques play a major role to estimate the SMC parameters of the radio channel. This resulted in the development of reliable and realistic models that can be used to design and optimize wireless communication systems. Moreover, it is a powerful and versatile approach which allows studying detailed behaviors and characteristics of any type of radio channels in any propagation environments. However, it must be highlighted that the majority of the results reported in the literature were obtained from estimators which do not include DMC. Hence, the propagation characteristics and related models undermine the contribution of DMC to the radio channel. The main objective of this thesis is to fill in this gap.

In this chapter, several well-known estimators will be introduced under two categories: spectral estimator and high-resolution estimator. Their advantages and disadvantages will be briefly introduced. Then, the maximum likelihood (ML) RiMAX estimator will be introduced. RiMAX is the most recent channel parameter estimator in the literature and includes not only SMC but also DMC in its radio

channel model. Hence, it been used throughout this thesis to extract these components from the measured radio channels to assess, in particular, the characteristics of the DMC and its contribution to the radio channel. Also, the polarimetric 16 × 16 radio channel sounder systems used in the measurement campaign to obtain the radio channels will be introduced and motivated with respect to the investigated scenarios. Their main features as well as the antenna array and elementary radiating element will be discussed. Finally, the performance of the RiMAX framework used in this work will be presented for both systems and related antenna array.

2.2 Radio channel parameter estimation techniques

Radio channel parameter estimation is not only one estimation technique but also a reflection on the radio channel structure. The data model of any estimators rely on the knowledge of the physical propagation mechanisms and their statistics. It follows that the development of better estimators can only be enabled if a deeper understanding of the radio channel is gained. The purpose of the parameter estimation algorithm is to extract or estimate the geometrical SMC parameters such as DOA, DOD, TOA and polarimetric amplitudes from the received complex signals. This multi-dimensional problem has a high degree of complexity related to the mathematical treatment and measurement system which explains why it has been progressively solved over the recent decades.

There are generally two types of estimation methods: spectral methods such as beamforming and high-resolution estimation such as SAGE, ESPRIT and RiMAX. Each estimator has its own specificity and performance. For instance, the performance is limited by the physical limitation of the measurement setup, data model design, search strategies, and measurement noise.

First, let's consider the observed narrow-band signal received over an antenna array:

$$\mathbf{X} = \begin{bmatrix} \mathbf{x}_1 & \mathbf{x}_2 & \cdots & \mathbf{x}_N \end{bmatrix} = \begin{bmatrix} x_{11}(f_0) & x_{12}(f_0) & \cdots & x_{1N}(f_0) \\ x_{21}(f_0) & x_{22}(f_0) & \cdots & x_{2N}(f_0) \\ \vdots & \vdots & \ddots & \vdots \\ x_{M1}(f_0) & x_{M2}(f_0) & \cdots & x_{MN}(f_0) \end{bmatrix} \tag{2.1}$$

where N is the number of observations or snapshots, M the number of antennas in the array, and f_0 the central frequency.

For each snapshot, the observed signal can be classically further described by:

$$\mathbf{x}_k = \mathbf{A} \cdot \mathbf{s}_k + \mathbf{n}_k \tag{2.2}$$

where $\mathbf{A} \in \mathbb{C}^{M \times D}$, D is the number of incident signals on the antenna array, and $\mathbf{n}_k$ the measurement noise. Each column of $\mathbf{A}$ describes the phase information for each propagation path. Some algorithms have been proposed in the literature to

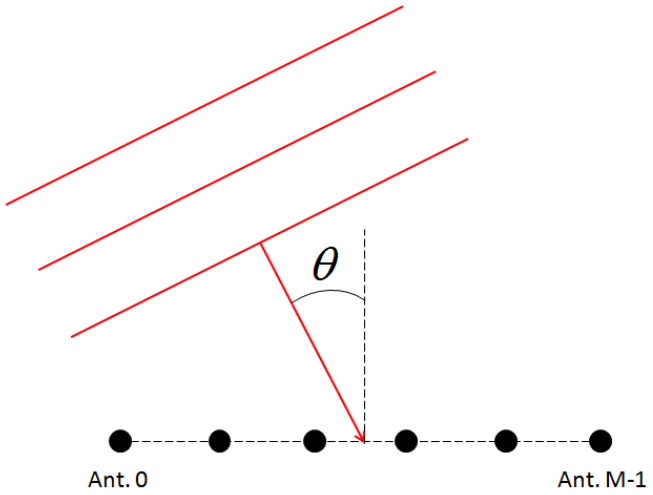

Figure 2.1: Example of DOA estimation problem with a ULA.

estimate D such as the AIC (Akaike Information Criterion) and MDL (Minimum Description Length) metrics. They rely on the eigenvalues of the covariance matrix $\mathbf{R}_{xx}$ computed from the observed signal $\mathbf{X}$ [100]:

$$\mathbf{R}_{xx} = \frac{\mathbf{X}\mathbf{X}^H}{N} = \frac{1}{N}\sum_{i=1}^{N}\mathbf{x}_i\mathbf{x}_i^H \tag{2.3}$$

The knowledge of the number of incident sources is critical as far as channel parameter estimators are considered. A correct estimate of the number of signals can greatly minimize the parameter estimation errors. On the other hand, an incorrect guess would result in poor estimates [101].

2.2.1 Spectral methods

The early channel parameter estimators fall under the category of spectral methods and have been widely used for treating angular estimation problems. They are based on the search of maxima in spectrum functions which depend on the parameter of interest. Each parameter is extracted from their respective spectrum function within a searching range. As an example (this approach can be extended to any dimensions), let's consider the DOA estimation θ of a propagation path impinging onto a M-element Uniform Linear Array (ULA) as illustrated in Figure 2.1. The beamforming [102] method can be considered as a spatial filter which weights the received signals on the antenna array:

$$\mathbf{y}_k = \mathbf{h}^{\mathbf{H}}(\theta_\mathbf{i})\mathbf{x}_k \tag{2.4}$$

The purpose is to find the weighted vector $\mathbf{h}^{\mathbf{H}}(\theta_\mathbf{i})$ which can maximize the signal component arriving under the direction θ_i while minimizing for other directions θ_j

with $i \neq j$. One solution for this problem was proposed in [103] and is now called conventional Bartlett beamformer:

$$\mathbf{h} = \frac{a(\theta)}{a^H(\theta)a(\theta)} \tag{2.5}$$

where $a(\theta)$ is called the steering vector of the antenna array. This steering vector describes the phase difference between all antennas as a function of the angle of incidence and, therefore, strongly depends on the array topology [1]. The angular-dependent power spectrum is computed from $y_k^H y_k$ after inserting (2.5) in (2.4). The underlying idea is to artificially steer the main lobe of the antenna array in all possible directions and then multiply with the received signal power. Obviously, the searched direction will be found for the antenna lobe pointing toward the desired direction. The main drawback of this method is its low spatial resolution which is limited by the number of antennas in the measurement system. Besides, this estimation method is highly sensitive to signal correlation between different elements in the antenna array as well as the noise which greatly degrades the estimation performance.

Another related estimator was introduced in [103] and named Minimum Variance Distorsionless Response (MVDR). The MVDR algorithm applies a spatial filter that minimizes the variance of the received signal such that the post-filtering result is not distorted. The MVDR/Capon spectrum proposed in [104] is based on the assumption that the covariance matrix of the received signal is invertible:

$$\mathbf{h} = \frac{\mathbf{R_{xx}^{-1}}a(\theta)}{a^H(\theta)\mathbf{R_{xx}^{-1}}a(\theta)} \tag{2.6}$$

where $\mathbf{R_{xx}^{-1}}$ is the inverted covariance matrix of the received signal. The performance of MVDR/Capon beamformer is better than the conventional Bartlett beamformer due to the pre-whitening. However, this comes at the expense of additional matrix inversion steps provided that the covariance matrix has a full-rank.

Generally, spectral methods do not provide sufficient estimate accuracy of the geometrical parameters. However, they are attractive and popular because of their simplicity of implementation and low computational time. This estimation principle is now widely used as the initialization step for other high-resolution estimations.

2.2.2 High-resolution parameter estimation techniques

High-resolution estimators provide an improved estimation resolution compared with spectral estimators. The most recent estimation techniques found in the literature are briefly presented hereafter.

1) MUSIC (Multiple Signal Classification) [105] exploits the properties of the covariance matrix $\mathbf{R}_{xx}$ of the measured signal to extract the characteristics of the signal components. The basic idea of MUSIC is to use the orthogonality property between the signal space and noise space [106]. The MUSIC spectrum needs to

be calculated from the steering vectors and noise space. The estimated parameters correspond to the maxima in the MUSIC spectrum. MUSIC estimation has been very popular to estimate the channel parameters in terms of delay and angle and can be applied to arbitrary antenna array configurations. However, its performance is largely influenced by the effective number of antennas in the array.

2) ESPRIT (Estimation of Signal Parameters via Rotational Invariance Techniques) was introduced for the first time in [107]. It is a fast, efficient and robust parameter estimator which can be used for estimating directions of incidence of multiple sources impinging on an antenna array. ESPRIT is based on the same signal model than MUSIC. However, it has the advantage of reducing considerably the computational time and memory required for storage. This arises from the decomposition of the total antenna array into sub-array structures invoking Rotational Invariance Techniques. This approach simplifies the numerous matrix operations within the estimation algorithm. Its main drawback lies in the restriction of antenna array configurations due to the invariance hypothesis. Also, it has a poor capability to distinguish closed signal components. Its performance may also be influenced by the pre-estimation of the number of signals.

3) SAGE (Space-Alternating Generalized Expectation Maximization) was introduced in [108, 109]. It is an iterative ML estimator. The main idea of SAGE is to divide the multi-dimensional parameters problem into several individual parameter problems. This provides a simplification of the grid-search technique used to initialize the geometrical parameters as well as the optimization steps. At each step, the parameters for a given SMC are optimized by maximizing the difference between the observed and estimated channel. The best estimated SMC is removed from the observation matrix and the previous step is repeated until a criterion is reached. However, SAGE requires a faithful estimate of the number of signals which is typically done with AIC or MDL. The performance of this estimator is therefore greatly dependent on the quality of the initial estimated parameters. Another drawback of SAGE is its slow convergence particularly for the case where the SMC parameters are strongly coupled.

4) The RiMAX algorithm introduced in [1] is the most recent method to estimate channel parameters. Similarly to SAGE, it is based on the exploitation of the ML function and provides an approach that circumvents the joint estimation problems encountered by the previous algorithms such as SAGE and ESPRIT. A sheer difference between RiMAX and the other algorithms lies into its data model and noise hypothesis [110]. From that point of view, it is considered a more realistic radio channel by taking into account DMC (Section 1.1.4.2). The drawback of RiMAX is its implementation complexity but the algorithm outperforms SAGE in terms of computational time.

The RiMAX framework was naturally selected to process the measured radio channels since the main scope of this work deals with the characterization and modeling of the MIMO radio links with diffuse scattering. A more detailed description of the data model and estimation principle will be introduced in the next section.

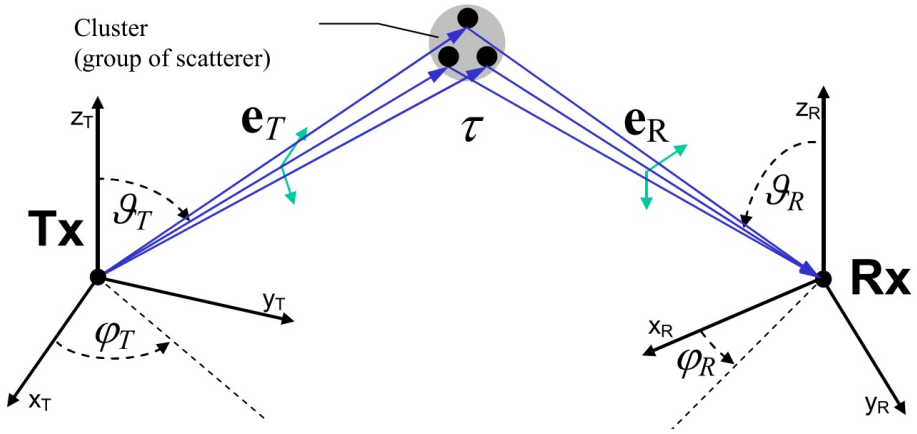

Figure 2.2: Definition of a propagation path or SMC after [1].

2.3 RiMAX Estimation technique

2.3.1 RiMAX radio channel and data model

The concept of paths or concentrated paths developed in the RiMAX framework is illustrated in Figure 2.2. The propagation path parameters are defined as the mean value of the parameters for a group of close rays. A single concentrated propagation path which is simply called SMC in this manuscript can be expressed under the double-directional radio channel model by a set of data including the TOA, DOA for azimuth and elevation, DOD for azimuth and elevation, doppler shift, and polarimetric amplitude.

The RiMAX channel model splits the received signal into a deterministic part $\mathbf{s}(\theta_{sp})$ and a stochastic part $\mathbf{n}_{dan}$ which contains DMC and AWGN. The deterministic part is built from the geometrical SMC parameter vector $\boldsymbol{\theta}_{sp}$ whereas the DMC is built using the DMC parameter vector $\boldsymbol{\theta}_{dan}$ introduced in chapter 2.4.2. All high-resolution algorithms proposed before RiMAX neglected the contribution of DMC to the radio channel such that only AWGN was added to the deterministic part.

$$\mathbf{h} = \underbrace{\mathbf{s}(\boldsymbol{\theta}_{sp})}_{SMCs} + \underbrace{\mathbf{n}_{dan}}_{DMC+Noise} \tag{2.7}$$

Hence, the sampled radio channel in the frequency domain can be considered as one realization of a complex circular symmetric Gaussian process with mean value $\mathbf{S}(\boldsymbol{\theta}_{sp})$ and covariance matrix $\mathbf{R}(\boldsymbol{\theta}_{dan})$ described by DMC and measurement noise.

$$\mathbf{h} \sim \mathcal{N}_C(\mathbf{s}(\boldsymbol{\theta}_{sp}), \mathbf{R}(\boldsymbol{\theta}_{dan}) \tag{2.8}$$

where $\mathbf{R}(\boldsymbol{\theta}_{dan}) = \mathbf{R}(\boldsymbol{\theta}_{dmc}) + \alpha_0\mathbf{I}$. If only measurement noise is assumed (i.e. DMC is omitted), then the sampled radio channel is given by:

$$\mathbf{h} \sim \mathcal{N}_C(\mathbf{s}(\boldsymbol{\theta}_{sp}), \alpha_0\mathbf{I}) \tag{2.9}$$

The most general parameter vector θ_{sp} that fully describes a single SMC is given by:

$$\boldsymbol{\theta}_{sp} = \left[\begin{array}{cccccccccc} \alpha & \tau & \vartheta_T & \varphi_T & \vartheta_R & \varphi_R & \gamma_{HH} & \gamma_{HV} & \gamma_{VH} & \gamma_{VV} \end{array} \right] \tag{2.10}$$

where α is the Doppler shift, τ the excess delay, ϑ and φ are the azimuth and elevation angle at transmission T and reception R, respectively.

The DMC parameter vector $\boldsymbol{\theta}_{dmc}$ is given by:

$$\boldsymbol{\theta}_{dmc} = \left[\begin{array}{ccc} \alpha_1 & \beta_d & \tau_d \end{array} \right] \tag{2.11}$$

where α_1 is the DMC peak, β_d the coherence bandwidth of the diffuse components, τ_d the base delay (Fig. 1.6). Also, the polarimetric complex amplitude of each path is represented by γ_{HH}, γ_{HV}, γ_{VH}, and γ_{VV}.

A compact form for the SMC channel model $\mathbf{s}(\boldsymbol{\theta}_{sp})$ is given by:

$$\mathbf{s}(\boldsymbol{\theta}_{sp}) = \mathbf{B} \cdot \gamma \tag{2.12}$$

where $\mathbf{B} \in \mathbb{C}^{M_T M_R M_f M_t \times 4P}$ is the channel matrix and $\gamma \in \mathbb{C}^{4P \times P}$ is the polarimetric matrix describing the complex amplitude of each path. M_T and M_R are the number of antennas at the transmitter and receiver side, respectively. M_f and M_t are the number of samples in the frequency and time domain. Finally, P is the number of SMC in the channel. The complete polarimetric specular MIMO channel model can be developed from (2.12) by assuming that all dimensions are independent from each other:

$$\begin{aligned} \mathbf{s}(\boldsymbol{\theta}_{sp}) =& (\mathbf{B}_{T_H} \diamond \mathbf{B}_{R_H} \diamond \mathbf{B}_f \diamond \mathbf{B}_t) \cdot \boldsymbol{\gamma}_{HH} + (\mathbf{B}_{T_H} \diamond \mathbf{B}_{R_V} \diamond \mathbf{B}_f \diamond \mathbf{B}_t) \cdot \boldsymbol{\gamma}_{HV} + \\ & (\mathbf{B}_{T_V} \diamond \mathbf{B}_{R_H} \diamond \mathbf{B}_f \diamond \mathbf{B}_t) \cdot \boldsymbol{\gamma}_{VH} + (\mathbf{B}_{T_V} \diamond \mathbf{B}_{R_V} \diamond \mathbf{B}_f \diamond \mathbf{B}_t) \cdot \boldsymbol{\gamma}_{VV} \end{aligned} \tag{2.13}$$

where $\mathbf{s}(\boldsymbol{\theta}_{sp}) \in M_T M_R M_f M_t \times P$.

In addition and without going into deeper details, the Effective Aperture Distribution Function (EADF) technique was introduced with the purpose of separating the radio channel model from the measurement system model [12]. This final form is motivated by the fact that the measurement system (antenna array pattern and frequency response of the system) must be taken into consideration to calibrate the

SMC channel matrix:

$$\begin{aligned}\mathbf{s}(\boldsymbol{\theta}_{sp}) = &\left(\underbrace{(\mathbf{G}_{T_H}\cdot(\mathbf{A}_{\vartheta_T}\diamond\mathbf{A}_{\varphi_T})}_{\mathbf{B}_{T_H}}\diamond\underbrace{(\mathbf{G}_{R_H}\cdot(\mathbf{A}_{\vartheta_R}\diamond\mathbf{A}_{\varphi_R})}_{\mathbf{B}_{R_H}}\diamond\underbrace{(\mathbf{G}_f\cdot\mathbf{A}_f)}_{\mathbf{B}_f}\diamond\underbrace{(\mathbf{I}\cdot\mathbf{A}_t)}_{\mathbf{B}_t}\right)\cdot\boldsymbol{\gamma}_{HH}+\\ &\left(\underbrace{(\mathbf{G}_{T_H}\cdot(\mathbf{A}_{\vartheta_T}\diamond\mathbf{A}_{\varphi_T})}_{\mathbf{B}_{T_H}}\diamond\underbrace{(\mathbf{G}_{R_V}\cdot(\mathbf{A}_{\vartheta_R}\diamond\mathbf{A}_{\varphi_R})}_{\mathbf{B}_{R_V}}\diamond\underbrace{(\mathbf{G}_f\cdot\mathbf{A}_f)}_{\mathbf{B}_f}\diamond\underbrace{(\mathbf{I}\cdot\mathbf{A}_t)}_{\mathbf{B}_t}\right)\cdot\boldsymbol{\gamma}_{HV}+\\ &\left(\underbrace{(\mathbf{G}_{T_V}\cdot(\mathbf{A}_{\vartheta_T}\diamond\mathbf{A}_{\varphi_T})}_{\mathbf{B}_{T_V}}\diamond\underbrace{(\mathbf{G}_{R_H}\cdot(\mathbf{A}_{\vartheta_R}\diamond\mathbf{A}_{\varphi_R})}_{\mathbf{B}_{R_H}}\diamond\underbrace{(\mathbf{G}_f\cdot\mathbf{A}_f)}_{\mathbf{B}_f}\diamond\underbrace{(\mathbf{I}\cdot\mathbf{A}_t)}_{\mathbf{B}_t}\right)\cdot\boldsymbol{\gamma}_{VH}+\\ &\left(\underbrace{(\mathbf{G}_{T_V}\cdot(\mathbf{A}_{\vartheta_T}\diamond\mathbf{A}_{\varphi_T})}_{\mathbf{B}_{T_V}}\diamond\underbrace{(\mathbf{G}_{R_V}\cdot(\mathbf{A}_{\vartheta_R}\diamond\mathbf{A}_{\varphi_R})}_{\mathbf{B}_{R_V}}\diamond\underbrace{(\mathbf{G}_f\cdot\mathbf{A}_f)}_{\mathbf{B}_f}\diamond\underbrace{(\mathbf{I}\cdot\mathbf{A}_t)}_{\mathbf{B}_t}\right)\cdot\boldsymbol{\gamma}_{VV}+\end{aligned} \tag{2.14}$$

where $\mathbf{G}_{T_H}$ and $\mathbf{G}_{T_V}$ are the EADF computed from the measured radiation pattern of the transmit antennas with H and V polarization, respectively. Similarly, $\mathbf{G}_{R_H}$ and $\mathbf{G}_{R_V}$ are the EADF computed from the measured radiation pattern of the receive antennas with H and V polarization, respectively. $\mathbf{A}_\vartheta$ and $\mathbf{A}_\varphi$ for T and R are the steering vectors of the antenna array and describe the relationship between the angle of interest and phase difference between each antenna. $\mathbf{G}_f$ is the frequency response of the measurement system without the antennas. In general, the columns of $\mathbf{A}$ are described by a family of complex exponential vectors:

$$\mathbf{A} = e^{-j\boldsymbol{\mu}} \tag{2.15}$$

where $\boldsymbol{\mu}$ is the normalized parameter vector which links the physical parameters to their respective dimension. As an example, the normalized parameter vector for the delay domain is linked to the frequency via Fourier theory and is given by:

$$\boldsymbol{\mu}_\tau = 2\pi j\boldsymbol{f}\boldsymbol{\tau} \tag{2.16}$$

where $\boldsymbol{f}$ is the sampled frequency vector and $\boldsymbol{\tau}$ the time-delay vector of all SMC. A full description of all these matrices, parameter normalization scheme, and implementation can be found in [1].

Under the assumption that the dimensions of the measurement system are uncorrelated and independent, the channel covariance matrix $\mathbf{R}(\boldsymbol{\theta}_{dmc})$ can be factorized into a Kronecker product:

$$\mathbf{R}(\boldsymbol{\theta}_{dmc}) = \mathbf{I}_R\otimes\mathbf{I}_T\otimes\mathbf{R}_f(\boldsymbol{\theta}_{dmc})\otimes\mathbf{I}_t, \in \mathbb{C}^{M_RM_TM_fM_t\times M_RM_TM_fM_t} \tag{2.17}$$

Furthermore, under the Wide-Sense Stationary Uncorrelated Scattering (WSSUS) hypothesis, the band-limited sampled version of the DMC PDP is obtained

from the time-delay domain model defined in (1.5). Its corresponding covariance matrix can be described with a Toeplitz-like structure:

$$\mathbf{R}_f(\boldsymbol{\theta}_{dmc}) = \begin{bmatrix} \Psi_H(0) & \Psi_H(-f_0) & \cdots & \Psi_H((M_f-1)f_0) \\ \Psi_H(f_0) & \Psi_H(0) & \ddots & \vdots \\ \vdots & \ddots & \ddots & \Psi_H(-f_0) \\ \Psi_H((M_f-1)f_0) & \cdots & \Psi_H(f_0) & \Psi_H(0) \end{bmatrix} \in \mathbb{C}^{M_f \times M_f} \tag{2.18}$$

Each element of (2.18) can be derived by the corresponding Fourier transformation of (1.5) given by (2.19):

$$\Psi_H(\Delta f) = \frac{\alpha_1}{\beta_d + j2\pi\Delta f} \cdot e^{-j2\pi\Delta f \tau_d} \tag{2.19}$$

where Δf is the frequency sampling.

Originally, the DMC is estimated from the covariance matrix of the complete data model (i.e., sum of all polarization links) such that the estimate is an average across all polarization states. However, the DMC power characteristics are typically not uniform across all polarization links like for the scenarios investigated in this work. Consequently, the covariance matrix can be broken down into polarimetric parts such that the DMC can be estimated for each polarization link XY as in [49]:

$$\mathbf{R}^{XY}(\boldsymbol{\theta}_{dmc}) = \mathbf{I}_R^{XY} \otimes \mathbf{I}_T^{XY} \otimes \mathbf{R}_f^{XY}(\boldsymbol{\theta}_{dmc}) \otimes \mathbf{I}_t^{XY} \tag{2.20}$$

where X and Y can either be Horizontal (H) or Vertical (V) polarization states of the transmitter and receiver, respectively.

2.3.2 Joint estimation of SMC and DMC parameters

In the previous section, the radio channel and system model have been briefly introduced. The Probability Density Function (PDF) of an observed radio channel $\mathbf{x}$ drawn from the process (2.9 is given by:

$$p(\mathbf{x}|\theta_{sp}, \mathbf{R}(\theta_{dan})) = \frac{1}{\pi^M det(\mathbf{R}(\theta_{dan}))} e^{-(x-\mathbf{s}(\theta_{sp}))^H \cdot \mathbf{R}(\theta_{dan})^{-1} \cdot (x-\mathbf{s}(\theta_{sp}))} \tag{2.21}$$

The log-likelihood function derived from (2.21) is given by:

$$\begin{bmatrix} \hat{\boldsymbol{\theta}}_{sp} \\ \hat{\boldsymbol{\theta}}_{dan} \end{bmatrix} = \arg\max \left(-\ln(\det(\mathbf{R}(\boldsymbol{\theta}_{dan}))) - (\mathbf{x} - \mathbf{s}(\boldsymbol{\theta}_{sp})^H \cdot \mathbf{R}_{dan}^{-1} \cdot (\mathbf{x} - \mathbf{s}(\boldsymbol{\theta}_{sp}))) \right) \tag{2.22}$$

From that point of view, this multi-dimensional parametric equation can be understood as a weighted nonlinear least-square problem which can be treated as such by known mathematical techniques. RiMAX algorithm was developed within this constrained problem an iterative ML estimator which sequentially estimates the

SMC and DMC parameter vectors. The general iterative framework is introduced in Figure 2.3.

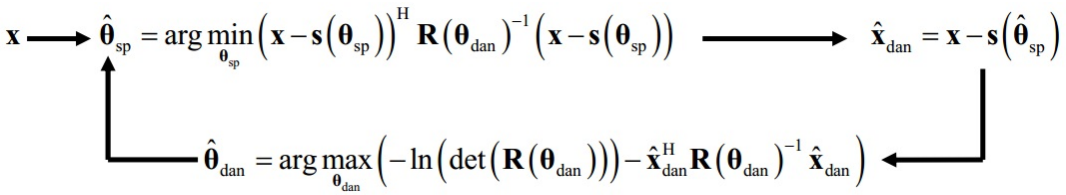

Figure 2.3: RiMAX iterative flowchart.

The main steps of the algorithm RiMAX are summarized below:

1) Compute initial estimation of SMC parameters under the assumption of white noise

2) Remove estimated SMC from channel and compute initial estimation of DMC parameters

3) Optimization of the DMC parameters

4) Optimization of the SMC parameters

5) Verification of the SMC reliability with criterion

6) if all SMC fail the criterion then stop otherwise jump to 1).

2.3.2.1 SMC parameter estimation

An initial guess of the parameters for each SMC can be obtained by using an extensive grid-search approach for each dimension. Basically, the **A** matrices are pre-computed over the desired searching window. These functions are then correlated with the observed radio channel in each dimension to obtain cost functions. Roughly, the cost function returns an oversampled PDP and oversampled beamformer in the time-delay and angular domains, respectively. The initial SMC parameters are found as the maxima in the cost functions. Typically, this step is the most computationally demanding in the whole algorithm and the number of SMC must be selected with care. It was empirically found that 5 SMC give the best tradeoff between convergence, time, and complexity. Typically, the initialization of the SMC parameters is performed with the following estimation sequence:

1) Initial estimation of $\hat{\tau}^{\{0\}}$.

2) Initial estimation of DOD, $\hat{\vartheta}_T^{\{0\}}$ and $\hat{\varphi}_T^{\{0\}}$ knowing $\hat{\tau}^{\{0\}}$.

3) Initial estimation of DOA, $\hat{\vartheta}_R^{\{0\}}$ and $\hat{\varphi}_R^{\{0\}}$ knowing $\hat{\tau}^{\{0\}}$, $\hat{\vartheta}_T^{\{0\}}$ and $\hat{\varphi}_T^{\{0\}}$.

4) Estimation of the coherent path weight $\hat{\gamma}^{\{0\}}$ knowing all previous estimates using the Blest Linear Unbiased Estimator (BLUE).

Then, the initial estimates are optimized using classical iterative routines dedicated to deterministic least-square problems. The iterative optimization step is given by:

$$\boldsymbol{\theta}^{\{i+1\}} = \boldsymbol{\theta}^{\{i\}} + \zeta \cdot \Delta\boldsymbol{\theta}^{\{i\}} \tag{2.23}$$

where ζ is an adjustable coefficient. Several optimization approaches have been proposed such as the steepest descent, Newton-Raphson, and Gauss-Newton or Levenberg-Marquardt method. The latter was selected as it provides the lowest level of complexity and the largest computational speed. These algorithms are not discussed in this manuscript but can found found here [1]. The algorithm stops once $|\boldsymbol{\theta}^{\{i+1\}} - \boldsymbol{\theta}^{\{i\}}|$ is below a pre-defined threshold.

2.3.2.2 DMC parameter estimation

An initial guess of the DAN (DMC and noise) parameter vector is obtained after subtracting the initial SMC from the observed channel.

$$\hat{\mathbf{x}}_{dan} = \mathbf{x} - \mathbf{s}(\hat{\boldsymbol{\theta}}_{sp}) \tag{2.24}$$

These parameters in $\hat{\boldsymbol{\theta}}_{dan}$ are subsequently identified using the mean PDP computed from the residual channel $\hat{\mathbf{x}}_{dan}$. Similarly to the SMC but using a stochastic approach, a Levenberg-Marquardt step is performed to optimize the DMC parameters.

2.4 Polarimetric MIMO radio channel sounder systems

Before applying channel parameter estimation techniques, polarimetric radio channel transfer functions must be assessed with a dedicated measurement equipment and antenna arrays. Such a scientific system is typically called a radio channel sounder. In this thesis, two types of MIMO sounder systems operating around 1.3 GHz, fully developed in the TELICE group, have been used for the two considered propagation scenarios with different array configurations. Their main features and antenna characteristics are introduced in the following sections. This central frequency was selected to describe the physical propagation phenomena for the mobile and WiFi standards without emitting in the licensed bands.

2.4.1 Virtual MIMO radio channel sounder

The first MIMO sounder system is based on a Vector Network Analyzer (VNA) which is a very popular and attractive solution in the propagation community for

its hardware simplicity and cost as such. Its main advantage lies in the fact that all ports are fully synchronized with the same Local Oscillor (LO) thus alleviating any issues related to signal synchronization and calibration. Also, a broad frequency range and frequency points can be selected within the specifications of the VNA while preserving a high dynamic range and SNR. Finally, it can easily be externally controlled for automatic measurement routines. However, several drawbacks must be highlighted. Since the number of ports of limited, two solutions are possible to measure a MIMO channel. On the one hand, all antennas of the array are sequentially switched. On the other hand, a single antenna can be moved at specific positions in space in order to describe the desired array and measurements are performed in-between each position. The latter solution called virtual sounding was the approach selected in TELICE but requires that the radio channel is stationary. Indeed, the measurement time is strongly dependent to the antenna motion time and is, therefore, not compatible with the measurements of time-varying radio channels. Depending on the number of virtual antennas, the measurement time necessary to probe a full polarimetric radio channel can easily exceed several minutes or dozens of minutes. Also, additional Radio-Frequency (RF) cables or RF to optical/optical to RF links must be used to increase the distance between the emitter and receiver resulting in an increased noise figure and reduced SNR. For the above reasons, the virtual channel sounder technique was used to probe the polarimetric radio channels in the investigated indoor scenario. The measurements can be done at night to ensure that the radio channel stationarity is enforced and long cables can also easily be deployed.

2.4.1.1 Sounder system description

The architecture of the TELICE virtual MIMO channel sounder is presented in Fig. 2.4 and relies on a 4-port VNA of reference Agilent E5071C. Two emitting ports are connected to the Horizontal (H) and Vertical (V) ports of the Tx antenna. The other two ports are connected to the H and V ports of the Rx antenna. The 4-port VNA allows measuring simultaneously the V and H components of Rx. A 50 dB isolation switch was placed behind Tx to manually or automatically switch between H and V. Hence, under for a given static Tx-Rx position, a full polarimetric SISO transfer function can be measured. In addition, A 500 m optical fiber was deployed for the transmitting side with an RF to optics/optics to RF interface to allow the Tx to move within a 500 m radius of the Rx. Typically, the system is Through calibrated to remove the attenuation introduced by the optical system setup and the RF cables. Only a Through calibration is required in this setup since only the normalized transmission coefficient between the emitting and receiving port is required. An additional 1 W power amplifier can be placed at the transmitting side to increase the SNR. Low Noise Amplifiers (LNA) with Noise Factor of $\sim$1.2 dB can be optionally added at each receive ports to boost the received signal power if necessary. It is noteworthy that the power amplifiers and LNAs were not included in the calibration. Their frequency-dependent characteristics were characterized

separately to correct the measured transfer functions.

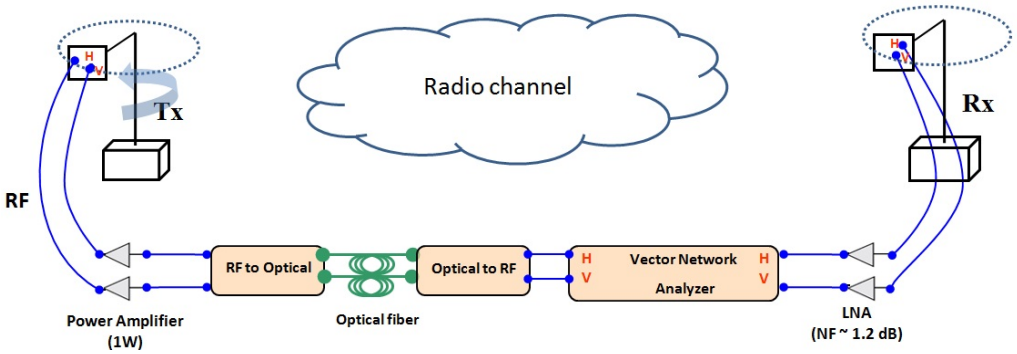

Figure 2.4: Architecture of the TELICE Virtual MIMO radio channel sounder.

2.4.1.2 Antenna array and element

At both link ends, a virtual antenna array was created by an antenna mounted on an automated rotating arm (Fig. 2.4). At both Tx and Rx side, dual-polarized antennas were used, installed at 1.60 m above ground level. The virtual array was a planar horizontal uniform circular array (UCA) with radius 15 cm and consisting of $M_T = M_R = 8$ dual-polarized antenna elements. Hence, a 16 x 16 MIMO radio channel can be measured under these conditions. For such an array, the generic steering vector is defined by:

$$\mathbf{A}_{\varphi,\vartheta} = e^{\frac{-2\pi j \mathbf{r}}{\lambda}\cos(\varphi)\sin(\vartheta)} \tag{2.25}$$

where $\mathbf{r}$ is the antenna position vector and λ the wavelength at 1.35 GHz. A UCA is rather adequate for indoor scenarios. It has a full 360° visibility in the azimuth plane to maximize the estimation of MPC around the transmitter and receiver. However, it comes at the expense of a limited 20° visibility in the elevation plane. Also, since the array is parallel to the ground, there is an ambiguity and the estimator can not know whether the MPC arrive below or above the array.

Figure 2.5 presents a front and rear view of the dual-polarized antennas used for Tx and Rx. They are identical 1.6-mm-thick FR4 ($\epsilon_r = 4.35$) square patches and the size of the copper ground plane is 11.06 cm ×11.06 cm and 55.9 mm ×55.9 mm for the active region. Via-hole SMA feeds were positioned horizontally and vertically at 1.575 cm from the center of the active region to obtain orthogonal modes between V and H with 50 Ω characteristic impedance.

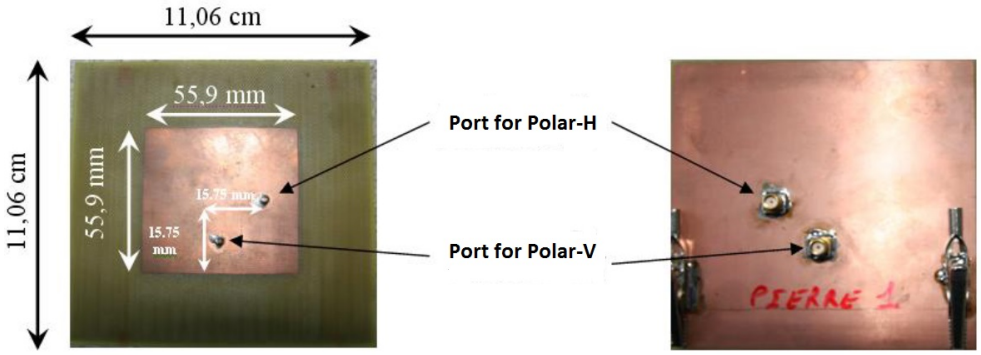

Figure 2.5: Dual-polarized patch antenna for the Virtual MIMO sounder.

The measured S-parameters are presented in Fig. 2.6. Both antennas display a 22 MHz bandwidth measured for a return loss lower than -10 dB with a 1.3 GHz central frequency. A 25 dB isolation between the ports is observed in the operating band. It should be mentioned that S_{HV} and S_{VH} are identical.

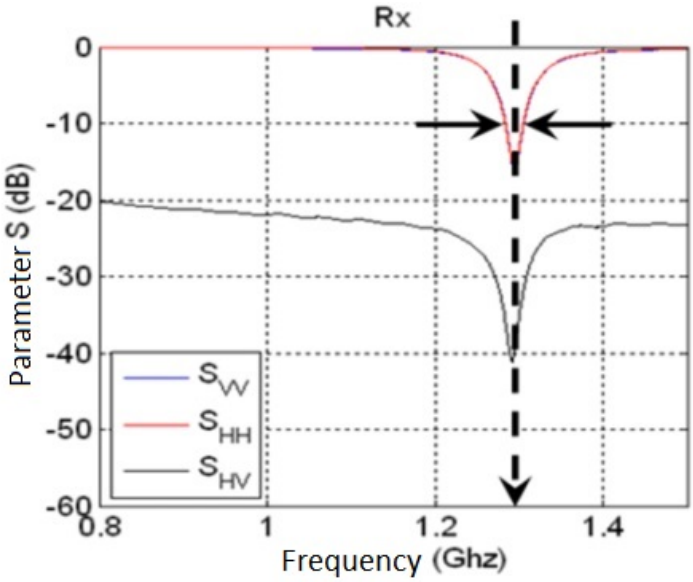

Figure 2.6: Measured S-parameters.

Finally, Figure 2.7 presents the normalized co- and cross-polar far-field radiating patterns for the H and V ports at 1.3 GHz. These polarimetric patterns were measured in an anechoic chamber at the University of Gent using a reference horn antenna. The antennas exhibit a 5 dBi gain. As shown, the antennas have a minimum 15 dB XPD with computed 120° and 100° beamwidth at half-power measured in the azimuth and elevation plane, respectively. There is also a maximum backward gain of -10 dB.

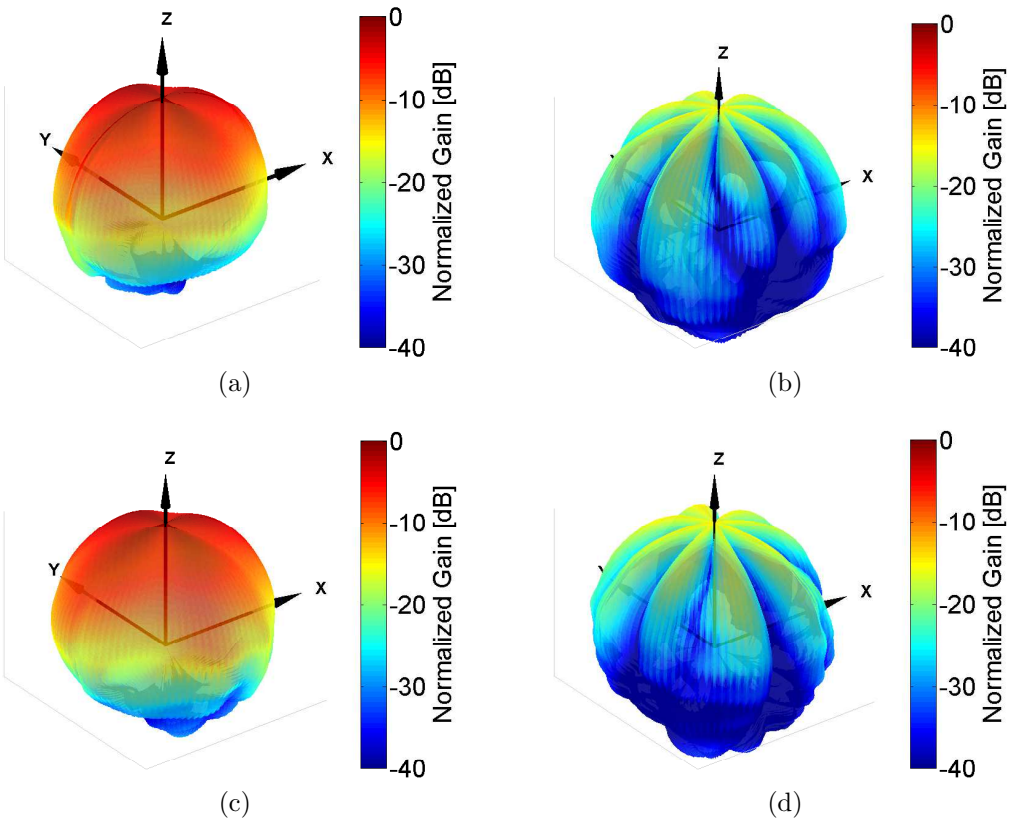

Figure 2.7: Normalized far-field radiating patterns for (a) VV, (b) VH, (c) HV, and (d) HH (in dB) measured at 1.3 GHz. The patterns have been normalized with respect to the maximum gain for each port.

2.4.2 MIMOSA radio channel sounder

In contrast with the in-house virtual radio channel sounder, true MIMO sounder systems can be commercially rented or bought from companies but are very complex and expensive scientific electronic equipments. Their main advantages lie in the possibility of measuring time-varying radio channels under less than milliseconds over very large distances without the need of a physical link between the emitter and receiver for LO synchronization purposes. Thus, since Tx and Rx are independent, the systems can be embedded into any fitting vehicles when low- to high-speed scenarios are considered. However, post-processing of the recorded data is mandatory to retrieve the complex transfer functions with all commercial systems available on the market. This problem can be rapidly intractable when large dataset are collected. The engineers and researchers of the TELICE group decided to develop their own radio channel sounder called MIMOSA which is briefly described hereafter. This sounder was used to assess the polarimetric radio channels in forest scenarios due to the dynamics of the channel discussed in chapter . Also, it circumvents the difficulties related to having the emitter away from the virtual sounder in a dense

vegetation environment.

2.4.2.1 Sounder system description

MIMOSA is a a 16 x 16 MIMO channel sounder operating with a 100 MHz bandwidth around 1.35 GHz and its basic architecture is presented in Figure 2.8. It is based on interleaved Orthogonal space-Frequency Division Multiplexing (OFDM), giving a large possibility of tone and antenna allocation. This channel sounder belongs to the new generation of software radio design based systems. The architecture was designed to comply with the highest flexibility thus opening a wide range of applications. In addition, the channel sounder has been built to avoid heavy post-processing: i) the Tx signal is pre-processed to include the non-linearity of the Tx and Rx chain, ii) thanks to the high sampling frequency of the FPGA (Field-Programmable Gate Array), a real digital baseband signal is transmitted to the RF chain avoiding I/Q impairment, iii) the output file gives transfer functions of the full polarimetric matrix in a versatile binary format. The power consumption of the sounder is low and can be powered with a 12 V/24 V vehicle battery. Finally, a friendly Graphic User Interface (GUI) was designed to parameterize the system.

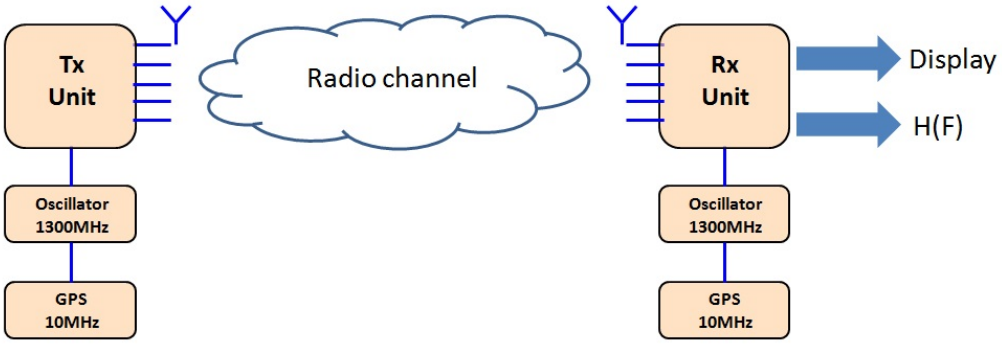

Figure 2.8: MIMOSA radio channel sounder architecture.

The transmitting frame structure consists in one preamble subsequently followed by N_s OFDM symbols which include the cyclic prefix. The preamble provides the time synchronization of the frame such that the OFDM symbols can be decoded. The total number of transmitted OFDM subcarriers N_t is 8192 which can be uniformly distributed on each antenna element. For example, with an 8-antenna array, the frequency space ΔF between the subcarriers of a single antenna is 97.66 kHz, meanwhile the frequency space Δf between subcarriers is 12.21 kHz. The main features of MIMOSA are presented in the Table 2.1.

Table 2.1: MIMOSA radio channel sounder main features.

RF			Baseband	
Center frequency	1350 MHz		Tx sampling rate	400 MHz
Tx max power	500 mW		Rx sampling rate	200 MHz
Number of channel	Tx (V/H)	8	Bandwidth	100 MHz
	Tx switch mode (V/H)	16	N_t	8192
			ΔF	97.66 kHz
			Δf	12.21 kHz
	Rx	8	Oversampling ratio R	2
Tx power Amp	1-6 GHz P_{out} = 1 W		IFFT length	32768
Rx LNA NF = 1 dB	1-4 GHz G = 40 dB		FFT length	16384

2.4.2.2 Antenna array and element

Two identical planar Uniform Rectangular Array (URA), shown in Figure 2.9, were selected at both link ends to probe the radio channel in forest scenarios. Each array consists in 8 dual-polarized antennas with inter-element spacing of 0.486λ at 1.35 GHz (10.8 cm) along x and y (0.5 cm from side to side). Since the number of antennas is even, the position of the antennas has been optimized with simulations to minimize the variance of the error between the real and estimated parameters. For such an array, the generic steering vector for each path is defined by:

$$\mathbf{A}_{\varphi,\vartheta} = \left(e^{\frac{-2\pi j\mathbf{dx}}{\lambda}\sin(\varphi)\cos(\vartheta)}\right) \otimes \left(e^{\frac{-2\pi j\mathbf{dy}}{\lambda}\sin(\vartheta)}\right) \tag{2.26}$$

where **dx** and **dy** are the antenna position matrices along x and y respectively. This array was placed perpendicular to the ground and has a 180° visibility in the azimuth and elevation plane such to maximize the estimation of MPC in front of the array. However, it is not capable to resolve MPC coming from the back plane. For those reasons, it is adequate to measure the propagation characteristics of a medium in-between the transmitter and receiver. Open forest scenarios fall under this category thus motivating our choice for this array topology.

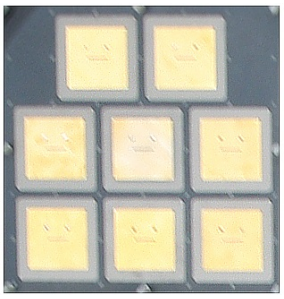

Figure 2.9: 8-element URA with dual-polarized slot patch antennas.

All the antennas used in the array are identical slot patch antennas with two orthogonal -45°/+45° polarization ports as illustrated in Figure 2.10. It is 10.3 mm

thick with a 103 mm × 103 mm × 103 mm ground plane. The thickness is used to reach the desired bandwidth and was achieved by bonding three duroid layers with dielectric adhesive layers. The two rear ports have a 50Ω characteristic impedance are connected to the active region with SMA via-holes.

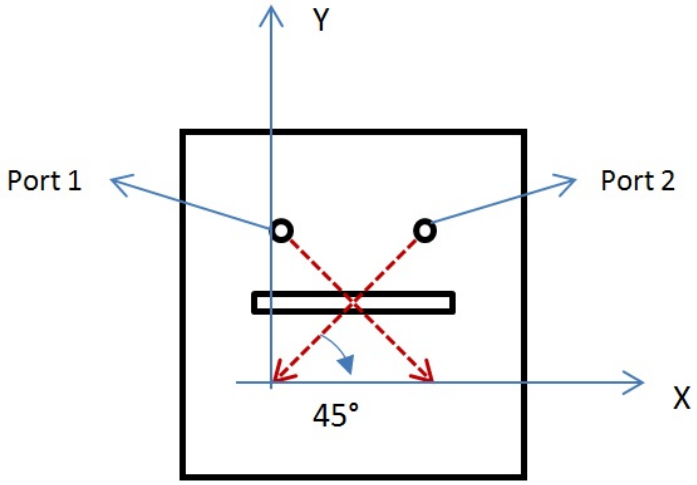

Figure 2.10: Dual-polarized slot patch antenna for MIMOSA. The red dash lines indicate the polarization direction of each port.

The simulated S-parameters shown in Figure 2.11 indicates a 1.35 GHz center frequency. A 72 MHz bandwidth is observed at -10 dB and the isolation between the two ports is larger than -18 dB. Since the antenna bandwidth is less than that of the measurement system, a 80 MHz bandwidth tradeoff was selected for the measurements. The measured polarimetric far-field patterns associating with different polarization state are showed in Fig. 2.12 with the measured antenna element placed at the X-Y plane. The antennas exhibit a ∼7 dBi gain with 80° beamwidth at -3 dB in the azimuth and elevation plane, respectively.

A drawback of the antenna topology is the -45°/+45° polarization scheme. It is not appropriate to transmit and receive H and V fields per se while polarimetric propagation characteristics are typically performed with these reference fields. This problem is simply solved by rotating the array by ±45° such that the port 1 (or 2) emits/receives a V (or H) field.

2.5 Theoretical performance of RiMAX for UCA and URA

The performance of the ML estimator RiMAX was assessed for the two radio channel sounder systems and their respective antenna arrays used in this work.

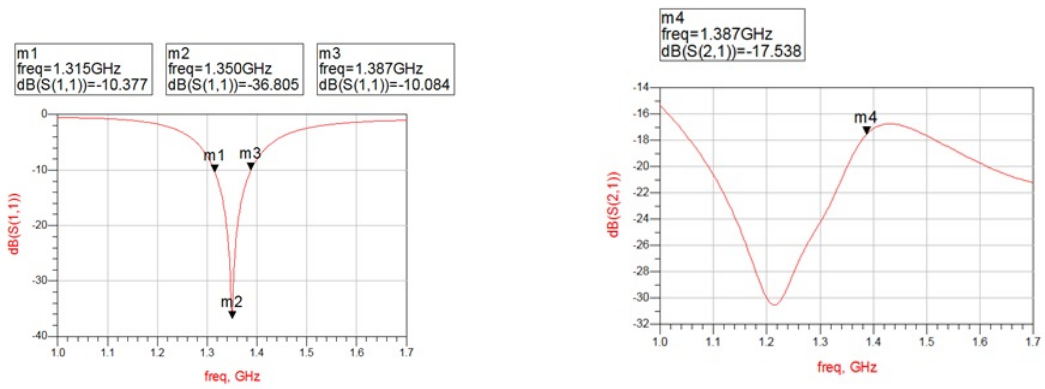

(a) (b)

Figure 2.11: Simulated S-parameters of the antenna ports by ADS Momentum simulation, (a) S_{11} , (b) S_{21}.

The purpose of this step is critical to investigate the resolution capabilities of the numerical technique when applied to real-world data. It was demonstrated in[1] that the Cramér-Rao Lower Bound (CRLB) is attained in the RiMAX framework for asymptotically uncoupled SMC (i.e. the parameters are not correlated). The CRLB is the uniform bound on the variance of any parameter estimator $\hat{\theta}$ for the parameters of a given model. It determines the variance of an unbiased estimator, which is minimum variance unbiased (MVUB). An unbiased estimator satisfies the following equation:

$$\mathbf{E}\left(\hat{\boldsymbol{\theta}} - \boldsymbol{\theta}\right) = 0 \tag{2.27}$$

where $\mathbf{E}$ is the expectation operator. The CRLB is then understood as the variance of the estimation error:

$$\mathbf{CRLB} = \mathbf{E}\left(\left(\hat{\boldsymbol{\theta}} - \boldsymbol{\theta}\right) \cdot \left(\hat{\boldsymbol{\theta}} - \boldsymbol{\theta}\right)^{T}\right) \tag{2.28}$$

The following methodology was used to evaluate the CRLB. For each antenna array and sounder frequency parameters, polarimetric synthetic radio channels were simulated with a single SMC using the adequate radio channel and polarimetric antenna patterns (EADF) and a 20 dB AWGN was added to the synthetic channel. The SMC parameters were randomly drawn from a uniform distribution within the search range of the measurement system. This range is dictated for the time-delay domain by the number of frequency points M_f, bandwidth, and central frequency. For the angular domain, it is a function of the number of antennas $M_{R/T}$, inter-element spacing, central frequency, and steering array (UCA or URA). An absolute amplitude of one and random phase were selected for all elements of the polarimetric path matrix. In addition, the CRLB was computed as a function of snapshots which was either 1, 10, 100, and 1000. Obviously, the larger the number of snapshots the

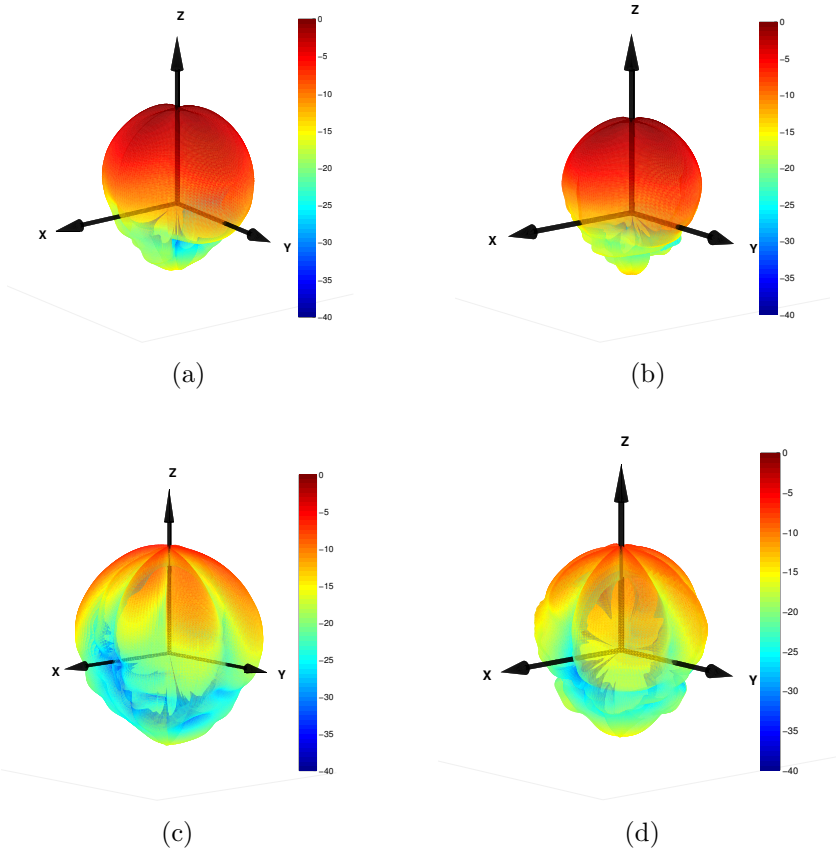

(a) (b)

(c) (d)

Figure 2.12: Measured normalized far-field antenna pattern for, (a) port 1 co-polarization, (b) port 2 co-polarization, (c) port 1 cross-polarization, and (d) port 2 cross-polarization.

better the estimation of the covariance matrix used in the optimization steps. During the measurement campaign, $M_f = 1601$ and $M_{R/T} = 8$ with a 22 MHz bandwidth and 1.3 GHz central frequency were taken for the virtual radio channel sounder. For MIMOSA, $M_f = 819$ and $M_R = 8$ with a 80 MHz bandwidth and 1.35 GHz central frequency were taken. Note that only the DOA was computed for MIMOSA as it will be discussed in chapter 5.

As discussed previously, the URA can be tilted by $\pm 45°$ to transmit/receive true H and V polarized fields. Hence, the CRLB was computed for both array orientations. Only the variance for γ_{HH} is shown for the sake of clarity as all other polarimetric gains are the same. Prior computing the variance, the TOA was expressed in ns and the angles in degrees. Figure 2.13 presents the computed CRLB for the virtual radio channel sounder with UCA (a) and MIMOSA with URA (b). In general, the variance is much below 10^{-1} for all investigated parameters (except for the elevation with UCA). For example, standard deviation values of 0.07 ns and 0.26° are obtained for TOA and DOA/DOD, respectively with the UCA. A lower

variance is obtained for the URA array. This is expected as the URA introduces an additional true elevation dimension. Indeed, the CRLB is roughly proportional to the inverse of the squared total number of samples brought by each dimension[1]. For the UCA, the elevation is initially estimated but can not be optimized due to the structure of the UCA steering array. This results in a resolution decreased by a factor of 64 (8^2) for all parameters compared to the URA. Also, the results show that the 45° orientation of the URA has no consequences on the quality of the estimated parameters.

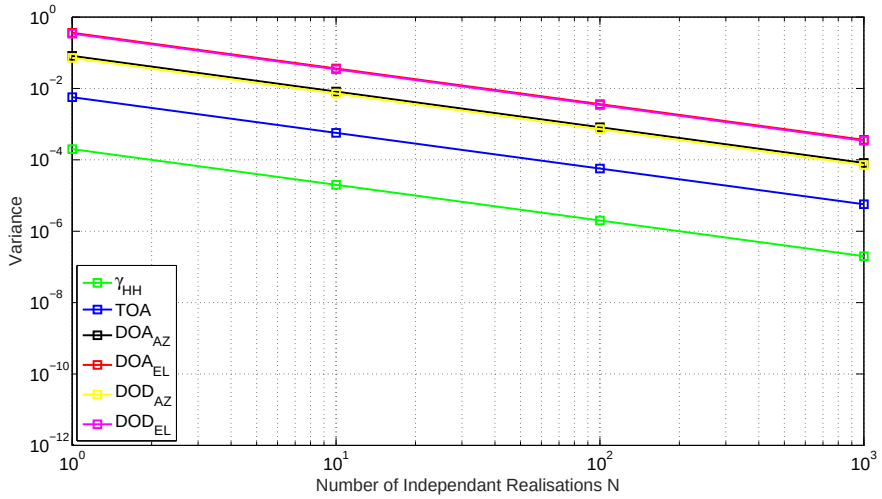

(a)

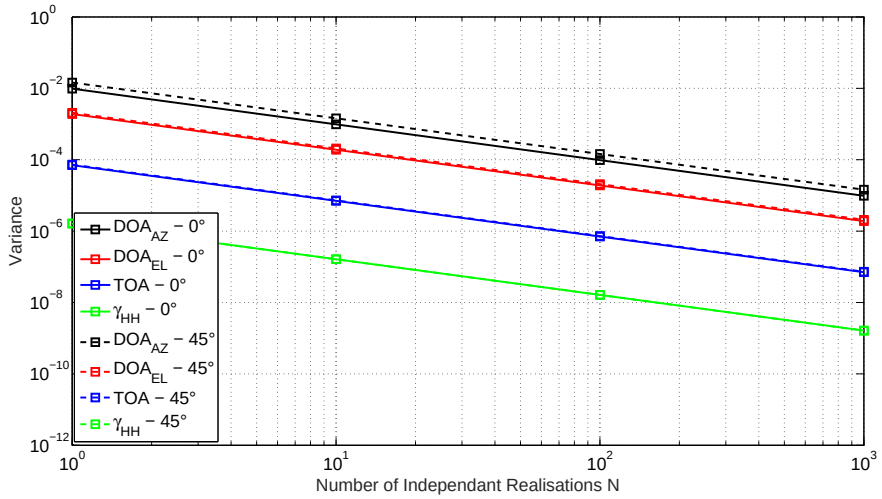

(b)

Figure 2.13: Variance of the estimation error computed for a) the UCA array (virtual sounder), and b) the URA array with 0° and 45° orientation (MIMOSA).

2.6 Conclusion

In this chapter, the classical and high-resolution radio channel parameters estimation techniques have been introduced along with a discussion on their advantages and disadvantages. The RiMAX framework including the radio channel and data model used in this thesis has been presented. The selection of the RiMAX algorithm was motivated by the fact that the radio channel model includes both SMC and DMC; the latter being the main focus of this thesis. In particular, the initialization and optimization steps of the SMC and DMC parameters have been briefly described starting from the ML function of the radio channel PDF. RiMAX provides a joint estimation of the SMC and DMC and the flowchart of the algorithm was discussed. Also, the SMC complex path gains estimates are free from the contribution of the polarimetric antenna patterns via the EADF technique. In addition, the two 16 x 16 polarimetric radio channel sounder systems used during the measurement campaigns have been described and their main features presented. First, the stationary indoor radio channel was assessed with a virtual channel sounder using horizontal UCAs at both link ends. For the more dynamic vegetation radio channel, the recently developed real-time MIMOSA sounder was used with vertical URAs at both link ends. For the sake of comparison, both systems were operated around $\sim$1.3 GHz with 22 and 80 MHz bandwidth, respectively. Also, the performance of the ML RiMAX estimator was evaluated to quantify the lowest variance of the estimation error that can be possibly reached for both systems . The purpose of the measurement campaigns is to provide a large set of radio channel transfer functions which then feed a high-resolution parameter estimator. Hence, the performance of the chosen RiMAX estimator was evaluated and discussed for each system and antenna array.

Chapter 3

Polarimetric distance-dependent model for scenarios with DMC and clustering approach of radio channel parameters

3.1 Introduction

Over the recent years, extensive experimental studies have been performed with the aim of providing a deeper physical comprehension of the propagation mechanisms and developing physically sound radio channel models for all types of scenarios.

Originally, the radio channel was commonly considered as a mere collection of specular multipath components (SMCs) that have well defined discrete locations in the different radio channel dimensions. Recently, distributed diffuse scattering on electrically small objects and SMCs with low SNR are also included into the channel but were historically interpreted as polluting noise. It has been widely accepted that the DMC is another important multipath radio channel component. From now, the existing channel model and channel model parameters need to be refined by including DMC. Faithful models of the DMC are critical to reproduce the propagation characteristics of the radio channel such as the path loss, mean delay, root-mean-squared delay spread (rms). These characteristics are used for typical coverage analysis, network optimization, localization [111], or even human exposure analysis [112].

On the other hand, modern radio channel models are expected to encompass a polarimetric description of the physical radio link that could be used for the optimization of diversity-based wireless communications or dedicated applications. In [49], the general radio characteristics, cross-polar discrimination (XPD) statistics, and propagation mechanisms were investigated from each estimated individual SMC and DMC as a function of distance and shadowing conditions. Inspite being appealing for the propagation community, polarimetric PDP and path gain models as well as path loss models including both the SMC and DMC are missing in the

literature.

In this chapter, a polarimetric model of the SMC and DMC PDP/path gain is developed to fulfill this gap. The proposed model is a strongly modified extension of [2]. In particular, it provides a finer polarimetric description of the SMCs which are decomposed into primary and secondary parts and the DMC. The polarimetric path gain model can be used to describe any general characteristics such as the rms delay spread, XPD, or DMC fractional power. From this approach, single-slope path loss models are discussed to take into account the contribution of the DMC. Furthermore, an additional important novelty of this work is the development of a two-step fitting method to obtain jointly the path loss characteristics for the primary SMC and DMC directly from the measured channels. This approach is validated with the measurement and modeled data. A connection between the DMC path loss characteristics and room electromagnetics theory is also highlighted.

Moreover, a generic clustering identification approach is developed and proposed. Clustering is one important MIMO channel analysis tool which aims at providing a better comprehension of the radio channel propagation mechanisms with reduced complexity. The performance of the proposed clustering identification approach is evaluated with simulated radio channels presenting realistic cluster like features. The results are also compared with different clustering identification algorithm. Furthermore, the developed approach uncovers a physical link between the best clustering solution and the propagation characteristics for a given scenario. This latter aspect could be used to categorize scenarios based on their clustering properties and to improve existing radio channel models.

3.2 Polarimetric Distance Dependent Model

The development of faithful path loss models is critical to the deployment of wireless systems in many propagation scenarios. For instance, indoor propagation models rely on the empirical path loss exponent n which links the received power with the logarithm of the distance [52]. A single-slope model is typically observed, but multi-slope (or multiple breakpoint) path loss models were also reported in office scenarios when the distance was large or when the receiver (transmitter) was located at a different floor [113].

Obviously, the path loss exponent retrieved from the measured channels must be a path loss weighted by the contribution of SMCs and DMCs if present, contribution which will depend on the Tx-Rx distance, room configuration, shadowing condition, etc. Moreover, DMC path loss models are missing to the knowledge of the authors. Hence, the computation of the DMC to the total power ratio is a prerequisite to analyze the contribution of each mechanism to the radio channel and impact on the path loss exponent. If we take the polarization aspect into account, one more detailed polarimetric radio channel model can be established.

Motivated by the experimental observation, one distance-dependent model was recently reported in [2]. The early part or primary SMC includes line of sight (LOS)

and first-order reflection off the walls, floor, ceiling, and objects. Similar to the room electromagnetics theory, the reverberant component is the remaining part of the PDP such that the DMC cannot be physically distinguished from the secondary SMC (high order reflections, diffractions, etc.).

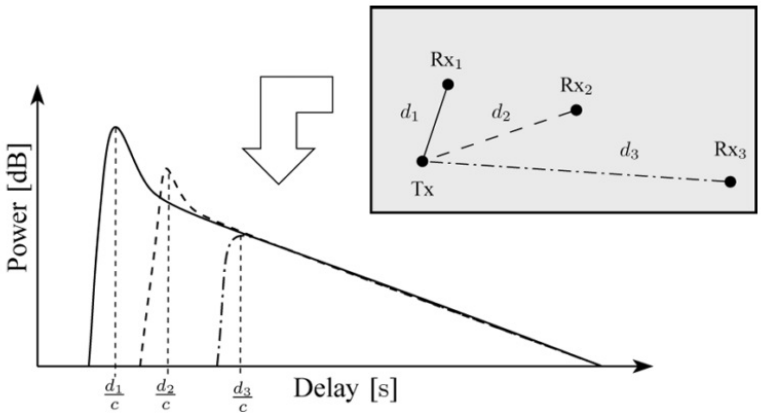

Figure 3.1: Illustration of the band limited PDP observation for in room environment in [2].

Such model can be illustrated in Figure 3.1 where the delay power spectrum is obtained by three measurement positions in the room. The peak is considered to be the primary components of SMC which follow a power law (d^{-n}). The tail part is modeled as the reverberant component which is exponentially decaying. The decay rate of the tail is considered to be identical in the whole room. Based on such conception, we propose one strong modification to refine such distance-dependent model.

3.2.1 PDP model

From the modeling point of view, the distance-dependent PDP can be understood as the sum of the band-limited SMC and DMC

$$\mathbf{G}(\tau, d) = \mathbf{G}_{SMC}(\tau, d) + \mathbf{G}_{DMC}(\tau, d) \tag{3.1}$$

Steinbock *et al* [2] recently proposed to decompose the PDP into primary and reverberation components which both display a dependence to the distance

$$\mathbf{G}(\tau, d) = \mathbf{G}_{pri}(\tau, d) + \mathbf{G}_{rev}(\tau, d) \tag{3.2}$$

The primary component describes the early part of the PDP and includes the LOS and first-order reflections (if present) off the floor, ceiling, walls, and objects. It was proposed to be simply modeled by

$$\mathbf{G}_{pri}(\tau, d) = \mathbf{G}_{0,pri} \left(\frac{d_0}{d}\right)^{n_{pri}} \delta\left(\tau - \frac{d}{c}\right) \tag{3.3}$$

where n_{pri} is the path loss exponent, $G_{0,pri}$ the reference gain for the primary component at reference distance $d = d_0$, and c the speed of light. In contrast, the reverberation component is the remainder of the channel after the primary component has been removed and describes the exponentially decaying behavior of the PDP tail as:

$$\mathbf{G}_{rev}(\tau, d) = \mathbf{G}_{0,rev} e^{-\tau/\mathbf{T}}, \quad \tau > \frac{d}{c} \tag{3.4}$$

where $\mathbf{T}$ is the reverberation time [23, 18]. From this point of view, it can be seen that the reverberation component could be the sum of DMC and the secondary SMC (high-order reflections, diffractions, etc.)

$$\mathbf{G}_{rev}(\tau, d) = \mathbf{G}_{sec}(\tau, d) + \mathbf{G}_{DMC}(\tau, d) \tag{3.5}$$

This modeling decomposition was shown to produce faithful distance dependent radio characteristics such as mean delay, delay spread, path gain, etc. However, the propagation properties and mechanisms of the DMC and secondary SMC could not be individually assessed. Here, we propose to alleviate this problem by introducing the following decomposition for the PDP:

$$\mathbf{G}(\tau, d) = \mathbf{G}_{pri}(\tau, d) + \mathbf{G}_{sec}(\tau, d) + \mathbf{G}_{DMC}(\tau, d) \tag{3.6}$$

As an example, the decomposition of the PDP into the primary/secondary SMC, and DMC is illustrated in Figure 3.2 for an indoor scenario with given transmitter-receiver distance d_i. This figure shows that the secondary SMC includes a wide collection of high-order SMCs that have different time delays and gains. It can simply be modeled as the superposition of weighted single Dirac terms with a power law model like with the primary component as proposed in equation 3.3.

$$\mathbf{G}_{sec}(\tau, d) = \sum_{k=1}^{N_{sec}} \mathbf{G}_{k,sec} \left(\frac{d_0}{d}\right)^{n_{sec}} \delta(\tau - \tau_k(d)) \tag{3.7}$$

where $\tau_k(d)$ and $G_{k,sec}$ are the distance-dependent time-delay and reference gain at reference distance $d = d_0$ for the kth secondary SMC, respectively. n_{sec} and N_{sec} are the path loss exponent and number of secondary SMC, respectively. In a simple empty environment such as the investigated one, it is assumed that N_{sec} does not change with the distance.

The exponential function from (3.8) was kept to model the N_{sec} secondary DMC in the delay domain.

$$\mathbf{G}^{exp}_{rev}(\tau, d) = \mathbf{G}^{exp}_{0,DMC} e^{-\tau/\mathbf{T}}, \quad \tau > \frac{d}{c} \tag{3.8}$$

where $\mathbf{G}^{Exp}_{0,DMC}$ is the reference gain at reference distance $d = d_0$. Moreover, when polarimetric measurements are considered, all components can be further decomposed into co-polar and cross-polar components.

$$\mathbf{G}^{XY}(\tau, d) = \mathbf{G}^{XY}_{pri}(\tau, d) + \mathbf{G}^{XY}_{sec}(\tau, d) + \mathbf{G}^{XY}_{DMC}(\tau, d) \tag{3.9}$$

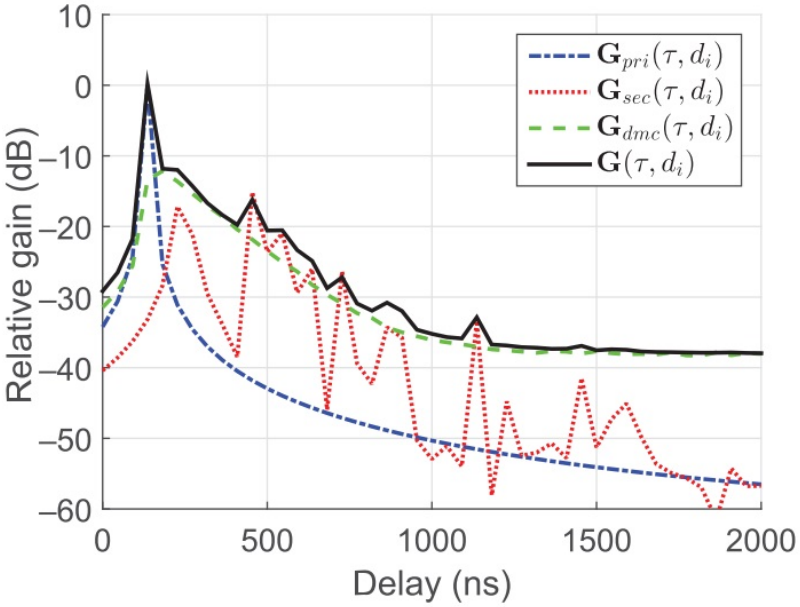

Figure 3.2: Illustration of the PDP behavior in an indoor scenario for certain transmitter-receiver distance d_i. The PDP includes the primary SMC, secondary SMC and DMC.

where the subscripts X and Y denote the polarization of the transmitting and receiving antenna, respectively. X and Y are either horizontal (H) or vertical (V). As discussed in chapter 2, this decomposition is motivated by the fact that electromagnetic waves might suffer strong depolarization mechanisms in highly reflective environments like indoor scenarios or outdoor scenarios with a vegetation environment. Necessarily, all components will experience depolarization effects but at different scales due to the nature of each propagation mechanism. Hence, the proposed distance-dependent polarimetric model for the primary SMC is given:

$$\mathbf{G}_{pri}^{HH}(\tau, d) = \chi_{pri}^{HH}(d)\mathbf{G}_{0,pri}^{HH}\left(\frac{d_0}{d}\right)^{n_{pri}^{HH}}\delta\left(\tau - \frac{d}{c}\right) \tag{3.10}$$

$$\mathbf{G}_{pri}^{HV}(\tau, d) = (1 - \chi_{pri}^{HH}(d))\mathbf{G}_{0,pri}^{HH}\left(\frac{d_0}{d}\right)^{n_{pri}^{HV}}\delta\left(\tau - \frac{d}{c}\right) \tag{3.11}$$

$$\mathbf{G}_{pri}^{VV}(\tau, d) = \chi_{pri}^{VV}(d)\mathbf{G}_{0,pri}^{VV}\left(\frac{d_0}{d}\right)^{n_{pri}^{VV}}\delta\left(\tau - \frac{d}{c}\right) \tag{3.12}$$

$$\mathbf{G}_{pri}^{VH}(\tau, d) = (1 - \chi_{pri}^{VV}(d))\mathbf{G}_{0,pri}^{VV}\left(\frac{d_0}{d}\right)^{n_{pri}^{VH}}\delta\left(\tau - \frac{d}{c}\right) \tag{3.13}$$

where χ_{pri}^{HH} and χ_{pri}^{VV} are the distance-dependent polarization coefficients for HH and VV, $\mathbf{G}_{0,pri}^{HH}$ and $\mathbf{G}_{0,pri}^{VV}$ the gain at reference distance $d = d_0$ for HH and VV,

and n_{pri}^{XY} the path loss exponent for each polarization link.

The distance-dependent polarimetric model for the secondary SMC is given with the similar conception:

$$\mathbf{G}_{sec}^{HH}(\tau,d)=\sum_{k=1}^{N_{sec}}\chi_k^{HH}(d)\mathbf{G}_{k,sec}^{HH}\left(\frac{d_0}{d}\right)^{n_{sec}^{HH}}\delta\left(\tau-\tau_k(d)\right) \tag{3.14}$$

$$\mathbf{G}_{sec}^{HV}(\tau,d)=\sum_{k=1}^{N_{sec}}(1-\chi_k^{HH}(d))\mathbf{G}_{k,sec}^{HH}\left(\frac{d_0}{d}\right)^{n_{sec}^{HV}}\delta\left(\tau-\tau_k(d)\right) \tag{3.15}$$

$$\mathbf{G}_{sec}^{VV}(\tau,d)=\sum_{k=1}^{N_{sec}}\chi_k^{VV}(d)\mathbf{G}_{k,sec}^{VV}\left(\frac{d_0}{d}\right)^{n_{sec}^{VV}}\delta\left(\tau-\tau_k(d)\right) \tag{3.16}$$

$$\mathbf{G}_{sec}^{VH}(\tau,d)=\sum_{k=1}^{N_{sec}}(1-\chi_k^{VV}(d))\mathbf{G}_{k,sec}^{VV}\left(\frac{d_0}{d}\right)^{n_{sec}^{VH}}\delta\left(\tau-\tau_k(d)\right) \tag{3.17}$$

where χ_k^{HH} and χ_k^{VV} are the distance-dependent polarization coefficient for HH and VV whereas $\mathbf{G}_{k,sec}^{HH}$ and $\mathbf{G}_{k,sec}^{VV}$ are the reference gain for HH and VV at reference distance $d=d_0$ for the kth SMC. Finally, n_{sec}^{XY} is the path loss exponent for each polarization link.

3.2.2 Polarimetric path gain model

From the developed distance-dependent polarimetric PDP model, the path gain $\mathbf{P}^{XY}$ averaged at distance d is derived by integrating the PDP with respect to delay for each propagation mechanism and polarization state.

$$\mathbf{P}^{XY}(d)=\int\mathbf{G}^{XY}(\tau,d)d\tau. \tag{3.18}$$

Consequently, the following path gain models are obtained for HH, HV, VH and VV, respectively:

$$\begin{aligned}\mathbf{P}^{HH}(d)=&\underbrace{\chi_{pri}^{HH}(d)\mathbf{G}_{0,pri}^{HH}(\frac{d_0}{d})^{n_{pri}^{HH}}}_{\mathbf{P}_{pri}^{HH}(d)}+\underbrace{\chi_{sec}^{HH}(d)\mathbf{G}_{0,sec}^{HH}(\frac{d_0}{d})^{n_{sec}^{HH}}}_{\mathbf{P}_{sec}^{HH}(d)}+\\&\underbrace{\chi_{DMC}^{HH}(d)\mathbf{G}_{0,DMC}^{HH}\mathbf{T}^{HH}e^{\frac{-d}{c\mathbf{T}^{HH}}}}_{\mathbf{P}_{DMC}^{HH}(d)}.\end{aligned} \tag{3.19}$$

$$\begin{aligned}\mathbf{P}^{HV}(d)=&\underbrace{(1-\chi_{pri}^{HH}(d))\mathbf{G}_{0,pri}^{HH}(\frac{d_0}{d})^{n_{pri}^{HV}}}_{\mathbf{P}_{pri}^{HV}(d)}+\underbrace{(1-\chi_{sec}^{HH}(d))\mathbf{G}_{0,sec}^{HV}(\frac{d_0}{d})^{n_{sec}^{HV}}}_{\mathbf{P}_{sec}^{HV}(d)}+\\&\underbrace{(1-\chi_{DMC}^{HH}(d))\mathbf{G}_{0,DMC}^{HH}\mathbf{T}^{HV}e^{\frac{-d}{c\mathbf{T}^{HV}}}}_{\mathbf{P}_{DMC}^{HV}(d)}.\end{aligned} \tag{3.20}$$

$$\mathbf{P}^{VV}(d) = \underbrace{\chi^{VV}_{pri}(d)\mathbf{G}^{VV}_{0,pri}(\frac{d_0}{d})^{n^{VV}_{pri}}}_{\mathbf{P}^{VV}_{pri}(d)} + \underbrace{\chi^{VV}_{sec}(d)\mathbf{G}^{VV}_{0,sec}(\frac{d_0}{d})^{n^{VV}_{sec}}}_{\mathbf{P}^{VV}_{sec}(d)} + \underbrace{\chi^{VV}_{DMC}(d)\mathbf{G}^{VV}_{0,DMC}\mathbf{T}^{VV}e^{\frac{-d}{c\mathbf{T}^{VV}}}}_{\mathbf{P}^{VV}_{DMC}(d)}. \tag{3.21}$$

$$\mathbf{P}^{VH}(d) = \underbrace{(1-\chi^{VV}_{pri}(d))\mathbf{G}^{VV}_{0,pri}(\frac{d_0}{d})^{n^{VH}_{pri}}}_{\mathbf{P}^{VH}_{pri}(d)} + \underbrace{(1-\chi^{VV}_{sec}(d))\mathbf{G}^{VV}_{0,sec}(\frac{d_0}{d})^{n^{VH}_{sec}}}_{\mathbf{P}^{VH}_{sec}(d)} + \underbrace{(1-\chi^{VV}_{DMC}(d))\mathbf{G}^{VV}_{0,DMC}\mathbf{T}^{VH}e^{\frac{-d}{c\mathbf{T}^{VH}}}}_{\mathbf{P}^{VH}_{DMC}(d)}. \tag{3.22}$$

In total, 24 parameters, some of which are distance dependent, are required to tune the PDP or path gain models where the DMC follows an exponential model in the delay domain. All model parameters are summarized in Table 3.1. Despite the high level of complexity, the proposed approach provides deep information about each mechanism for any polarization link. For instance, the model grants flexibility to derive other desired characteristics such as path loss models for each propagation component which will be later discussed in the following chapter.

Table 3.1: Proposed Model Parameters

		SMC		DMC
Param.	Polar.link	Primary	Secondary	Exp.law
n^{XY}	HH	$n_{pri^{HH}}$	n_{sec}^{HH}	X
	HV	$n_{pri^{HV}}$	n_{sec}^{HV}	X
	VH	$n_{pri^{VH}}$	n_{sec}^{VH}	X
	VV	$n_{pri^{VV}}$	n_{sec}^{VV}	X
$\mathbf{G}_0^{XY}$	HH	$\mathbf{G}_{0,pri}^{HH}$	$\mathbf{G}_{0,sec}^{HH}$	$\mathbf{G}_{0,DMC}^{HH}$
	VV	$\mathbf{G}_{0,pri}^{VV}$	$\mathbf{G}_{0,sec}^{VV}$	$\mathbf{G}_{0,DMC}^{VV}$
χ^{XY}	HH	χ_{pri}^{HH}	χ_{sec}^{HH}	χ_{DMC}^{HH}
	VV	χ_{pri}^{VV}	χ_{sec}^{VV}	χ_{DMC}^{VV}
$\mathbf{T}^{XY}$	HH	X	X	$\mathbf{T}^{HH}$
	HV	X	X	$\mathbf{T}^{HV}$
	VH	X	X	$\mathbf{T}^{VH}$
	VV	X	X	$\mathbf{T}^{VV}$

3.2.3 Polarimetric reverberation ratio

In the previous section, the total polarimetric path gain model has been introduced. In addition, the polarimetric DMC to total power ratio $\mathbf{R}^{XY}(d)$ is defined to provide a deeper understanding of the DMC contribution to the radio channel. The chosen definition is similar to the ones reported in previous works [25, 49, 114] without consideration of secondary SMC and is given by:

$$\mathbf{R}^{XY}(d) = \frac{\mathbf{P}_{DMC}^{XY}(d)}{\mathbf{P}^{XY}(d)} \tag{3.23}$$

This parameter directly presents the distance-dependent DMC contribution to the total received power and is bounded in the $[0, 1]$ range. It was shown in [2] that the reverberation ratio converges toward zero when the Tx-Rx distance approaches zero or infinity:

$$\lim_{d\to 0} \mathbf{R}^{XY}(d) = 0, \quad \lim_{d\to\infty} \mathbf{R}^{XY}(d) = 0 \tag{3.24}$$

As an example, the polarimetric reverberation ratio is presented for HH and HV in Figure 3.3 for selected values of the model parameters. A 0.9 depolarization constant was chosen to highlight the effect of strong depolarization mechanisms to the DMC characteristics and contribution to the radio channel. Also, under the assumption that room electromagnetic theory is satisfied, the reverberation time was varied between 20 ns and 40 ns for both HH and HV. The model predicts that the reverberation characteristics are rather different between the co-polar and cross-polar links for which DMC is particularly strong. In addition, it can be observed that the reverberation ratio increases with the reverberation time which is an expected physical effect. Finally, the distance at which the maximum value of the reverberation ratio occurs also depends on the reverberation time.

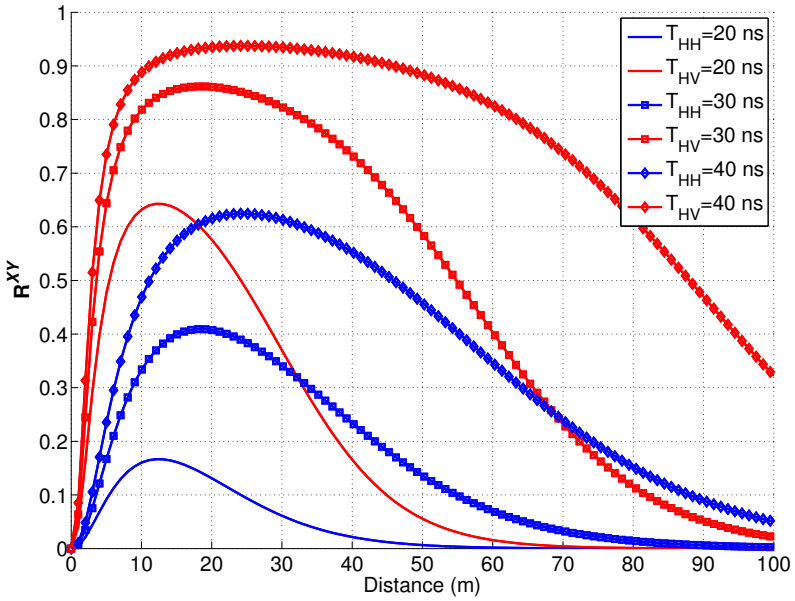

Figure 3.3: Illustration of the polarimetric reverberation ratio characteristics with the proposed model. The model parameters were set arbitrarily: $\mathbf{G}_{pri}^{HH} = 1$ dB, $\chi_{pri}^{HH} = 0.9$, $n_{pri}^{HH} = 2$, $\mathbf{G}_{sec}^{HH} = 1$ dB, $\chi_{sec}^{HH} = 0.9$, $n_{sec}^{HH} = 3$, $\mathbf{G}_{DMC}^{HH} = 60$ dB, $\chi_{DMC}^{HH} = 0.5$. T^{HH} and T^{HV} were varied between 20 ns and 40 ns.

Figure 3.4 presents the effect of DMC to the path gain using the same parameters than in Figure 3.3. For the sake of comparison, the black lines depict the path gain when no reverberation mechanisms are considered (i.e. $\mathbf{T}^{XY} = 0$). For this case, the proposed distance-dependent model simply turns back into a power law model. The convex parts clearly demonstrate the reverberation effect to the path gain model. With the considered model parameters, it is also observed that the reverberation mechanism has a greater impact on the cross-polarization state than the co-polarization one.

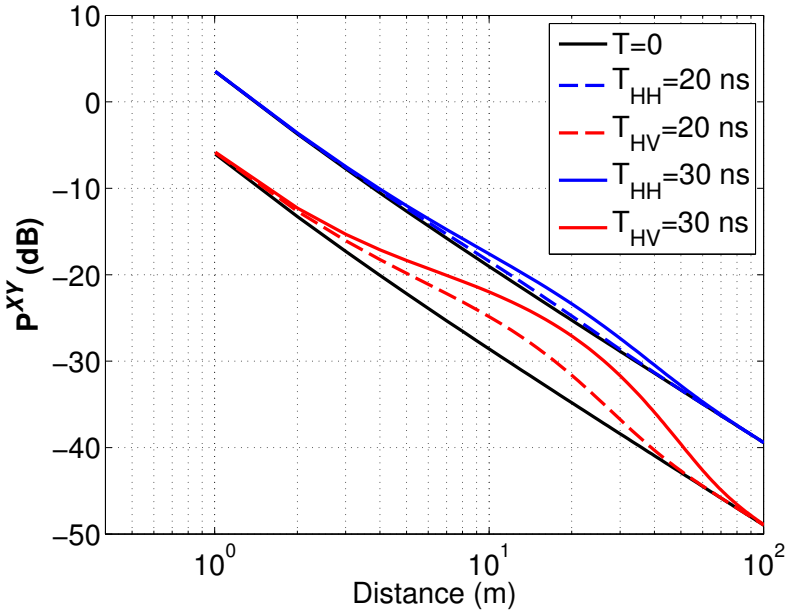

Figure 3.4: Illustration of the polarimetric path gain in presence of DMC. The same model parameters than in Figure 3.3 were used.

3.3 Low Complexity Path Loss Parameters Fitting Technique

The presented path loss models require a priori estimation of the SMC and DMC path gains from the measured polarimetric radio channels. It is reminded that the estimation process is a highly complex mathematical treatment requiring huge computational post-processing time especially when the dataset comprises hundreds or even thousands measurement points. In addition, modeling errors due to the antenna array calibration or assumptions in the data model could result in degraded estimates [12]. In contrast, classical log-distance path loss models have been widely used because they follow the opposite philosophy. They do not make any assumptions at all about the propagation mechanisms, and the fitting steps exhibit low complexity and fast processing time characteristics. Here, we explore the possibility to use the SMC plus DMC path loss models as fitting metrics. The motivation is to develop a low complexity technique to obtain joint estimates of the SMC and DMC path loss parameters without the need for estimation technique.

Inspired by the effects observed in Figure 3.3 and Figure 3.4, it is clear that the contribution of the DMC to the path gain occurs when the reverberation ratio is much above 50%. For this case, the main channel propagation mechanism is DMC and the channel path gain does not follow a power law (linear with the logarithm of distance) anymore but an exponential law (linear with distance). Therefore, it is considered that a low complexity path loss parameter fitting approach could be

developed if the path gain is overlooked with a different distance scale.

3.3.1 Path loss models including DMC for low complexity fitting technique

It is considered that the radio channel only includes DMC or that the contribution of the secondary SMC is weak compared to DMC. This case could happen if shadowing conditions are harsh [strong Non Line-Of-Sight (NLOS)] or if polarization coefficients are close to unity. For the latter case, the path gain model for the channel could be simplified by taking into account only the DMC path gain.

For instance, the polarimetric path loss $\mathbf{PL}_{DMC}^{XY}$ is obtained from the DMC path gain models $\mathbf{P}_{DMC}^{XY}$. Only the cross-polar links such as HV with exponential law are treated in the discussion, which is believed that the DMC is much more important in one cross polarization link. However, the model can be derived in the similar fashion for other links.

$$\left[\mathbf{PL}_{DMC}^{HV}(d)\right]_{dB} = -\left[(1-\chi_{DMC}^{HH})\mathbf{G}_{0,DMC}^{HH}\mathbf{T}^{HV}\right]_{dB} + \frac{10d}{c\mathbf{T}^{HV}log(10)} \tag{3.25}$$

Provided that $\mathbf{T}^{HV}$ and χ_{DMC}^{HV} are constant, it follows that the DMC path loss is linear with the distance and inversely proportional to $\mathbf{T}^{HV}$. This proportionality parameter or DMC path loss factor denoted here η_{DMC}^{HV} is given by

$$\eta_{DMC}^{HV} = \frac{10}{c\mathbf{T}^{HV}log(10)} \tag{3.26}$$

Equation (3.26) establishes a direct relationship between $\mathbf{T}^{HV}$ and η_{DMC}^{HV} and provides an attractive approach to link the room electromagnetics theory characterized by $\mathbf{T}^{HV}$ with the loss mechanisms of the channel characterized by the DMC path loss factor. Evidently, η_{DMC}^{HV} will also change if the room electromagnetics theory does not apply ($\mathbf{T}^{XY}$ not constant across all polarization links). Finally, it is possible to reformulate the DMC path gain model by substituting (3.26) in (3.8) to highlight η_{DMC}^{HV}

$$\mathbf{P}_{DMC}^{HV}(d) = ((1-\chi_{DMC}^{HH})\mathbf{G}_{0,DMC}^{HH}\mathbf{T}^{HV})e^{\frac{-\eta_{DMC}^{HV}d\cdot log(10)}{10}} \tag{3.27}$$

The more general case appears when the primary SMC and DMC are both included into the radio channel like the co-polar links in this work. As an example (all other polarization can be similarly derived), the path loss model for HH is given by

$$\left[\mathbf{PL}_{DMC}^{HH}(d)\right]_{dB} = -\left[\chi_{pri}^{HH}\mathbf{G}_{0,pri}^{HH}\left(\frac{d_0}{d}\right)^{n_{pri}^{HH}} + (\chi_{DMC}^{HH}\mathbf{G}_{0,DMC}^{HH}\mathbf{T}^{HH})e^{\left(\frac{-\eta_{DMC}^{HH}d\cdot log(10)}{10}\right)}\right] \tag{3.28}$$

The secondary SMC was omitted in (3.28) since its contribution to the radio channel could be marginal. This expression provides more insight about the path loss mechanisms of the radio channel and highlights the competition between the two components. For instance, when the transmitter−receiver distance is really short or really large (Figure 3.3), the primary SMC dominates the DMC and the contribution of the DMC to the path loss is small. Conversely, there is a transmitter−receiver distance range for which the DMC is the dominant propagation mechanism such that the contribution of the primary SMC is now small.

3.3.2 Two-step path loss parameters fitting method

The joint analysis of the reverberation results and SMC plus DMC path loss models in the previous section reveals that the characterization of the path loss parameter for each propagation mechanism can be split into two fitting steps. Two cases can be distinguished in Figure 4.7. In a first case, $\mathbf{R}^{XY}$ is below 0.5 (see horizontal line) such that the SMC power is larger than that of the DMC (co-polar links). For the second case, $\mathbf{R}^{XY}$ is above 0.5 such that the DMC power is now much larger than that of the SMC (cross-polar links)

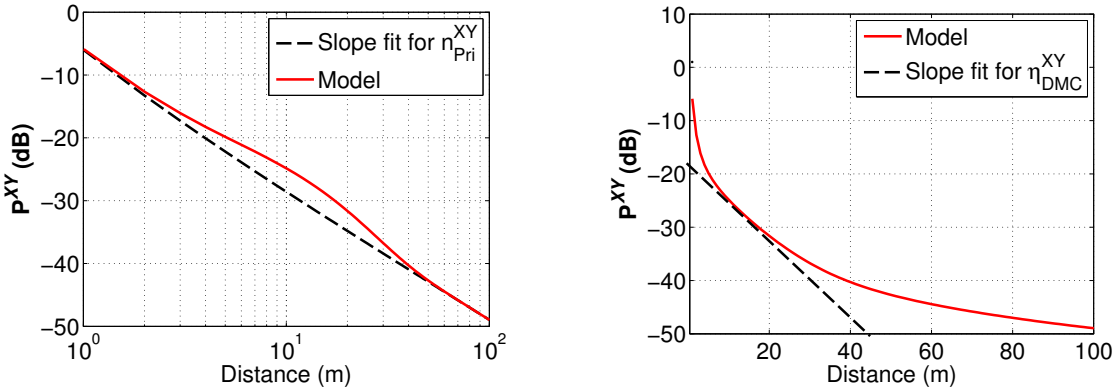

(a) (b)

Figure 3.5: Example of the two-step path loss exponent fitting for the polarimetric radio channel. The dotted line (black) is the slope fit for (a) the SMC $\left(n_{pri}^{XY-I}\right)$ and (b) DMC $\left(\eta_{DMC}^{XY-II}\right)$.

As an example, Figure 3.5 illustrates this two-step fitting procedure. In a first step [Figure 3.5(a)], the path loss exponent for the primary SMC noted n^{HH-I} is computed from the linear region of the log-distance curve for distances where the SMC gain is greater than the DMC. In a second step [Figure 3.5(b)], the DMC path loss factor η_{DMC}^{HH-II} is computed from the linear region of the linear-distance curve where the DMC gain is greater than the SMC. It is observed that the fitting slope follows well the asymptotic behavior of the model for each region (power law for the SMC and exponential law for the DMC). In addition, the SMC to DMC

transition distance between the two propagation mechanisms can be obtained with the intersection of the log- and linear-distance lines. For this example, a transition distance is obtained when $\mathbf{R} = 0.5$.

Therefore, the parameters n_{pri}^{XY-I} and η_{DMC}^{XY-II} developed in (3.26) can be estimated by one simply line regression fitting. This approach also indicates that the reverberation time $\mathbf{T}$ could be estimated from (3.26) without applying complex parametric estimation techniques.

Overall, this approach is possible to grasp the path loss characteristics of each mechanism with the two-step fitting method. This method is general and could be applied to any path loss data already collected in environments with DMC wherein room electromagnetics applies.

3.4 Clustering identification method

Clustering methods are widely used techniques to group multi-dimensional data presenting a high degree of correlation between one or many dimensions. For instance, these methods have greatly improved over the last decades when it comes to radio channel modeling. The most basic cluster classification technique is achieved by visual inspection [115] but becomes rapidly intractable when large datasets are considered like with MIMO radio channel parameters. For those cases, not only an automatic clustering approach is required but it should also be able to encompass multi-dimensional data to find the most appropriate clustering solution. Once a clustering solution is obtained, its goodness or quality can be evaluated with Clustering Validity Indices (CVIs) which individually give a definition of how the data should be clustered [116, 117, 118].

The automatic clustering approach can trace back to the well-known K-means clustering algorithm [119]. It is a popular iterative descent clustering method. Some K-means based clustering algorithms have been specifically developed for radio channel analysis such as K-means MCD and K-means Power (KPM) [120]. These method rely on the Multipath Component Distance (MCD) [121] in the main body of the algorithm as a metric to quantify the distance between SMC. These approaches focus on clustering the dataset as a whole. In other words, the definition of a cluster is revealed after the algorithm has converged.

Another approach takes into account the radio channel structure as a-priori known information like the S-V approach shown in Figure 1.7. The SMC are grouped with an MCD threshold as recently reported in [122] and [123] for millimeter-wave data obtained in indoor scenarios. These approaches focus on the local cluster description in the dataset via the MCD. In other words, the clustering is performed based on a pre-defined description of what should be a cluster.

3.4.1 Distance metric and cluster validity indices

3.4.1.1 Multipath Component Distance metric

The MCD was originally introduced in [121] as a metric to cluster real-world data that often present different units and orders of magnitude. It also solves the angular ambiguity issue. For instance, the large-scale parameters of the SMC estimated from measured MIMO radio channels such as the TOA and DOA/DOD greatly differ by nature. This metric was shown to be particularly effective compared with the Euclidean metric [124]. The angular MCD between an SMC pair with index (i, j) is given by:

$$MCD_{DOA/DOD,ij} = \frac{1}{2}\left|\begin{pmatrix} sin(\theta_i)cos(\varphi_i) \\ sin(\theta_i)sin(\varphi_i) \\ cos(\theta_i) \end{pmatrix} - \begin{pmatrix} sin(\theta_j)cos(\varphi_j) \\ sin(\theta_j)sin(\varphi_j) \\ cos(\theta_j) \end{pmatrix}\right| \tag{3.29}$$

where θ and φ are the co-elevation and azimuth angle, respectively.

For the time-delay dimension, the MCD metric is given by:

$$MCD_{\tau,ij} = \zeta \cdot \frac{|\tau_i - \tau_j|}{\Delta\tau_{max}} \cdot \frac{\tau_{std}}{\Delta\tau_{max}} \tag{3.30}$$

where $\Delta\tau_{max} = max_{i,j}\{|\tau_i - \tau_j|\}$ and ζ is a scaling factor that provides additional flexibility to treat real-world data [124]. Finally, the complete MCD distance is given by:

$$MCD_{ij} = \sqrt{\|MCD_{DOA,ij}\|^2 + \|MCD_{DOD,ij}\|^2 + \|MCD_{\tau,ij}\|^2} \tag{3.31}$$

The angular MCD is normalized in the interval of $[0, 1]$ whereas MCD_τ is in the range of $[0, \zeta]$. The MCD was reported as a meaningful approach to compute the distance between SMC [125].

To provide a direct insight on how MCD works, an example of angular MCD is shown in Figure 3.6. An angle with 0° azimuth and 90° co-elevation was selected as a reference point. This figure was obtained by spanning all azimuth and co-elevation angles in the [-π,π] and [0,π] range respectively.

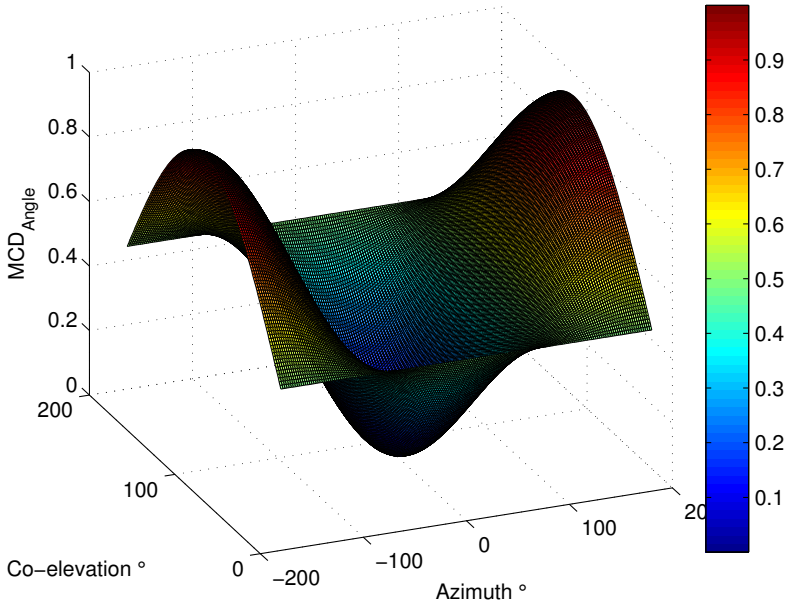

Figure 3.6: Illustration of angular MCD computed from (3.29). An angle with 0° azimuth and 90° co-elevation was selected as a reference point.

3.4.1.2 Cluster Validity Indices

The goodness of the clustering solution obtained from any techniques can be assessed with Cluster Validity Indices (CVI) as recently reported in the literature for radio channels [117, 118]. These CVI individually focus on certain properties and features of the clusters like the compactness, cluster separation, intra-cluster distance, etc. In this work, three validation indices which rely on the MCD metric have been investigated: the Calinski-Harabasz, Xie-Beni, and PBM.

3.4.1.2.1 Calinski-Harabasz index The Calinski-Harabasz (CH) index was presented in [126]:

$$\nu_{CH} = \frac{\frac{\sum_{k=1}^{K} L_k (MCD(c_k, c))^2}{K-1}}{\frac{\sum_{k=1}^{K}\sum_{l=1}^{L_k} (MCD(s_l, c_k)^2)}{L-K}} \tag{3.32}$$

where L_k and L are the number of rays in the kth cluster and the total number of rays respectively. s_l is the data of the lth subpath in cluster k. c_k and c are the positions of the k^{th} cluster centroid and global centroid, respectively. Finally, K is the total number of clusters. The optimal solution is provided by the highest CH value.

3.4.1.2.2 Xie-Beni index The Xie-Beni (XB) index was introduced in [127] and describes the cluster compactness to cluster separation ratio:

$$\nu_{XB} = \frac{\sum_{k=1}^{K}\sum_{l=1}^{L_k} L_k (MCD(s_l, c_k))^2}{L \times \left[\min_{k1,k2}(MCD(c_{k1}, c_{k2}))^2\right]} \tag{3.33}$$

The optimal solution is provided by the smallest XB value.

3.4.1.2.3 PBM Finally, the PBM index is given by:

$$\nu_{PBM} = \left(\frac{1}{K} \times \frac{\max_{k1,k2}(MCD(c_{k1}, c_{k2}))}{\sum_{k=1}^{K}\sum_{l=1}^{L_k} MCD(s_l, c_k)}\right)^2 \tag{3.34}$$

The optimal solution is provided by the highest PBM value.

3.4.1.2.4 CVI fusion technique In [116], it was concluded that no matter how good the CVI is, it may not work at all for all types of data. Therefore, in order to increase the versatility of the CVI for a given data set, it was proposed in [128] to combine all CVIs to compute a global clustering score or score fusion. It was reported that the performance of the fusion indices outperforms the single indices [117]. Here, the Score Fusion was computed as the geometrical mean (SFg) of all CVIs and is given by:

$$SFg(k) = \left(\prod_{i=1}^{M} \nu_i(k)\right)^{1/M} \tag{3.35}$$

where M represents the number of CVIs. The decision rank fusion method (Kr) was not explored in this work. In our simulations, each index was scaled to $[0, 1]$ (min-max normalization) before computing SFg. The normalized XB index used in (3.35) is modified into $1 - \nu_{XB}$ such that the optimal clustering solution is obtained for the maximum SFg value.

3.4.1.3 CVI property study

In this section, an intuitive example of the CVIs and its performance is demonstrated. The simplest cluster-like radio channel includes only two clusters. The WINNER II advanced model was selected to generate the radio channels since it is a GSCM with a double-directional cluster-like structure [45]. First, a double-directional MIMO radio channel with two clusters is generated using arbitrarily the urban micro-cell B1 scenario. Each cluster includes 20 SMCs. The PDP, DOA and DOD of the simulated radio channels are shown in Figure 3.7 and the two clusters can be well identified with different colors.

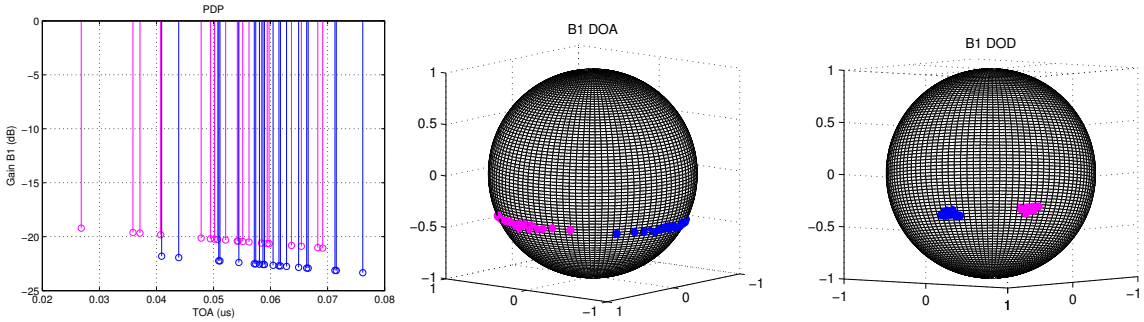

(a) (b)

Figure 3.7: Simulated SMC using WINNER II B1 radio channel with two clusters in the: (a) time-delay domain (PDP), (b) and angular domain (DOA and DOD).

For this scenario, some overlap is observed in the time-delay domain (Figure 3.7(a)) but not in the DOA and DOD domains. Also, the DOA is statistically more spread than the DOD (Figure 3.7(b)). The idea is to artificially and progressively make the clusters overlap in all dimensions. This can be done by adding an arbitrary offset in the domain of interest as shown in Figure 3.8. In Figure 3.8(a), the clusters overlapp in the DOA domain but are still well separated in the DOD domain. In Figure 3.8(b), these two clusters are completely overlapped in both dimensions.

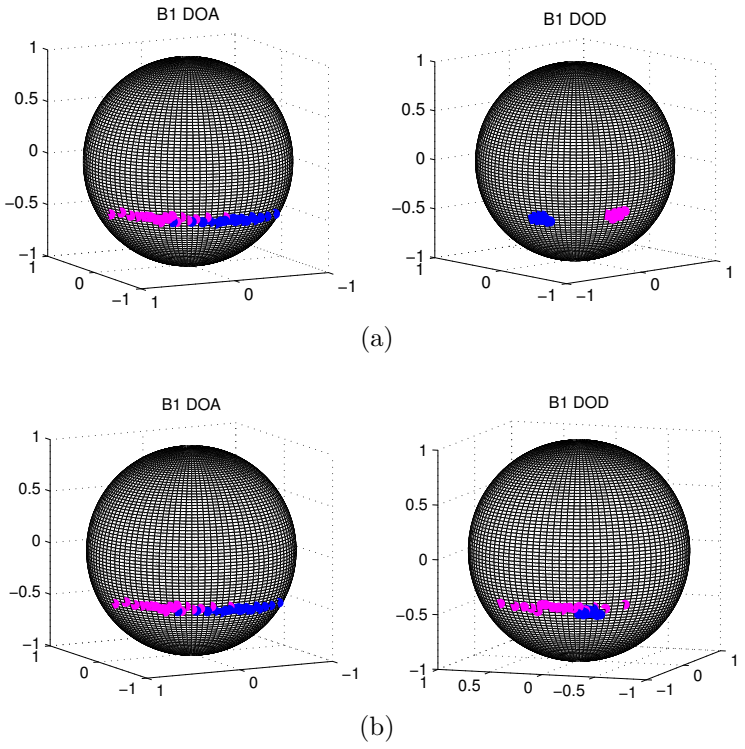

(a)

(b)

Figure 3.8: Modified simulated channel: (a) nearby clusters, (b) overlapping clusters.

In a first step, the CVIs are computed assuming that the clustering solution is correct (i.e. the SMC are all assigned to their respective cluster). The results in Table 3.2 indicate that the CVI values do not differ much and a standard deviation less than 3% was computed for the three cases. Nonetheless, the optimal solution is different depending on the selected index. The CH index considers the overlapped case as the best solution (maximum value). The XB index considers the original case as the best solution (minimum value). Meanwhile, PBM considers the three cases as good solutions. Finally, the fusion index SFg indicates that the overlap case is the optimal solution. Surprisingly, this result is reasonable. Since the SMC are originally correctly assigned to their cluster, any position of the cluster with respect to each other in all dimensions will provide a good solution and it is expected the CVI values to be strongly similar. In summary, this simulation demonstrates the stability of the CVI provided that the clustering solution is correct.

	Original	Nearby	Overlap
CH	35.3072	36.8792	37.6445
XB	0.1400	0.1421	0.1422
PBM	0.0011	0.0011	0.0011
SFg	0.1698	0.1716	0.1723

Table 3.2: CVIs for the B1 two-cluster scenario.

In a second step, the CVI values are computed from a clustering solution which is progressively degraded. This is performed by reassigning the SMC to the wrong cluster. Table 3.3 presents the CVI values for an error rate (percentage of SMC incorrectly assigned to their true cluster) of 0% (perfect case), 15%, 25%, and 40%. The results indicate that the XB, PBM, and SFg values diverge well from the optimal solution as the error rate is increased. On the other hand, the CH index does not perform well and this is attributed to the characteristics of the clusters for the selected radio channel scenario.

In summary, the CVI values were found to be good indicators of the clustering goodness. They were used to assess the performance of the classical and developed clustering techniques which were then applied to simulated and real-world data.

Error rate	0%	15%	25%	40%
CH	35.3072	37.4622	39.02	39.2606
XB	0.1400	0.2083	0.6658	0.9412
PBM	1.1×10^{-3}	7.51×10^{-4}	2.34×10^{-4}	1.66×10^{-4}
SFg	0.1698	0.1442	0.0846	0.0499

Table 3.3: CVIs as a function of clustering goodness.

3.4.2 MCD-based clustering algorithm

3.4.2.1 K-means MCD

Under the scope of K-means clustering, K-means MCD algorithm must be initialized with the number of clusters K present in the radio channel; information that is a-priori unknown. K can be initially fixed by the user either manually (i.e. best visual guess) or automatically using the Kim-Parks index [129]. Then, an initial position for the K centroids are typically estimated by selecting K SMC randomly from the dataset. A deterministic approach using a weighted MCD metric was also developed in [130] to jointly estimate the number of clusters and centroid positions, thus reducing the overall complexity of the algorithm. In any cases, K-means was reported to be highly sensitive to the initial position of the centroids [131] but also to outliers and noise resulting in non-convergence problems and a low capability to pass the local optimum. Consequently, the algorithm must be applied to the same data with different initial centroid positions to statistically obtain the best clustering solution. Finally, it does not work well with non-circular cluster shape and clusters which do not have well defined centers. This latter point is attributed to the data type and inadequate metric distance. This is partially solved by replacing the squared Euclidean norm with the MCD in the main body of the K-means MCD algorithm as suggested by [125].

A brief description of the K-means MCD algorithm developed for this work is shown in Algorithm (1) which is considered as the reference algorithm for our proposed clustering approach. First, the SMC which contribute the most to the radio channel (i.e. most energetic) are selected from the whole dataset by applying a power threshold. For a given number of clusters K_{init} , the centroids c_k are randomly generated from the data and the MCD between the SMC and centroids is computed. A deterministic approach was also proposed in [130] to initialize the clustering algorithm using a power weighted MCD metric. It offers the advantage of reducing the complexity of the clustering algorithm and was reported to produce satisfactory results. However, it was not investigated in the present work since the classical K-means algorithm is typically initialized with a random guess. The algorithm assigns the SMC to the nearest centroids and updates all centroid positions. The centroid positions are computed as the average position of the SMC for each dimension. Note that the power was not included to weight the average. The algorithm stops once all centroids are stable.

3.4.2.2 Automatic Cluster Identification (ACId)-MCD

The clustering approach developed in this work is motivated by the approaches reported in [122, 123]. Their method consists in sorting the rays either by delay or power. Then, the joint MCD is computed and a preset threshold is used to group rays. In other words, rays with MCD less than the threshold form a new cluster. Steps are repeated until all rays are grouped. In contrast with K-means MCD, an

Algorithm 1 K-means MCD

1: Define $\mathbf{K}_{init}$ and SMC threshold power $\mathbf{P}_T$
2: Randomly generate c_k^i
3: Select SMC with power $> \mathbf{P}_T$
4: **while** $c_k^{i+1} \neq c_k^i$ **do**
5: Compute $MCD(l_k^i, c_k^i)$
6: Assign SMC l_k^i to nearest centroid c_k^i
7: Update centroid position c_k^i
8: $i = i + 1$
9: **end while**

attractive characteristic of this algorithm is the fact that the number of clusters is the resulting output. Hence, no pre-processing of the data is necessary to choose an initial number of clusters like with K-means. However, both studies did not investigate which MCD threshold would be best even though visual inspection of the data was explored by [123] to physically link the SMC distribution with the threshold. The algorithm reported by [122] suffers two major drawbacks: 1) the position of the centroid is never updated and 2) some assigned SMC could be closer to new clusters and should be re-allocated. Martinez-Ingles *et al* [123] modified the algorithm by taking into account the second problem. Nonetheless, MCD-based clustering techniques are very promising and computationally-efficient algorithms compared to K-means MCD but comprehensive works on this topic are scarce in the literature.

A novel MCD-based clustering technique called Automatic Cluster Identification (ACId) is introduced to fulfill this gap. The proposed approach (Algorithm (2) is an improved variant of the algorithm reported in [123]. As such, SMC are iteratively assigned to a cluster provided that the cluster-SMC MCD is within a MCD threshold set by the user. Analysis of (3.31) shows that the cluster shape can vary from cluster to cluster as the axis length for each dimension is physically bounded by the MCD threshold. Necessarily, it follows that the SMC distribution, number of clusters, and cluster size/shape are strongly dependent to the threshold value which should be carefully selected to find the optimal clustering solution. For example, a MCD threshold of 0.25 was used in [122] without being deeply motivated. A 0.1 threshold was used in [123] by manually inspecting the data. An attractive characteristic of the algorithm is the fact that the number of clusters is the resulting output. Hence, no pre-processing of the data is necessary to choose an initial number of clusters like with the typical K-means.

ACId-MCD has been designed to dynamically update the centroid position like K-means and reassigning SMC that might be closer to existing clusters. Even though MCD matrices must be iteratively computed between unassigned SMC and centroids, this approach was found to be computationally effective since the MCD matrix size, large with the original dataset, decreases as SMC are progressively being assigned. For a given MCD threshold, the MCD-based clustering techniques

converge fast towards a unique solution even when large datasets are considered. This is a strong advantage compared with the classical K-means for which a family of solutions is obtained for each input K due to the random aspect of the initialization step. The optimal clustering distribution must be then selected from this family for each K and, therefore, adds additional complexity. Furthermore, it also increases the computational time since the probability to find the optimal solution decreases as the dataset is increased. Finally, a newly defined centroid is defined as the strongest SMC. This is motivated by the physical structure of clusters which often include a single or few strong SMC with weaker SMC satellites.

Algorithm 2 ACId-MCD

Define MCD threshold MCD_T and power threshold $\mathbf{P}_T$,
Select SMC with power $> \mathbf{P}_T$
Compute $MCD(i,j)$
while Unassigned SMC$\geqslant 1$ **do**
  Pick strongest unassigned SMCas new centroid c_k^i
  while $c_k^{i+1} \neq c_k^i$ **do**
    Assign SMC l_k^i satisfying $MCD(l, c_k^i) \leqslant MCD_T$
    Update c_k^i
    Compute $MCD(l_k^i, c_{k-m}^i)$ with $m < k$
    Reassign SMC l_k^i satisfying $MCD(l_k^i, c_{k-m}^i) < MCD(l_k^i, c_k^i)$ to nearest centroid c_{k-m}^i
    Update l_k^i, l_{k-m}^i, c_k^i and c_{k-m}^i
    $i = i + 1$
  end while
  $k = k + 1$
end while

3.4.3 Evaluation framework

3.4.3.1 Cluster-like radio channel simulations

Before assessing the solution of the clustering techniques with the CVIs, realistic radio channels must be simulated. Once again, the WINNER II advanced model was selected since it is a GSCM with a double-directional cluster-like structure [45]. Four scenarios were considered: indoor office (A1), large indoor hall (B3), urban macro-cell (C2), and rural macro-cell (D1) with the presence of the Line-Of-Sight (LOS). These four scenarios were selected as they are representative of typical indoor and outdoor propagation scenarios with different cluster characteristics and also representative of the investigated scenarios of this work. These cluster features for each scenario are presented in Table 3.4: Azimuth Spread of Departure and Arrival (ASD and ASA), Elevation Spread of Departure and Arrival (ESD and ESA). Since the ESD and ESA are not supported in the WINNER II Matlab program, elevation

angles were drawn from a normally distributed angle with 5° spread. This value is arbitrary and corresponds to values obtained for the azimuth. In addition, the number of subpath (i.e. SMC) in each cluster is 20 but the power and TOA of every SMC in one cluster are set to equal. Therefore, the Saleh-Valenzuela multipath propagation model [35] was introduced to produce clusters with more realistic time-delay and power properties. The TOA of each SMC in each cluster was drawn from a normal distribution with mean of the simulated TOA SMC and arbitrary $\sigma_{TOA} = 10$ ns standard deviation. In addition, the power of each subpath exponentially decays as a function of delay.

Table 3.4: Modified Winner II cluster features

	A1	B3	C2	D1
Number of cluster	11	10	8	9
Number of SMC per cluster	20	20	20	20
$\sigma_{TOA}(ns)$	10	10	10	10
ASA (°)	5°	5°	12°	3°
ESA (°)	5°	5°	5°	5°
ASD (°)	5°	5°	6°	2°
ESD (°)	5°	5°	5°	5°
$\Delta TOA(ns)$	37.6	35.8	45	32.4
$\Delta DOA_{az}(°)$	21.5	21.5	90.1	12.9
$\Delta DOA_{el}(°)$	17.6	19	16.2	19.1
$\Delta DOD_{az}(°)$	21.5	21.5	25.9	8.6
$\Delta DOA_{el}(°)$	18.1	20.6	17.2	18.6

A single drop or realization was simulated for each scenario and saved. Table. 3.4 lists the average cluster size computed for each dimension (in ns for TOA and degree for DOA/DOD) and saved reference scenario. The average cluster size is given by:

$$\Delta X = \frac{1}{K} \sum_{i=1}^{K} |\mathbf{X}_{max}^{i} - \mathbf{X}_{min}^{i}| \tag{3.36}$$

where X is either the TOA, DOA azimuth, DOA elevation, DOD azimuth, or DOD elevation. K is the number of clusters for a given scenario. The synthesis channel output is a $L \times 6$ matrix where L is the total number of SMC and the dimensions are [Power, TOA, DOA azimuth, DOA elevation, DOD azimuth, DOD elevation]. As an example, Figure 3.9 presents the DOA and DOD angular distribution obtained for scenario A1 and indicates that some clusters can overlap in one or more dimensions. Clustering algorithms make use of the diversity provided by the different dimensions to correctly assign the SMC to the best cluster candidate. For instance, some clusters

do not overlap simultaneously in all dimensions such that the clusters can still be distinguished (e.g. simulated scenarios A1, B3, C2). If some clusters overlap in all dimensions simultaneously then it is safe to assume that any clustering algorithms would fail to correctly estimate the true number of clusters. This case happens for scenario D1.

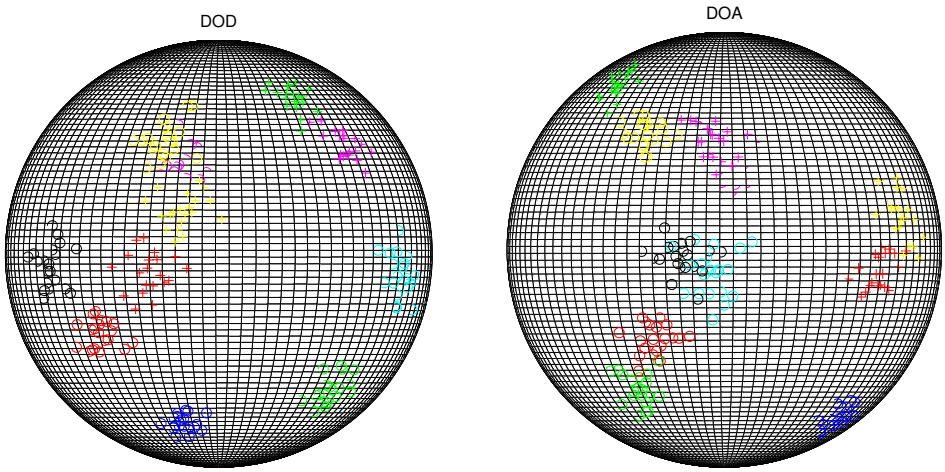

(a) (b)

Figure 3.9: A1 scenario of the distribution of SMC in azimuth and elevation. (a). DOD. (b). DOA

3.4.3.2 Evaluation protocol

The goodness of the clustering solution and optimal solution are evaluated with the protocol presented in Algorithm (3) for K-means MCD and ACId-MCD.

3.4.4 Performance of ACId-MCD and K-means MCD

The evaluation protocol is applied to the investigated scenarios and a 30 dB power threshold is used to select the SMC. The computation of MCD_τ is done with the scaling factor $\zeta = 2.5$. For K-means MCD, $N_{Ite} = 500$ and K_{init} was ranging between $K_{min} = 3$ and $K_{max} = 15$. For ACId-MCD, 50 values of MCD_T were taken between $MCD_{min} = 0.02$ and $MCD_{max} = 0.3$. The lower and upper limit, arbitrarily chosen, correspond to an angular difference between two SMC of about 15° and 60°, respectively (for $MCD_\tau = 0$). For a given scenario, the total computational time is a bit less than 2 hours (111.6 min) with K-means MCD (1.03 s per run) whereas it is merely 40 seconds with ACId-MCD (0.8 s per run), thus showing the superiority of the proposed approach on this aspect.

Figure 3.10 presents the normalized SFg as a function of the input number of clusters with K-means MCD for the four investigated scenarios. The optimum

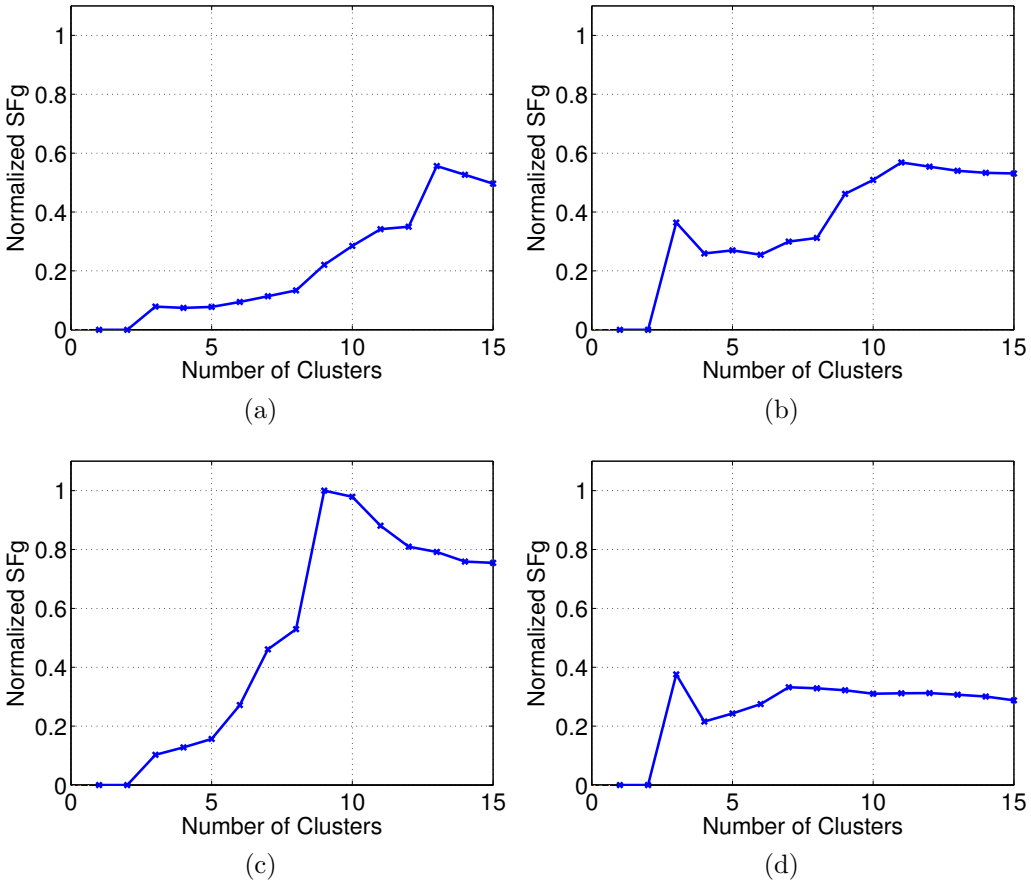

Figure 3.10: Normalized SFg as a function of K for K-means MCD, (a) Scenario A1, (b) Scenario B3, (c) Scenario C2, (d) Scenario D1.

Algorithm 3 Evaluation Protocol

```
Simulate and save WINNER II scenario
Define power threshold P_T
Select SMC with power > P_T
Define K range= [K_min, K_max] and number of iterative steps N_Ite
for K_init = K_min to K_max do
    while N_Ite ≠ 0 do
        Apply K-means MCD
        Save cluster Solution CS_Kmeans = f(K_init, N_Ite)
    end while
end for
Compute normalized SFg to obtain K_opt and N_Ite_opt
Define MCD range = [MCD_min, MCD_max]
for MCD_T = MCD_min to MCD_max do
    Apply ACId-MCD
    Save Cluster Solution CS_ACId = f(MCD_T)
end for
Compute normalized SFg to obtain MCD_opt and K_opt
```

number of clusters K_{opt} is given by the maximum SFg value and are presented in Table 3.5. It is observed that K-means slightly overestimates the true number of clusters K_{true} listed in Table 3.4 for the scenario A1 ($K_{opt} = 13$), B3 ($K_{opt} = 11$), and C2 ($K_{opt} = 3$). However, only 3 clusters are obtained for scenario D1. This is attributed to the overlapping of some clusters with small ASA/ASD values which is believed to severely disturb the clustering algorithm. Nonetheless, a local maximum is reached for $K = 7$ close to $K_{true} = 9$. Moreover, it is also observed that a local maximum is obtained with all scenarios for $K = 3$. These results seem pervasive of the CVIs definition of a cluster.

Table 3.5: Number of clusters and optimal MCD threshold.

		ACId-MCD		K-means MCD
	K_{true}	K_{opt}	MCD_T^{opt}	K_{opt}
A1	11	11	$0.01 - 0.04$	13
B3	10	10	0.125	11
C2	8	8	0.15	9
D1	9	18	0.05	3

Since the optimal solution is statistically obtained by applying K-means MCD N_{Ite} times for a given radio channel data, it is clear that many attempts will result in sub-optimal solutions with relatively low SFg values. This is verified in Figure 3.11 which presents the histogram of SFg obtained from the $N_{Ite} = 500$ solutions with

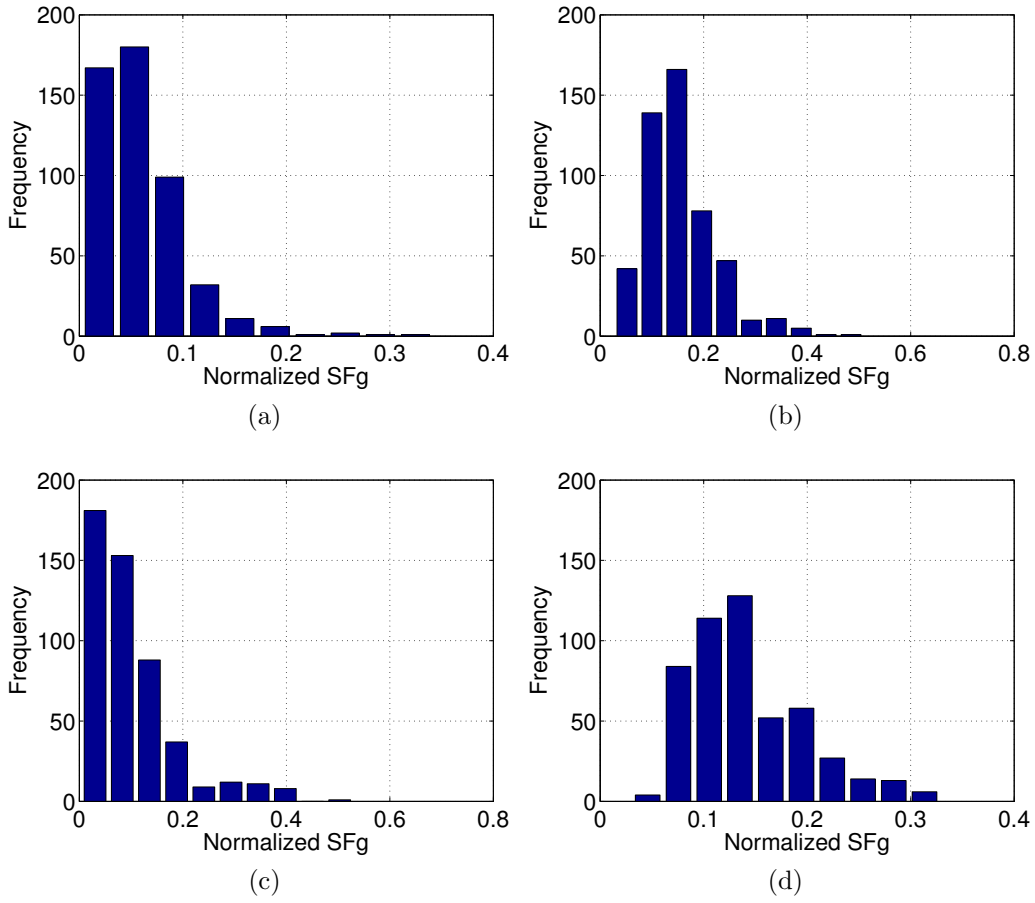

Figure 3.11: Normalized SFg histogram for K-means MCD with $N_{Ite} = 500$ and $K = K_{true}$. (a) Scenario A1, (b)Scenario B3, (c) Scenario C2, and (d) Scenario D1,

$K = K_{true}$ for all scenarios. The results show that the probability of having a high SFg value (better solution) is relatively low. In addition, this demonstrates that the singularity and uniqueness of the true solution makes it difficult for the algorithm to reach it. Consequently, N_{Ite} should be as large as possible but this comes at the expense of the overall computational time. Hence, it should be selected carefully when using K-means.

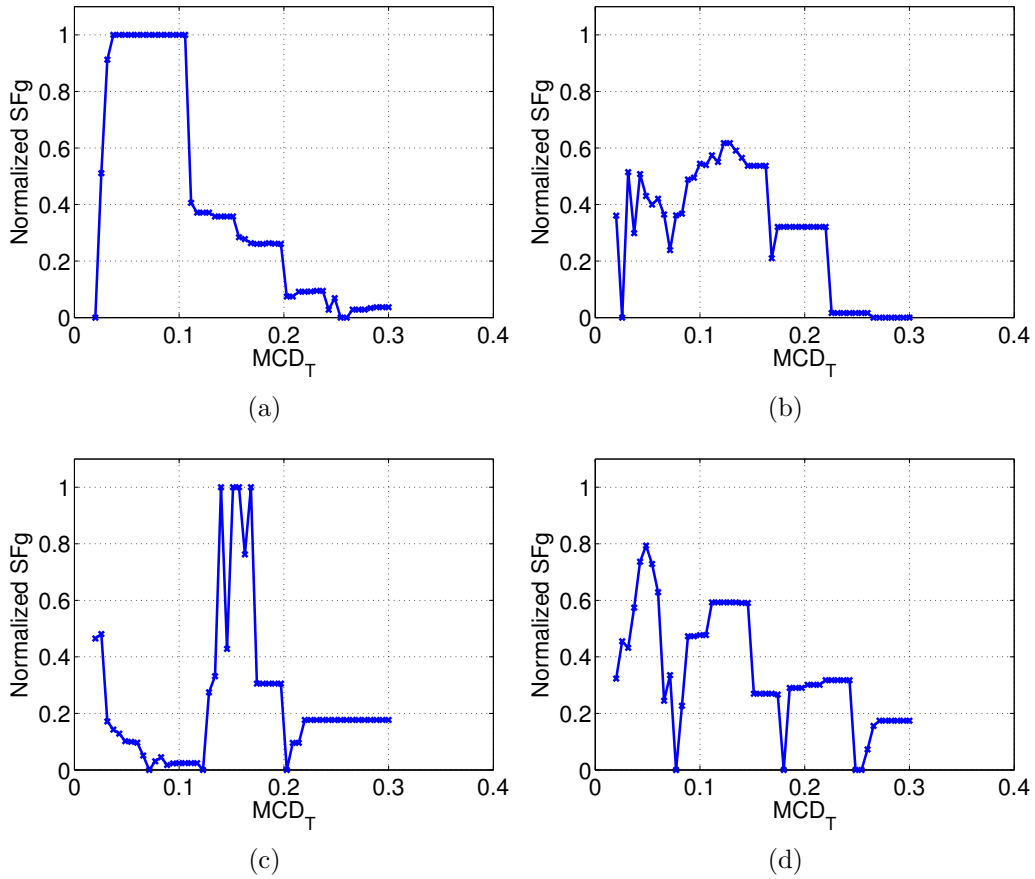

Figure 3.12: Normalized SFg as a function of K for ACId-MCD,(a) Scenario A1,(b) Scenario B3,(c) Scenario C2,(d) Scenario D1.

Figure 3.12 presents the normalized SFg as a function of the input MCD threshold MCD_T with ACId-MCD for the four investigated scenarios. The optimal $MCD_{T_{opt}}$ is given by the maximum SFg value. It is observed rather different behaviors for SFg depending upon the scenario indicating that the algorithm is highly sensitive to the data type. Furthermore, the results shown in Table. 3.5 indicate that $MCD_{T_{opt}}$ not only depends on the scenario but is also unique for each scenario. For instance, $MCD_{T_{opt}}$ varies between 0.01 and 0.04 for A1, is ~ 0.125 for B3, is ~ 0.15 for C2, and ~ 0.05 for D1. Conversely, this means that scenarios could be categorized based upon the clustering properties characterized by MCD_T . This is an elegant approach to physically link the SMC distribution with the propagation

scenario. In addition, Figure 3.13 presents the normalized SFg as a function of K. In contrast with the results shown in Figure 3.10, sharp maxima are observed for all scenarios and $K_{opt} = K_{true}$ for scenario A1, B3, and C2. K_{opt} is overestimated for scenario D1 (18 clusters) even though a local maximum is reached like with K-means for $K = 8$ close to $K_{true} = 9$ (see Table 3.5).

Table 3.6: Percentage of correct intra-cluster SMC

	ACId-MCD		K-means MCD	
	$K = K_{opt}$	$K = K_{true}$	$K = K_{opt}$	$K = K_{true}$
A1	100%	100%	95.45%	86.82%
B3	97%	97%	98%	88.5%
C2	100%	100%	93.75%	95%
D1	60%	N/A	26%	96.11%

Even though the correctness of the number of clusters is a good indicator for the clustering goodness, the performance of the clustering techniques is further evaluated by checking whether the SMC assigned to a given cluster for the best solution are the same than the ones for the true solution. This is simply performed by comparing the index or label of the SMC between the best and true solution for each cluster. Two cases are considered for this study and are presented in Table 3.6. First, the percentage of correct indices is computed for $K = K_{opt}$. Then, it is computed for the case where the algorithm finds the correct number of clusters $K = K_{true}$. For $K = K_{opt}$, a perfect success rate is achieved for the scenario A1, B1 (97%), and C2 with ACId-MCD but it has to be recalled that $K_{opt} = K_{true}$ for those scenarios. 60% is obtained for D1 which could be attributed to the fact that twice as much clusters are found for this scenario. Note that no results were available with $K = K_{true}$ for D1 due to the selected MCD threshold range. Good rates are also obtained with K-means MCD with $K = K_{opt}$ except for D1. Nevertheless, results also indicate that when $K = K_{true}$, generally the K-means algorithm, assigns most of the SMC correctly (even for scenario D1) as percentages obtained were higher than 86% in all the four scenarios. This suggests that, probably, some clusters existing in the dataset are incorrectly grouped in a single cluster and maybe some other ones are incorrectly split. Thus, the algorithm could not identify correctly the existing clusters, although, the number of requested clusters is the same as the actually existing in the data set. An increase in K, will allow that some of the grouped clusters are finally correctly identified, yielding to a solution which may be better under the considered evaluation criteria and presenting also more SMC correctly assigned to the corresponding cluster. The number of SMC incorrectly assigned reduces to those in clusters that were incorrectly split.

Finally, the average cluster size was computed for each dimension (in ns for TOA and degree for DOA/DOD) from the optimal clustering output of the K-means MCD and ACId-MCD algorithms ($K = K_{opt}$). The results presented in

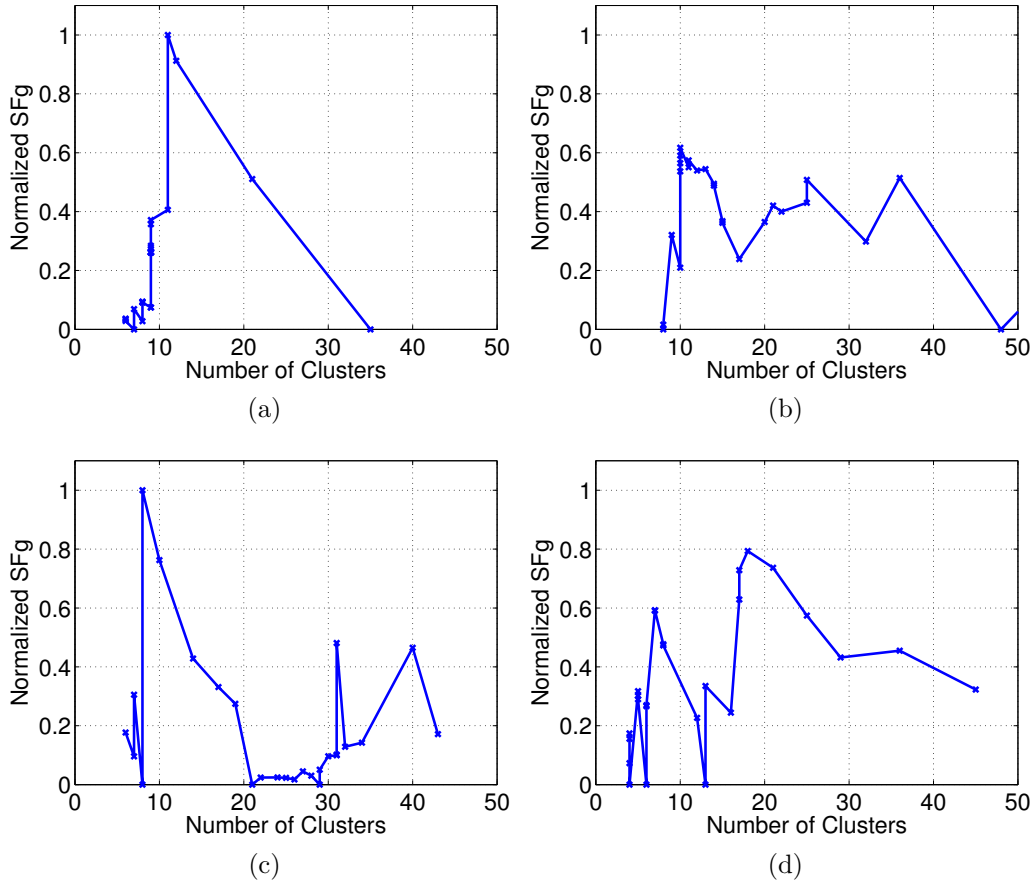

Figure 3.13: Normalized SFg as a function of MCD_T for ACId-MCD, (a) Scenario A1, (b) Scenario B3, (c) Scenario C2, and (d) Scenario D1.

Table 3.7: Average cluster size with ACId-MCD and K-means MCD

	A1		B3		C2		D1	
	ACId	K-means	ACId	K-means	ACId	K-means	ACId	K-means
$\Delta TOA(ns)$	37.6	31.1	38.5	31.9	45	63	14.5	15.4
$\Delta DOA_{az}(°)$	21.5	20.6	23	20.3	90.1	108.2	10.1	8.1
$\Delta DOA_{el}(°)$	17.6	16.4	18.9	20.6	16.2	14	15.2	15.7
$\Delta DOD_{az}(°)$	21.5	18.5	20.7	29.5	25.9	28.3	5.5	4.4
$\Delta DOD_{el}(°)$	18.1	16.6	21.3	21.8	17.2	16.5	15	13.2

Table 3.7 can be compared with those of Table 3.5 and demonstrate the ability of the ACId-MCD algorithm to correctly grasp the radio channel clustering size. For ACId-MCD, a perfect agreement is found for the scenarios A1 and C2 since the number of clusters is correct and the percentage of correct intra-cluster SMC is 100% for these two scenarios. The values are also close for B3 for similar reasons whereas a slightly larger deviation is obtained for D1 in spite of a number of clusters largely overestimated with a percentage of correct intra-cluster SMC of only 60%. For K-means MCD, the optimal number of clusters is incorrect for all scenarios and the percentage of intra-cluster SMC correctly assigned never reaches 100%. Hence, the average cluster size values present a larger deviation compared with ACId-MCD. This is particularly true for the scenarios C2 and D1.

3.4.5 Robustness of ACId-MCD

In this section, it is proposed to evaluate the robustness of the developed ACId-MCD algorithm using Monte-Carlo simulations. This is performed by generating the same radio channel with the method introduced in section 3.4.3.1. ACId-MCD has been applied to 500 radio channels emulated from the A1 scenario. Since the SMC-cluster assignment is a-priori known from the simulator, the error percentage can be computed from the clustering results. The histogram of the error percentage is presented in Figure 3.14. The results show that an error less than 5% is obtained for more than 425 simulated channels (85% of the 500 channels). This is a considerable improvement compared to other clustering algorithms [118] and demontrastes the robustness of the developed approach.

3.4.6 Definition of cluster parameters

In this paragraph, the relevant cluster parameters used to perform the statistical analysis in chapters 4 and 5 are defined. These parameters are computed from the estimated cluster index of each SMC and their respective time-delay and angular parameters. First, the cluster power is defined as the sum of the power of all SMC belonging to the same cluster as proposed by [132]:

$$P_k^{XY} = \sum_{L_k} |\gamma_{k,l}^{XY}|^2 \tag{3.37}$$

Then, the cluster-level XPD XPD_k^X can be obtained by:

$$XPD_k^X = \frac{P_k^{XX}}{P_k^{XY}} \tag{3.38}$$

The computation of the cluster-level XPD does not take into account single-SMC cluster.

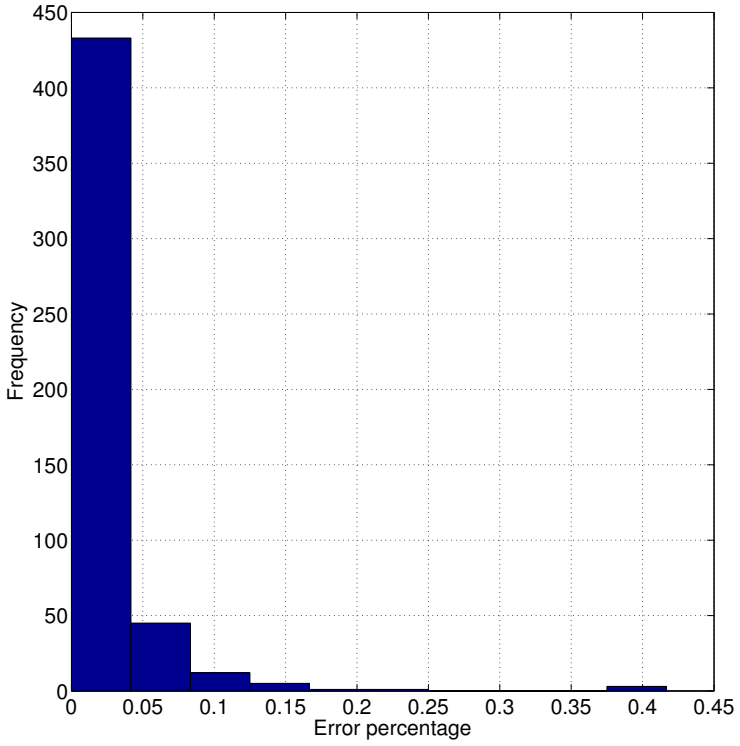

Figure 3.14: Error percentage of uncorrectly assigned SMC using ACId-MCD. 500 Winner II channels were generated using scenario A1.

The averaged cluster XPD is obtained as the mean value of all cluster XPD for the same measurement position:

$$\overline{XPD}^{X}_{cluster} = \mathbf{E}[XPD^{X}_{k}] \tag{3.39}$$

The cluster mean delay and RMS delay spread are defined as suggested in [133]:

$$\bar{\mu}_{\tau,k} = \frac{\sum_{l=1}^{L_k} |\gamma_{k,l}|^2 \tau_{k,l}}{\sum_{l=1}^{L_k} |\gamma_{k,l}|^2} \tag{3.40}$$

where $\gamma_{k,l}$ and $\tau_{k,l}$ are the complex path amplitude and time-delay of the l^{th} SMC in the k^{th} cluster, respectively.

$$\tau_{rms,k} = \sqrt{\frac{\sum_{l=1}^{L_k} |\gamma_{k,l}|^2 (\tau_{k,l} - \bar{\mu}_{\tau,k})^2}{\sum_{l=1}^{L_k} |\gamma_{k,l}|^2}} \tag{3.41}$$

The averaged cluster delay spread is calculated with the same manner than in (4.24):

$$\bar{\mu}_{rms,cluster} = \mathbf{E}[\tau_{rms,k}] \tag{3.42}$$

Finally, the correlation coefficients for the cluster-level parameters are given by:

$$\rho_{x,y} = \frac{\mathbf{C}_{xy}}{\sqrt{\mathbf{C}_{xx}\mathbf{C}_{yy}}} \tag{3.43}$$

where $\mathbf{C}_{xy}$ is the cross-covariance of two parameters. This method follows the parameters computation methodology proposed in the WINNER II channel model [45].

3.5 Conclusion

In this chapter, two complementary modeling approaches have been proposed and developed to analyze the characteristics of polarimetric links from the estimated radio channel SMC and DMC parameters and their related PDP. First, a comprehensive polarimetric distance-dependent model of the PDP and path gain is proposed for scenarios including DMC. This model considers the respective contribution of different radio channel multi-path components. The conventional path loss model which is based on the power law was re-evaluated by including DMC. This model provides a deeper physical insight into the propagation mechanisms when polarimetric radio channels with DMC are considered. Furthermore, a two-step method with low complexity to compute the joint path loss characteristics of the SMC and DMC directly from the measured data has been developed. This highlights the need to include not only a complete polarimetric description of both the SMC and DMC into polarimetric radio channel models such as the COST2100 [47] but also that polarimetric SMC plus DMC path loss models must be carefully thought.

These results have been published in [134, 135]. The proposed path loss model will be validated and evaluated in the following chapter.

Furthermore, a novel MCD-based clustering algorithm, ACId-MCD, was proposed to group the SMC obtained from MIMO radio channels. The performance of the novel algorithm was compared with the popular K-means MCD algorithm using a dedicated evaluation protocol. The radio channels were simulated by the GSCM WINNER II channel model under four scenarios. The results indicate that ACId-MCD outperforms K-means MCD for all investigated scenarios. Clearly, the capability of ACId-MCD to estimate correctly without ambiguity the radio channel clusters and intra-cluster SMC is demonstrated. Also, its robustness has been demonstrated with Monte-Carlo simulations. Moreover, the optimal clustering solution is obtained without performing computationally extensive statistical studies on the same radio channel as required by the investigated K-means MCD. Furthermore, the optimal number of clusters is associated with a unique MCD threshold. This threshold is physically linked to the cluster size/distribution and, therefore, deeply rooted to the large-scale parameters of the radio channel. From the radio channel modeling point of view and specifically GSCM ones, it is believed that the MCD threshold could be used as an additional large-scale parameter to categorize propagation scenarios based on their clustering properties. These results have been published in [136, 137, 138]. The application of ACId-MCD to real-world data will be introduced and discussed in the following chapter.

Chapter 4

Indoor scenario with DMC: industrial radio channel

4.1 Introduction

In this chapter, it is proposed to investigate the radio channel propagation characteristics of an indoor scenario including DMC. The selected environment is a large open hall which is the host of high-tech small and medium-sized enterprises (SMEs) and is categorized under the industrial radio channel.

First, the polarimetric distance-dependent and path loss models proposed in the previous chapter were applied to the SMC and DMC PDPs estimated from measured polarimetric MIMO transfer functions. The validation of the proposed model will be followed by a discussion of the propagation mechanisms and their relative contribution to the radio channel.

Then, clustering of the estimated SMC was performed with the ACId-MCD algorithm developed in the framework of this thesis. In order to evaluate the contribution of DMC to the cluster statistics and distributions for this environment, it is proposed to compare the clustering results obtained for the two following cases. 1) it is assumed that the radio channel only includes SMC. This is the classical hypothesis from which all GSCM were built on. 2) the radio channel includes both SMC and DMC. The cluster features for these two cases will be compared and discussed.

4.2 Measurement campaign and data processing

4.2.1 Measurement setup and scenario

The validity of the developed model is assessed with data collected in a large atrium (48.8 m $\times$ 36.35 m $\times$ 18 m) of the EuraTechnologies Center, Lille, France. The polarimetric radio channel transfer functions were obtained at 1.3 GHz over a 22 MHz bandwidth with the virtual 16 $\times$ 16 MIMO channel sounder presented in

chapter 2 (section 2.4.1). Prior being refurbished into a high-technology building, this three level high environment was the host of a textile plant, explaining the presence of traditional brick walls, marble floor, large windows surface, and metallic structure, as depicted in Figure 4.1(a). A few chairs, tables, benches, and decoration plants are located around the center for social events such that the environment can be considered as almost empty. Figure 4.1(b) presents the 13 LOS Tx-Rx positions in the hall with distances ranging between 10 and 45 m. The measurement campaign was performed at night without workers and visitors to ensure that the radio links are static over time. The transmitting unit was moved around the hall whereas the receiving unit was set to the same position for all measurements. A virtual UCA was used for both Tx and Rx with dual-polarized patch antennas located at 1.6 m high.

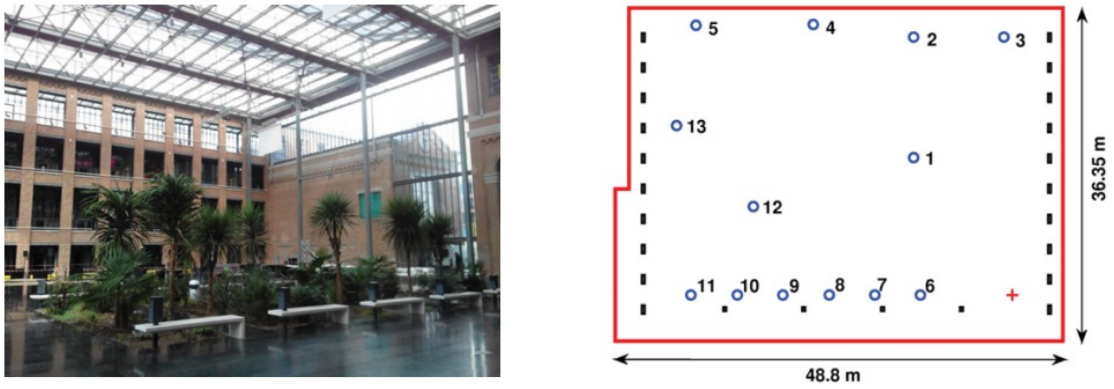

(a) (b)

Figure 4.1: (a) Picture of the EuraTechnologies Center atrium (Lille, France) from the receiving array point of view. (b) Tx (blue circles), Rx (red cross) measurement pairs in the EuraTechnologies Center atrium. The black squares indicate the vertical brick beams visible in (a).

It is recalled here that the complex impulse response of the distance-dependent polarimetric MIMO radio channel $\mathbf{h}^{XY}(\tau, d, m, n)$ can be obtained by Fourier transforming sampled versions of the frequency response $\mathbf{H}^{XY}(f, d, m, n)$ measured for all Tx-Rx links:

$$\mathbf{h}^{XY}(\tau, d, m, n) = \mathcal{F}^{-1}(\mathbf{H}^{XY}(f, d, m, n)) \tag{4.1}$$

where d is the Tx-Rx distance, τ is the time-delay, f the sampled frequency, m the m^{th} antenna of the Tx array, n the n^{th} antenna of the Rx array, and $\mathcal{F}^{-1}$ the inverse Fourier operator. The polarimetric distance-dependent PDP $\mathbf{G}^{XY}(\tau, d)$ can be obtained from the expectation of the squared magnitude of $\mathbf{h}^{XY}$.

$$\mathbf{G}^{XY}(\tau, d) = \mathbf{E}\left[|\mathbf{h}^{XY}(\tau, d, m, n)|^2\right] \tag{4.2}$$

The expectation operator is applied over all Tx-Rx links to remove the small-scale fading. As an example, Figure 4.2 presents the measured polarimetric PDP for

position 6 (short Tx-Rx distance) and 13 (large Tx-Rx distance). The exponential decay of the PDP indicates the presence of DMC for all polarization links. In addition, SMC clusters can be clearly observed for the co-polar PDP, but individual SMC cannot be visually distinguished from each other due to the limited bandwidth.

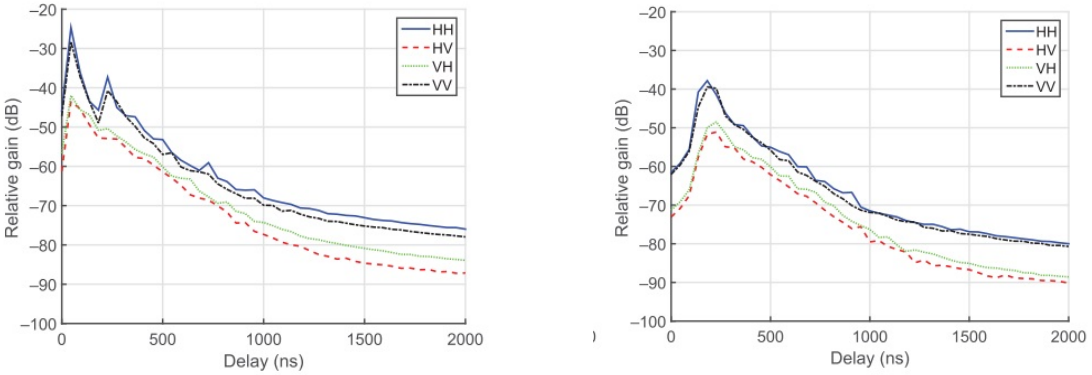

(a) (b)

Figure 4.2: Example of measured polarimetric PDP for (a) position 6 and (b) position 13.

4.2.2 Parametric Estimation and PDP

The polarimetric SMC and DMC parameters were initially estimated with the ML estimator RiMAX described in chapter 2 [1]. The wideband polarimetric MIMO measurements with a UCA at both link ends allow to access the TOA, DOA, DOD, polarimetric complex gain for each SMC, as well as the DMC. In addition, the antennas were de-embedded from the measured radio channels with the sampled polarimetric radiating patterns of the patch antennas. The effective aperture distribution function (EADF) technique was used to store and interpolate the polarimetric gain for each SMC as a function of azimuth and elevation angles for both DOA and DOD.

Here, the number of new SMCs per iteration was set to five as originally suggested in [1]. This number was chosen as a good trade-off between the estimator computational time and its ability to split coupled SMC. Note that no significant change in the results was obtained with a larger number. The reliability of each new SMC is checked with an SNR criterion and the algorithm stops itself when all five SMCs fail the criterion. Fifty iterations were chosen such that the maximum number of SMCs was potentially 250. However, the algorithm stopped before reaching this limit for all positions and the mean number of estimated SMCs per position was found to be around 75. For the sake of comparison, this value is in-between the

number of SMCs obtained by ray tracing in an empty parallelepipedic scenario with a 5th (61) and 6th (85) order of reflection.

4.2.2.1 PDP Estimation

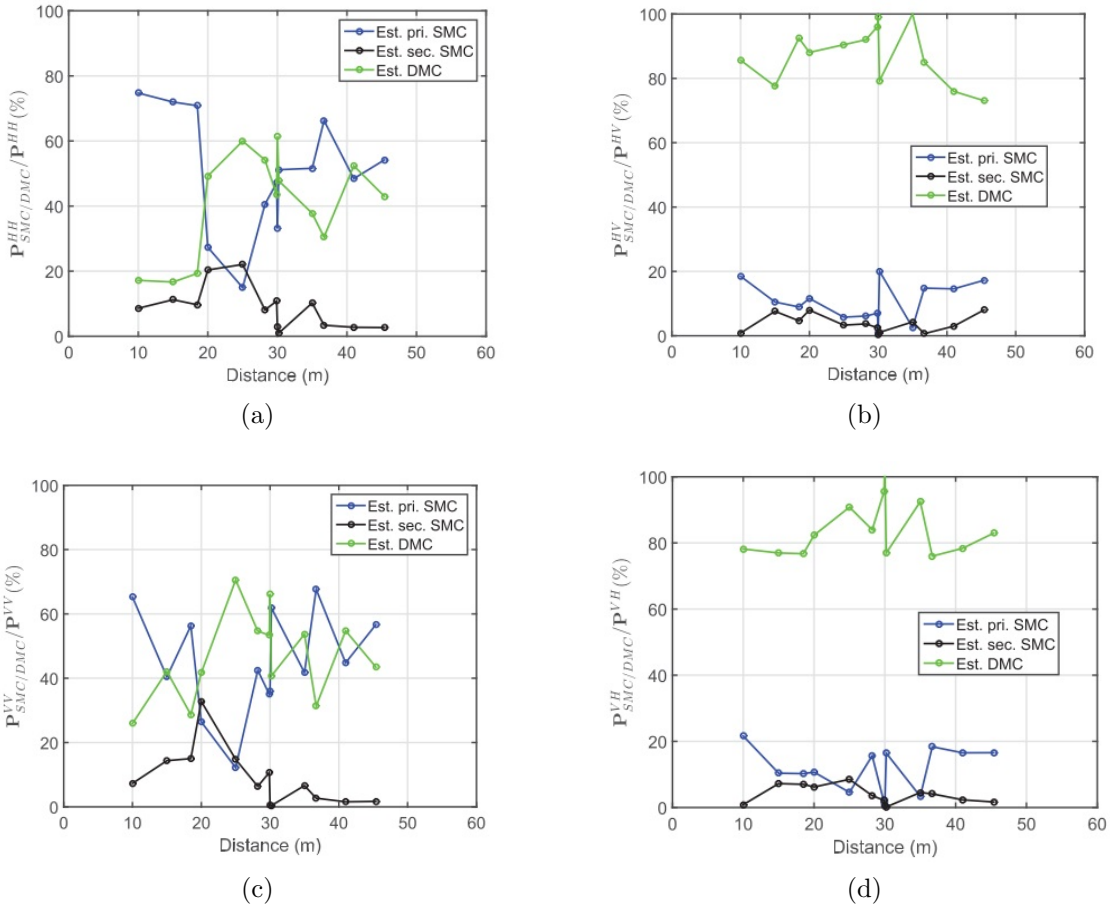

Figure 4.3: Estimated contribution of the primary SMC, secondary SMC and DMC (in %) to the total path gain as a function of distance for polarimetric links (a) HH, (b) HV, (c) VV, (d) VH.

The developed polarimetric distance-dependent path gain model relies on the estimated versions of the primary and secondary SMC and DMC PDP and subsequent path gain. These band-limited $\mathbf{G}_{pri}^{XY}$, $\mathbf{G}_{sec}^{XY}$, and $\mathbf{G}_{DMC}^{XY}$ can be reconstructed from the SMC and DMC parameters thanks to the estimator data model. At this point, it is necessary to define which SMCs contribute to the primary and secondary components. For indoor scenarios with low room volumes, the LOS and first-order components typically arrive within a short delay period and contribute all to the primary part of the PDP. However, for large volume scenarios such as the one considered in this work, some of the first-order components may arrive much later than

the LOS. This is particularly true when the Tx-Rx distance is short like for position 6, see Figure 4.1(b). For this position, peaks are observed 180 ns (54 m) later than the LOS and attributed to reflections off the left and up walls. Here, only the SMCs which contribute to the first observed peak of the PDP were considered for the primary SMC. This is done by picking all SMCs within one delay bin (45 ns) with respect to the LOS, and all the remaining SMCs are thrown into the secondary SMC. This criterion was found to be simple to implement and in-line with the proposed model.

Figure 4.3 presents the estimated contribution of the primary SMC, secondary SMC, and DMC to the total path gain as a function of distance for all polarimetric links. It is observed that the primary SMC and DMC contributions are not only dependent to the distance but also polarization links. In contrast, the contribution of the secondary SMC to the total path gain is weaker than the primary SMC and DMC with less than 9% on average for the co-polar and 4% for the cross-polar links, respectively.

4.3 Application of the polarimetric distance-dependent path gain model

4.3.1 Reference model

As discussed earlier, an exponential law is selected to describe the distance-dependent properties of DMC whereas those of the SMC are modeled with a power law. The development of path loss models is always performed with the latter model, and it can be useful to compare with already published path loss results for radio channels where DMC was identified as the strongest component. Hence and for the sake of comparison, a reference path gain model for DMC with a power law must be also considered. However, we would like to emphasize that the connection to room electromagnetics theory is completely missing when a power law is used. Such a reference model is given by:

$$\mathbf{G}_{DMC}^{Pow}(\tau, d) = \sum_{k=1}^{N_{DMC}} \mathbf{G}_{k,DMC} \left(\frac{d_0}{d}\right)^{n_{DMC}} \delta(\tau - \tau_k(d)) \tag{4.3}$$

where n_{DMC} is the path loss exponent and $\mathbf{G}_{k,DMC}$ is the reference gain for the DMC at reference distance $d = d_0$ for the k^{th} path, respectively. N_{DMC} is the number of paths contributing to the DMC.

Similarly to the path gain equations derived in chapter 3 from 3.18, equations can be derived for the DMC part:

$$\mathbf{P}_{Pow,DMC}^{HH}(d) = \chi_{DMC}^{HH}(d)\mathbf{G}_{0,DMC}^{HH} \left(\frac{d_0}{d}\right)^{n_{DMC}^{HH}} \tag{4.4}$$

$$\mathbf{P}^{HV}_{Pow,DMC}(d) = (1 - \chi^{HH}_{DMC}(d))\mathbf{G}^{HH}_{0,DMC}\left(\frac{d_0}{d}\right)^{n^{HV}_{DMC}} \tag{4.5}$$

$$\mathbf{P}^{VV}_{Pow,DMC}(d) = \chi^{VV}_{DMC}(d)\mathbf{G}^{VV}_{0,DMC}\left(\frac{d_0}{d}\right)^{n^{VV}_{DMC}} \tag{4.6}$$

$$\mathbf{P}^{VH}_{Pow,DMC}(d) = (1 - \chi^{VV}_{DMC}(d))\mathbf{G}^{VV}_{0,DMC}\left(\frac{d_0}{d}\right)^{n^{VH}_{DMC}} \tag{4.7}$$

The complete reference path gain model can be simply obtained by replacing the $\mathbf{P}^{XY}_{DMC}$ in (3.19-3.22) by the above equations.

4.3.2 Summary of the model parameters

In total, it is recalled that 24 parameters, some of which are distance-dependent, are required to tune the PDP or path gain models where the DMC follows an exponential model or power law model (reference model) in the delay domain. All model parameters are summarized in Table 4.1.

Table 4.1: Proposed Model and reference model Parameters

		SMC		DMC	
Param.	Polar.link	Primary	Secondary	Exp.law	Power law
n^{XY}	HH	$n_{pri^{HH}}$	n^{HH}_{sec}	X	n^{HH}_{DMC}
	HV	$n_{pri^{HV}}$	n^{HV}_{sec}	X	n^{HV}_{DMC}
	VH	$n_{pri^{VH}}$	n^{VH}_{sec}	X	n^{VH}_{DMC}
	VV	$n_{pri^{VV}}$	n^{VV}_{sec}	X	n^{VV}_{DMC}
$\mathbf{G}^{XY}_0$	HH	$\mathbf{G}^{HH}_{0,pri}$	$\mathbf{G}^{HH}_{0,sec}$	$\mathbf{G}^{HH}_{0,DMC}$	$\mathbf{G}^{HH}_{0,DMC}$
	VV	$\mathbf{G}^{VV}_{0,pri}$	$\mathbf{G}^{VV}_{0,sec}$	$\mathbf{G}^{VV}_{0,DMC}$	$\mathbf{G}^{VV}_{0,DMC}$
χ^{XY}	HH	χ^{HH}_{pri}	χ^{HH}_{sec}	χ^{HH}_{DMC}	χ^{HH}_{DMC}
	VV	χ^{VV}_{pri}	χ^{VV}_{sec}	χ^{VV}_{DMC}	χ^{VV}_{DMC}
$\mathbf{T}^{XY}$	HH	X	X	$\mathbf{T}^{HH}$	X
	HV	X	X	$\mathbf{T}^{HV}$	X
	VH	X	X	$\mathbf{T}^{VH}$	X
	VV	X	X	$\mathbf{T}^{VV}$	X

4.3.2.1 Path gain model parameter estimation

For the estimation of proposed model parameters, after computing $\mathbf{P}_{pri}^{XY}$, $\mathbf{P}_{sec}^{XY}$, and $\mathbf{P}_{DMC}^{XY}$ from their respective PDP, a linear regression is performed to estimate the polarimetric path loss exponent n_{pri}^{XY} and n_{sec}^{XY} respectively. χ_{SMC}^{HH}, χ_{SMC}^{VV}, χ_{DMC}^{HH} and χ_{DMC}^{VV} are obtained indirectly as a function of the **XPD** and it can be shown that:

$$\chi_{SMC}^{HH}(d) = \frac{\mathbf{XPD}_{SMC}^{H}(d)}{(\frac{d_0}{d})^{(n_{SMC}^{HH}-n_{SMC}^{HV})} + \mathbf{XPD}_{SMC}^{H}(d)} \tag{4.8}$$

$$\chi_{SMC}^{VV}(d) = \frac{\mathbf{XPD}_{SMC}^{V}(d)}{(\frac{d_0}{d})^{(n_{SMC}^{VV}-n_{SMC}^{VH})} + \mathbf{XPD}_{SMC}^{V}(d)} \tag{4.9}$$

where the distance-dependent **XPD** with respect to H and V is computed from the estimated path gain for the SMC (both primary and secondary) or DMC by:

$$\mathbf{XPD}_{SMC/DMC}^{H}(d) = \left(\frac{\mathbf{P}_{SMC/DMC}^{HH}}{\mathbf{P}_{SMC/DMC}^{HV}}\right) \tag{4.10}$$

$$\mathbf{XPD}_{SMC/DMC}^{V}(d) = \left(\frac{\mathbf{P}_{SMC/DMC}^{VV}}{\mathbf{P}_{SMC/DMC}^{VH}}\right) \tag{4.11}$$

Finally, the reference gains for the primary/secondary SMC are computed at reference distance d_0 from:

$$\mathbf{G}_{0,SMC}^{HH} = \frac{\mathbf{P}_{SMC}^{HH}}{\chi_{SMC}^{HH}(d_0)} \tag{4.12}$$

$$\mathbf{G}_{0,SMC}^{VV} = \frac{\mathbf{P}_{SMC}^{VV}}{\chi_{SMC}^{VV}(d_0)} \tag{4.13}$$

Similarly, provided that $\mathbf{T}^{XY}$ is a byproduct of the estimator, χ_{DMC}^{HH} and χ_{DMC}^{VV} are given by:

$$\chi_{DMC}^{HH}(d) = \frac{\mathbf{XPD}_{DMC}^{H}(d)}{(\frac{\mathbf{T}^{HH}}{\mathbf{T}^{HV}})e^{\frac{-d}{c}\left(\frac{\mathbf{T}^{HV}-\mathbf{T}^{HH}}{\mathbf{T}^{HV}\mathbf{T}^{HH}}\right)} + \mathbf{XPD}_{DMC}^{H}(d)} \tag{4.14}$$

$$\chi_{DMC}^{VV}(d) = \frac{\mathbf{XPD}_{DMC}^{V}(d)}{(\frac{\mathbf{T}^{VV}}{\mathbf{T}^{VH}})e^{\frac{-d}{c}\left(\frac{\mathbf{T}^{VH}-\mathbf{T}^{VV}}{\mathbf{T}^{VH}\mathbf{T}^{VV}}\right)} + \mathbf{XPD}_{DMC}^{V}(d)} \tag{4.15}$$

where $\mathbf{XPD}_{DMC}^{H}$ and $\mathbf{XPD}_{DMC}^{V}$ are also computed with (4.10)and (4.11). Finally, $\mathbf{G}_{0,DMC}^{HH}$ and $\mathbf{G}_{0,DMC}^{VV}$ are computed at reference distance d_0 from:

$$\mathbf{G}_{0,DMC}^{HH} = \frac{\mathbf{P}_{DMC}^{HH}(d_0)}{\chi_{DMC}^{HH}(d_0)\mathbf{T}^{HH}e^{\frac{-d_0}{c\mathbf{T}^{HH}}}} \tag{4.16}$$

$$\mathbf{G}_{0,DMC}^{VV} = \frac{\mathbf{P}_{DMC}^{VV}(d_0)}{\chi_{DMC}^{VV}(d_0)\mathbf{T}^{VV}e^{\frac{-d_0}{c\mathbf{T}^{VV}}}} \tag{4.17}$$

4.3.2.2 Reference path gain model parameter estimation

n_{DMC}^{XY}, χ_{DMC}^{XY}, and $\mathbf{G}_{DMC}^{XY}$ need to be estimated for the reference model . A linear regression is used to estimate the n_{DMC}^{XY} from $\mathbf{P}_{DMC}^{XY}$. χ_{DMC}^{HH} and χ_{DMC}^{VV} are obtained similarly to (4.8) and (4.9):

$$\chi_{DMC}^{HH}(d) = \frac{\mathbf{XPD}_{DMC}^{H}(d)}{(\frac{d_0}{d})^{(n_{DMC}^{HH}-n_{DMC}^{HV})} + \mathbf{XPD}_{DMC}^{H}(d)} \tag{4.18}$$

$$\chi_{DMC}^{VV}(d) = \frac{\mathbf{XPD}_{DMC}^{V}(d)}{(\frac{d_0}{d})^{(n_{DMC}^{VV}-n_{DMC}^{VH})} + \mathbf{XPD}_{DMC}^{V}(d)} \tag{4.19}$$

wherein $\mathbf{XPD}_{DMC}^{H}$ and $\mathbf{XPD}_{DMC}^{V}$ can be computed from (4.10) and (4.11) respectively. Finally, the reference gain for the DMC can be obtained as (4.12) and (4.13) at reference distance d_0:

$$\mathbf{G}_{0,DMC}^{HH} = \frac{\mathbf{P}_{DMC}^{HH}(d_0)}{\chi_{DMC}^{HH}(d_0)} \tag{4.20}$$

$$\mathbf{G}_{0,DMC}^{VV} = \frac{\mathbf{P}_{DMC}^{VV}(d_0)}{\chi_{DMC}^{VV}(d_0)} \tag{4.21}$$

4.3.2.3 Estimated path gain model parameters

With the previously introduced estimation methods, the polarimetric path loss exponents were fitted from the estimated primary and secondary SMCs, and DMC path gains. Then, the polarization coefficients as well as the reference gains were computed for the SMC and DMC from (4.8) to (4.17). It is shown in Figure 4.4 that the primary and secondary SMCs do not exhibit strong depolarization effects. (i.e., $\chi_{SMC}^{XY} \approx 1$) over the whole distance range. In contrast, a larger depolarization

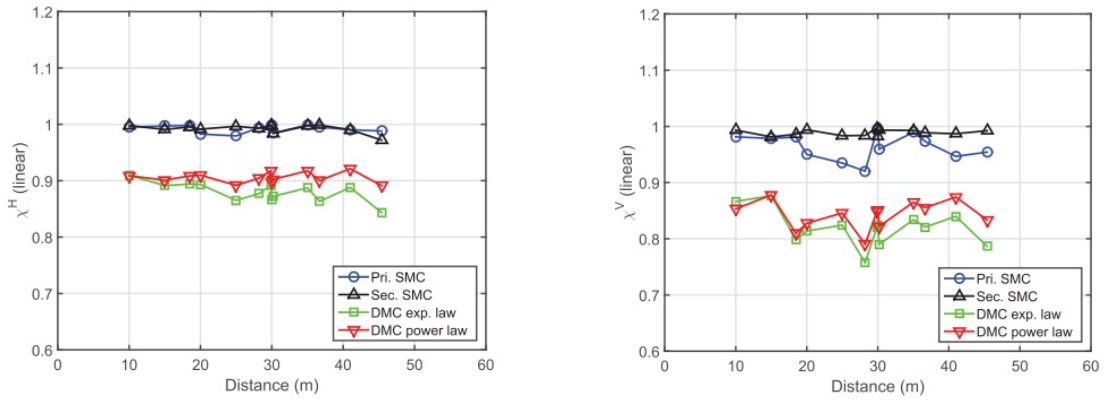

(a) (b)

Figure 4.4: Primary/secondary SMC and DMC polarization coefficients χ^{XY} for (a) H and (b) V.

is observed for the DMC but still constant. It is only noted a slight change trend for the DMC with exponential model, greater for VV than for HH. This change is too weak to be considered, and the complexity of the model can be decreased by taking the averaged value over the studied distance range. Similarly, $\mathbf{T}^{XY}$ was not found to be distance-dependent across all polarization links. A standard deviation of 14.7, 3.7, 2.7, and 5.5 ns was computed for HH, HV, VH, and VV, respectively. Hence, the averaged value was also selected to tune the model. Moreover, not only this confirms the validity of the room electromagnetics theory and applicability of the proposed model but also that the estimation of $\mathbf{T}$ is more faithful for the cross-polar links. Finally, the reference gains were computed from the data at reference distance $d_0 = 10$ m for the SMC and DMC with the reference model (power law), meanwhile $d_0 = 10$ m for SMC and $d_0 = 41$ m for the DMC with proposed model (exponential law).

Table. 4.2 summarizes the complete set of parameters required to tune the proposed PDP and path gain model for the investigated scenario.

Table 4.2: Estimated Model Parameters

		SMC		DMC	
Param.	Polar.link	Primary	Secondary	Exp.law	Power law
n^{XY}	HH	2.19	2.88	X	1.14
	HV	1.47	1.26	X	0.85
	VH	1.53	1.11	X	0.78
	VV	1.56	3.16	X	1.11
$\mathbf{G}_0^{XY}(dB)$	HH	-0.9	-10.3	60.9	-6.88
	VV	-4.6	-14.2	60.2	-8
χ^{XY}	HH	0.99	0.99	0.88	0.91
	VV	0.97	0.99	0.82	0.84
$\mathbf{T}^{XY}(ns)$	HH	X	X	125.6	X
	HV	X	X	126.6	X
	VH	X	X	126.6	X
	VV	X	X	116	X

4.4 Validation of the proposed model

4.4.1 Polarimetric path gain

The validation of the proposed polarimetric path gain model including the reference model (i.e. DMC with power law) is performed by comparing with the data

estimated from the measurements. Figure 4.5 presents a comparison between the estimated and modeled path gains for each propagation mechanism and polarization link. In addition, Figure 4.6 presents the distance-dependent total path gain of the estimated and modeled data, respectively. The path gain models were built from (3.19) to (3.22) with the parameters as listed in Table 4.2.

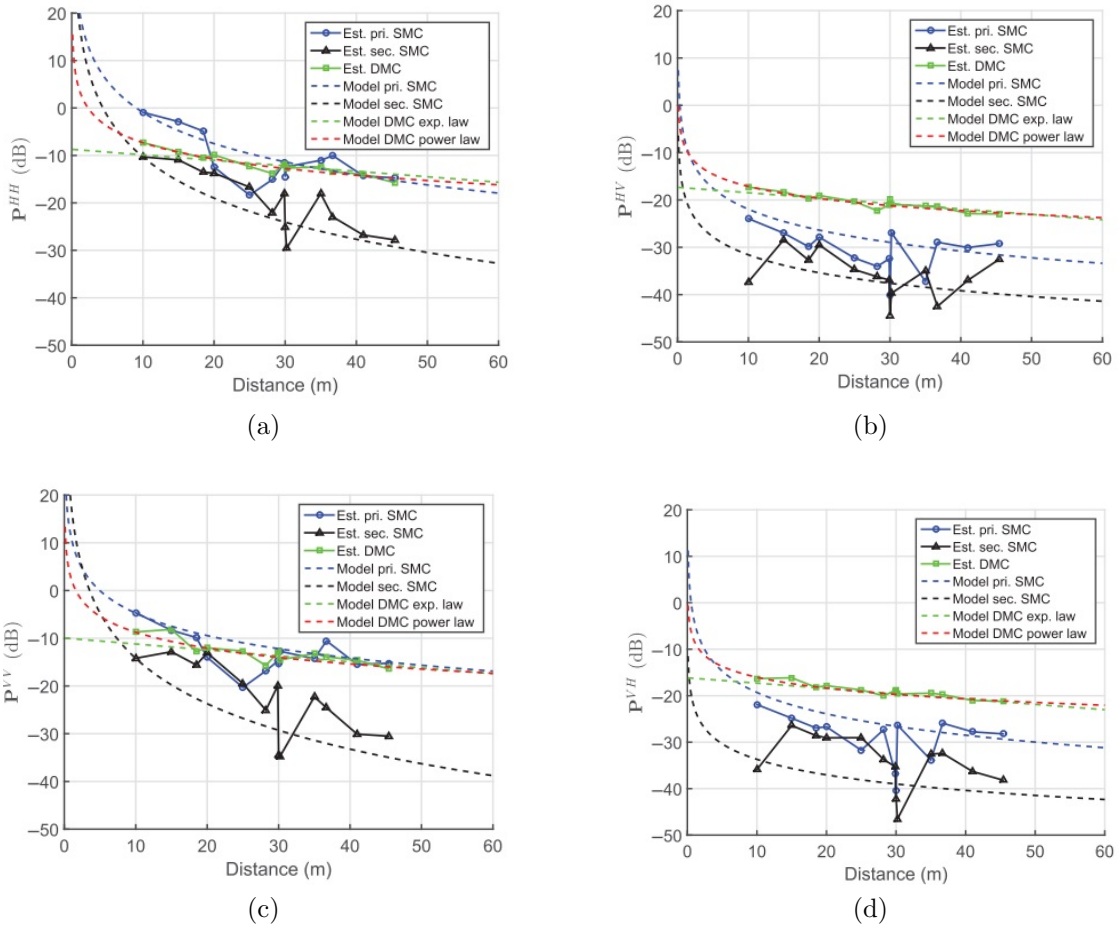

Figure 4.5: Estimated and modeled primary/secondary and DMC path gain as a function of distance for polarimetric links (a) HH, (b) HV, (c)VV, (d) VH.

The results show a good agreement between the model and data estimated from the measurements. This goodness of fit is demonstrated by the root-mean-squared error (RMSE) values computed between the path gain deduced from the models and measurements (in dB) for each polarization link and shown in Table 4.3.

The RMSE values are found as good with a power law or an exponential model for the investigated range. It is observed larger RMSE values for the cross-polar primary SMC than for the co-polar links. Conversely, smaller RMSE values are obtained for the cross-polar DMC than for the co-polar links. The secondary SMCs present almost the largest RMSE values across the polarization links. The large

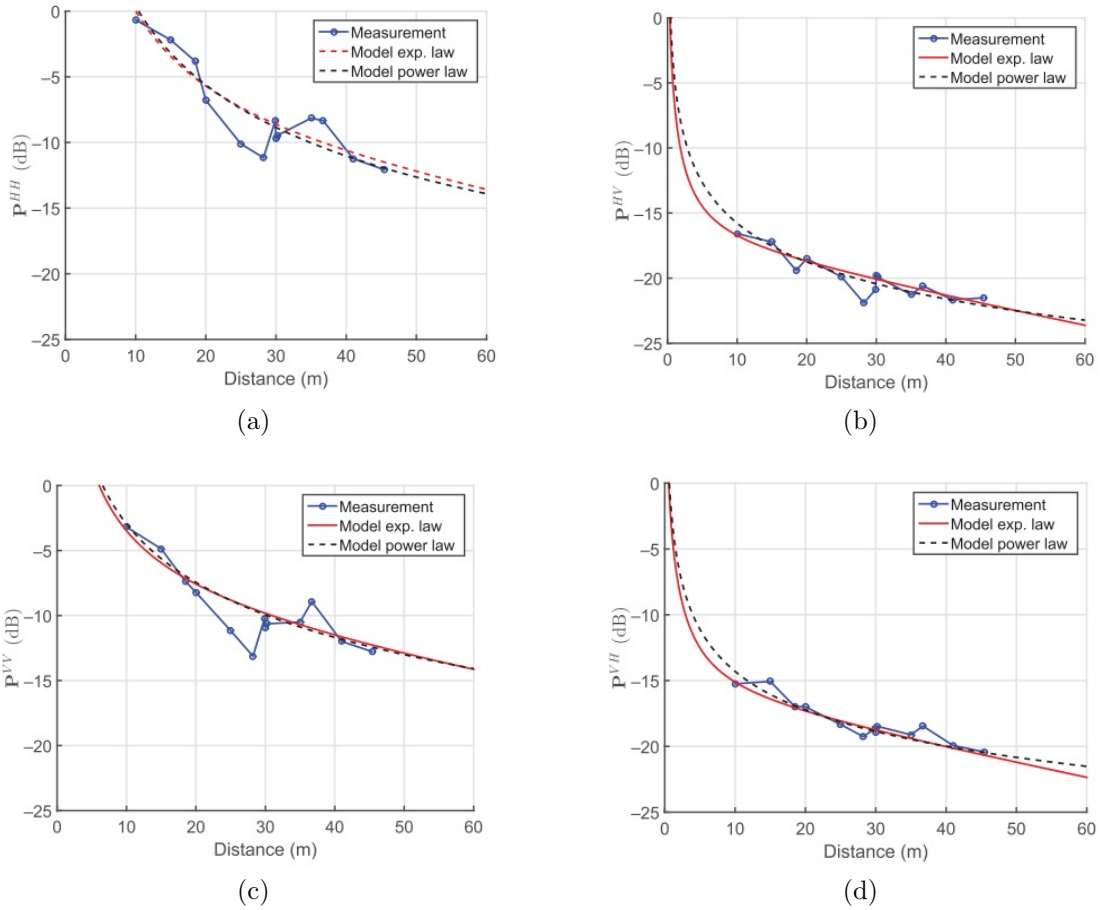

Figure 4.6: Estimated and modeled total path gain as a function of distance for polarimetric links (a) HH, (b) HV, (c)VV, (d) VH.

Table 4.3: RMSE (dB) of Path Gains

			$\mathbf{P}^{XY}_{DMC}$		$\mathbf{P}^{XY}$	
	$\mathbf{P}^{XY}_{pri}$	$\mathbf{P}^{XY}_{sec}$	Exp.model	Power law	Exp.law	Power law
HH	3.41	4.31	1.16	0.72	1.76	1.75
HV	4.64	4.32	0.74	0.63	0.81	0.7
VH	5.65	6.45	0.73	0.63	0.46	0.48
VV	3.55	6.73	1.53	1.22	1.39	1.42

RMSE values for the SMC could be attributed to the time-gating approach used to select the SMC which has not been optimized. It is noteworthy that a deeper analysis of the polarization mechanisms for each component is not discussed here since that we primarily focus on developing and validating the model.

4.4.2 Polarimetric Reverberation ratio

The prediction of polarimetric reverberation ratio is another good indicator to check the validity of the proposed polarimetric model. As introduced in section 3.2.3, the distance-dependent polarimetric reverberation ratio $\mathbf{R}^{XY}$ was computed with the data and model in which the power law and exponential model were both considered. The results are presented in Figure 4.7. A good agreement is found between the

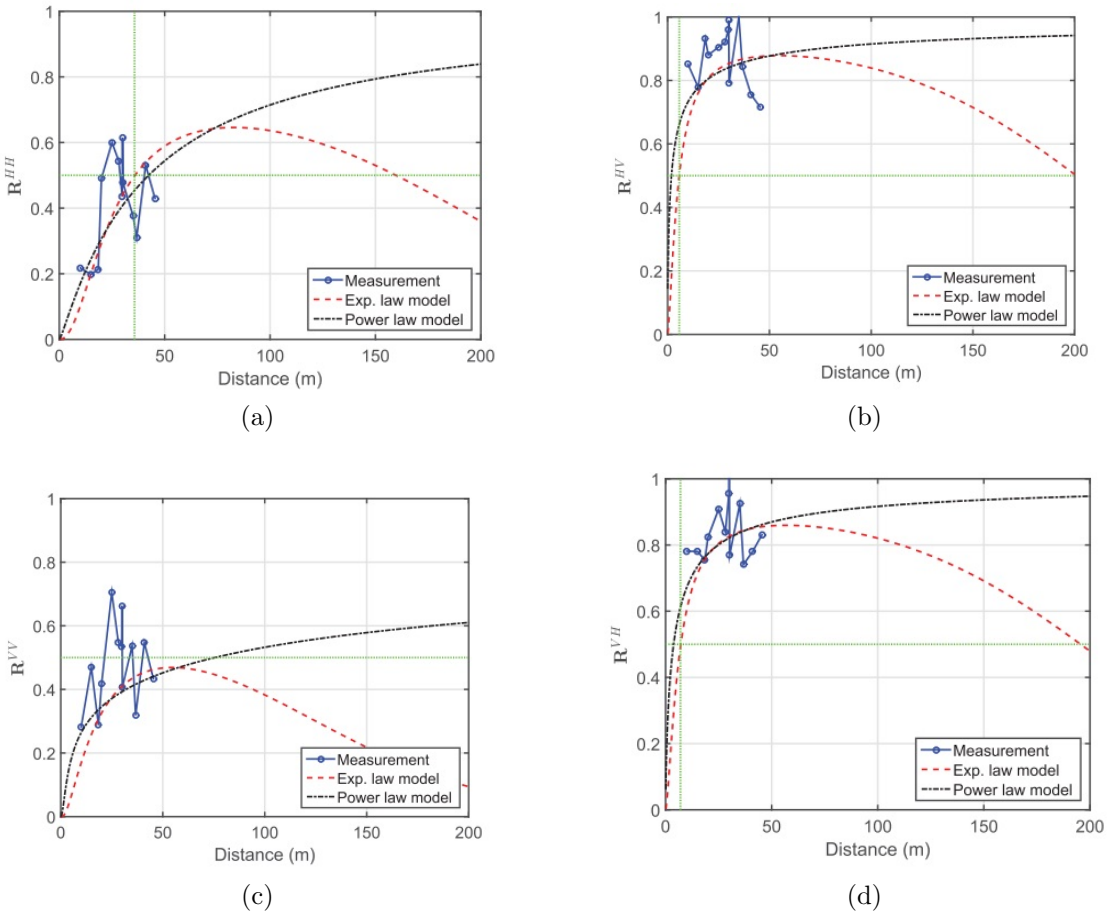

Figure 4.7: $\mathbf{R}^{XY}$ as a function of distance (a) HH, (b) HV, (c) VV, (d) VH.

measured and modeled data for the investigated distance range. Results with the exponential and power laws are similar for distances up to 50 m but differ greatly for larger distances. As originally shown in [2] with an exponential model, $\mathbf{R}^{XY}$ tends toward zero when the distance between the transmitter and receiver exceeds

several hundred meters. However, the behavior of $\mathbf{R}^{XY}$ is rather different with the power law and converges toward unity without passing through a maximum value. For the exponential model, the distance at which $\mathbf{R}^{XY}$ is maximal is equal to $50m$ for both HV and VH but is equal to 75 m for HH and 50 m for VV. However, it is noted that it is not possible at this point to experimentally verify which model holds for longer distances. Further experimental study on larger distance is needed but could not be investigated in this thesis. In contrast to the path gain models, a strong asymmetry (shape and distance at which the maximum value is obtained) is observed between all polarimetric subchannels and, in particular, the co-polar ones. The fact that reverberation effects are non-uniform across all polarization links highlights the complexity of propagation mechanisms even in simple scenarios and that polarimetric radio channel models including DMC must be designed with care.

The measured reverberation ratio values are ranging between 20 and 75 for $\mathbf{R}^{HH}$ and $\mathbf{R}^{VV}$ similar to other investigated indoor scenarios [14, 139, 25, 49] and above 75 up to 100 for $\mathbf{R}^{HV}$ and $\mathbf{R}^{VH}$. High reverberation ratio values are expected in indoor or industrial scenarios (when the room electromagnetic theory applies) since intermediate distances are typically used. Consequently, this result confirms the findings of all previous studies on this topic.

4.5 Application of path loss model with DMC

4.5.1 Two-step path loss parameter fitting method

The two-step parameter fitting technique which has been introduced in section 3.3 has also been applied on the measurement data. The parameters were obtained using a linear regression fitting. Here, the application case is illustrated with the HH sub-channel.

Figure 4.8 illustrates this two-step fitting procedure for the measured HH radio channel data. In a first step [Figure 4.8(a)], the path loss exponent for the primary SMC noted n^{HH-I} is computed from the linear region of the log-distance curve for distances where the SMC gain is greater than the DMC. In a second step [Figure 4.8(b)], the DMC path loss factor η_{DMC}^{HH-II} is computed from the linear region of the linear-distance curve where the DMC gain is greater than the SMC. It is observed that the fitting slope follows well the asymptotic behavior of the model for each region (power law for the SMC and exponential law for the DMC). In addition, the SMC to DMC transition distance between the two propagation mechanisms can be obtained with the intersection of the log- and linear-distance lines. For this case, a transition distance $d = 37$ m is obtained in agreement with the value in Figure 4.7(a) (see vertical line).

In summary, Table 4.4 presents the SMC path loss exponent n_{pri}^{XY-I} and DMC path loss factor η_{DMC}^{XY-II} fitted from this procedure for each polarization link. For the sake of comparison, n^{XY} , n_{pri}^{XY} , n_{DMC}^{XY} (Table 4.2), and η_{DMC}^{XY} computed with

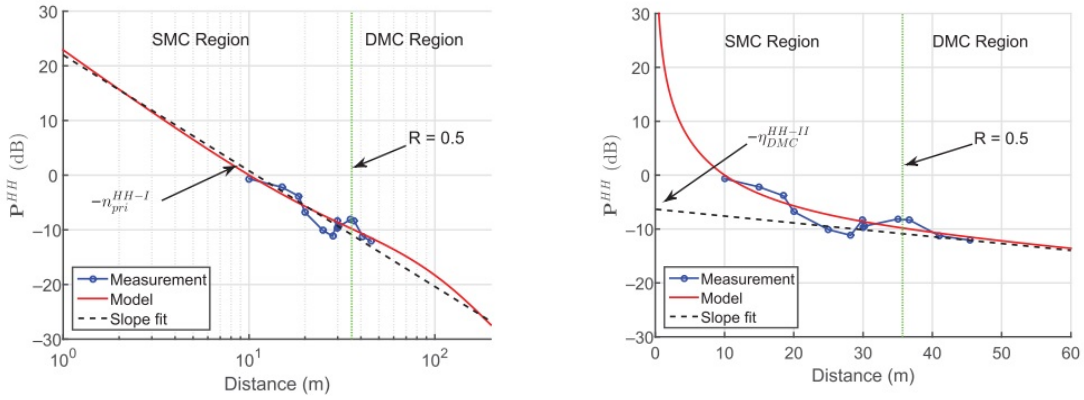

(a) (b)

Figure 4.8: Two-step path loss exponent fitting for the HH radio channel. the dotted line (black) is the slope fit for (a) the SMC $\left(n_{pri}^{HH-I}\right)$ and (b) DMC $\left(\eta_{DMC}^{HH-II}\right)$. The vertical line indicates the transmission distance at which $\mathbf{R} = 0.5$ (37 m here).

Table 4.4: RMSE (dB) of Path Gains

	Meas.	Pri.SMC		DMC		
	n^{XY}	n_{pri}^{XY}	n_{pri}^{XY-I}	n_{DMC}^{XY}	η_{DMC}^{XY}	η_{DMC}^{XY-II}
HH	1.63	2.19	2.17	1.14	0.12	0.17
HV	0.88	1.47	0.95	0.85	0.11	0.11
VH	0.86	1.53	0.9	0.78	0.11	0.11
VV	1.21	1.56	1.89	1.11	0.13	0.17

(3.26) from the values of $\mathbf{T}_{DMC}^{XY}$ (Table 4.2) were also added. As discussed at the beginning of this section, it is confirmed that n^{XY} is not only in-between n_{pri}^{XY} and n_{DMC}^{XY} but also in line with values reported in [52, 49, 140]. Hence, the need for path loss models where DMC is included is clearly demonstrated. Furthermore, a relatively good agreement is obtained between n_{pri}^{XY} with n_{pri}^{XY-I}, and an excellent fit is obtained between n_{DMC}^{XY} and η_{DMC}^{XY-II} . This latter result indicates that the reverberation time can be estimated with great accuracy for the cross-polar channels from (3.26) without applying complex parametric estimation techniques.

Overall, the results show that it is possible to grasp the path loss characteristics of each mechanism with the two-step fitting approach which is a strong contribution of this work. Finally, even if the investigated distance span and related measurement dataset were limited, it was sufficient to develop the model since the measured data overlap over both regions. This method is general and could be applied to any path loss data already collected in environments wherein the contribution of DMC is strong and room electromagnetics applies.

4.6 Application of ACId-MCD

In this section, the previously introduced automatic clustering algorithm ACId-MCD was applied to the measured data. This novel clustering tool was fed with SMC parameters estimated by RiMAX. In the literature, the SMC used to perform the clustering analysis are always estimated with algorithms which do not include DMC in their data model. It is expected that the statistics and distributions of these clusters to be different if DMC is jointly estimated. To assess the impact of neglecting DMC in the data model, a comparative study was performed and the results are discussed in the following paragraphs.

For the sake of comparison, the measured radio channels were treated with two different estimators and the estimated SMC were then processed with ACId-MCD. First, the RiMAX estimator which includes both SMC and DMC in its data model was used to process the data. This approach is called method 1 for the following results and figures. In addition, a second RiMAX estimator which does not include DMC was also used to estimate the SMC and is called method 2. All the MPC falling under the DMC umbrella (method 1) will obviously be picked up as SMC in the method 2. Note that the weak SMC were classified as DMC clusters in the work of [132] which is an alternative approach to this work. For instance, and with a 40 dB power threshold, about 50 SMCs on average are found for method 1 whereas 300 SMCs on average are found for method 2 at each measurement position. The large difference in the number of paths will obviously result in different clustering characteristics. As an example, Figure 4.9 presents the raw SMC parameters (no threshold), SMC and DMC PDPs estimated using both methods for position 5.

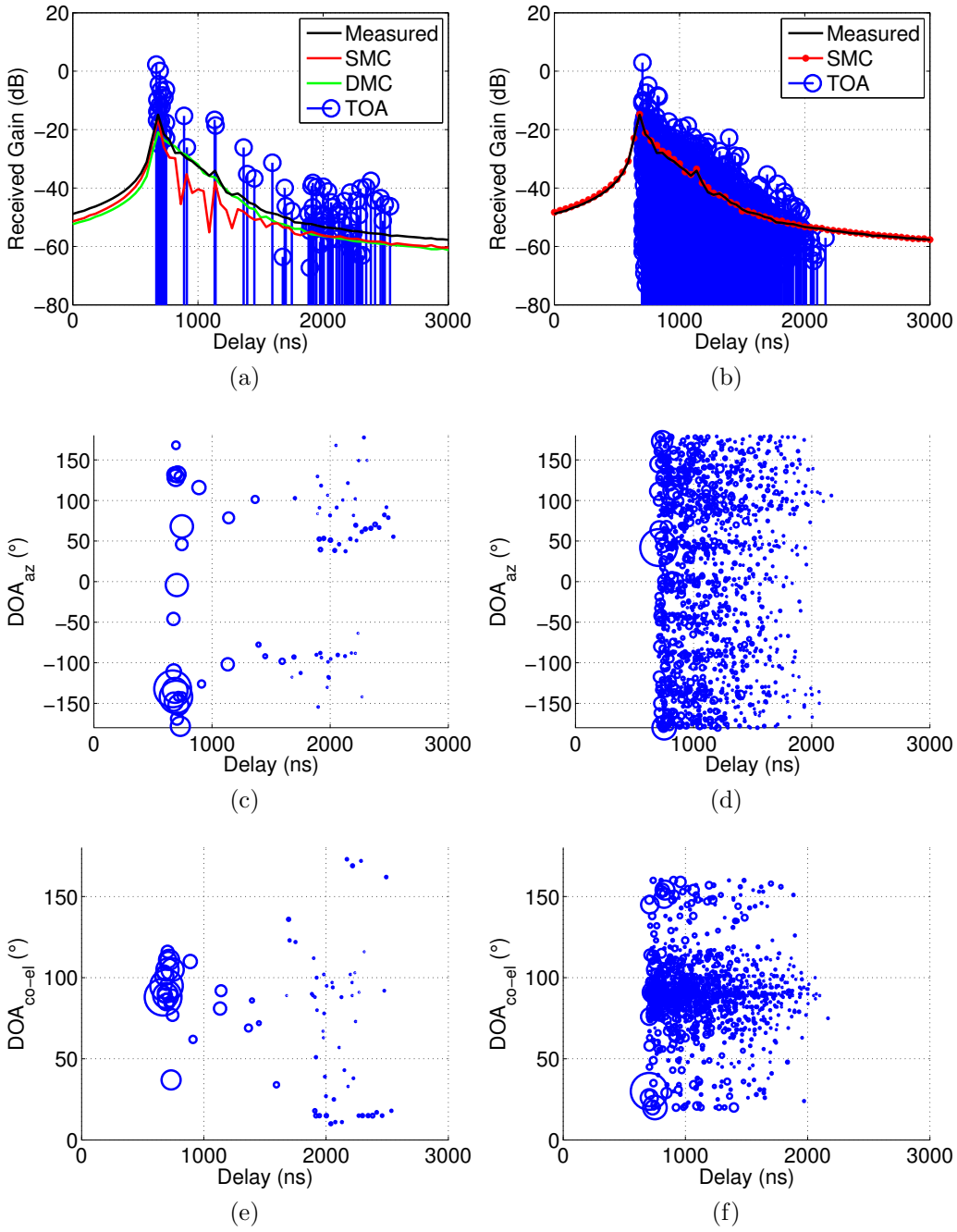

Figure 4.9: Example of estimation results for position 5 using method 1 (left column) and method 2 (right column) for the following dimension: (a) and (b) TOA (SMC and DMC), (c) and (d) DOA_{az}, and (e) and (f) DOA_{co-el}.

4.6.1 Definition of cluster parameters

It is meaningful to define some cluster parameters based on the estimated cluster index of each SMC. The cluster power is defined as the sum of total SMCs power in the same cluster, which is in line with [132]. It is showed in (4.22).

$$P_k^{X/Y} = \sum_{L_k} |\gamma_{k,l}^{X/Y}|^2 \tag{4.22}$$

with L being the total number of SMC in the k-th cluster, and X/Y being the two orthogonal polarization states. Then the cluster-level XPD_H can be obtained by

$$XPD_k^H = \frac{P_k^{HH}}{P_k^{HV}} \tag{4.23}$$

The calculation of the cluster-level XPD does not take into account the single SMC cluster.

Due to several estimated clusters at one measurement position, the averaged cluster XPD is obtained by the mean value of all cluster XPD at the same measurement position. This value is believed to reflect one overall cluster XPD at certain measurement position.

$$\overline{XPD}_{cluster}^H = \mathbf{E}[XPD_k^H] \tag{4.24}$$

The cluster mean delay and RMS delays spread are defined as following which are inline with [133].

$$\bar{\mu}_{\tau,k} = \frac{\sum_{l=1}^{L_k} |\gamma_{k,l}|^2 \tau_{k,l}}{\sum_{l=1}^{L_k} |\gamma_{k,l}|^2} \tag{4.25}$$

$$\tau_{rms,k} = \sqrt{\frac{\sum_{l=1}^{L_k} |\gamma_{k,l}|^2 (\tau_{k,l} - \bar{\mu}_{\tau,k})^2}{\sum_{l=1}^{L_k} |\gamma_{k,l}|^2}} \tag{4.26}$$

The averaged cluster delays spread is calculated with the same manner than (4.24).

$$\bar{\mu}_{rms,cluster} = \mathbf{E}[\tau_{rms,k}] \tag{4.27}$$

The correlation coefficients of cluster-level parameters are calculated as following

$$\rho_{x,y} = \frac{\mathbf{C}_{xy}}{\sqrt{\mathbf{C}_{xx}\mathbf{C}_{yy}}} \tag{4.28}$$

where $\mathbf{C}_{xy}$ is the cross-covariance of two parameters. Such method is inline with the parameters calculation of WINNERII channel model.

4.6.2 Clustering analysis

The SMC parameters estimated with method 1 and 2 were processed with the ACId-MCD algorithm. The MCD searching range was set from 0.02 to 0.8 for all clustering data. The clustering was initially performed with the co-polarized HH and VV links but the results were found to be similar. Therefore, only the clustering analysis for HH is presented hereafter. Table A.1 (Annex section of the manuscript) summarizes all the large-scale parameters of the channel, cross-correlation parameters, as well as the clustering parameters computed from the ACId-MCD output for the two methods. The presented parameters are inline with the GSCM philosophy of the WINNER II radio channel model [45].

Table A.1 presents the channel delay and spread parameters for the HH link (HH being used for clustering). The delay spread is typically computed from the measured PDP at each measurement position with a 20 dB threshold. The computed mean value is 85 ns which is inline with the findings in [57]. The DOA azimuth spread mean value is $\sim$100° and do not show a dependence with distance. This is attributed to the emptiness of the propagation scenario and the lack of scatterers around Tx and Rx. Finally, the DOA elevation spread is found to have a mean value of 17° for method 1 and 28° for method 2.

4.6.2.1 Preliminary analysis

The preliminary results of the clustering analysis are presented in Figure 4.10 as a function of distance . The average number of SMC per cluster (Figure 4.10(a)) is a good indicator of the cluster density. For method 1, the average number of SMC per cluster is relatively large at short distance values and then decreases down to a few SMC for the intermediate distance range (25 m - 40 m). A large spike is also observed at 20 m but is difficult to interpret at this stage. The number of clusters (Figure 4.10(b)) was found to vary greatly highlighting the complexity of the cluster distribution from position to position. For the method 2 data, the average number of SMC per cluster is much larger than in method 2. However, the same behavior is observed and the clusters are denser at short distance. This can be explained by the presence of weaker SMC around the most energetic ones. Figure 4.10(b) show 5-10 clusters at short distance values whereas 10-20 clusters are found between 25 and 40 m. This could be attributed to the fact that the SMC are more widely spread out in the time-delay and angular domains for a larger distance range resulting in more clusters. Finally, Figure 4.10(c) presents the optimal MCD threshold (MCD_T) as a function of distance. This parameter is quite important because it provides a physical indication of the optimal average cluster size with respect to the MCD metric. It is clearly demonstrated that the cluster size in method 2 is much larger than that of method 1 for all positions. This means that the presence of weaker SMC in method 2 increase the cluster size. Conversely, the incorporation of these paths in DMC (method 1) tend to decrease the cluster size. In summary, it can be observed that the introduction of DMC results in lighter and smaller clusters.

However, the number of clusters does not seem to be drastically affected and this confirms the physical clusterlike nature of the investigated double-directional radio channel.

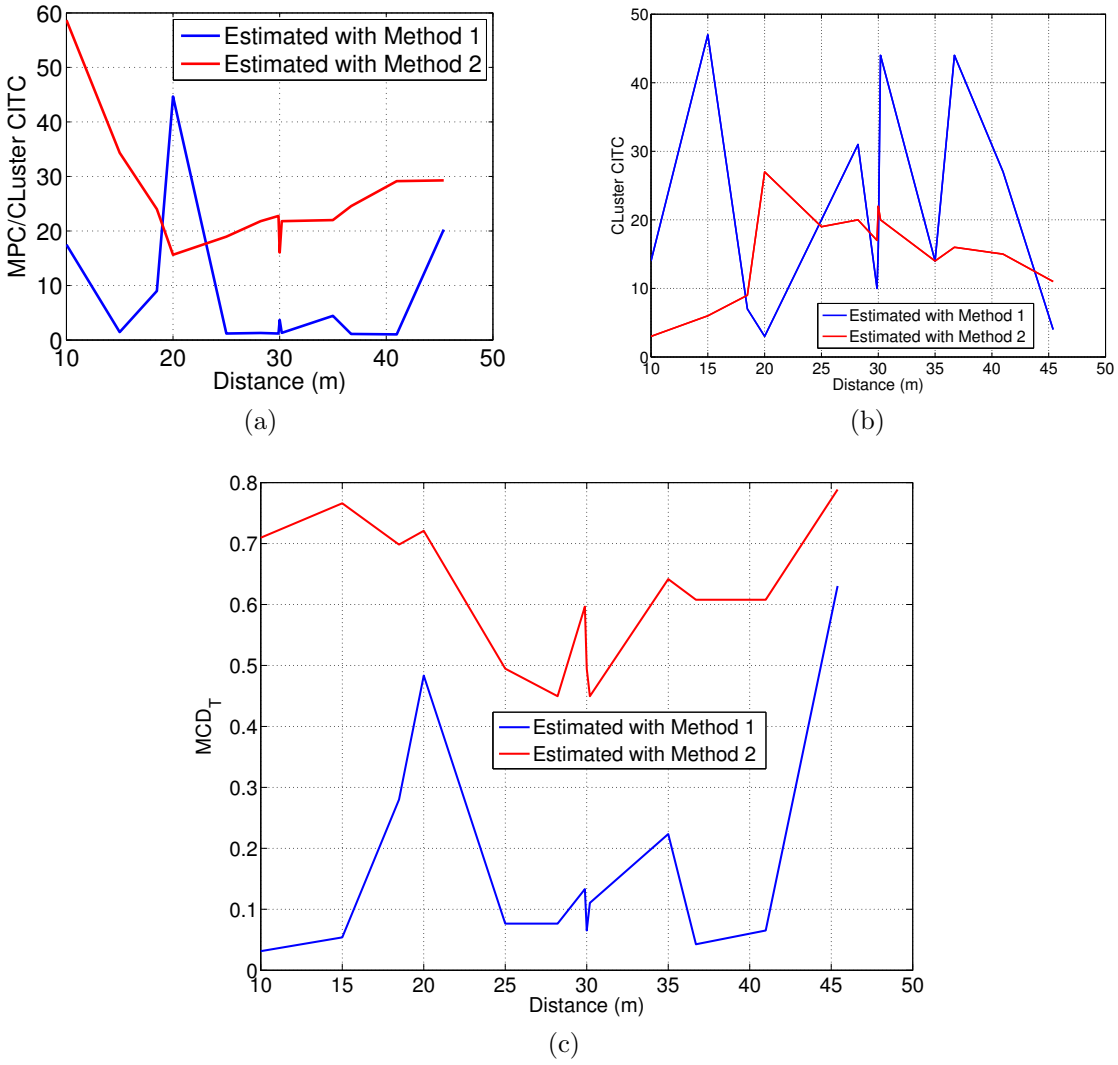

Figure 4.10: ACId-MCD clustering results as a function of distance. (a) Averaged number of SMC per cluster, (b) number of clusters, (c) estimated MCD_T.

4.6.3 Statistical analysis

Beyond this preliminary analysis, a statistical study was performed to investigate in details the cluster and intra-cluster characteristics and related distributions from the equations presented in Section 4.6.1.

4.6.3.1 RMS time-delay/angular spreads

First, Figure 4.11 presents the averaged cluster RMS delay spread $\bar{\mu}_{\tau_{rms},cluster}$ computed as the mean value of all cluster RMS delay spread for the same measurement position (4.27). Larger spread values are obtained for method 2 compared to method 1 and this is attributed to a larger SMC number in each cluster (Figure 4.10). The spread values vary between 80 and 110 ns for method 2 but are somewhat constant across the distance range (except at 20 m). On the other hand, the values for method 1 are more spread out and vary between 20 to 90 ns such that a dependence to the distance is not observed.

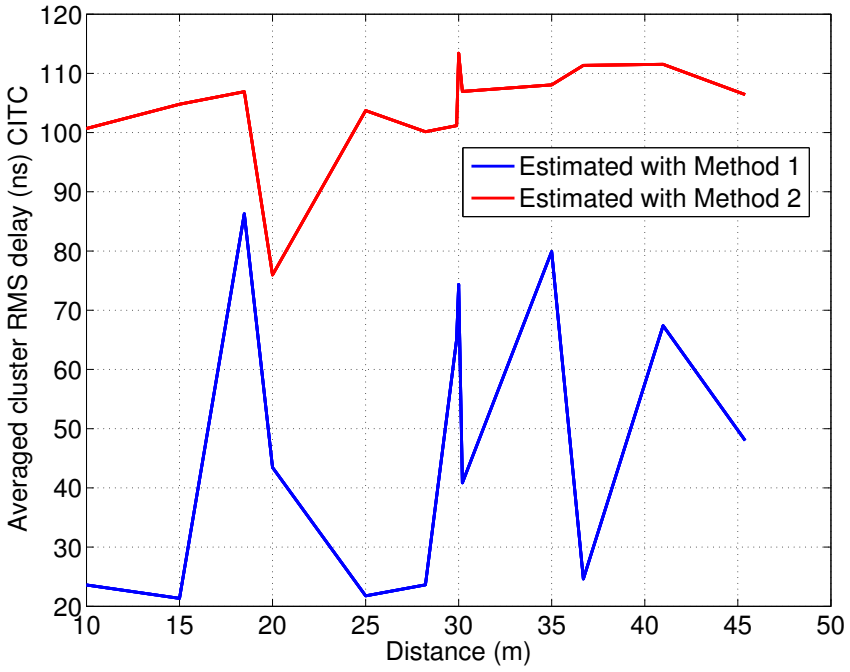

(a)

Figure 4.11: Averaged cluster delay spread $\bar{\mu}_{\tau_{rms},cluster}$ as a function of distance.

In addition, the averaged cluster angle spread $\bar{\mu}_{\phi_{rms},cluster}$ was investigated and Figure 4.12 presents the spread values for DOA and DOD in azimuth and co-elevation, respectively. As observed in the previous Figure for the delay spreads and for the same reasons, a strong difference is observed between the 2 methods. Indeed, much larger angle spread values are computed for method 2 data. For method 1, the spread values for DOA in azimuth are large at short distance and then decrease importantly with distance. The co-elevation spreads for DOA and DOD and azimuth spreads for DOD are more constant across the distance range with values ranging between 2° and 25°. For method 2, the elevation spreads for DOA and DOD are also relatively constant. On the other hand, the azimuth spread for DOA and DOD vary greatly with the measurement distance but seem strongly correlated.

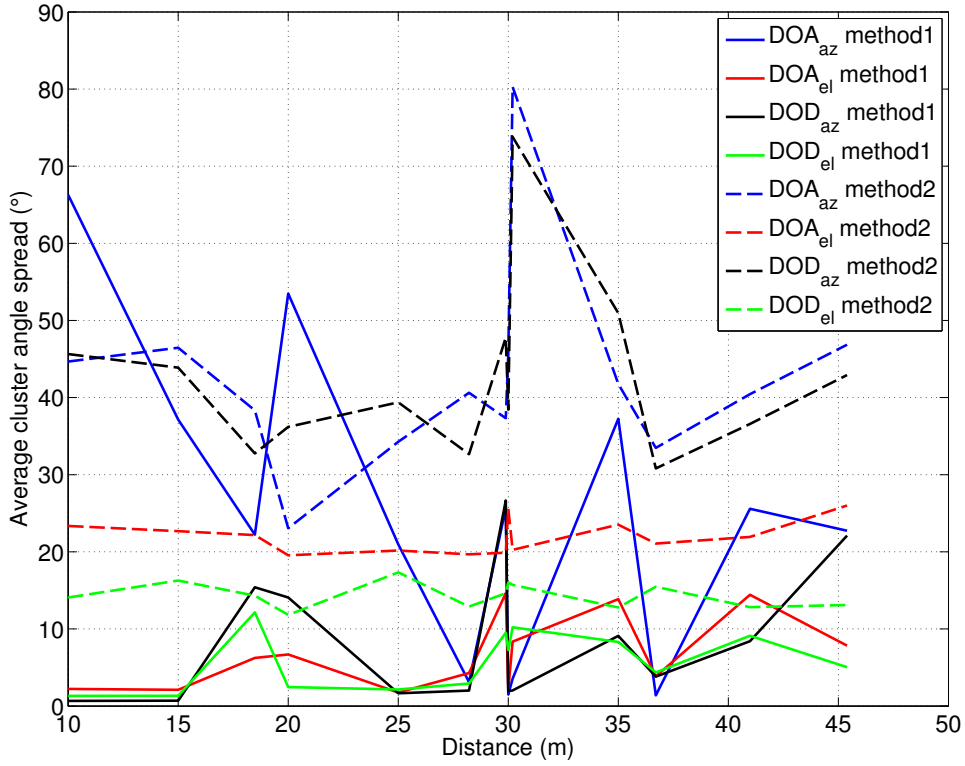

Figure 4.12: Averaged cluster RMS angle spread $\bar{\mu}_{\phi_{rms},cluster}$ as a function of distance.

The empirical cumulative distribution function (ECDF) of the averaged cluster angle spread parameters are shown in 4.13. It is clearly shown that the angle spread mean value for method 1 (either azimuth or co-elevation) is relatively smaller than that of method 2. Once again, this is attributed to the presence of weak higher-order reflection SMC in the method 2 data. For the azimuth spreads (Figure 4.13(a)), the DOA and DOD show a high degree of correlation as observed in 4.12 for method 2 but the spreads are larger for DOA than DOD when method 2 is considered. This suggests that the clusters around the receiver are larger than the clusters around the emitter when DMC is included resulting in an asymmetry with respect to the double-directional features of the radio channel. Also, it is recalled that Tx is located in the corner of the measurement hall (Figure 4.1) and could be another reasonable explanation to the larger DOA deviation at the receiver side. However, a complete opposite behavior is observed for the elevation spreads (Figure 4.13(b)). The DOA and DOD spreads are now strongly correlated for method 1 and more distributed for method 2. This could be explained by the presence of weak SMC with higher elevation angles coming from the floor or ceiling.

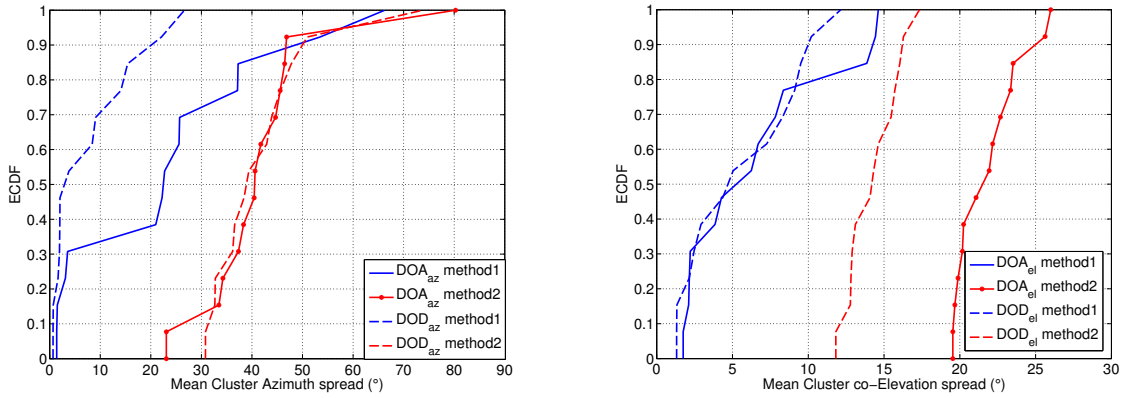

(a) (b)

Figure 4.13: ECDF of averaged angle spread for: (a) azimuth, and (b) co-elevation spread.

4.6.3.2 Cluster XPD

In addition to the spreads, Figure 4.14 presents the averaged cluster XPD_H and XPD_V as a function of distance. In general, it can be observed that the cluster XPD decreases as the distance increasing and this trend is more pronounced for method 1 than for 2. In other words, the effect of the depolarization mechanisms to the cluster XPD increase with the distance and is more keen to method 1. When the Tx-Rx distance is small, the LOS and first-order SMC contribution to the cluster XPD is large as expected. For method 1, no substantial difference is found between XPD_H and XPD_V and it could be concluded that the radio channel favors equally

H and V. In contrast, XPD_V is larger than XPD_H for method 2 for distance values above 20 m. Under this method hypothesis, it could be concluded that the radio channel favors V over H. In addition, the XPD for method 1 are on average 10 dB larger than for method 2. This indicates that DMC contributes largely to the depolarization mechanisms of the radio channel as it was also reported in [49] on a more general radio channel analysis. However, it is demonstrated here an additional direct impact of DMC to the cluster characteristics.

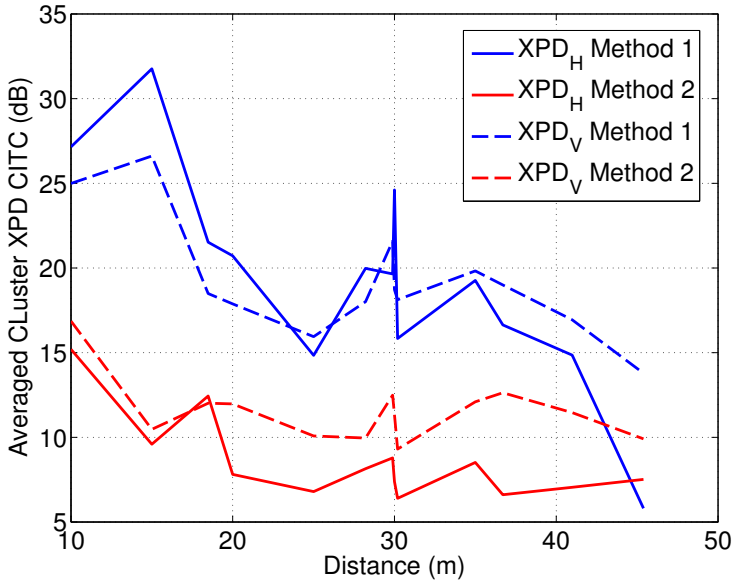

Figure 4.14: Averaged cluster XPD to distance.

From all the previous observations, it is also interesting to link the DMC reverberation ratio with the cluster XPD obtained with method 1. This study is presented in Figure 4.15 which shows the reverberation ratio as a function of XPD_H and XPD_V. It is observed that the reverberation ratio is inversely proportional to the averaged cluster XPD and similar values are obtained for H and V. When the reverberatio ratio is small (i.e. DMC is weak), then the contribution of the early SMC (primary SMC) is particularly strong as discussed in the first part of this chapter. Hence, it is expected that the clusters display a high XPD. On the other hand, when the reverberation ratio is large (i.e. DMC is strong), the primary SMC is now weak and only the secondary SMC contribute to the cluster XPD. These components suffer a high-order of interactions with the environment resulting in stronger depolarization, thus resulting in lower cluster XPD values.

4.6.4 Intra-cluster parameter distributions

For the radio channel modeling purpose, it is always useful to characterize and model the intra-cluster parameters. As an example, a single cluster of position 1 was selected to present the analysis but the analysis was performed onto the

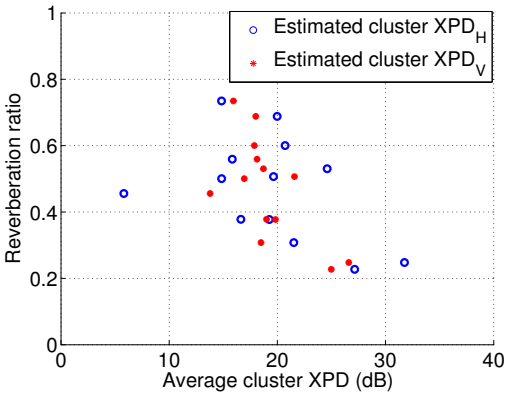

Figure 4.15: Reverberation ratio as a function of the averaged cluster XPD (method 1).

whole dataset. The selection of the distribution functions was performed using the maximum likelihood criterion. For instance, Figure 4.16 presents the ECDF of the intra-cluster amplitude and delay parameters for method 1 (top) and method 2 (bottom). The lognormal distribution was computed as the best candidate to fit all the data. In addition, the Weibull distribution was also found as a good distribution to fit the SMC amplitude for method 1.

On the other hand, the Von Mises distribution realized with the help of [141] was the best fitting distribution for the intra-cluster angle parameter in azimuth or elevation due to its periodic characteristics. For instance, Figure 4.17 and 4.18 present the intra-cluster distribution of DOA and DOD and their respective Von Mises fitted distribution (Figure 4.17).

4.7 Conclusion

In this chapter, the contribution of the DMC to the radio channel has been evaluated for an indoor scenario under two complementary modeling approaches. First, the polarimetric distance-dependent model of the PDP and path gain has been validated with polarimetric measurements of the large hall radio channel under LOS conditions at 1.3 GHz. This approach provides the main characteristics of the DMC and its contribution to the radio channel propagation mechanisms. The measured MIMO channels were processed by RiMAX to separate the polarimetric primary/secondary SMC and DMC from which the parameters of the path gain model were retrieved. The validity and robustness of the proposed approach are provided by the good agreement between the polarimetric data and models. In particular, the description of the radio channel with path loss models is discussed for cases when the DMC is included. Furthermore, a two-step method to compute the joint path loss characteristics of the SMC and DMC directly from the measured data has also been applied and validated. It has been showed that this two-step

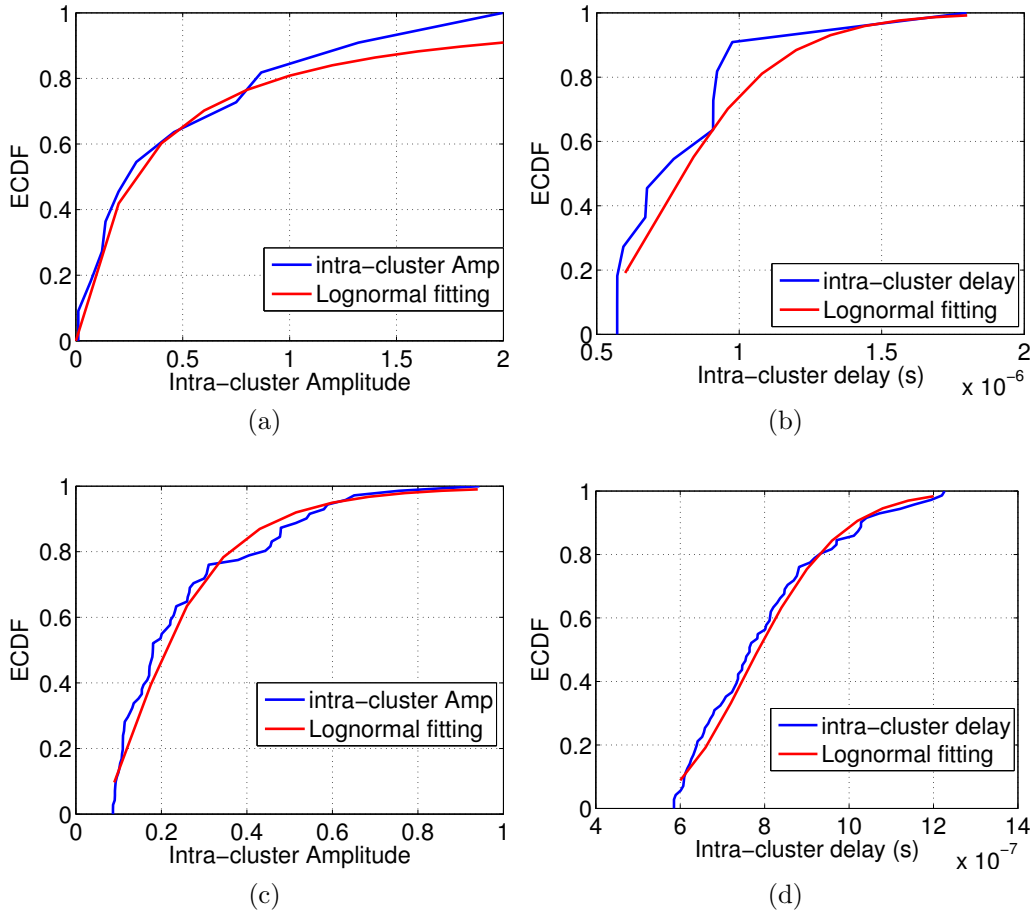

Figure 4.16: ECDF of the intra-cluster amplitude and delay parameters for a single cluster of position 1 and fitting distributions: (a) Amplitude (method 1), (b) delay (method 1), (c) amplitude (method 2), (d) delay (method 2).

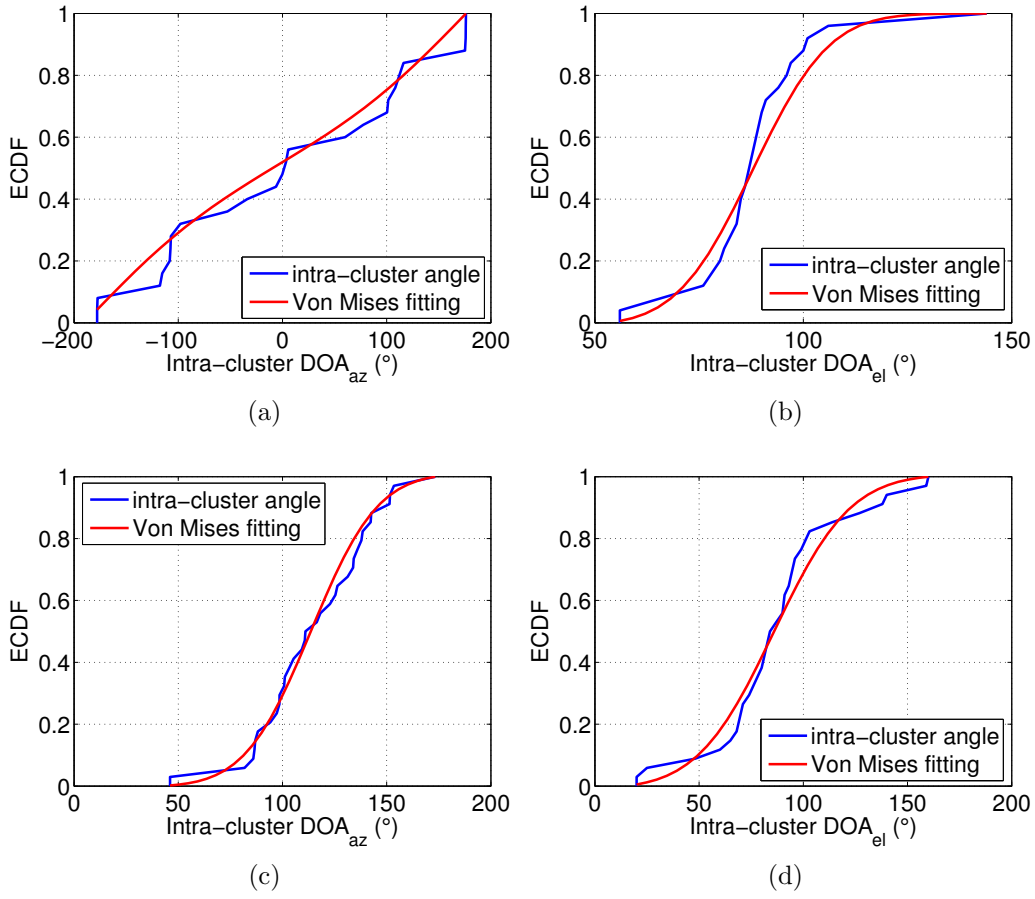

Figure 4.17: ECDF of the intra-cluster DOA parameters for a single cluster of position 1 and fitting distributions: (a) azimuth (method 1), (b) co-elevation (method 1), (c) azimuth (method 2), (d) co-elevation (method 2).

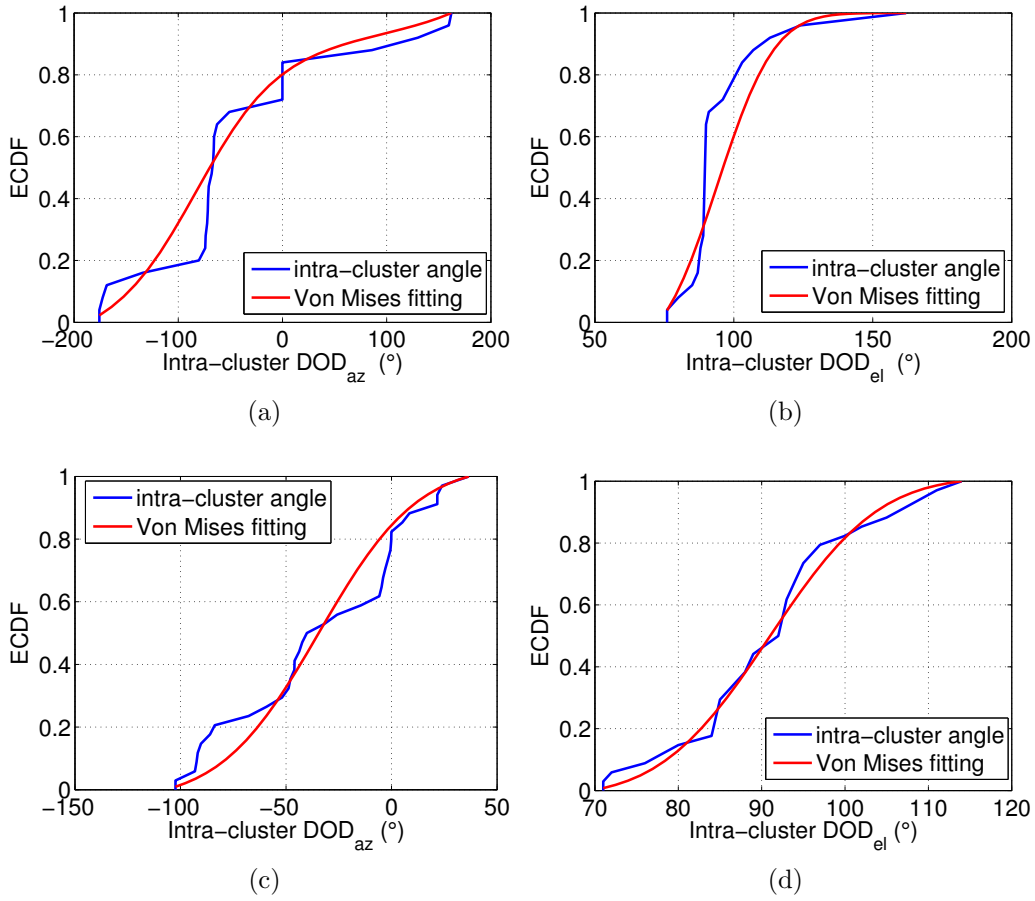

Figure 4.18: ECDF of the intra-cluster DOD parameters for a single cluster of position 1 and fitting distributions: (a) azimuth (method 1), (b) co-elevation (method 1), (c) azimuth (method 2), (d) co-elevation (method 2).

fitting method can grasp the path loss characteristics of the propagation mechanism without the application of complex parametric estimation techniques. This method has the potential to be applied on indoor radio channel measurement data wherein room electromagnetic applies and was published in [134, 135].

In addition, the ACId-MCD clustering algorithm has been applied on the estimated SMC. Two estimation methods have been applied to highlight the consequence of having DMC or not in the data model. The cluster analysis results have been extensively presented in terms of the clusters and intra-cluster statistics as a function of the Tx-Rx distance. It can be concluded that DMC has a strong impact on the large-scale clustering parameters (cluster size, XPD, etc.) but not on the intra-cluster distributions. In addition, a strong correlation was found between the cluster XPD with the reverberation ratio which is an elegant approach to link the DMC characteristics (PDP model) with the depolarization mechanisms observed at the cluster level (cluster model). Nonetheless, further studies need to be conducted to confirm this observation.

In conclusion, the results presented in this chapter demonstrate without any ambiguities that DMC is an important propagation mechanism in the investigated indoor scenario which can not be neglected any more. Furthermore, the clustering results obtained without DMC in the data model channel are in great contrast with those having DMC. This is another major contribution and originality of this manuscript and it must be highlighted, to the knowledge of the author, that this has not been discussed or reported in the literature yet. Those results seem pervasive of scenarios wherein diffuse scattering is observed and this aspect will be investigated in the final chapter of this manuscript for an outdoor scenario in the presence of vegetation.

Chapter 5

Outdoor scenario with DMC: radio channel propagation through vegetation

5.1 Introduction

Environments with vegetation is a particularly challenging propagation scenario for radio communication systems. The radio propagation phenomena are rather complex due to the particular structure brought by vegetation as discussed in chapter 2. Several studies have been reported in such environments with the aim of evaluating the propagation characteristics and proposing simple path loss and clustering models. Inspite this environment is prone to strong diffuse scattering, the investigation of the propagation mechanisms under the DMC scope has not been addressed in the literature. Following the philosophy of chapter 4, the objectives of this chapter are to investigate the DMC contribution to the radio channel in dense vegetation and how it could potentially impact the development of a cluster-based channel model. A deeper understanding of the propagation mechanisms and subsequent modeling is pre-requisite to improve the radio channel communication systems in such scenarios.

In this chapter, the data collected from an extensive measurement campaign in a typical European forest has been analyzed in terms of vegetation excess attenuation. Furthermore, the RiMAX channel parameter estimator was used to obtain estimates of the SMC and DMC parameters from the measurement data. As in the previous chapter, the aforementioned techniques developed in Chapter 3 were applied on the estimated data.

5.2 Measurement campaign

The measurement campaign was performed in one of the numerous forests of Monterfil located near Rennes, France. A top view of the measurement site is showed in Figure 5.1 and consists in a light airplane runway and open fields around

the ∼20000 m^2 (2 ha) forest of interest. The main tree species mostly include beech and oak trees (see Figure 5.2(a)) with a canopy height between 6 and 15 m. Dense fern is also spread out across the forest but was not fully grown when the measurement took place. A polarimetric MIMO radio channel sounding was performed at 1.35 GHz with a 80 MHz bandwidth using the MIMOSA radio channel sounder introduced in section 2.4.2. Several Tx-Rx configurations were considered during the measurement campaign as shown in Figure 5.1. The Tx was placed at two different positions, deep in the forest (Tx1) and on a side way (Tx2). Tx1 was set at -3 m high with respect to the plateau where the receiver was moved whereas Tx2 was set 5 m higher than Tx1 due to the ground height change. The receiver was moved using a crane (Figure 5.2(b)) along Rx1 and Rx2 for a total distance of 43 m and 41 m, respectively. The crane was moving at ∼0.5 m/s with the receiver placed in its platform and a snapshot was recorded every 0.5 s. It is recalled that a snapshot is measured under 250 μs with MIMOSA. The number of snapshots measured for each configuration was between 180 to 261. Three heights have been considered in this work: H1=3.5 m, H2=6.4 m, and H3=19.5 m, respectively. Figure 5.2(a) and Figure 5.2(c) present the front and back view of the emitting and receiving antenna array, respectively. The 8-elements patch antenna array was rotated 45° to emit and measure H and V polarization fields as explained in section 2.10.

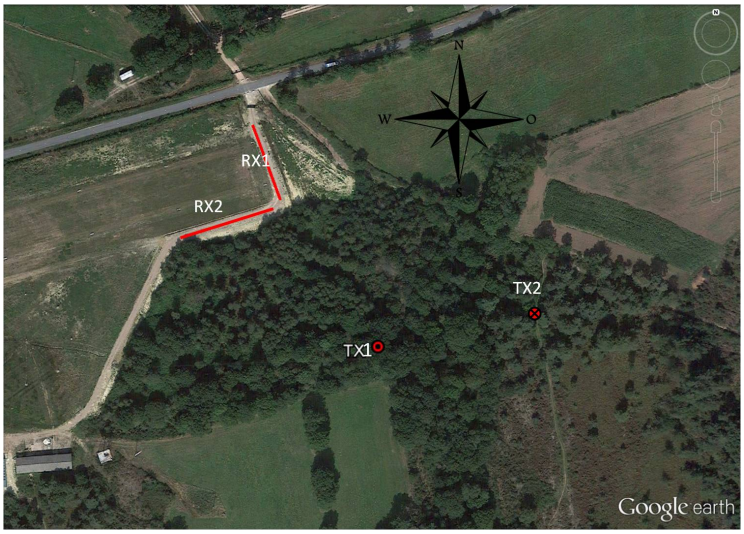

Figure 5.1: Measurement location of Monterfil.

5.3 Vegetation excess loss

In this section, a preliminary analysis of the excess attenuation due to the vegetation is presented. Due to the selected scenarios, the Tx1-Rx2 and Tx2-Rx2 were used to evaluate the excess attenuation. Indeed, the forest depth variation is very

(a)

(b)

(c)

Figure 5.2: Transmission and reception views: (a) Tx1, (b) side-view of the crane with Rx at H3 = 19.5 m, (c) View from the crane platform at H3 = 19.5 m.

small for Tx1-Rx1 and for Tx2-Rx1. The Tx1-Rx2 and Tx2-Rx2 distance was between 97 m to 140 m and 151 m to 190 m, respectively. Figure 5.3 presents the measured vegetation excess loss as a function of distance for Tx1-Rx2 and Tx2-Rx2 at different antenna height with respect to the HH and VV co-polarization states. The excess attenuation due to the vegetation is computed by removing the attenuation in free space loss model as suggested in the literature. It can be noticed that the slope of excess loss due to vegetation is dependent to the Rx antenna height. For instance, the excess attenuation slope (in dB/m) decreases as Rx is elevated from H1 to H3. Furthermore, it is observed that the foliage excess loss for H3 is no longer suitable for the application of vegetation exponentially decaying models (1.11). More importantly, it seems less sensitive to the Tx-Rx distance. This can be explained by the fact that Rx is higher than the forest canopy at this height such that diffraction effects off the canopy becomes the main propagation effect. Therefore, the contribution of the vegetation excess loss is weak in the considered Tx-Rx distance.

In the literature, several vegetation or excess loss (or foliage excess attenuation) models have been proposed to predict the path loss introduced by vegetation. A summary on most used path loss models was presented in section 1.6. Here, the vegetation excess loss derived from our measurement campaign is compared with the ITU-R and Weissberger vegetation excess loss models which fit in our scenario parameters in terms of frequency and distance. In addition, the obtained excess loss has been fitted by the conventional exponential decaying (ED) model (1.11). All these models are also shown in Figure 5.3. The Table 5.1 provides the fitted c parameter which characterizes the decaying rate of the vegetation excess loss for the ED model. Since a single operating frequency was used in our measurement campaign, only c can be estimated. It can be seen that the c values are generally comparable to the ITU-R and Weissberger model parameters (Table 1.6).

Table 5.1: Estimated parameter c for exponential decaying (ED) model

c	HH		VV	
	Tx1	Tx2	Tx1	Tx2
H1	0.56	1.47	0.81	1.51
H2	0.12	0.73	0.30	0.70

Then, the goodness of fit was computed by the root-mean-squared error (RMSE) values computed between the path gain deduced from the models and measurements (in dB) for each polarization link and antenna height. Table 5.2 demonstrates that the best fitting is provided by the direct application of (1.11) which confirms the generic of exponential decaying model under vegetation scenario. However, due to the empirical nature of this model, less physical explanation can be discussed from these models.

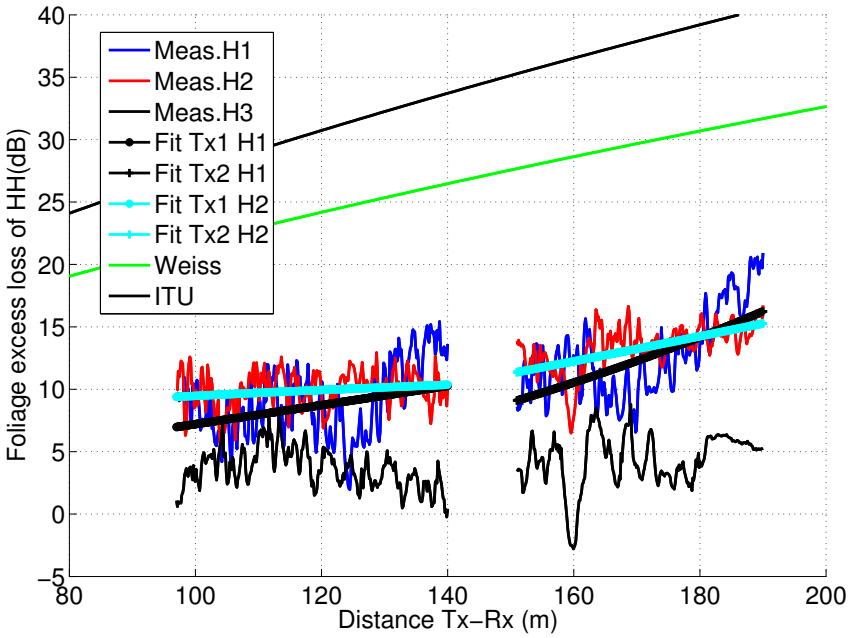

(a)

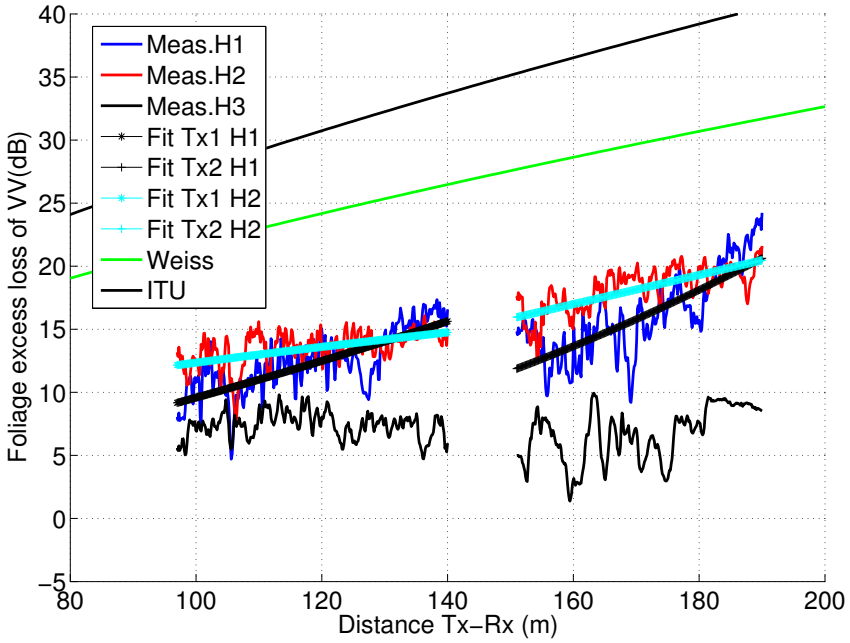

(b)

Figure 5.3: Foliage excess attenuation as a function of distance for co-polarized links (a) HH , and (b) VV computed from the Tx1-Rx2 and Tx2-Rx2 configurations.

Table 5.2: RMSE (dB) of foliage attenuation models.

		HH		VV	
Model type	H_{ant}	Tx1	Tx2	Tx1	Tx2
Exp.Decay	H1	1.14	1.17	1.52	1.98
	H2	1.43	1.49	2.63	2.44
Weissberger	H1	10.51	11.52	11.66	13.78
	H2	14.09	16.38	15.13	17.19
ITU-R	H1	16.99	19.71	18.11	21.88
	H2	20.58	24.58	21.57	25.33

5.4 Application of the polarimetric distance-dependent model

The Tx1-Rx1 configuration was selected as the excess attenuation loss is constant and will not impact the investigated propagation characteristics. On the other hand, the structure of the forest seen by Rx will change as a function of height and Tx-Rx distance. This section aims to investigating the propagation characteristics of the SMC and DMC as a function of these parameters. Similarly to chapter 4, it is proposed here to apply the polarimetric distance-dependent model to the vegetation scenario with the aim of discussing whether it can be extended to outdoor scenarios wherein DMC is observed and room electromagnetics applies. As before, the same parameter estimation techniques were applied to derive the necessary parameters for the model. However, since Tx was surrounded by dense vegetation, it follows that the DOD parameters are widely spread out and strongly correlated with the DMC reducing the capacity of the estimator to converge and correctly assess the DOA parameters. Hence, a SIMO version of RiMAX was used to estimate the polarimetric radio channel parameters such as the TOA and DOA in azimuth and elevation.

5.4.1 Discussion on Application scope of Polarimetric Distance Dependent Model

Based on the observation of the data in the previous section 5.3, it is suggested that the contribution of the primary SMC, secondary SMC, and DMC may strongly depend on the Rx antenna height. Hence, the contribution of these components to the radio channel are investigated for the different antenna height.

Figure 5.4 presents the ECDF of the estimated contribution of the primary SMC, secondary SMC, and DMC with respect to each polarimetric link. In addition, Table 5.3 presents the mean and standard deviation values as a function of height and polarization link. The distance information is evidently hidden but the ECDFs provide a general view of the respective contribution of the main propagation com-

ponents. First, it can be seen in this set of Figures that the contribution of the primary and secondary SMC depend on the Rx height. For H1, Figure 5.4 indicates that the primary SMC for HH (a) and HV (b) is the largest contributing component to the total received power whereas it is the secondary component for VV (c) and VH (d). This is attributed to the fact the V-polarized waves are strongly depolarized by the trunks. The contribution of the primary for HH and HV decrease as the Rx height is increased whereas the secondary SMC contribution increases. The VV and VH primary SMC have about the same contribution for H2 and H3 but the secondary SMC is the strongest component for those heights. This could be due to the tree canopy which introduces a higher-degree of waves interaction and depolarization and also obstructs the LOS. Finally, it is observed that the DMC is relatively constant for HH, HV, and VH and more spread out for VV at which its contribution is the lowest.

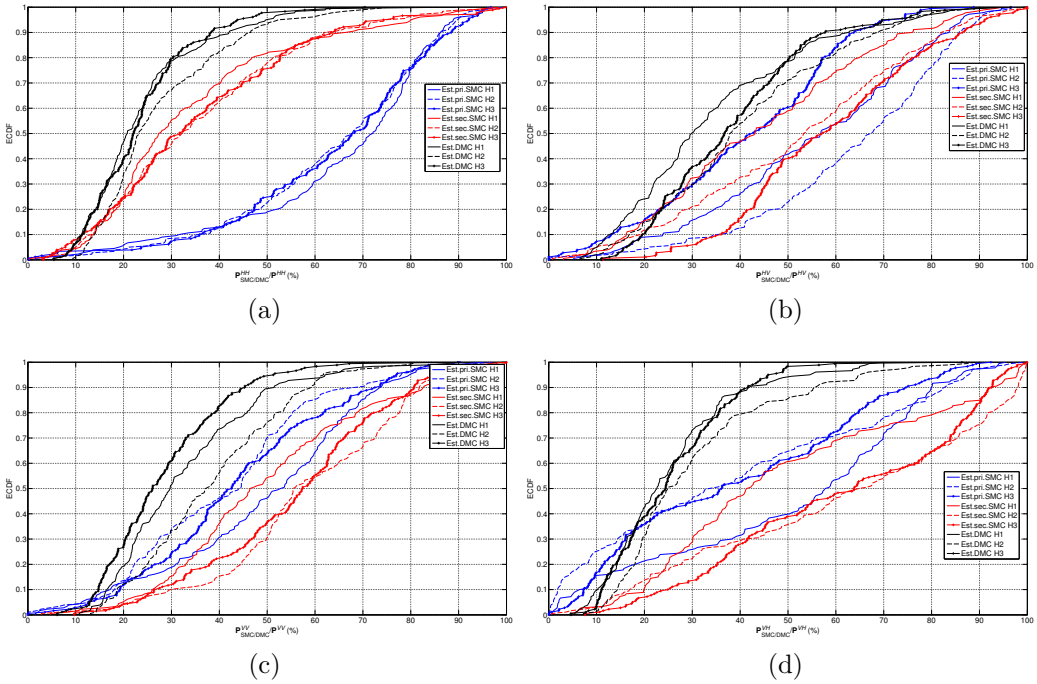

Figure 5.4: ECDF of the estimated contribution of the primary SMC, secondary SMC, and DMC (in %) to the total path gain as a function of height H1, H2 and H3 for (a) HH, (b) HV, (c) VV, and (d) VH.

The ECDF of the polarimetric reverberation time $\mathbf{T}_{rev}^{XY}$ computed from the estimated DMC is shown in Figure 5.5 for the three studied heights and the corresponding averaged and standard deviation values are summarized in Table 5.4. Similar mean values are obtained for HH, HV, and VH for all antenna heights. However, VV is found to be more dependent to the Rx height. There results are also in agreement with the DMC contribution to the radio channel for this link. It is also shown that the ECDF for VV and VH almost coincide at H3. In other words,

Table 5.3: Mean and standard deviation values (%) as a function of height and polarization link from Figure 5.4.

			HH	HV	VH	VV
H1	pri	mean	65.3	55.0	50.4	49.2
		std	21.6	22.3	27.4	21.0
	sec	mean	34.1	44.3	49.0	50.2
		std	21.1	22.3	27.3	21.0
	dmc	mean	23.9	34.6	25.1	32.8
		std	12.8	19.4	13.5	15.1
H2	pri	mean	63.8	63.3	38.6	41.1
		std	20.9	20.9	30.0	19.8
	sec	mean	35.9	52.0	60.8	58.2
		std	20.5	24.0	30.2	20.0
	dmc	mean	27.7	40.9	30.4	38.4
		std	13.5	19.0	16.8	15.0
H3	pri	mean	63.8	41.1	38.8	43.9
		std	21.5	19.6	26.1	19.5
	sec	mean	35.7	58.4	60.6	55.5
		std	21.1	19.7	26.2	19.5
	dmc	mean	23.6	38.4	25.3	28.3
		std	11.2	16.5	12.3	12.9

this indicates again that the DMC created by the vegetation medium at this height under a V-polarized transmitted wave displays the same characteristics for V than for H received waves. Moreover, it also suggests that since room electromagnetic theory is validated, therefore, the polarimetric distance-dependent model could be potentially used for this special case.

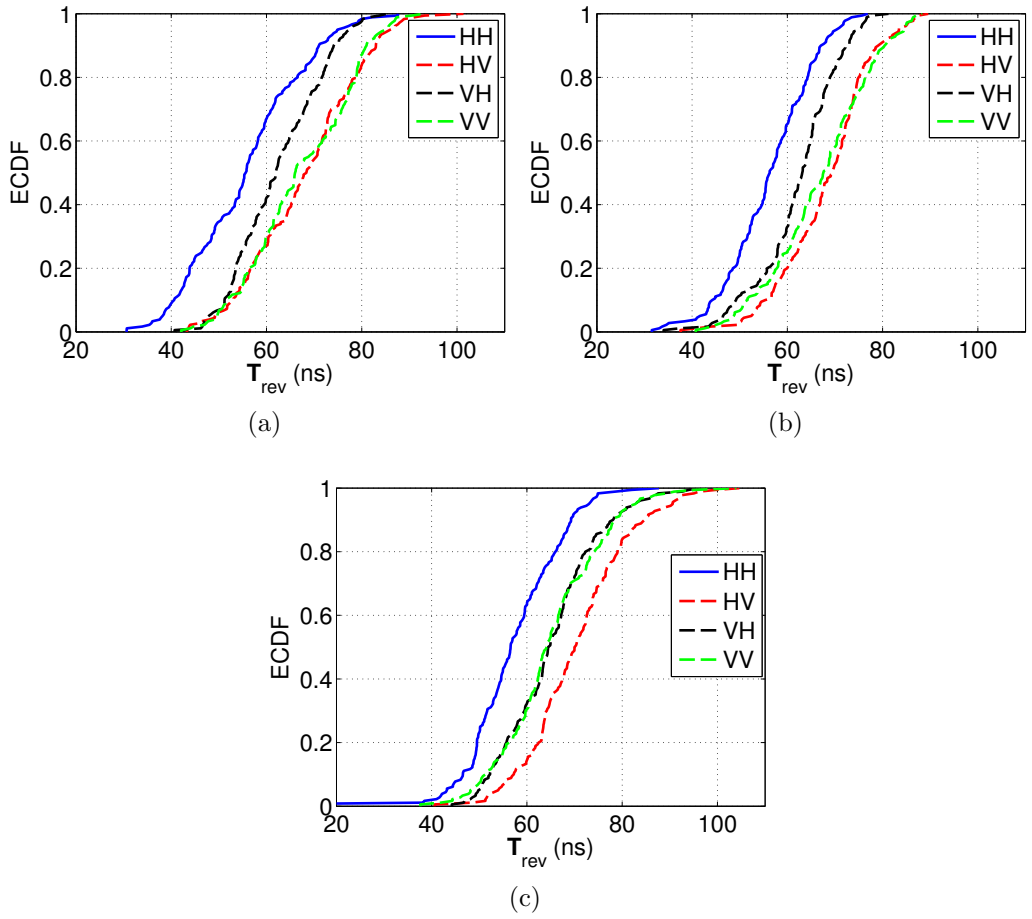

Figure 5.5: ECDF of the Estimated polarimetric reverberation time $\mathbf{T}_{rev}^{XY}$ for (a) H1, (b) H2, and (c) H3.

5.4.2 Estimated path gain model parameters

Based on the previous discussion, we will focus in this section on the application of our model for the Tx1-Rx1 configurationon at height H3. First, the methodology used to compute the model parameters described in (4.8)-(4.21) was applied for this scenario. Figure 5.6 presents the ECDF of the estimated polarization coefficients χ^H and χ^V for the primary SMC, secondary SMC, and DMC. The data show that χ^H is rather spread out across all mechanisms in contrast to χ^V. It is noticed that primary/secondary SMC and DMC present a larger depolarization rate for

Table 5.4: $\mathbf{T}_{rev}^{XY}$ averaged and standard deviation values (in ns) as a function of height.

		Mean value	Std
H1	HH	55.76	11.78
	HV	68.00	11.52
	VH	62.49	9.12
	VV	67.39	11.26
H2	HH	56.26	8.91
	HV	68.18	9.42
	VH	62.25	8.38
	VV	67.00	10.57
H3	HH	57.38	9.92
	HV	70.66	10.70
	VH	65.11	9.96
	VV	65.09	10.68

VV compared to HH. Again, this is explained by the fact that forests strongly depolarize V waves. Also, the polarization coefficients present a dependence to the distance and the variation varies upon the considered mechanism. This effect was not observed at this scale in the indoor scenario investigated in chapter 4. Hence, in order to apply the model and estimate the other parameters, only the mean values were taken.

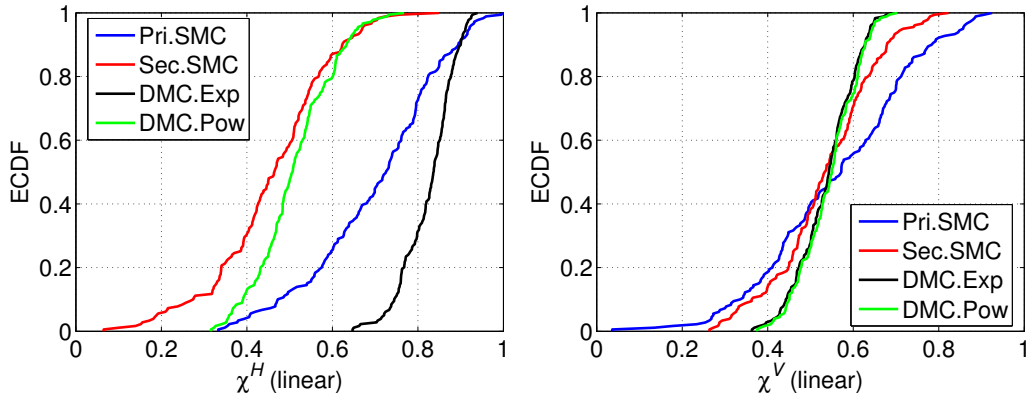

(a) (b)

Figure 5.6: Primary/secondary SMC and DMC polarization coefficients at H3: (a) χ^H, (b) χ^V.

Table 5.5 presents the estimated parameters for the proposed model. The reference gains were computed from the data at reference distance $d_0 = 100m$ for the SMC and DMC with the reference model (power law), meanwhile $d_0 = 100m$ for

SMC and $d_0 = 120m$ for the DMC with proposed model (exponential law).

Table 5.5: Estimated model parameters for Tx1-Rx1 at H3.

		SMC		DMC	
Param.	Polar.link	Primary	Secondary	Exp.law	Power law
n^{XY}	HH	5.43	4.62	X	5.26
	HV	6.53	5.83	X	5.85
	VH	8.23	3.84	X	4.18
	VV	7.89	5.04	X	5.47
$\mathbf{G}_0^{XY}(dB)$	HH	-40.64	-40.20	55.39	-44.76
	VV	-42.47	-40.40	49.97	-45.04
χ^{XY}	HH	0.70	0.45	0.82	0.51
	VV	0.56	0.55	0.54	0.58
$\mathbf{T}^{XY}(ns)$	HH	X	X	57.38	X
	HV	X	X	70.66	X
	VH	X	X	65.11	X
	VV	X	X	65.09	X

5.4.3 Validation of the model

5.4.4 Polarimetric path gain

The performance of the proposed polarimetric path loss model is compared with the reference model (DMC Power law) with the same manner than that is described in the previous chapter. In Figure 5.7, the estimated and modeled path gains for each propagation mechanism and polarization links are compared. Overall, the models do not follow well the rapid fluctuations of the path gains introduced by the environment with distance but grasp correctly, on average, the behavior of each propagation mechanism.

The distance-dependent total path gain of the estimated and modeled data are presented in Figure 5.8. The path gain models were built with the parameters listed in Table 5.5. It is found that the results show a good agreement between the model and data estimated from the measurements. The goodness of fit for the estimated model is confirmed by the small RMSE values computed between the measured path gains and estimated models and which are presented in Table 5.6. Finally, the difference between the exponential and power law for DMC is found to be not significant. In comparison with the indoor scenario investigated in the previous chapter (Table 4.3), only a 1 dB difference in the RMSE values is observed.

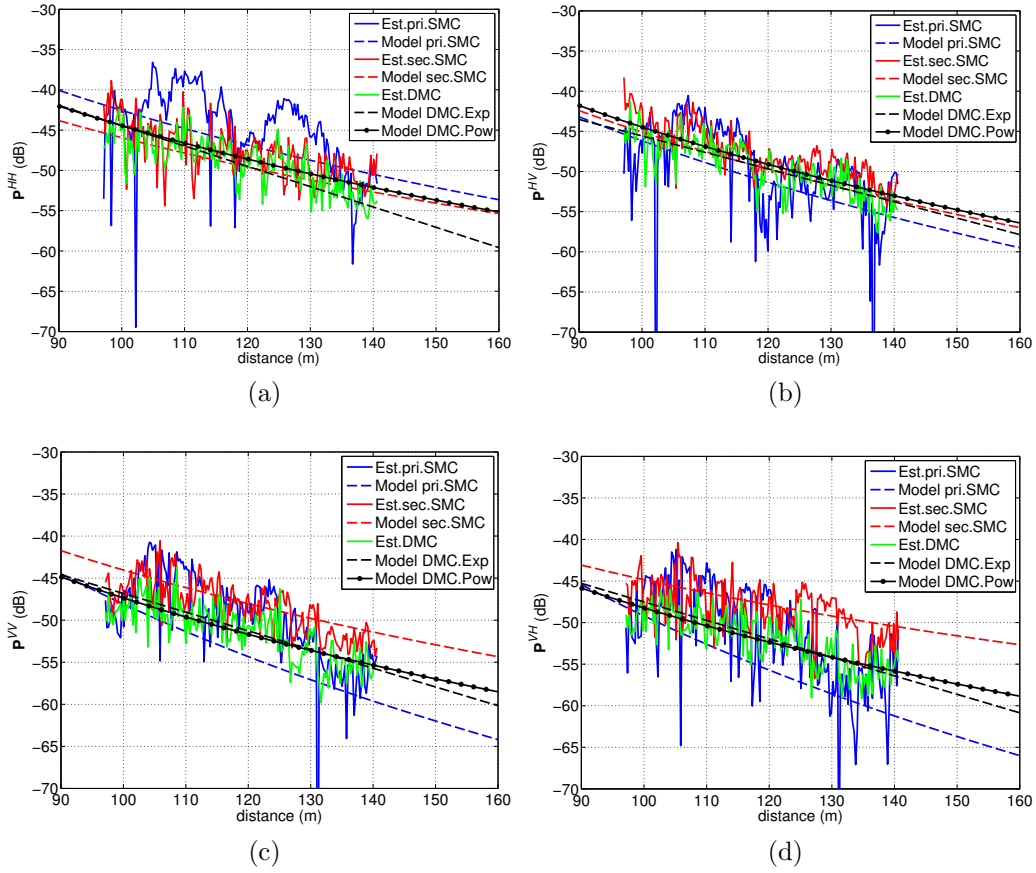

Figure 5.7: Estimated and modeled primary/secondary and DMC path gain as a function of distance for polarimetric links at H3: (a) HH, (b) HV, (c) VV, (d) VH.

Table 5.6: RMSE (dB) of Path Gains at H3

				$\mathbf{P}^{XY}_{DMC}$		$\mathbf{P}^{XY}$	
		$\mathbf{P}^{XY}_{pri}$	$\mathbf{P}^{XY}_{sec}$	Exp.model	Power law	Exp.law	Power law
H3	HH	4.59	2.39	2.45	2.55	2.15	2.21
	HV	5.99	1.75	2.37	2.43	2.14	1.71
	VH	4.77	3.01	2.05	2.35	1.99	2.11
	VV	4.55	2.60	2.10	2.10	2.34	2.43

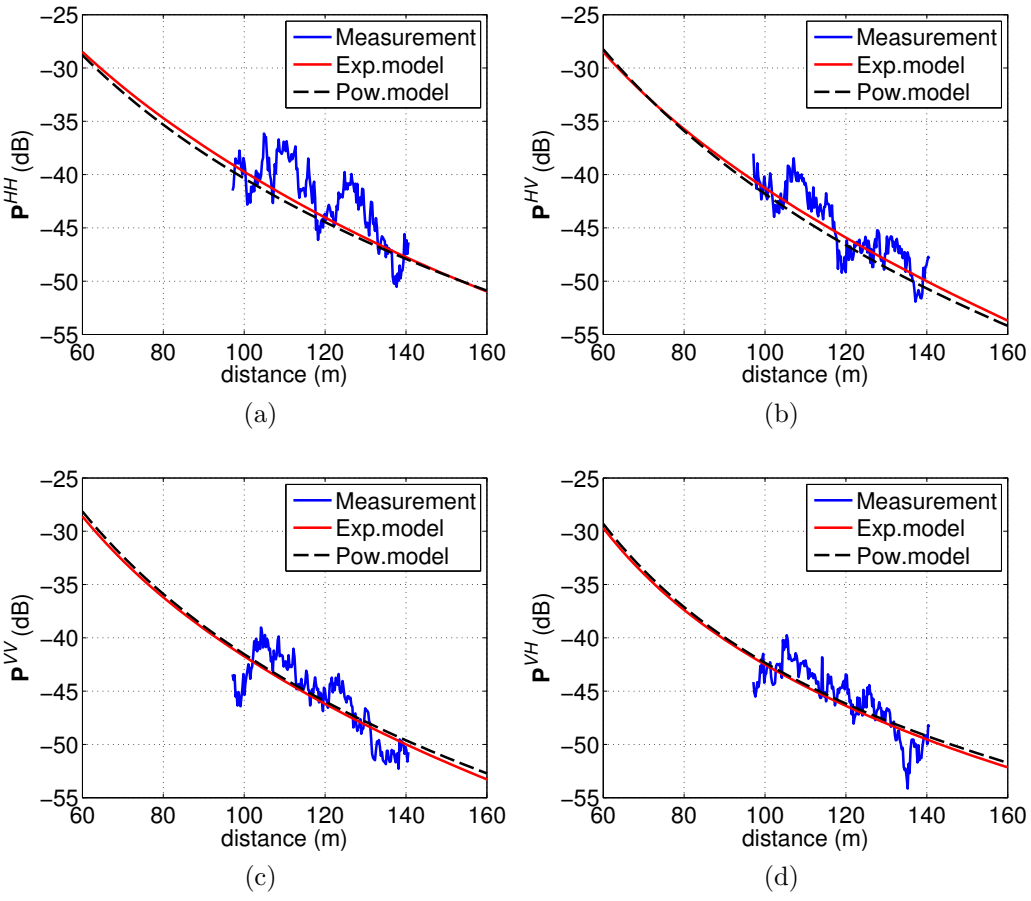

Figure 5.8: Estimated and modeled total path gain as a function of distance for polarimetric links at H3: (a) HH, (b) HV, (c) VV, (d) VH.

5.4.5 Polarimetric Reverberation Ratio

In addition to the path gains, Figure 5.9 presents the estimated polarimetric reverberation ratios computed from the model using the exponential model and reference model (power law model). All models predict a maximum reverberation value but a monotonic change for HH and HV is obtained with the reference model for the investigated distance range. A good agreement is observed between the proposed model with exponential law and the measured reverberation ratio. The maximum reverberation distance predicted by the exponential model is 90 m for HH, 126 m for HV and 128 m for VV, 104 m for VH, respectively. The results suggest that the reverberation ratio fits and measurements are rather different across polarization links for a vegetation scenario with values ranging between 10% and 95%. Furthermore, the reverberation ratio is strongly dependent to the distance which highlights the high complexity of the propagation mechanisms. Even though the validity of the proposed approach to model the different radio channel components is demonstrated, it is only for a limited distance range. Hence, further studies must be performed with a longer Tx-Rx distance.

5.5 Application of ACId-MCD

In this section, clustering analysis is performed on the Tx1-Rx1 measurement data using the ACId-MCD clustering technique developed in chapter 3. Since a SIMO version of RiMAX was used to estimate the polarimetric radio channel parameters, the SMC are only described by γ_{XH}, γ_{XV}, τ, ϑ_R and φ_R. X is the polarization at the transmitter side (H or V). Hence, it should be noted that the estimated SMC parameters may not be identical for H and V due to the SIMO estimation model as they are not jointly estimated any more. The two estimation methods introduced in section 4.6 were also adopted to assess the contribution of DMC to the clustering results.

The average number of SMC estimated with method 1 is ∼25 and ∼70 for method 2 after applying a 20 dB power threshold. In comparison, it is recalled that 50 and 300 SMC were estimated for the industrial radio channel under the same estimation conditions but this large difference is expected since outdoor scenarios are open propagation environments. Since DOD angles could not be estimated, it was removed from the MCD metric. This was done by setting the SMC parameters $\vartheta_T = 0°$ and $\varphi_T = 90°$. The MCD searching range was set from 0.07 to 0.8 for all considered clustering data and Rx heights.

Table B presents the computed channel parameters as well as the cluster parameters similarly to Table A.1. Delay spreads ranging between 29 ns and 44 ns were computed; values which are slightly larger to those reported in [99] for a vegetation depth varying between 0 to 50 m. DOA azimuth spread mean values varying between 37° and 44° for method 1 and from 69° to 75° for method 2 were obtained. These values are found to be larger compared to values reported in the literature. In

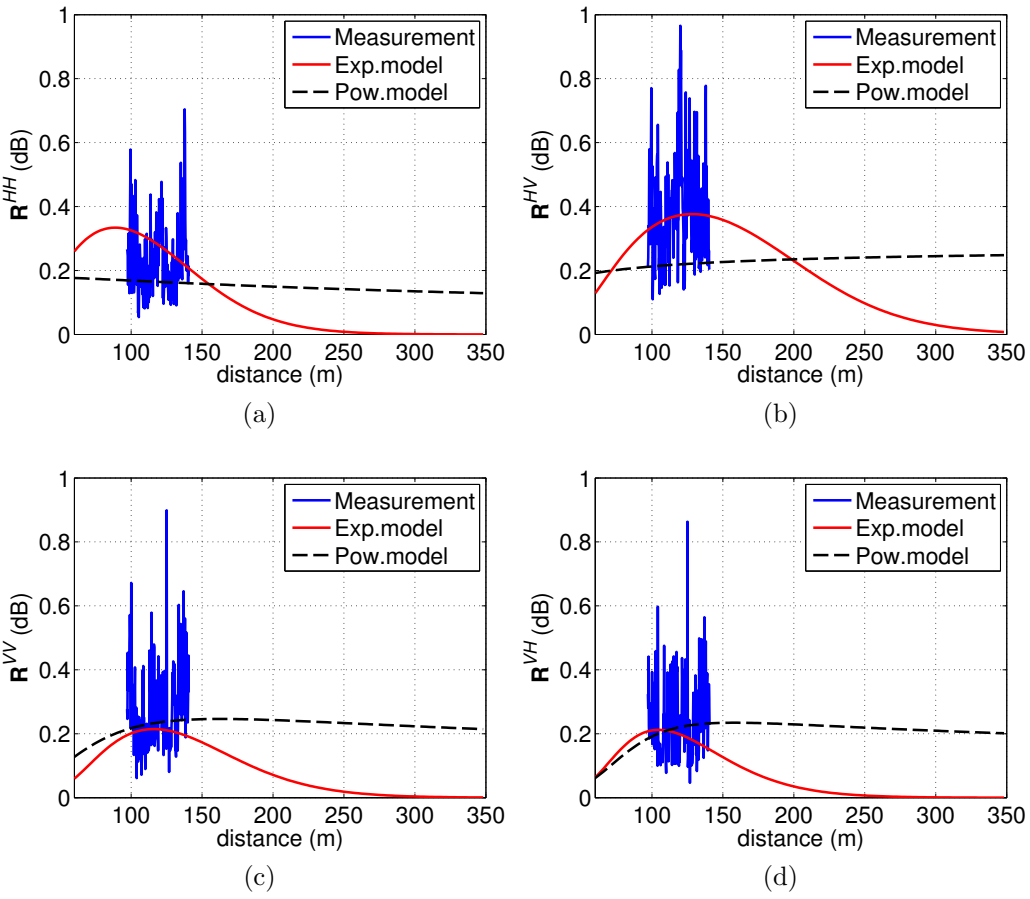

Figure 5.9: $\mathbf{R}^{XY}$ as a function of distance at H3 for polarimetric links: (a) HH, (b) HV, (c) VV, and (d) VH.

addition, the DOA elevation spread mean value is found to vary between 19° to 48° for method 1. The results indicate a weak dependence of the azimuth and elevation spreads to the Rx height as reported in [96].

5.5.1 Preliminary analysis

Figure 5.10 presents the ECDF of the number of clusters estimated from both method 1 and method 2 for all considered Rx heights. The number of estimated clusters follow the same distribution for all Rx heights and polarization links although the number of clusters is larger for method 2 than 1. The method 2 ECDFs are less spread out than the ones obtained from method 2. For method 1, 20% of positions are described by 2 clusters and 40% for method 2. This result indicates that the structure of the clusterlike radio channel model can be greatly simplified for certain Tx-Rx distance values. This also shows that the power arrives at the receiver side from specific directions dictated by the environment geometry and more specifically the trunks.

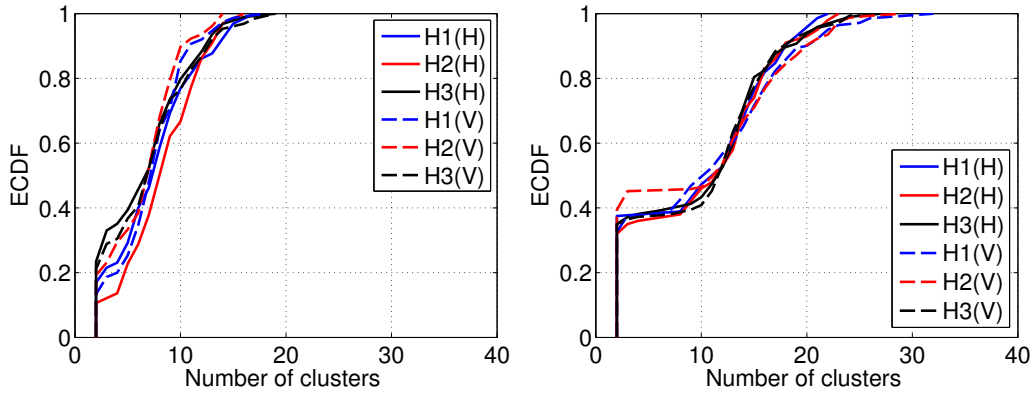

Figure 5.10: ECDF of the number of estimated clusters with: (a) method 1, and (b) method 2.

Figure 5.11 presents the averaged number of SMC per cluster. The data from method 1 (Figure 5.11(a)) show that 60 to 80% of the measurement positions have a small number of SMC per cluster. The average number of SMC varies from 2 to 35. More importantly, it appears the number of SMC per cluster vary as a function of Rx height and is the largest for H3. This could be due to the diffusion mechanisms provided by the forest canopy. For the method 2, (Figure 5.11(b)), the clustering characteristics seem to be less effected by the Rx height. Overall, the averaged number of SMC per cluster is generally larger than for method 1. This could be explained by the presence of higher-order SMC in the method 2 data.

MCD_T is presented in Figure 5.12 for method 1 and 2. It can be noticed that about 50% of the positions display an MCD_T value of 0.07 which is the lower limit of

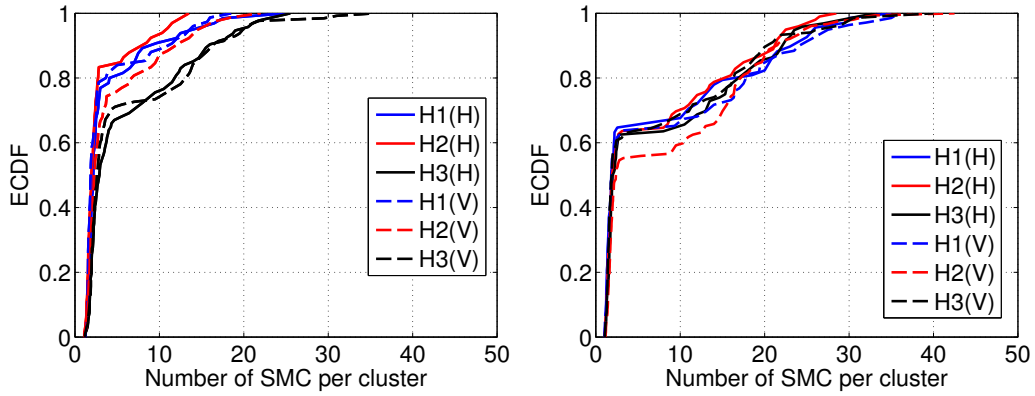

Figure 5.11: ECDF of the averaged number of SMC per cluster with: (a) method 1, and (b) method 2.

the MCD_T searching range. This indicates a high degree of separation between the SMC for these cases. From Figure 5.12(a), it can be observed that the largest MCD_T is obtained for H3 for both polarization states. This observation is consistent with that in Figure 5.11(a). The polarization V is found to provide a larger MCD_T for H2 and H3 but the opposite is obtained for H1. The results in Figure 5.11(b) indicate that 60% of the positions can be described with a low MCD_T whereas the other 40% are described with larger MCD_T values. Again, the values are generally larger than that in method 1 due to the presence of higher-order SMC. As to the polarization aspect, MCD_T seems less affected by the different polarization states at H3, which could be explained as the high level of diffusion due to forest canopy. In summary, the distribution of MCD_T suggests that the clustering characteristics greatly differ whether DMC is included or not. In addition, the dependence with the Rx height suggests that the canopy plays a role to the DMC propagation mechanisms.

5.5.2 Statistical analysis

In this section, a deeper statistical analysis of the clustering characteristics are provided to the reader. The same cluster parameter definition detailed in section 4.6.1 is used, as in chapter 4. The following parameters are calculated for clusters having more than one SMC.

5.5.2.1 RMS time-delay/angular spreads

First, Figure 5.13 shows that the averaged cluster delay spread is nearly constant across all considered Rx heights and polarization links for a given method. Values ranging between 10 and 50 ns are obtained with method 1 and 5 to 60 ns with method 2 but larger values are obtained on average with method 1. This result could be attributed to the presence of stronger secondary SMC under this configuration.

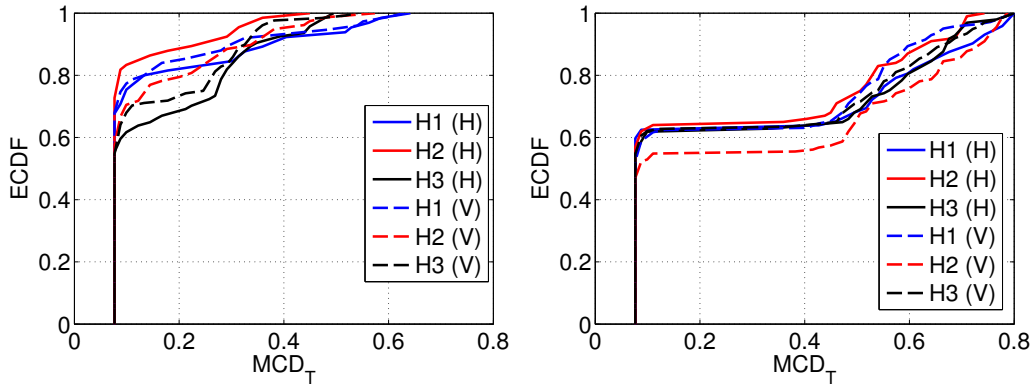

Figure 5.12: ECDF of the estimated MCD_T for (a) method 1, and (b) method 2.

Moreover, it is noted that the cluster delay spread values are much less than those computed for the indoor scenario.

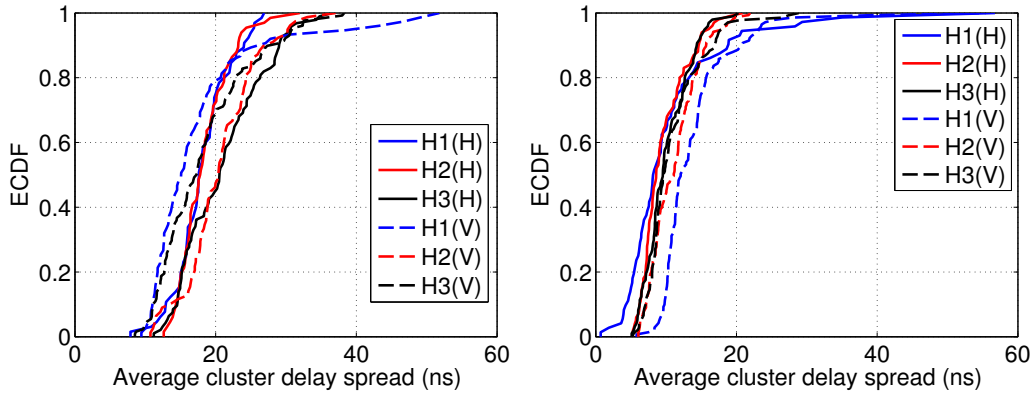

Figure 5.13: ECDF of the averaged cluster delay spread (ns) for (a) method 1, and (b) method 2.

The averaged cluster azimuth spreads of DOA are presented in Figure 5.14 for both methods. The results shows that the values are weakly dependent to the Rx height whether it is for method 1 or 2 and present the same distributions. Nonetheless, it is observed that the V-polarized clusters are slightly larger in size compared to the H ones. Figure 5.14(b) indicates that the spread values are generally larger than that of method 1 resulting in bigger clusters in this dimension. This is probably attributed to the higher-order SMC which are weaker but arrive from larger azimuth angles.

Finally, Figure 5.15 presents the averaged cluster co-elevation spread for method 1 and method 2. In contrast with the azimuth spreads, a clear difference in values

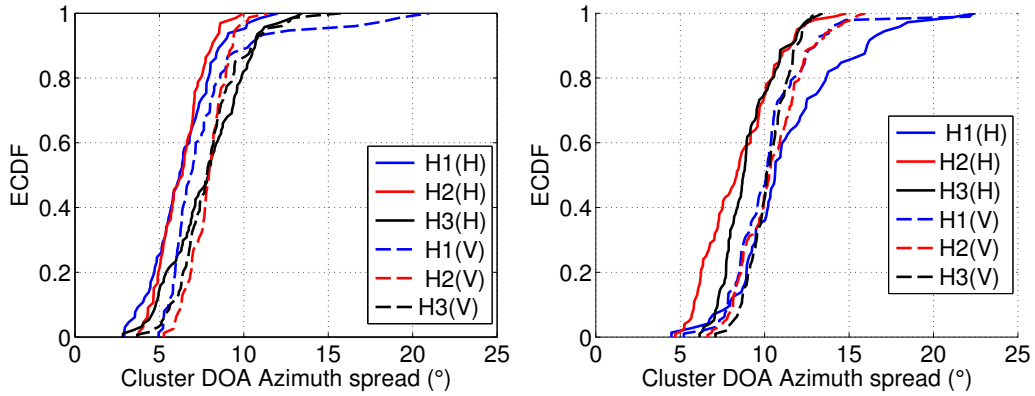

(a) (b)

Figure 5.14: ECDF of the averaged cluster azimuth spread (in °) for (a) method 1, and (b) method 2.

and distributions is observed between Figure 5.15(a) and (b). For instance, the cluster spread values are ranging between a few degrees and 12 degrees for method 1 and between 5 degrees and 30 degrees for method 2. Hence, it appears most of the high-order SMC in method 2 display larger co-elevation angles than the SMC in method 1. In other words, DMC contributes to increase the cluster size in the co-elevation dimension. In addition, the co-elevation spreads do not seem to be dependent to the Rx height as for the delay and azimuth spreads. From that point of view, it could be concluded that the forest acts as an isotropic medium whose characteristics are only dependent on the Tx-Rx distance but not generally on Rx height.

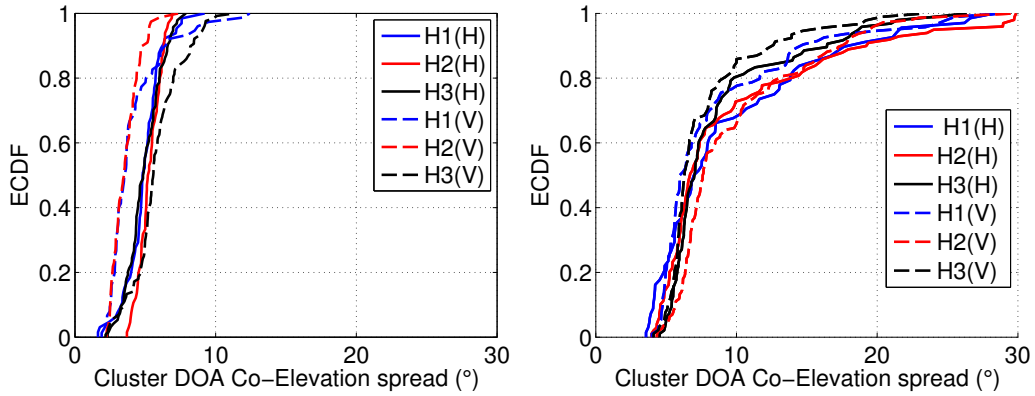

(a) (b)

Figure 5.15: ECDF of the averaged cluster co-elevation spread (in °) for (a) method 1, and (b) method 2.

5.5.2.2 Cluster XPD

The averaged cluster XPD is presented in Figure 5.16 for method 1 and method 2. When DMC is included in the data model (Figure 5.16(a)), the spread values and distributions present a high degree of similarity across all heights and polarizations with a 3 dB median value. Whether it is for H or V, more than 80% of the clusters present a large depolarization (XPD values below 7 dB). Larger XPD values are obtained for method 2 (Figure 5.16(b)) indicating that the clusters are less prone to depolarization effects. In contrast with the method 1 data, the averaged cluster XPD for V also seems to depend on the Rx height clusters.

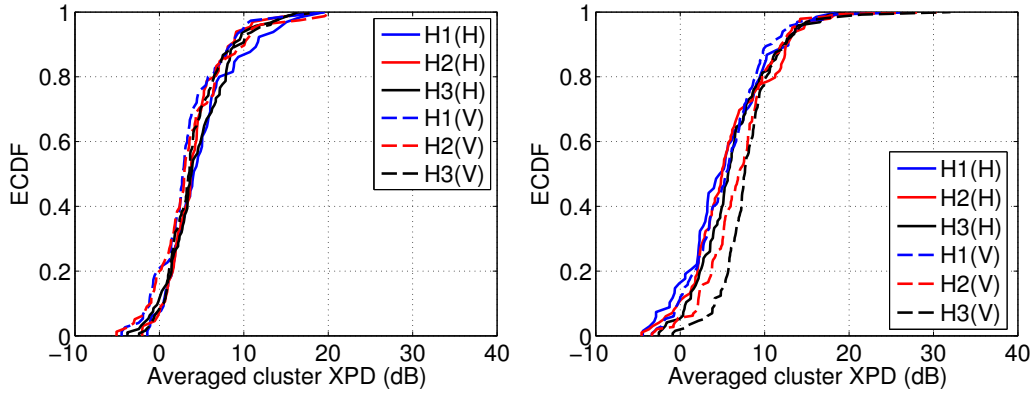

Figure 5.16: ECDF of the averaged cluster XPD for (a) method 1, and (b) method 2.

5.5.3 Intra-cluster parameter distributions

In this section, the characteristics of the intra-cluster parameters and related distributions are investigated with the purpose of establishing building bricks which could then be used for the development of suitable GSCM-type emulation channel models for vegetation scenarios. Without the loss of generality and for the sake of presentation simplicity, the following figures describe the cluster distribution results for a single cluster at H2 with polarization H. The complete list of parameters and distributions for all other heights can be found in Appendix . As previously, the largest log-likelihood value was selected as the criterion to choose among all possible fitting distributions.

Figure 5.17(a) and (b) present the ECDF of the intra-cluster amplitude which can be generally fitted by Lognormal distributions. Lognormal or Weibull distributions are found to be best to model the intra-cluster delay distribution as shown in Figure 5.17(c) and (d).

Finally, the intra-cluster spatial parameter distribution fitting results are presented for DOA in Figure 5.18 where it is shown that the Von Mises distribution

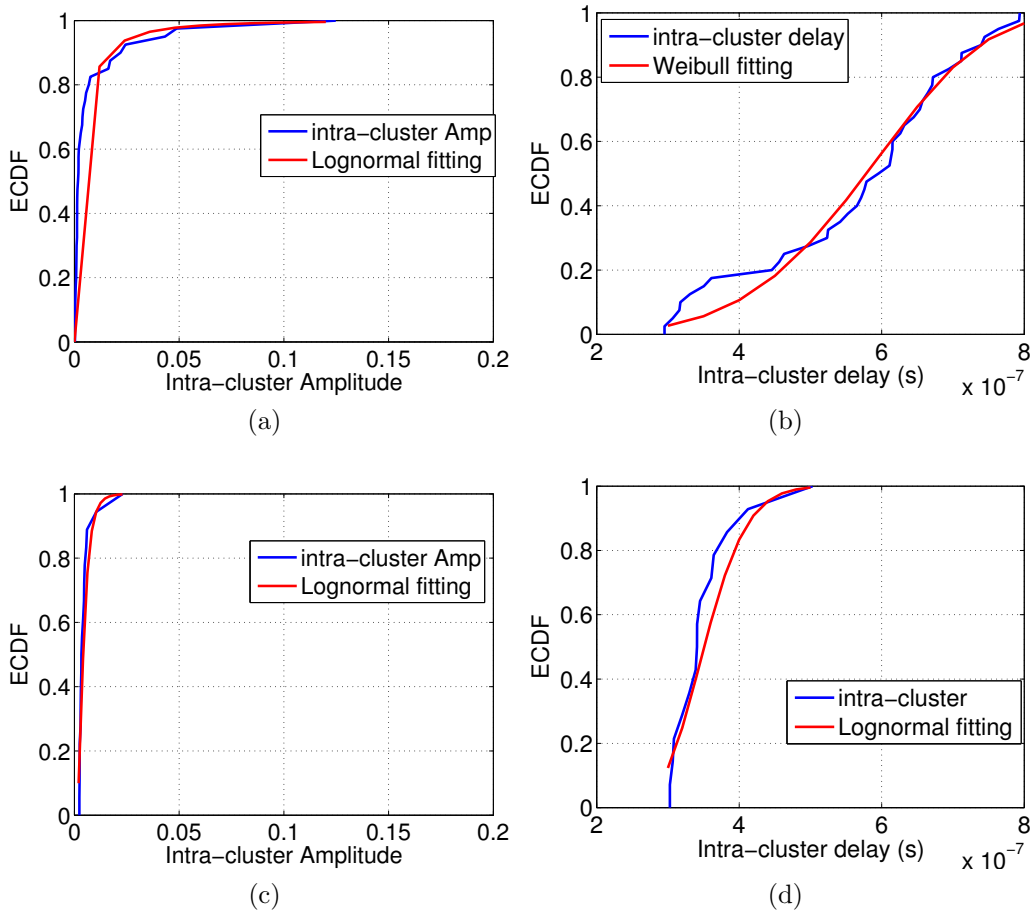

Figure 5.17: ECDF of the intra-cluster amplitude and delay parameters for a single cluster at H2 with polar H and fitting distributions: (a) Amplitude (method 1), (b) delay (method 1), (c) amplitude (method 2), (d) delay (method 2).

is also a good candidate to describe the intra-cluster spatial parameters due to its periodic angular feature.

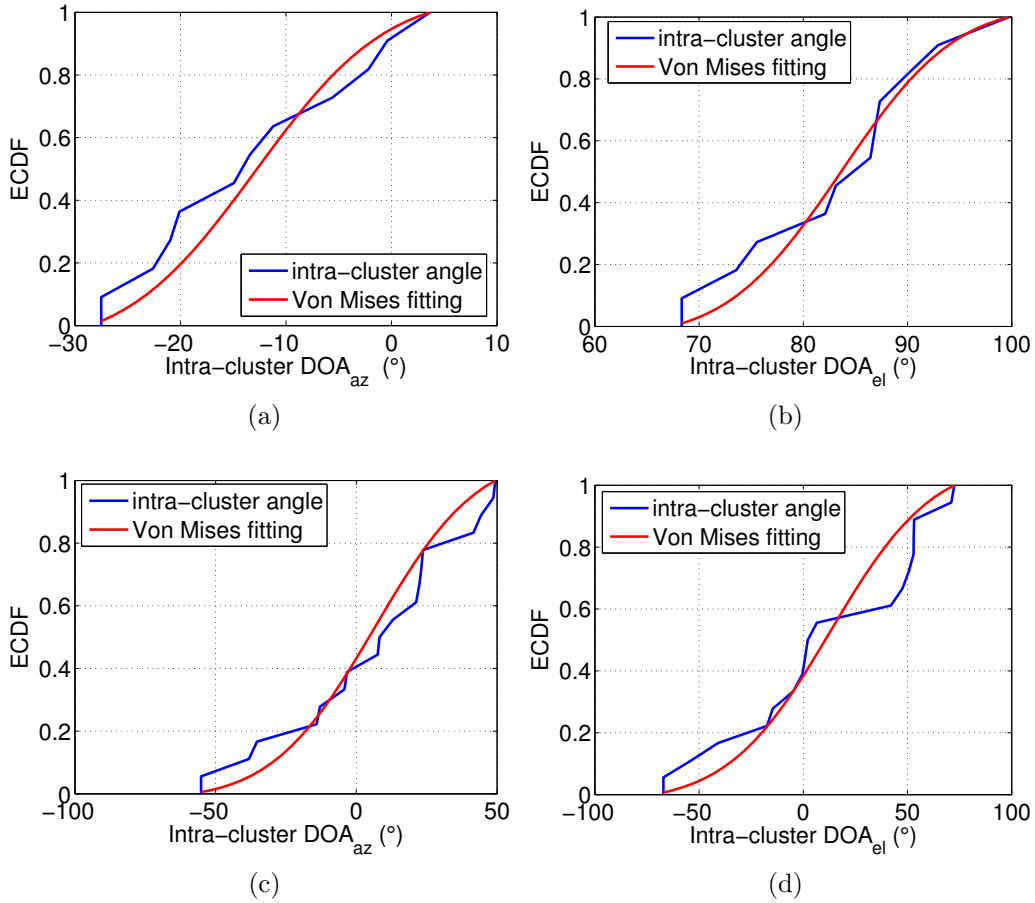

Figure 5.18: ECDF of the intra-cluster DOA parameters for a single cluster at H2 with polar H and fitting distributions: (a) azimuth (method 1), (b) co-elevation (method 1), (c) azimuth (method 2), (d) co-elevation (method 2).

5.6 Conclusion

In this chapter, the contribution of the DMC to the radio channel has been evaluated for an outdoor scenario with dense vegetation under two complementary modeling approaches.

First, a polarimetric MIMO measurement campaign was performed at 1.35 GHz in a European forest environment. Several Tx-Rx configurations and Rx height were considered to evaluate the contribution of the forest structure to the DMC observed in the radio channel. The measured vegetation excess loss was fitted using conventional exponential decaying models and compared with the ITU-R and Weissberger

foliage path loss models. It was concluded that the ED model is not suitable for the highest Rx height H3 since the antenna array is above the forest canopy. On the other hand, the polarimetric distance-dependent model was considered for the H3 measurement data to extend its potential application scope. The measured MIMO channels have been processed by RiMAX to separate the polarimetric primary SMC, secondary SMC and DMC from which the parameters of the path gain model were constructed. It has been demonstrated that the proposed model can generally predict well the measured polarimetric path gain with respect to distance with low RMSE values.

Furthermore, the clustering features of the radio channel have been investigated with the ACId-MCD clustering algorithm for the investigated Tx-Rx distance and receiving antenna heights. The measured MIMO channels were processed by RiMAX with a SIMO data model to estimate the SMC parameters used for clustering. The cluster analysis results have been extensively presented in terms of the clusters and intra-cluster statistics as a function of polarization and Rx height to study the effect of the forest structure to the propagation mechanisms and subsequent clustering characteristics. The same conclusion than in chapter4 is reached. Overall, it can be concluded that DMC has a strong impact on the large-scale clustering parameters (cluster size, XPD, etc.) but not on the intra-cluster distributions.

From the application of the PDP, path gain models and clustering analysis tool, it can be concluded that the polarimetric propagation mechanisms and clustering characteristics strongly depend on the physical interaction between the propagation mechanisms and the forest structure. In particular, the effect of the canopy has been highlighted from the path gain model. Clearly, assuming DMC in the radio channel greatly impacts the clustering spreads and distributions in all dimensions more than the Tx-Rx distance and Rx height. It is also highlighted that these results are inline with those obtained for the industrial scenario.

General conclusion and perspectives

The main objectives of thesis dealt with the characterization and modeling of indoor and outdoor wireless radio channels in the presence of diffuse scattering or Dense Multipath Components (DMC). Due to the natural presence of rich metallic scatterers and forest tree structure, the industrial and vegetation environments have been investigated, respectively.

A review of the radio channel models such as path loss or clustering-based models for these specific scenarios was presented. Generally, these models are not only scarce but also completely undermine the contribution of DMC. The propagation conditions are very complex and this might be a reason why these scenarios were not deeply explored in the literature. Thus, the level of understanding of the propagation mechanisms is rather low or not sufficient and must to be redefined when DMC is included in the data model.

The contributions of this thesis are multifold with strong implications on both the experimental and theoretical levels. Results presented in this thesis rely on the experimental measurement of polarimetric multidimensional radio channels in harsh scenarios and subsequent processing with highly-advanced parameter estimation algorithms in order to obtain specular multipath components (MPC) and DMC estimates. The measurements were performed with a virtual and MIMOSA radio channel sounder operating around $\sim$1.3 GHz which were built in TELICE. This frequency was chosen to describe the physical propagation phenomena for the mobile and WiFi standards without emitting in the licensed bands. The main characteristics such as the delay spread or depolarization effects were observed to be in agreement with the values reported in the literature for equivalent scenarios. The underlying radio channel data model was specifically developed under the framework of DMC to investigate the contribution of this component to the radio channel properties as a joint deterministic and stochastic maximum-likelihood (ML) problem. Another strong contribution of this work includes the development of novel path gain and automatic clustering methods to analyze the radio channel propagation characteristics of the considered scenarios. These techniques have been validated with either experimentally measured or simulated radio channels. It must be emphasized that some of the results presented in this work have been published in the literature.

1) Polarimetric distance-dependent path gain model

The first contribution is the development of a flexible polarimetric distance-dependent path gain model for indoor scenarios. This model is built on the consideration of room electromagnetics to predict the DMC path gain. The model was validated from SMC and DMC path gains estimated from measurements of the two investigated scenarios. However, the introduction of DMC was demonstrated to open a new depth of understanding and a direct connection between the propagation mechanisms and reverberation effects were highlighted. In addition, the proposed model has the potential to highlight the various depolarization mechanisms for each component (primary/secondary SMC and DMC). Furthermore, a low complexity parameter fitting approach was derived from the model and applied to the measurement data. This approach allows estimating the contribution of SMC and DMC in indoor scenarios without using high resolution parameter estimation techniques.

2) ACId-MCD clustering tool

The development of an automatic clustering identification algorithm has been proposed and is the second contribution of this work. The algorithm named ACId-MCD allows to sort and group the SMC into clusters from measured or simulated radio channels. It relies on the multipath component distance (MCD) as a mean to preset the cluster maximum size. The validation of this algorithm has been assessed with a dedicated evaluation protocol including clustering validity indices (CVI) and radio channels simulated with the clusterlike WINNER II GSCM. Its performance has been evaluated by comparing with the classical K-means clustering technique and robustness studied via Monte-Carlo simulations. The proposed clustering algorithm is found to be highly versatile and can potentially be applied to any radio propagation scenarios where clusterlikes features are observed.

Propagation and clustering characteristics

The polarimetric distance-dependent path gain model was successfully applied to the indoor industrial radio channel. For this scenario, the DMC is demonstrated to be a particularly strong distance-dependent component with reverberation values up to 75%. It is the main source of the depolarization observed in the radio channel and the results clearly demonstrate that this component can not be neglected to describe and understand the radio channel propagation mechanisms. For instance, the difference in H and V polarization is now better understood in terms of DMC. The application range of the model was also extended to the vegetation scenario for a special case wherein room electromagnetics is valid. Similarity on the reverberation time behavior has been noticed between the indoor and vegetation scenarios. However, the reverberation values are smaller than for the indoor scenario with values varying between 15 to 95% but 40% on average across all polarizations. Also, the impact of the forest was investigated by comparing the propagation properties for different receiver (Rx) heights. Rather different propagation and polarization mechanisms have been observed from the model in comparison with the indoor scenario due to the forest trunk/canopy specific structure. The validity of the path gain model with both scenarios suggests the versatility of this model to describe radio

channels when DMC is observed. Finally, the model parameters for each scenario have been provided to the reader. It is noteworthy that the path loss behavior can be well predicted with empirical exponential decay models.

In addition, the ACId-MCD algorithm has been applied to the indoor and outdoor measurement data. The cluster and intra-cluster parameters have been computed with the WINNER II approach and discussed. The contribution of DMC has been evaluated by comparing the cluster characteristics with and without DMC in the estimator data model which is, yet, another originality of the present work. Moreover, the parameter distributions have been studied with the purpose of simulating these scenarios with clusterlike radio features are were found more or less in agreement with the previous studies on this topic. All presented results strongly indicate that DMC has a strong impact on the large-scale clustering parameters (cluster size, XPD, etc.) but not on the intra-cluster distributions. It is finally concluded that some of the cluster size depend on the Rx height due to the trunk and canopy.

In conclusion, a comprehensive and complete framework has been proposed to evaluate the contribution of DMC in scenarios where this component is likely to occur. Several dedicated tools have been successfully developed and validated with extensive experimental measurements. This thesis has clearly highlighted the importance of including DMC into the data model and that all existing radio channel models from simple path loss to more advanced GSCM models must be revisited. The introduction of DMC provides a deeper level of understanding for the propagation properties. From that point of view, it must be acknowledged that current complex models could lead users to reach incorrect interpretations and non-physical propagation effects.

Perspectives

The polarimetric distance-dependent model proposed in this thesis includes three multipaths components which are the primary SMC, secondary SMC and DMC. Furthermore, it was assumed that the secondary SMC follows a power law model like the primary SMC and this was only validated for the investigated LOS (industrial) and OLOS (vegetation) environments. Hence, this hypothesis needs to be confirmed for propagation scenarios wherein the contribution of the secondary SMC to the radio channel is large. Even though this has not been discussed in this work, it was noticed a strong correlation between the DMC peak gain α_1 and primary SMC gain. In addition, a connection between the DMC and secondary SMC was also shown. These interesting aspects of the propagation mechanisms could be studied in future works to develop simpler polarimetric path gain models based on the correlation between the received components. In this thesis, a few selected scenarios and unique frequency band/bandwidth have been investigated. Hence, the proposed model could be applied under other propagation scenarios and frequency parameters in order to find a more-defined application range and limitations.

In addition, the proposed automatic clustering identification technique ACId-

MCD was observed to be a powerful approach for clustering analysis purposes but the computation of the optimal solution still relies on the Cluster Validation Indices (CVIs). The CVIs found in the literature have been designed for general clustering applications and the definition of a cluster may not be in line with this research topic. It follows further research could focus on the development of novel CVI specifically built for radio channel clustering. Also, the cluster size and distribution strongly depends on the propagation scenarios such that CVIs may apply to given scenarios but not to others. Furthermore, the performance of the ACId-MCD could be improved by considering an adaptive MCD_T for each cluster at the expense of computational complexity. Finally, a relationship between MCD_T and the propagation environment has been highlighted. This aspect could be further investigated with the aim of including this cluster parameter into GSCM radio channel models.

Appendix A

INDOOR SCENARIO: EURATECHNOLOGIES, LILLE

Table A.1: Indoor radio channel large-scale and clustering parameters for HH link

Environment type		CITC (13 positions)	
RIMAX estimation model	MIMO	Only SMC	SMC+DMC
Channel Delay spread (DS) $log_{10}([s])$	μ	-7.07	-7.07
	σ	0.11	0.11
Channel DOA azimuth spread $log_{10}([^\circ])$	μ	2.01	2.05
	σ	0.06	0.10
Channel DOA EL spread $log_{10}([^\circ])$	μ	1.45	1.25
	σ	0.11	0.29
Channel DOD AZ spread $log_{10}([^\circ])$	μ	1.92	1.73
	σ	0.09	0.19
Channel DOD EL spread $log_{10}([^\circ])$	μ	1.31	0.98
	σ	0.14	0.21
Channel cross-correlation	DOA_{az} vs DS	-0.31	-0.38
	DOA_{el} vs DS	0.27	-0.16
	DOD_{az} vs DS	0.24	0.17
	DOD_{el} vs DS	-0.53	-0.05
	DOA_{az} vs Distance	0.14	-0.41
	DOA_{el} vs Distance	0.42	0.33
	DOD_{az} vs Distance	0.33	0.46
	DOD_{el} vs Distance	0.06	-0.43
Cluster RMS DS $log_{10}([s])$	μ	-6.98	-7.32
	σ	0.04	0.24
Cluster RMS DOA_{az} $log_{10}([^\circ])$	μ	1.63	1.39
	σ	0.12	0.59
Cluster RMS DOA_{el} $log_{10}([^\circ])$	μ	1.34	0.83
	σ	0.04	0.34
Cluster RMS DOD_{az} $log_{10}([^\circ])$	μ	1.63	0.92
	σ	0.10	0.55
Cluster RMS DOD_{el} $log_{10}([^\circ])$	μ	1.16	0.76
	σ	0.05	0.34
Cluster XPD_H (dB)	μ	9.53	23.61
	σ	2.53	6.41
Cluster XPD_V (dB)	μ	12.07	20.73
	σ	1.93	3.47
Cluster cross-correlation	DOA_{az} vs DS	-0.02	-0.07
	DOA_{el} vs DS	0.48	0.48
	DOD_{az} vs DS	0.10	0.09
	DOD_{el} vs DS	0.45	0.44
	DOA_{az} vs Distance	0.11	0.11
	DOA_{el} vs Distance	0.02	0.22
	DOD_{az} vs Distance	0.23	0.02
	DOD_{el} vs Distance	-0.22	-0.21
MCD_T	μ	0.62	0.17
	σ	0.12	0.19
Intra-cluster distribution	delay	lognormal	lognormal
	Amp	lognormal	lognormal/Weibull
	DOA_{az}	Von Mises	Von Mises
	DOA_{el}	Von Mises	Von Mises
	DOD_{az}	Von Mises	Von Mises
	DOD_{el}	Von Mises	Von Mises
Number of clusters		15.3	21.6
SMC per cluster		26.1	8.3
Cluster average DOA_{az} size (°)		45.5	22.2
Cluster average DOA_{el} size (°)		18.3	7.2
Cluster average DOD_{az} size (°)		45.9	8.0
Cluster average DOD_{el} size (°)		11.3	6.1

Appendix B

OUTDOOR SCENARIO: MONTERFIL FOREST

Table B.1: Outdoor radio channel large-scale and clustering parameters for HH link

Monterfil (140 m - 180 m)		H1(H)	H1(V)	H2 (H)	H2(V)	H3(H)	H3(V)	H1 (H)	H1(V)	H2(H)	H2(V)	H3 (H)	H3(V)
RIMAX estimation model	SIMO	Only SMC						SMC+DMC					
Channel Delay spread (DS) $log_{10}([s])$	μ	-7.53	-7.41	-7.54	-7.35	-7.52	-7.41	-7.53	-7.41	-7.54	-7.35	-7.52	-7.41
	σ	0.37	0.19	0.34	0.18	0.26	0.20	0.37	0.19	0.34	0.18	0.26	0.20
Channel DOA_{az} spread $log_{10}([°])$	μ	1.84	1.87	1.85	1.88	1.85	1.88	1.61	1.62	1.57	1.61	1.59	1.65
	σ	0.14	0.13	0.14	0.10	0.12	0.12	0.28	0.28	0.31	0.34	0.31	0.32
Channel DOA_{el} spread $log_{10}([°])$	μ	1.64	1.70	1.67	1.70	1.63	1.69	1.37	1.45	1.33	1.34	1.28	1.34
	σ	0.15	0.13	0.17	0.12	0.12	0.12	0.33	0.33	0.31	0.34	0.35	0.34
Channel cross-correlation	DOA_{az} vs DS	-0.04	-0.07	0.11	0.17	0.14	0.04	-0.10	-0.07	-0.12	0.19	-0.05	0.07
	DOA_{el} vs DS	0.02	-0.03	0.21	0.10	0.19	0.21	0.00	-0.02	-0.08	-0.04	-0.06	-0.01
	DOA_{az} vs Distance	-0.36	-0.09	-0.10	-0.10	-0.26	-0.17	-0.33	0.04	-0.23	-0.44	-0.32	-0.41
	DOA_{el} vs Distance	-0.17	0.27	-0.11	0.04	0.04	0.01	-0.18	-0.01	-0.23	-0.27	-0.24	-0.34
Cluster DS $log_{10}([s])$	μ	-7.98	-7.85	-8.01	-7.95	-8.00	-7.96	-7.74	-7.75	-7.73	-7.68	-7.67	-7.74
	σ	0.24	0.14	0.14	0.13	0.13	0.14	0.10	0.17	0.08	0.11	0.12	0.15
Cluster DOA_{az} $log_{10}([°])$	μ	1.04	1.03	0.92	1.02	0.95	0.99	0.80	0.89	0.79	0.90	0.89	0.90
	σ	0.12	0.09	0.11	0.09	0.08	0.07	0.14	0.13	0.10	0.06	0.14	0.10
Cluster DOA_{el} $log_{10}([°])$	μ	0.97	0.97	0.98	1.03	0.94	0.94	0.69	0.62	0.72	0.56	0.69	0.76
	σ	0.24	0.24	0.23	0.19	0.18	0.19	0.13	0.17	0.07	0.11	0.11	0.14
Cluster XPD_H (dB)	μ	8.50	N/A	9.08	N/A	8.91	N/A	8.19	N/A	6.59	N/A	4.51	N/A
	σ	5.18	N/A	5.14	N/A	4.44	N/A	4.45	N/A	3.60	N/A	3.99	N/A
Cluster XPD_V (dB)	μ	N/A	10.09	N/A	11.57	N/A	13.27	N/A	6.63	N/A	7.84	N/A	6.27
	σ	N/A	4.73	N/A	4.27	N/A	4.09	N/A	4.08	N/A	4.73	N/A	3.71
Cluster cross-correlation	DOA_{az} vs DS	0.71	0.73	0.51	0.61	0.74	0.56	0.46	0.83	0.36	0.53	0.83	0.72
	DOA_{el} vs DS	0.05	0.75	0.44	0.52	0.71	0.47	0.61	0.64	0.26	0.13	0.65	0.37
	DOA_{az} vs Distance	0.28	0.002	-0.11	-0.26	-0.43	0.34	0.54	0.42	0.11	0.07	0.60	0.31
	DOA_{el} vs Distance	0.25	0.14	-0.14	0.16	-0.19	0.18	-0.25	0.26	0.08	-0.33	0.39	-0.45
MCD_T	μ	0.28	0.26	0.26	0.32	0.28	0.27	0.15	0.14	0.18	0.14	0.17	0.15
	σ	0.28	0.25	0.24	0.28	0.27	0.26	0.15	0.13	0.04	0.11	0.12	0.11
intra-cluster distribution	delay	lognormal/weibull	lognormal/weibull	lognormal/weibull	lognormal/weibull	lognormal/weibull	lognormal/weibull	lognormal/weibull	lognormal/weibull	lognormal/weibull	lognormal/weibull	lognormal/weibull	lognormal/weibull
	Amp	lognormal/weibull	lognormal/Weibull	lognormal/weibull	lognormal/weibull	lognormal/weibull	lognormal/weibull	lognormal/weibull	lognormal/weibull	lognormal/weibull	lognormal/weibull	lognormal/weibull	lognormal/weibull
	DOA_{az}	Von Mises	Von Mises	Von Mises	Von Mises	Von Mises	Von Mises	Von Mises	Von Mises	Von Mises	Von Mises	Von Mises	Von Mises
	DOA_{el}	Von Mises	Von Mises	Von Mises	Von Mises	Von Mises	Von Mises	Von Mises	Von Mises	Von Mises	Von Mises	Von Mises	Von Mises
Number of clusters		9.91	10.36	10.23	9.96	10.07	10.13	7.77	7.49	8.45	6.85	6.95	7.28
SMC per cluster		8.24	8.7	7.13	9.25	8.08	7.86	3.99	3.71	3.15	4.53	6.31	6.35
$Cluster average DOA_{az}$ size (°)		11.55	10.7	8.96	11.03	9.40	10.40	7.54	8.09	7.14	8.23	8.58	8.42
$Cluster average DOA_{el}$ size (°)		13.44	9.52	10.98	10.80	9.47	9.07	5.35	4.55	5.78	4.24	5.55	6.32

Bibliography

[1] Andreas Richter. Estimation of radio channel parameters: Models and algorithms. ISLE, 2005.

[2] G Steinbock, Troels Pedersen, B Fleury, Wei Wang, and Ronald Raulefs. Distance Dependent Model for the Delay Power Spectrum of In-room Radio Channels. *IEEE Transactions on Antennas and Propagation*, 61(8):4327–4340, 2013.

[3] Michael Cheffena. Propagation channel characteristics of industrial wireless sensor networks [wireless corner]. *IEEE Antennas and Propagation Magazine*, 58(1):66–73, 2016.

[4] Alexandros Palaios, Yann Labou, and Petri Mähönen. A study on the forest radio propagation characteristics in european mixed forest environment. In *2014 IEEE Military Communications Conference*, pages 376–381. IEEE, 2014.

[5] Claude Oestges, Belén Montenegro Villacieros, and Danielle Vanhoenacker-Janvier. Radio channel characterization for moderate antenna heights in forest areas. *IEEE Transactions on Vehicular Technology*, 58(8):4031–4035, 2009.

[6] Yu Song Meng, Yee Hui Lee, and Boon Chong Ng. Investigation of rainfall effect on forested radio wave propagation. *IEEE Antennas and Wireless Propagation Letters*, 7:159–162, 2008.

[7] Theodore S Rappaport et al. *Wireless communications: principles and practice*, volume 2. Prentice Hall PTR New Jersey, 1996.

[8] K. Bullington. Radio Propagation at Frequencies above 30 Megacycles. *Proceedings of the IRE*, 35(10):128–136, 1947.

[9] Lucien Boithias and L-J Libols. *Radio wave propagation*. North Oxford acad. London, 1987.

[10] Michael R Andrews, Partha P Mitra, and Robert DeCarvalho. Tripling the Capacity of Wireless Communications Using Electromagnetic Polarization. *Nature*, 409(6818):316–318, 2001.

[11] Seok Chul Kwon and Gordon L. Stüber. Geometrical theory of channel depolarization. *IEEE Transactions on Vehicular Technology*, 60(8):3542–3556, 2011.

[12] Markus Landmann. *Limitations of Experimental Channel Characterisation*. PhD thesis, 2008.

[13] Andreas Richter. Parametric modelling and estimation of distributed diffuse scattering components of radio channels parametric modelling and estimation of distributed diffuse scattering components of radio. *cost273 TD(03)198*, 2003.

[14] Juho Poutanen, Jussi Salmi, Katsuyuki Haneda, Veli-Matti Kolmonen, and Pertti Vainikainen. Angular and shadowing characteristics of dense multipath components in indoor radio channels. *Antennas and Propagation, IEEE Transactions on*, 59(1):245–253, 2011.

[15] Francesco Mani, François Quitin, and Claude Oestges. Directional spreads of dense multipath components in indoor environments: Experimental validation of a ray-tracing approach. *Antennas and Propagation, IEEE Transactions on*, 60(7):3389–3396, 2012.

[16] Andreas Richter, Jussi Salmi, and Visa Koivunen. Distributed scattering in radio channels and its contribution to mimo channel capacity. In *Antennas and Propagation, 2006. EuCAP 2006. First European Conference on*, pages 1–7. IEEE, 2006.

[17] Andreas Richter and Reiner S Thomä. Parametric modelling and estimation of distributed diffuse scattering components of radio channels. 2003.

[18] David A Hill. *Electromagnetic fields in cavities: deterministic and statistical theories*, volume 35. John Wiley & Sons, 2009.

[19] Wallace Clement Sabine. *Collected papers on acoustics*. Harvard university press, 1922.

[20] Carl F Eyring. Reverberation time in dead rooms. *The Journal of the Acoustical Society of America*, 1(2A):168–168, 1930.

[21] C.L. Holloway, M.G. Cotton, and P. McKenna. A model for predicting the power delay profile characteristics inside a room. *IEEE Transactions on Vehicular Technology*, 48(4):1110–1120, jul 1999.

[22] R.F. Rudd. The prediction of indoor radio channel impulse response. *IET Seminar Digests*, (m):392–392, 2007.

[23] J Bach Andersen, J Ø Nielsen, GF Pedersen, G Bauch, and M Herdin. Room electromagnetics. *Antennas and Propagation Magazine, IEEE*, 49(2):27–33, 2007.

[24] Jesper Ødum Nielsen, Jorgen Bach Andersen, Gert Frolund Pedersen, and Mauro Pelosi. On Polarization and Frequency Dependence of Diffuse Indoor Propagation. *2011 IEEE Vehicular Technology Conference (VTC Fall)*, (2):1–5, sep 2011.

[25] Emmeric Tanghe, Davy P. Gaillot, Martine Liénard, Luc Martens, and Wout Joseph. Experimental analysis of dense multipath components in an industrial environment. *IEEE Transactions on Antennas and Propagation*, 62(7):3797–3805, 2014.

[26] Aliou Bamba, Wout Joseph, Emmeric Tanghe, Gunter Vermeeren, and Luc Martens. Circuit model for diffuse multipath and electromagnetic absorption prediction in rooms. *IEEE Transactions on Antennas and Propagation*, 61(6):3292–3301, 2013.

[27] Gerhard Steinböck, Troels Pedersen, Bernard Henri Fleury, Wei Wang, and Ronald Raulefs. Experimental Validation of the Reverberation Effect in Room Electromagnetics. *IEEE Transactions on Antennas and Propagation*, 63(5):2041–2053, 2015.

[28] Adel AM Saleh and Reinaldo Valenzuela. A statistical model for indoor multipath propagation. *IEEE Journal on selected areas in communications*, 5(2):128–137, 1987.

[29] Suiyan Geng and Pertti Vainikainen. Clustering Characterization for UWB Indoor Communications. pages 1–5., 2010.

[30] Nicolai Czink, Xuefeng Yin, Hüseyin Özcelik, Markus Herdin, Ernst Bonek, and Bernard H. Fleury. Cluster characteristics in a MIMO indoor propagation environment. *IEEE Transactions on Wireless Communications*, 6(4):1465–1474, 2007.

[31] Chia-Chin Chong, Youngeil Kim, and Seong-Soo Lee. A statistical based uwb multipath channel model for the indoor environments wpan applications. In *IEEE Proceedings. Intelligent Vehicles Symposium, 2005.*, pages 525–530. IEEE, 2005.

[32] Lassi Hentila, Mikko Alatossava, Nicolai Czink, and Pekka Kyosti. Cluster-level parameters at 5.25 ghz indoor-to-outdoor and outdoor-to-indoor mimo

radio channels. In *2007 16th IST Mobile and Wireless Communications Summit*, pages 1–5. IEEE, 2007.

[33] Weihui Dong, Jianhua Zhang, Xinyin Gao, Ping Zhang, and Yufei Wu. Cluster identification and properties of outdoor wideband mimo channel. In *2007 IEEE 66th Vehicular Technology Conference*, pages 829–833. IEEE, 2007.

[34] Kuo Hui Li, Mary Ann Ingram, and Anh Van Nguyen. Impact of clustering in statistical indoor propagation models on link capacity. *IEEE Transactions on Communications*, 50(4):521–523, 2002.

[35] Quentin H. Spencer, Brian D. Jeffs, Michael a. Jensen, and Lee L. Swindlehurst. Modeling the statistical time and angle of arrival characteristics of an indoor multipath channel. *IEEE Journal on Selected Areas in Communications*, 18(3):347–360, 2000.

[36] Mahdi Golparvar Roozbahani and Esrafil Jedari. A new statistical wideband spatio-temporal channel model for 5-GHz band WLAN systems. *IEEE Journal on Selected Areas in Communications*, 26(7):1328–1330, 2008.

[37] Nicolai Czink, Ernst Bonek, Lassi Hentilä, Jukka Pekka Nuutinen, and Juha Ylitalo. Cluster-based MIMO channel model parameters extracted from indoor time-variant measurements. *GLOBECOM - IEEE Global Telecommunications Conference*, (1):1–5, 2006.

[38] Joseph B Keller. Geometrical theory of diffraction. *JOSA*, 52(2):116–130, 1962.

[39] Robert G Kouyoumjian and Prabhakar H Pathak. A uniform geometrical theory of diffraction for an edge in a perfectly conducting surface. *Proceedings of the IEEE*, 62(11):1448–1461, 1974.

[40] Constantine A Balanis. Antenna theory: A review. *Proceedings of the IEEE*, 80(1):7–23, 1992.

[41] RH Clarke. A statistical theory of mobile-radio reception. *Bell system technical journal*, 47(6):957–1000, 1968.

[42] Arjan Meijerink and Andreas F Molisch. On the physical interpretation of the saleh–valenzuela model and the definition of its power delay profiles. *Antennas and Propagation, IEEE Transactions on*, 62(9):4780–4793, 2014.

[43] Luis M Correia. *Wireless flexible personalized communications*. John Wiley & Sons, Inc., 2001.

[44] T Kürner and T Neubauer. Wireless flexible personalised communications, 2001.

[45] P Kyosti et al. Ist, tech. rep. ist-4-027756 winner ii d1. 1.2 v1. 2. *WINNER II channel models*.

[46] Nicolai Czink. *The random-cluster model: a stochastic MIMO channel model for broadband wireless communication systems of the 3rd generation and beyond*. Institut fur Nachrichtentechnik und Hochfrequenztechnik,Vienna: Technische U niversitat Wien, 2007.

[47] Lingfeng Liu, Claude Oestges, Juho Poutanen, Katsuyuki Haneda, Pertti Vainikainen, François Quitin, Fredrik Tufvesson, and Philippe Doncker. The COST 2100 MIMO channel model. *IEEE Wireless Communications*, 19(6):92–99, 2012.

[48] Emmeric Tanghe, Wout Joseph, Leen Verloock, Luc Martens, Henk Capoen, Kobe Van Herwegen, and Wim Vantomme. The industrial indoor channel: Large-scale and temporal fading at 900, 2400, and 5200 MHz. *IEEE Transactions on Wireless Communications*, 7(7):2740–2751, 2008.

[49] Davy P. Gaillot, Emmeric Tanghe, Wout Joseph, Pierre Laly, Viet Chi Tran, Martine Lienard, and Luc Martens. Polarization properties of specular and dense multipath components in a large industrial hall. *IEEE Transactions on Antennas and Propagation*, 63(7):3219–3228, 2015.

[50] M. Cheffena Y. Ai and Q. Li. Power Delay Profile Analysis and Modeling of Industrial Indoor Channels. *2015 9th European Conference on Antennas and Propagation (EuCAP), Lisbon*, pages 1–5, 2015.

[51] M. Cheffena Y. Ai and Q. Li. Radio Frequency Measurements and Capacity Analysis for Industrial Indoor Environments. *2015 9th European Conference on Antennas and Propagation (EuCAP)*, pages 1–5, 2015.

[52] Theodore S. Rappaport and Clare D. Mcgillem. UHF Fading in Factories. *IEEE Journal on Selected Areas in Communications*, 7(1):40–48, 1989.

[53] S. Kjesbu Brunsvik and T. Radiowave propagation in industrial environments. *Industrial Electronics Society, 2000. IECON 2000. 26th Annual Confjerence of the IEEE, Nagoya*, 4:2425–2430, 2000.

[54] Zoubir Irahhautent, G. J M Janssen, Homayoun Nikookar, Alex Yarovoy, and Leo P. Ligthart. UWB channel measurements and results for office and industrial environments. *ICUWB2006: 2006 IEEE International Conference on Ultra-Wideband - Proceedings*, pages 225–230, 2007.

[55] Johan Karedal, Shurjeel Wyne, Peter Almers, Fredrik Tufvesson, and Andreas F. Molisch. A measurement-based statistical model for industrial ultra-wideband channels. *IEEE Transactions on Wireless Communications*, 6(8):3028–3037, 2007.

[56] Emmeric Tanghe, Wout Joseph, Jeffrey D. Bruyne, Leen Verloock, and Luc Martens. The industrial indoor channel: Statistical analysis of the power delay profile. *AEU - International Journal of Electronics and Communications*, 64(9):806–812, 2010.

[57] Dirk Hampicke, Andreas Richter, Axel Schneider, Gerd Sommerkorn, RS Thoma, and Uwe Trautwein. Characterization of the directional mobile radio channel in industrial scenarios, based on wideband propagation measurements. In *Vehicular Technology Conference, 1999. VTC 1999-Fall. IEEE VTS 50th*, volume 4, pages 2258–2262. IEEE, 1999.

[58] A. Miaoudakis, A. Lekkas, G. Kalivas, and S. Koubias. Radio channel characterization in industrial environments and spread spectrum modem performance. *2005 IEEE Conference on Emerging Technologies and Factory Automation*, 1:87–93, 2005.

[59] LR Nair and Bodhaswar T Maharaj. Comparative model analysis for a dual-polarized indoor and industrial mimo system. In *2009 IEEE International Conference on Wireless and Mobile Computing, Networking and Communications*, pages 7–12. IEEE, 2009.

[60] Daniel Sexton, Michael Mahony, Michael Lapinski, and Jay Werb. Radio channel quality in industrial wireless sensor networks. In *Sensors for Industry Conference*, pages 88–94, 2005.

[61] Shuiping Luo, Nagesh Polu, Zhizhang Chen, and Jeff Slipp. Rf channel modeling of a wsn testbed for industrial environment. In *2011 IEEE Radio and Wireless Symposium*, pages 375–378. IEEE, 2011.

[62] V.C. Gungor, Bin Lu, and G.P. Hancke. Opportunities and Challenges of Wireless Sensor Networks in Smart Grid. *IEEE Transactions on Industrial Electronics*, 57(10):3557–3564, 2010.

[63] Claude Oestges, D. Vanhoenacker-Janvier, and Bruno Clerckx. Channel Characterization of Indoor Wireless Personal Area Networks. *IEEE Transactions on Antennas and Propagation*, 54(11):3143–3150, 2006.

[64] Theodore S. Rappaport, Scott Y. Seidel, and Koichiro Takamizawa. Statistical Channel Impulse Response Models for Factory and Open Plan Building Radio Communication System Design. *IEEE Transactions on Communications*, 39(5):794–807, 1991.

[65] Yun Ai, Michael Cheffena, Matthias Pätzold, et al. Geometry-based modeling of wideband industrial indoor radio propagation channels. In *Industrial Electronics Society, IECON 2015-41st Annual Conference of the IEEE*, pages 4299–4304. IEEE, 2015.

[66] Michael Cheffena. Industrial indoor multipath propagationa physical-statistical approach. In *2014 IEEE 25th Annual International Symposium on Personal, Indoor, and Mobile Radio Communication (PIMRC)*, pages 68–72. IEEE, 2014.

[67] M. A. Matin, Kazi Afrina Yasmeen, M. A. Mohd Ali, A. K. M. Wahiduzzaman, and Md. Ahamed Imtiaz. Statistical model for UWB channel in an industrial environment. *2008 International Conference on Microwave and Millimeter Wave Technology*, (4):1015–1017, 2008.

[68] Yi-Cheng Lin and Kamal Sarabandi. A Monte Carlo coherent scattering model for forest canopies using fractal-generated trees. *IEEE Transactions on Geoscience and Remote Sensing*, 37(1):440–451, 1999.

[69] M.G. Cuinas, I.; Acuna, J.; Sanchez. Propagation Model for Small Urban Macrocell in Actual Vegetation Scenarios. *Antennas and Propagation (EuCAP), 2013 7th European Conference on*, pages 3505–3507, 2013.

[70] Gaurav G Joshi, Carl B Dietrich, Christopher R Anderson, William G Newhall, William A Davis, J Isaacs, and Gregory Barnett. Near-ground channel measurements over line-of-sight and forested paths. *IEE Proceedings-Microwaves, Antennas and Propagation*, 152(6):589–596, 2005.

[71] R Tewari, S Swarup, and M Roy. An empirical result for the height gain in forest medium. *IEEE transactions on antennas and propagation*, 32(11):1265–1268, 1984.

[72] RK Tewari, S Swarup, and Manujendra N Roy. Radio wave propagation through rain forests of india. *IEEE transactions on antennas and propagation*, 38(4):433–449, 1990.

[73] Empirical near ground path loss modeling in a forest at VHF and UHF bands. *IEEE Transactions on Antennas and Propagation*, 57(5):1461–1468, 2009.

[74] MO Al-Nuaimi and RBL Stephens. Measurements and prediction model optimisation for signal attenuation in vegetation media at centimetre wave frequencies. *IEE Proceedings-Microwaves, Antennas and Propagation*, 145(3):201–206, 1998.

[75] CCIR. Influences of terrain irregularities and vegetation on troposphere propagation. *CCIR Rep,Geneva*, pages 235–236, 1986.

[76] COST 235. Radio propagation effects on the next-generation fixed-service terrestrial telecommunication systems. *Luxembourg,Final Rep*, 1996.

[77] Mark A Weissberger. An initial critical summary of models for predicting the attenuation of radio waves by trees. 1982.

[78] A Seville. Vegetation attenuation: Modelling and measurements at millimetric frequencies. In *Antennas and Propagation, Tenth International Conference on (Conf. Publ. No. 436)*, volume 2, pages 5–8. IET, 1997.

[79] MO Al-Nuaimi and AM Hammoudeh. Measurements and predictions of attenuation and scatter of microwave signals by trees. *IEE Proceedings-Microwaves, Antennas and Propagation*, 141(2):70–76, 1994.

[80] R Matschek, B Linot, and H Sizun. Model for wave propagation in presence of vegetation based on the utd associating transmitted and lateral waves. In *IEE conference publication*, pages 120–123. Institution of Electrical Engineers, 1999.

[81] Dirk Didascalou, Marwan Younis, and Werner Wiesbeck. Millimeter-wave scattering and penetration in isolated vegetation structures. *IEEE transactions on geoscience and remote sensing*, 38(5):2106–2113, 2000.

[82] Saul a. Torrico and Henry L. Bertoni. Modeling tree effects on path loss in a residential environment. *IEEE Transactions on Antennas and Propagation*, 46(6):872–880, 1998.

[83] R.a.N. De Oliveira, G. Protasio Dos Santos Cavalcante, and G.L. Siqueira. Ray tracing model for mobile systems in a forested environment. *ITS'98 Proceedings. SBT/IEEE International Telecommunications Symposium (Cat. No.98EX202)*, 1998.

[84] Feinian Wang and Kamal Sarabandi. A physics-based statistical model for wave propagation through foliage. *IEEE Transactions on Antennas and Propagation*, 55(3):958–968, 2007.

[85] Neil C Rogers, A Seville, J Richter, D Ndzi, N Savage, R Caldeirinha, AK Shukla, M Al-Nuaimi, K Craig, E Vilar, et al. A generic model of 1-60 ghz radio propagation through vegetation-final report. *Radio Agency, UK*, 2002.

[86] Jürgen Richter, Rafael FS Caldeirinha, Miqdad O Al-Nuaimi, Andy Seville, Neil C Rogers, and Nick Savage. A generic narrowband model for radiowave propagation through vegetation. In *2005 IEEE 61st Vehicular Technology Conference*, volume 1, pages 39–43. IEEE, 2005.

[87] Theodor Tamir. On radio-wave propagation in forest environments. *IEEE Transactions on Antennas and Propagation*, 15(6):806–817, 1967.

[88] Le-Wei Li, Jin-Hou Koh, Tat-Soon Yeo, Mook-Seng Leong, and Pang-Shyan Kooi. Analysis of radiowave propagation in a four-layered anisotropic forest environment. *IEEE transactions on geoscience and remote sensing*, 37(4):1967–1979, 1999.

[89] RBL Stephens, MO Al-Nuaimi, and R Caldeirinha. Characterisation of depolarisation of radio signals by single trees at 20 ghz. In *Radio Science Conference, 1998. NRSC'98. Proceedings of the Fifteenth National*, pages B12–1. IEEE, 1998.

[90] István Z Kovács, PCF Egger, and Kim Olesen. Characterization of cross polarization discrimination in forest environments. In *Vehicular Technology Conference, 2000. IEEE-VTS Fall VTC 2000. 52nd*, volume 2, pages 725–731. IEEE, 2000.

[91] Petr Lédl, P Pechac, and Miloš Mazánek. Time-series prediction of attenuation caused by trees for fixed wireless access systems operating in millimeter waveband. In *Antennas and Propagation, 2003.(ICAP 2003). Twelfth International Conference on (Conf. Publ. No. 491)*, volume 2, pages 646–649. IET, 2003.

[92] M. H. Hashim and S. Stavrou. Dynamic impact characterization of vegetation movements on radiowave propagation in controlled environment. *IEEE Antennas and Wireless Propagation Letters*, 2:316–318, 2003.

[93] Mohamed H. Hashim and Stavros Stavrou. Measurements and modelling of wind influence on radiowave propagation through vegetation. *IEEE Transactions on Wireless Communications*, 5(5):1055–1064, 2006.

[94] MH Hashim, D Mavrakis, and SR Saunders. Measurement and analysis of temporal fading due to moving vegetation. In *Antennas and Propagation, 2003.(ICAP 2003). Twelfth International Conference on (Conf. Publ. No. 491)*, volume 2, pages 650–653. IET, 2003.

[95] Yu Song Meng, Yee Hui Lee, and Boon Chong Ng. Study of the diversity reception in a forested environment. *IEEE Transactions on Wireless Communications*, 8(5):2302–2305, 2009.

[96] Chaymaly Phakasoum, Mir Ghoraishi, Jun-ichi Takada, Koshiro Kitao, and Tetsuro Imai. Frequency characteristics of angular spread for radio wave propagation through foliage. In *Proceedings of the 5th European Conference on Antennas and Propagation (EUCAP)*, pages 3289–3292. IEEE, 2011.

[97] Hung Vu Le, Jun-ichi Takada, Mir Ghoraishi, Chaymaly Phakasoum, Koshiro Kitao, and Tetsuro Imai. Angular spread of the radio wave propagation in foliage environment. In *2012 6th European Conference on Antennas and Propagation (EUCAP)*, pages 3356–3360. IEEE, 2012.

[98] Mir Ghoraishi, Jun-ichi Takada, Chaymaly Phakasoum, Tetsuro Imai, and Koshiro Kitao. Azimuth and delay dispersion of mobile radio wave propagation through vegetation. In *Proceedings of the Fourth European Conference on Antennas and Propagation*, pages 1–4. IEEE, 2010.

[99] N. Savage, D.L. Ndzi, J. Austin, and E. Vilar. Signal propagation through vegetation: consideration for future broadband communication systems. In *Antennas and Propagation, 2003. (ICAP 2003). Twelfth International Conference on (Conf. Publ. No. 491)*, volume 2, pages 641–645 vol.2, March 2003.

[100] Abdelmottaleb Nasr. *Contribution à la caractérisation et à la modélisation des canaux MIMO*. PhD thesis, Lille 1, 2009.

[101] Paul Stefanut. *Application des algorithmes de haute résolution à la localisation de mobiles en milieu confiné*. PhD thesis, Lille 1, 2010.

[102] T Engin Tuncer and Benjamin Friedlander. *Classical and modern direction-of-arrival estimation*. Academic Press, 2009.

[103] Petre Stoica and Randolph L Moses. *Introduction to spectral analysis*, volume 1. Prentice hall Upper Saddle River, 1997.

[104] Jack Capon. High-resolution frequency-wavenumber spectrum analysis. *Proceedings of the IEEE*, 57(8):1408–1418, 1969.

[105] Ralph Schmidt. Multiple emitter location and signal parameter estimation. *IEEE transactions on antennas and propagation*, 34(3):276–280, 1986.

[106] Ralph Otto Schmidt. A signal subspace approach to multiple emitter location spectral estimation. *Ph. D. Thesis, Stanford University*, 1981.

[107] Richard Roy and Thomas Kailath. Esprit-estimation of signal parameters via rotational invariance techniques. *Acoustics, Speech and Signal Processing, IEEE Transactions on*, 37(7):984–995, 1989.

[108] Jeffrey A Fessler and Alfred O Hero. Space-alternating generalized expectation-maximization algorithm. *Signal Processing, IEEE Transactions on*, 42(10):2664–2677, 1994.

[109] Pei Jung Chung and Johann F Böhme. Doa estimation using fast em and sage algorithms. *Signal Processing*, 82(11):1753–1762, 2002.

[110] Emmeric Tanghe, Davy Paul Gaillot, Wout Joseph, Martine Lienard, Degauque Pierre, and Luc Martens. Robustness of high-resolution channel parameter estimators in presence of dense multipath components. *Electronics Letters*, 48(2):130–132, 2012.

[111] Hui Liu, Houshang Darabi, Pat Banerjee, and Jing Liu. Survey of wireless indoor positioning techniques and systems. *IEEE Transactions on Systems, Man, and Cybernetics, Part C (Applications and Reviews)*, 37(6):1067–1080, 2007.

[112] Aliou Bamba, Wout Joseph, Gunter Vermeeren, Emmeric Tanghe, Davy Paul Gaillot, Jørgen B Andersen, Jesper Ødum Nielsen, Martine Lienard, and Luc Martens. Validation of experimental whole-body sar assessment method in a complex indoor environment. *Bioelectromagnetics*, 34(2):122–132, 2013.

[113] Dag Akerberg. Properties of a tdma pico cellular office communication system. In *Vehicular Technology Conference, 1989, IEEE 39th*, pages 186–191. IEEE, 1989.

[114] François Quitin, Claude Oestges, François Horlin, and Philippe De Doncker. Polarization measurements and modeling in indoor nlos environments. *IEEE transactions on wireless communications*, 9(1):21–25, 2010.

[115] Lasse Vuokko, Pertti Vainikainen, and Jun-ichi Takada. Clusterization of measured direction-of-arrival data in an urban macrocellular environment. In *Personal, Indoor and Mobile Radio Communications, 2003. PIMRC 2003. 14th IEEE Proceedings on*, volume 2, pages 1222–1226. IEEE, 2003.

[116] Weina Wang and Yunjie Zhang. On fuzzy cluster validity indices. *Fuzzy sets and systems*, 158(19):2095–2117, 2007.

[117] Susana Mota, F Perez-Fontan, and Armando Rocha. Estimation of the Number of Clusters in Multipath Radio Channel Data Sets. *IEEE transactions on antennas and ...*, 61(5):2879–2883, 2013.

[118] Christian Schneider, Maysam Ibraheam, Stephan Häfner, Martin Käske, Matthias Hein, and Reiner S Thomä. On the reliability of multipath cluster estimation in realistic channel data sets. In *The 8th European Conference on Antennas and Propagation (EuCAP 2014)*, pages 449–453. IEEE, 2014.

[119] Jerome Friedman, Trevor Hastie, and Robert Tibshirani. *The elements of statistical learning*, volume 1. Springer series in statistics Springer, Berlin, 2001.

[120] Christian Schneider, Martin Bauer, Milan Narandzic, WA Th Kotterman, and Reiner S Thoma. Clustering of mimo channel parameters-performance comparison. In *Vehicular Technology Conference, 2009. VTC Spring 2009. IEEE 69th*, pages 1–5. IEEE, 2009.

[121] Martin Steinbauer, Huseyin Ozcelik, Helmut Hofstetter, Christoph F Mecklenbrauker, and Ernst Bonek. How to quantify multipath separation. *IEICE transactions on electronics*, 85(3):552–557, 2002.

[122] Carl Gustafson, Katsuyuki Haneda, Shurjeel Wyne, and Fredrik Tufvesson. On mm-wave multipath clustering and channel modeling. *Antennas and Propagation, IEEE Transactions on*, 62(3):1445–1455, 2014.

[123] Maria-Teresa Martinez-Ingles, Davy P Gaillot, Juan Pascual-Garcia, Jose-Maria Molina Garcia-Pardo, Martine Lienard, José-Víctor Rodríguez, and Leandro Juan-Llácer. Impact of clustering at mmw band frequencies. In *2015 IEEE International Symposium on Antennas and Propagation & USNC/URSI National Radio Science Meeting*, pages 1009–1010. IEEE, 2015.

[124] Nicolai Czink, Pierluigi Cera, Jari Salo, Ernst Bonek, Jukka-Pekka Nuutinen, and Juha Ylitalo. *Automatic clustering of MIMO channel parameters using the multi-path component distance measure*. Citeseer, 2005.

[125] N. Czink, P. Cera, J. Salo, E. Bonek, J. P. Nuutinen, and J. Ylitalo. Improving clustering performance using multipath component distance. *Electronics Letters*, 42(1):33–45, Jan 2006.

[126] Ujjwal Maulik and Sanghamitra Bandyopadhyay. Performance evaluation of some clustering algorithms and validity indices. *IEEE Transactions on Pattern Analysis and Machine Intelligence*, 24(12):1650–1654, 2002.

[127] Malay K. Pakhira, Sanghamitra Bandyopadhyay, and Ujjwal Maulik. Validity index for crisp and fuzzy clusters. *Pattern Recognition*, 37:487–501, 2004.

[128] Krzysztof Kryszczuk and Paul Hurley. Estimation of the number of clusters using multiple clustering validity indices. In *International Workshop on Multiple Classifier Systems*, pages 114–123. Springer, 2010.

[129] Kim Do-Jong, PARK Yong-Woon, and PARK Dong-Jo. A novel validity index for determination of the optimal number of clusters. *IEICE Transactions on Information and Systems*, 84(2):281–285, 2001.

[130] Nicolai Czink, Ruiyuan Tian, Shurjeel Wyne, Fredrik Tufvesson, Jukka-Pekka Nuutinen, Juha Ylitalo, Ernst Bonek, and Andreas F Molisch. Tracking time-variant cluster parameters in mimo channel measurements. In *Communications and Networking in China, 2007. CHINACOM'07. Second International Conference on*, pages 1147–1151. IEEE, 2007.

[131] Greg Hamerly and Charles Elkan. Alternatives to the k-means algorithm that find better clusterings. In *Proceedings of the eleventh international conference on Information and knowledge management*, pages 600–607. ACM, 2002.

[132] J Salmi, J Poutanen, K Haneda, A Richter, V-M Kolmonen, P Vainikainen, and AF Molisch. Incorporating diffuse scattering in geometry-based stochastic mimo channel models. In *Proceedings of the Fourth European Conference on Antennas and Propagation*, pages 1–5. IEEE, 2010.

[133] Nicolai Czink, Ernst Bonek, Lassi Hentila, Jukka-Pekka Nuutinen, and Juha Ylitalo. Wlc06-2: Cluster-based mimo channel model parameters extracted

from indoor time-variant measurements. In *IEEE Globecom 2006*, pages 1–5. IEEE, 2006.

[134] S. Cheng, D. P. Gaillot, P. Laly, M. Linard, T. Demol, E. Tanghe, W. Joseph, and L. Martens. Polarimetric properties and modeling of the power delay profile in large hall scenarios. In *Networks and Communications (EuCNC), 2015 European Conference on*, pages 113–117, June 2015.

[135] S. Cheng, D. P. Gaillot, E. Tanghe, P. Laly, T. Demol, W. Joseph, L. Martens, and M. Liénard. Polarimetric distance-dependent models for large hall scenarios. *IEEE Transactions on Antennas and Propagation*, 64(5):1907–1917, May 2016.

[136] S. Cheng, M. T. Martinez-Ingles, D. P. Gaillot, J. M. Molina-Garcia-Pardo, M. Linard, and P. Degauque. Performance of a novel automatic identification algorithm for the clustering of radio channel parameters. *IEEE Access*, 3:2252–2259, 2015.

[137] D. P. Gaillot J. M. Molina-Garcia-Pardo Martine Liénard S. Cheng, M. T. Martinez-Ingles and Pierre Degauque. Evaluation of a novel automatic identification algorithm for the clustering of radio channels. In *2015 Joint NEWCOM - COST Workshop on Wireless Communications (JNCW) 2015, Barcelona, Spain 2015, Temporary Document TD(15)W1015*, 2015.

[138] M. Liénard P. Degauque M. T. Martinez-Ingles S. Cheng, D. P. Gaillot and J. M. Molina-Garcia-Pardo. Clustering of radio channel parameters: Evaluation of a novel automatic identification algorithm. In *2016 IEEE Antennas and Propagation Society International Symposium, Fajardo Puerto Rico*, 2016.

[139] François Quitin, Claude Oestges, François Horlin, and Philippe De Doncker. Diffuse multipath component characterization for indoor mimo channels. In *Proceedings of the Fourth European Conference on Antennas and Propagation*, pages 1–5. IEEE, 2010.

[140] Ding Xu, Jianhua Zhang, Xinying Gao, Ping Zhang, and Yufei Wu. Indoor office propagation measurements and path loss models at 5.25 ghz. In *Vehicular Technology Conference, 2007. VTC-2007 Fall. 2007 IEEE 66th*, pages 844–848. IEEE, 2007.

[141] Philipp Berens et al. Circstat: a matlab toolbox for circular statistics. *J Stat Softw*, 31(10):1–21, 2009.